APPLIED COMPUTATIONAL ELECTROMAGNETICS SOCIETY JOURNAL

October 2022
Vol. 37 No. 10
ISSN 1054-4887

The ACES Journal is abstracted in INSPEC, in Engineering Index, DTIC, Science Citation Index Expanded, the Research Alert, and to Current Contents/Engineering, Computing & Technology.

The illustrations on the front cover have been obtained from the ARC research group at the Department of Electrical Engineering, Colorado School of Mines

Published, sold and distributed by: River Publishers, Alsbjergvej 10, 9260 Gistrup, Denmark

OCTOBER 2022 REVIEWERS

Agarwal
Ravi Kumar Arya
Toure Baidy
Behrokh Beiranvand
Mahendran C.
Vinh Dang
Zaheer Ahmed Dayo
Bernhard J. Hoenders
Ashutosh Kedar
Liu
Matteo Bruno Lodi
Fabrizio Loreto
Valentin Mateev
Antonino Musolino
Antonio Orlandi
Jagadheswaran Rajendran
Suganthi Santhanam
Vladimir Stanković
Qusai Hadi Sultan
Marsellas Waller
Li Wu
Pei Xiao
Abubakar Yakubu
Shihyuan Yeh
Wentao Yuan

THE APPLIED COMPUTATIONAL ELECTROMAGNETICS SOCIETY JOURNAL

Vol. 37 No. 10 October 2022

TABLE OF CONTENTS

An Efficient Method for Predicting the Shielding Effectiveness of an Apertured Enclosure with an Interior Enclosure based on Electromagnetic Topology

Jin-Cheng Zhou and Xue-Tian Wang

School of Integrated Circuits and Electronics
Beijing Institute of Technology, Beijing, 100081, China
zjc.chn@gmail.com, wangxuetian@bit.edu.cn

Abstract **–** A fast analytical method has been proposed for predicting the shielding effectiveness (SE) and resonances of an apertured enclosure with an interior enclosure. Under the concept of electromagnetic topology, the monitor point and the walls are treated as nodes, and the space between them is treated as tubes. The propagation relationships at tube level and reflection relationships at node level are derived as the propagation matrix. After modeling the front wall of the interior enclosure as a junction between two waveguides, an equivalent circuital model of the enclosures is derived. The front wall and the window structure in front of the adjacent space of the interior enclosure are considered as a three-port scattering matrix. Then we can use the extended BLT equations to calculate the voltage response at each node. Results from the proposed method are compared with those from the numerical method, and the results have a good agreement while it can dramatically save calculation time.

Index Terms **–** aperture coupling, general Baum-Liu-Tesche equation, Shielding effectiveness

I. INTRODUCTION

Nowadays, because electronic devices contain a lot of high sensitive and valuable electronic devices, including processors, field-programmable gate arrays, and other chips, they may often become victims of electromagnetic interference.

Electromagnetic shielding is one of the most widely used techniques to protect valuable electronics. The performance of a shielding enclosure is quantified by its shielding effectiveness (SE), in which means the ratio of the electric field is compared at a monitor point without and with the enclosure [1].

The calculation methods for shielding effectiveness (SE) of shielding enclosure mainly includes numerical methods and analytical methods, including finite-difference time-domain method [2], method of moments [3, 4], transmission line matrix (TLM) method [5], and finite element (FEM) method [6]. Numerical methods can handle complicated structures but need a lot of time to set up model and always consume more computational resources.

The analytical formulations have many simplifications and approximations in the calculation process, but also have a much higher calculation efficiency and input parameters are more concise. For instance, in the Robinson's method [7, 8], the rectangular enclosure is modeled by a short-circuited rectangular waveguide and the aperture is represented by a coplanar strip transmission line. However, the equivalent circuit models mentioned above can barely handle complex enclosure structures.

Electromagnetic topology (EMT) provides a useful tool to study the coupling problems of complicated electrical systems, which treat the complex interaction problem as smaller and more manageable problems [9]. By applying the EMT concept, the Baum-Liu-Tesche (BLT) equation can be derived to calculate the voltage and current responses at the nodes of a general multiconductor transmission-line network. The extended BLT equation can deal with the voltage and current at all junctions [10, 11]. After transforming the enclosure and aperture into nodes, we can use BLT equation to calculate the SE. Adding another layer of shielding can markedly improve the SE [12–14]. For this reason, the cascaded enclosures have been widely discussed and studied [15–17], but cascaded enclosures will increase physical space. An interior enclosure can also offer another layer of shielding, consequently, the SE will be effectively increased. Compared to cascaded enclosures, the interior enclosure needs less space and can also be used to improve SE.

In this paper, we propose an electromagnetic topology-based method to predict the shielding effectiveness for an apertured enclosure with an interior enclosure. The SE can be predicted fast and accurately over a wide frequency range by this method.

II. ELECTROMAGNETIC TOPOLOGICAL MODEL

The geometry of the apertured enclosure with an interior enclosure on the bottom tail-end illuminated by an external plane wave is shown in Fig. 1. The overall size

Submitted On: July 6, 2022
Accepted On: November 24, 2022
https://doi.org/10.13052/2022.ACES.J.371001

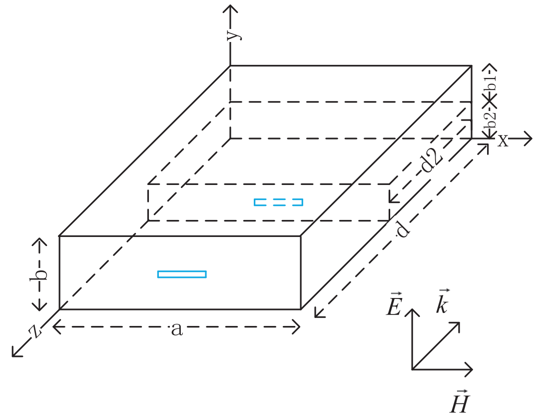

Fig. 1. Apertured enclosure with an interior enclosure on bottom tail-end and the coordinate system, all apertures are positioned centrally in the walls.

of the enclosure is $a \times b \times d$ mm, and the size of the interior enclosure is $a \times b_2 \times d_2$ mm.

The size of the aperture on the front wall and interior wall are $l \times w$ and $l_2 \times w_2$ respectively, and its central point locates at the center of the wall. Additionally, the monitor point P inside the enclosure has the coordinates of (x_p, y_p, z_p). In this paper, we divided the inner structure of the mentioned enclosure in Fig. 1 into three part: the space 1 in front of the interior enclosure, the interior enclosure 2, and the space 3 adjacent to the interior enclosure 2.

The equivalent circuit of the enclosure in Fig. 1 is given in Fig. 2. The side wall is treated as waveguide, then the impedance and propagation constant z_g and k_g are given by:

$$Z_g = Z_0 / \sqrt{1-(\frac{m\lambda}{2a})^2-(\frac{n\lambda}{2b})^2}, \tag{1}$$

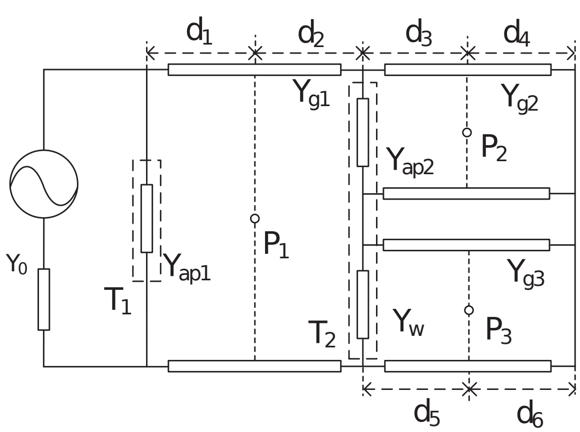

Fig. 2. Equivalent circuit of the enclosure.

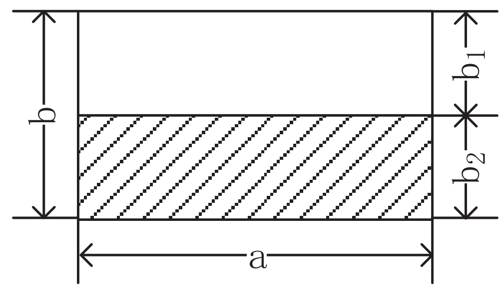

Fig. 3. Cross sectional view of the obstacle, the shadow part is the front wall of the interior enclosure.

$$k_g = k_0 \sqrt{1-(\frac{m\lambda}{2a})^2-(\frac{n\lambda}{2b})^2}. \tag{2}$$

The radiating source is represented by voltage V_0 and impedance of free space $Z_0 = 377\Omega$. The apertures are treated as a coplanar strip transmission line which shorted at each end, its characteristic impedance is given by Gupta et al [18]:

$$Z_{ap} = \frac{j}{2}\frac{l}{a} Z_{os} tan(\frac{k_0 l}{2}). \tag{3}$$

Z_{os} is the aperture characteristic impedance:

$$Z_{os} = 120\pi^2 [\ln(2\frac{1+\sqrt[4]{1-(w_e/b)^2}}{1-\sqrt[4]{1-(w_e/b)^2}})]. \tag{4}$$

Since the enclosure have a thickness, when the $w_e \leqslant \frac{b}{\sqrt{2}}$, we have effective width w_e :

$$w_e = w - \frac{5t}{4\pi}[1+\ln\frac{4\pi w}{t}], \tag{5}$$

where t represents enclosure wall's thickness, w is the width of the slot.

The aperture on the inner enclosure also calculated by Equation 3, where b is replaced by b_2.

In this paper, we modeled the front wall of the interior enclosure as a junction between two different rectangular waveguides, as shown in Fig. 2, when the height of rear waveguide is nearly half of the front one, the equivalent impedance can be writen as [19]:

$$\begin{aligned} Y_w &= \frac{4jb_1}{Z_g \lambda_g}[ln(\frac{1-\alpha^2}{4\alpha})(\frac{1+\alpha}{1-\alpha})^{\frac{1}{2}(\alpha+(1/\alpha))}+\frac{2}{A}], \\ A &= (\frac{1+\alpha}{1-\alpha})^{2\alpha}\frac{1+\sqrt{1-(2b_1/\lambda_g)^2}}{1-\sqrt{1-(2b_1/\lambda_g)^2}} - \frac{1+3\alpha^2}{1-\alpha^2}, \end{aligned} \tag{6}$$

where $\alpha = b_2/b$. Figure 4 gives electromagnetic topology for the enclosure shown in Fig. 1. Node N_1 represents the monitor point in free space, and nodes N_3, N_5, N_7 denote monitor points P_1, P_2 and P_3 inside the sub-enclosures respectively. The aperture on the front wall is represented by nodes N_2, he aperture on the interior wall and the window are represented by node N_4 as a three ports network, and the shorted end of enclosure 2

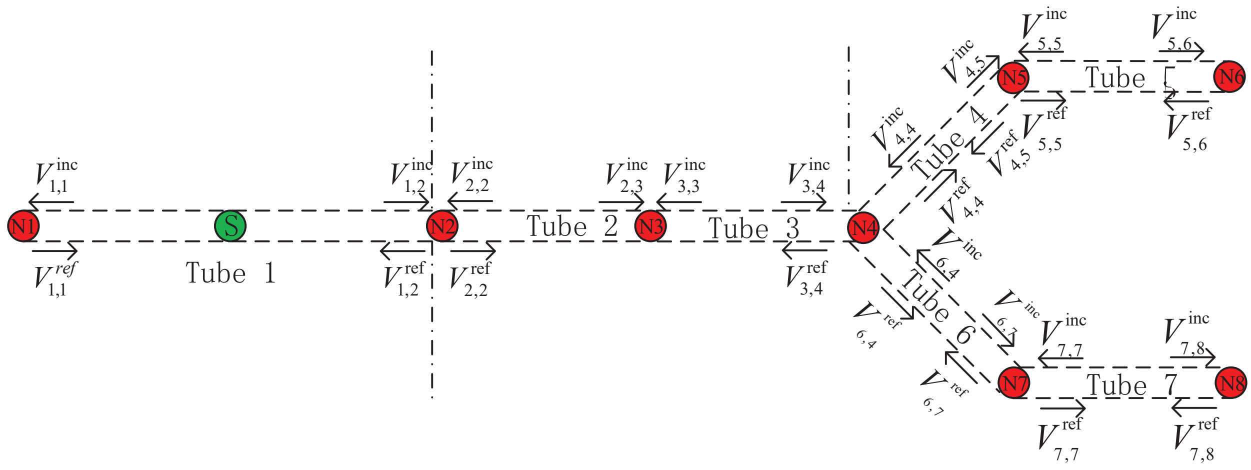

Fig. 4. Signal flow graph of the enclosure.

and space 3 is represented by N_6, N_8. The monitor point N_1 in free space and shorted ends N_6, N_8 are equivalented by a one-port network. Tube 1 denotes the electromagnetic wave propagation in free space, while Tube 2, Tube 3, Tube 4, and Tube 6 are the wave propagation between the monitor points and the apertures/window in sub-enclosures. Tube 5 and Tube 7 denote the wave propagation to the short end of enclosure 2 and space 3 respectively.

The extended BLT equation can be expressed as [10]:

$$\mathbf{V} = (\mathbf{E}+\mathbf{S}) \times (\blacksquare - \mathbf{S})^{-\mathbf{1}} \times \mathbf{V_s}, \tag{7}$$

where $\mathbf{V}$ is the voltage response matrix, $\mathbf{E}$ is the unit matrix, $\mathbf{S}$ is the scattering parameter matrix, $\blacksquare$ represents the propagation matrix, and $\mathbf{V_s}$ represents the source matrix.

Based on Fig. 4, the propagation equation can be given by:

$$\begin{bmatrix} V_{1,1}^{ref} \\ V_{1,2}^{ref} \\ V_{2,2}^{ref} \\ V_{2,3}^{ref} \\ V_{3,3}^{ref} \\ V_{3,4}^{ref} \\ V_{4,4}^{ref} \\ V_{6,4}^{ref} \\ V_{4,5}^{ref} \\ V_{5,5}^{ref} \\ V_{5,6}^{ref} \\ V_{6,7}^{ref} \\ V_{7,7}^{ref} \\ V_{7,8}^{ref} \end{bmatrix} = \begin{bmatrix} 0 & e^{\gamma_0 l_x} & 0 & 0 & 0 & 0 & 0 & 0 & 0 & 0 & 0 & 0 & 0 & 0 \\ e^{\gamma_0 l_x} & 0 & 0 & 0 & 0 & 0 & 0 & 0 & 0 & 0 & 0 & 0 & 0 & 0 \\ 0 & 0 & 0 & e^{g_1 d_1} & 0 & 0 & 0 & 0 & 0 & 0 & 0 & 0 & 0 & 0 \\ 0 & 0 & e^{g_1 d_1} & 0 & 0 & 0 & 0 & 0 & 0 & 0 & 0 & 0 & 0 & 0 \\ 0 & 0 & 0 & 0 & 0 & e^{g_1 d_2} & 0 & 0 & 0 & 0 & 0 & 0 & 0 & 0 \\ 0 & 0 & 0 & 0 & e^{g_1 d_2} & 0 & 0 & 0 & 0 & 0 & 0 & 0 & 0 & 0 \\ 0 & 0 & 0 & 0 & 0 & 0 & 0 & 0 & e^{g_2 d_3} & 0 & 0 & 0 & 0 & 0 \\ 0 & 0 & 0 & 0 & 0 & 0 & 0 & 0 & 0 & 0 & 0 & e^{g_2 d_4} & 0 & 0 \\ 0 & 0 & 0 & 0 & 0 & 0 & e^{g_2 d_3} & 0 & 0 & 0 & 0 & 0 & 0 & 0 \\ 0 & 0 & 0 & 0 & 0 & 0 & 0 & 0 & 0 & 0 & e^{g_3 d_5} & 0 & 0 & 0 \\ 0 & 0 & 0 & 0 & 0 & 0 & 0 & 0 & 0 & e^{g_3 d_5} & 0 & 0 & 0 & 0 \\ 0 & 0 & 0 & 0 & 0 & 0 & 0 & e^{g_2 d_4} & 0 & 0 & 0 & 0 & 0 & 0 \\ 0 & 0 & 0 & 0 & 0 & 0 & 0 & 0 & 0 & 0 & 0 & 0 & 0 & e^{g_3 d_6} \\ 0 & 0 & 0 & 0 & 0 & 0 & 0 & 0 & 0 & 0 & 0 & 0 & e^{g_3 d_6} & 0 \end{bmatrix} \begin{bmatrix} V_{1,1}^{inc} \\ V_{1,2}^{inc} \\ V_{2,2}^{inc} \\ V_{2,3}^{inc} \\ V_{3,3}^{inc} \\ V_{3,4}^{inc} \\ V_{4,4}^{inc} \\ V_{6,4}^{inc} \\ V_{4,5}^{inc} \\ V_{5,5}^{inc} \\ V_{5,6}^{inc} \\ V_{6,7}^{inc} \\ V_{7,‘7}^{inc} \\ V_{7,8}^{inc} \end{bmatrix} - \begin{bmatrix} V_0 \\ 0 \\ 0 \\ 0 \\ 0 \\ 0 \\ 0 \\ 0 \\ 0 \\ 0 \\ 0 \\ 0 \\ 0 \\ 0 \end{bmatrix} \tag{8}$$

l_x is the distance between electromagnetic wave and the aperture on the front wall; $\gamma_0 = jk_0$ is the phase constant of freespace. Where $g_i = jk_0\sqrt{1-(m\lambda/2a_i)^2-(n\lambda/2b_i)^2}$, i is the number of the space/enclosure, d_j shown in Fig. 2 represent the distance between each point in the planar wave propagation direction.

The scattering equation contains the scattering matrix **S** is given by:

$$\begin{bmatrix} V^{ref}_{1,1} \\ V^{ref}_{1,2} \\ V^{ref}_{2,2} \\ V^{ref}_{2,3} \\ V^{ref}_{3,3} \\ V^{ref}_{3,4} \\ V^{ref}_{4,4} \\ V^{ref}_{6,4} \\ V^{ref}_{4,5} \\ V^{ref}_{5,5} \\ V^{ref}_{5,6} \\ V^{ref}_{6,7} \\ V^{ref}_{7,7} \\ V^{ref}_{7,8} \end{bmatrix} = \begin{bmatrix} \rho^1 & 0 & 0 & 0 & 0 & 0 & 0 & 0 & 0 & 0 & 0 & 0 & 0 & 0 \\ 0 & S^2_{11} & S^2_{12} & 0 & 0 & 0 & 0 & 0 & 0 & 0 & 0 & 0 & 0 & 0 \\ 0 & S^2_{21} & S^2_{22} & 0 & 0 & 0 & 0 & 0 & 0 & 0 & 0 & 0 & 0 & 0 \\ 0 & 0 & 0 & S^3_{11} & S^3_{12} & 0 & 0 & 0 & 0 & 0 & 0 & 0 & 0 & 0 \\ 0 & 0 & 0 & S^3_{21} & S^3_{22} & 0 & 0 & 0 & 0 & 0 & 0 & 0 & 0 & 0 \\ 0 & 0 & 0 & 0 & 0 & S^4_{11} & S^4_{12} & S^4_{13} & 0 & 0 & 0 & 0 & 0 & 0 \\ 0 & 0 & 0 & 0 & 0 & S^4_{21} & S^4_{22} & S^4_{23} & 0 & 0 & 0 & 0 & 0 & 0 \\ 0 & 0 & 0 & 0 & 0 & S^4_{31} & S^4_{32} & S^4_{33} & 0 & 0 & 0 & 0 & 0 & 0 \\ 0 & 0 & 0 & 0 & 0 & 0 & 0 & 0 & S^5_{11} & S^5_{12} & 0 & 0 & 0 & 0 \\ 0 & 0 & 0 & 0 & 0 & 0 & 0 & 0 & S^5_{21} & S^5_{22} & 0 & 0 & 0 & 0 \\ 0 & 0 & 0 & 0 & 0 & 0 & 0 & 0 & 0 & 0 & \rho^6 & 0 & 0 & 0 \\ 0 & 0 & 0 & 0 & 0 & 0 & 0 & 0 & 0 & 0 & 0 & S^7_{11} & S^7_{12} & 0 \\ 0 & 0 & 0 & 0 & 0 & 0 & 0 & 0 & 0 & 0 & 0 & S^7_{21} & S^7_{22} & 0 \\ 0 & 0 & 0 & 0 & 0 & 0 & 0 & 0 & 0 & 0 & 0 & 0 & 0 & \rho^8 \end{bmatrix} \begin{bmatrix} V^{inc}_{1,1} \\ V^{inc}_{1,2} \\ V^{inc}_{2,2} \\ V^{inc}_{2,3} \\ V^{inc}_{3,3} \\ V^{inc}_{3,4} \\ V^{inc}_{4,4} \\ V^{inc}_{6,4} \\ V^{inc}_{4,5} \\ V^{inc}_{5,5} \\ V^{inc}_{5,6} \\ V^{inc}_{6,7} \\ V^{inc}_{7,7}V^{inc}_{7,8} \end{bmatrix} \tag{9}$$

$\rho^1 = 0$ is the free space, and $\rho^6 = \rho^8 = -1$ are the short ends. S^3 , S^4 and S^5 represents p_1 , p_2 and p_3:

$$S^3 = S^5 = S^7 = \begin{bmatrix} 0 & 1 \\ 1 & 0 \end{bmatrix}. \tag{10}$$

S^2 can be obtained from network T_1 in Fig 2:

$$S^2 = \begin{bmatrix} \frac{Y_0-Y_{g1}-Y_{ap1}}{Y_0+Y_{g1}+Y_{ap1}} & \frac{2Y_{g1}}{Y_0+Y_{g1}+Y_{ap1}} \\ \frac{2Y_0}{Y_0+Y_{g1}+Y_{ap1}} & \frac{Y_{g1}-Y_0-Y_{ap1}}{Y_0+Y_{g1}+Y_{ap1}} \end{bmatrix}. \tag{11}$$

We neglect the coupling between aperture 2 and window 1, assume that $S^4_{23} = S^4_{32} = 0$ then S^4 is:

$$S^4_{11} = (Y_{g1}Y_{g3} + Y_{g1}Y_w + Y_{g1}Y_{ap2} + Y_{g1}Y_{g2}$$
$$- Y_{g3}Y_{g2} - Y_wY_{g2} - Y_{ap2}Y_{g3} - Y_{ap2}Y_w)/Y^4_t,$$
$$S^4_{12} = 2(Y_{g1}Y_{g3} + Y_{g1}Y_w)/Y^4_t,$$
$$S^4_{13} = 2(Y_{g1}Y_{g2} + Y_{g1}Y_{ap2})/Y^4_t,$$
$$S^4_{21} = 2(Y_{g1}Y_{g2} + Y_{g2}Y_{g3} + Y_{g2}Y_w)/Y^4_t,$$
$$S^4_{22} = (Y_{g1}Y_{g2} + Y_{g2}Y_{g3} + Y_{g2}Y_w - Y_{g1}Y_{ap2}$$
$$- Y_{g3}Y_{ap2} - Y_{ap2}Y_w - Y_{g1}Y_w - Y_{g1}Y_{g3})/Y^4_t,$$
$$S^4_{31} = 2(Y_{g1}Y_{g3} + Y_{g2}Y_{g3} + Y_{g3}Y_{ap2})/Y^4_t,$$
$$S^4_{33} = (Y_{g1}Y_{g3} + Y_{g2}Y_{g3} + Y_{g3}Y_{ap2} - Y_{g1}Y_w -$$
$$Y_{g2}Y_w - Y_{g1}Y_w - Y_{g1}Y_{g2} - Y_{ap2}Y_w)/Y^4_t,$$
$$Y^4_t = Y_{g1}Y_{g3} + Y_{g1}Y_w + Y_{g1}Y_{ap2} + Y_{g1}Y_{g2}$$
$$+ Y_{g2}Y_{g3} + Y_{g2}Y_w + Y_{g3}Y_{ap2} + Y_{ap2}Y_w,$$

where Y_0, Y_g, Y_{ap}, and Y_w are the admittances of free space, rectangular waveguide, aperture and window respectively, and $Y_0 = \frac{1}{Z_0}, Y_g = \frac{1}{Z_g}, Yap = \frac{1}{Z_{ap}}, Y_w = \frac{1}{Z_w}$.

Then the SE at point P is calculated by $SE = -20log(V_p/V_0)$.

III. RESULTS AND DISCUSSION

In this section, the enclosure with an interior enclosure on bottom tail-end are performed to validate the proposed model, the simulation results of the proposed model are compared with the CST-MS software. The walls of the enclosure are assumed to be perfectly conducting, and their thicknesses are defined as 1 mm.

A. Verification for the apertured enclosure with an interior enclosure on bottom tail-end

It is assumed that the dimensions of enclosure shown in Fig. 1 are 200 mm × 120 mm × 600 mm,

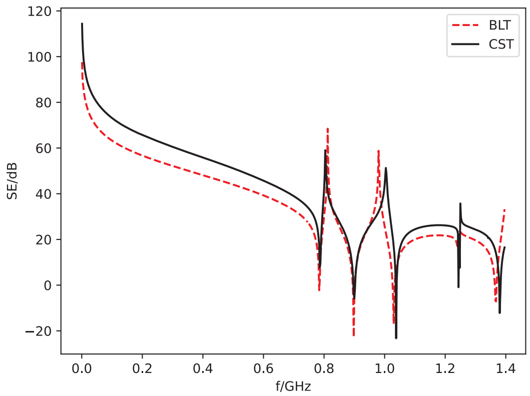

Fig. 5. Comparison between the SE result from proposed method with result of CST for observe point 1.

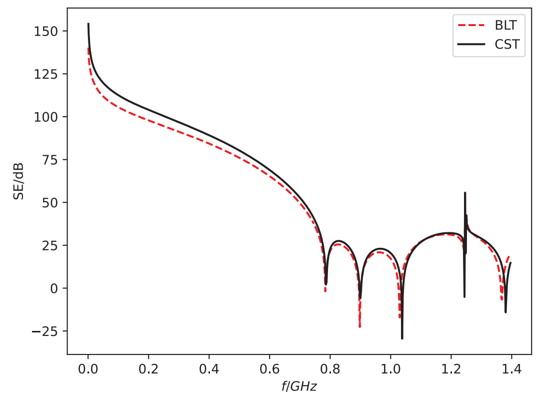

Fig. 6. Comparison between the SE result from proposed method with result of CST for observe point 2.

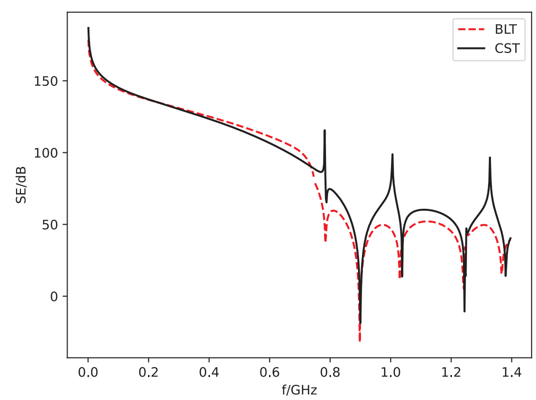

Fig. 7. Comparison between the SE result from proposed method with result of CST for observe point 3.

$b_1 = b_2 = 60mm$, other parameter settings of case 1 are listed in Table 1, including the enclosure dimensions, the aperture size, and the monitor point positions.

Figures 5 to 7 show the SE results of monitor point P_1, P_2, and P_3 obtained by the CST and the proposed method, respectively. The discontinuity in the curve is due to removing the frequency point having a term with a zero denominator in the calculation process. It is observed that the SE results given by these two methods are match up relatively well, indicating that the proposed model is effective in predicting the SE and resonances of a metallic enclosure with an interior enclosure. Besides, in a wide frequency range near the resonant frequency of the enclosure, the SE changes dramatically, and even appears negative values. The physical significance of these values indicates that the apertured enclosure has the worst shielding performance in this condition, and the above phenomenon should be attributed to the resonance effect.

From the comparison between the SE results from different enclosures, it can be seen that: (1) as a double shield enclosure, enclosure 2 has the best shielding performance; (2) a more pronounced deviation can be seen in enclosure 2, the potential reason may be due to the reflection and diffraction between aperture and the window structure. Such reflection are likely to have influenced the results in enclosure 1. Also, the aperture scattering matrix of junction N_4 cannot fully consider the direct electromagnetic coupling between the the aperture of enclosure 2 and the window of space 3.

Table 1: Parametars of the enclosure

No	Enclosure	Aperture	Monitor point
1	$200 \times 120 \times 300$	60×10	100, 60, 450
2	$200 \times 60 \times 300$	50×10	100, 30, 150
3	$200 \times 60 \times 300$		100, 90, 150

B. Parameter analysis

Since the method proposed in this paper can efficiently calculate the shielding effectiveness, in the following discussion, the proposed method is employed to analyze the effect of dimensional variation on shielding effectivenes.

Figure 8 demonstrates the effect of enclosure width a on the shielding effectiveness in space 1. Except for the enclosure width, all parameters are the same as the case mentioned before, and the enclosure widths represented by the three sets of curves in the Fig. 8 are 300, 320, and 340 mm, respectively, while the observation point is always located in the middle of the enclosure. It can be seen that the enclosure width changes have a great influence on the resonant point frequency and shielding effectiveness, which will cause the frequency shift of the resonant point. As the cavity width increases, the resonant point frequency will be reduced.

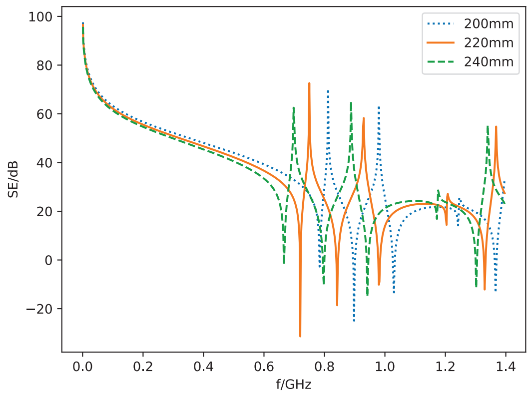

Fig. 8. Effect of enclosure width variation on shielding effectiveness in space 1.

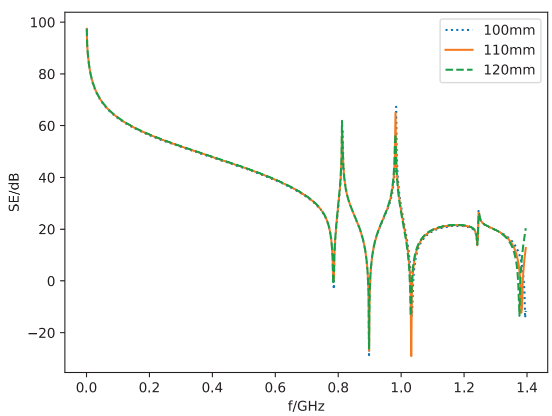

Fig. 9. Effect of enclosure height variation on shielding effectiveness in space 1.

Figure 9 demonstrates the effect of enclosure height b variation on shielding effectiveness in space 1. Due to the direction of the electric field of the incident wave, the effect of height variation on shielding performance and resonant frequency is very small.

Figure 10 demonstrates the effect of the variation of the rear depth d_2 on the shielding effectiveness in space 1. All parameters are the same as the case mentioned before except for the rear depth, and the depths d_2 represented by the three sets of curves in the Fig. 10 are 240, 270, and 300 mm, respectively, while the observation point is always located in the middle of space 1. It can be seen that as the depth of the rear enclosure increases, the shielding effectiveness increases at lower frequencies, and the resonant frequency also shifts to lower frequencies as the depth of the rear enclosure increases, which leads to a decrease in shielding effectiveness in some frequency bands above the cutoff frequency.

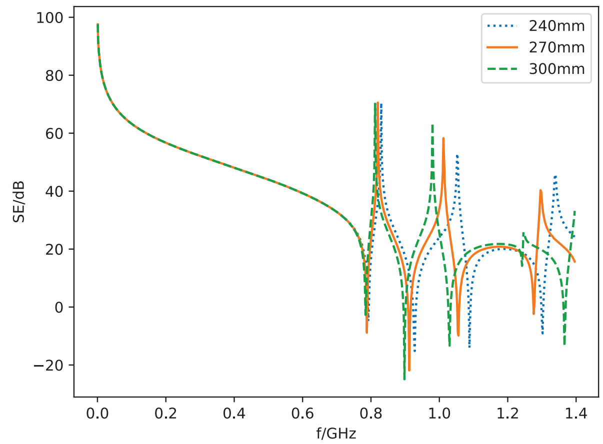

Fig. 10. Effect of rear enclosure depth variation on shielding effectiveness in space 1.

All the cases are computed on the same computer, which has a 2.2-GHz Intel i7-8750 CPU. The CST takes 20 minutes to complete a 200 frequency point simulation, while the fast algorithm takes no more than 0.2 s for the same case, indicating the high computational efficiency of the fast algorithm compared with the CST simulation.

IV. CONCLUSION

A method based on the EMT theory and BLT equation is presented to analyze the shielding performance of an apertured enclosure with an interior enclosure illuminated by an external plane wave. By modeling the front wall of the interior enclosure as a junction between two different rectangular waveguides, we derive a three-port scattering matrix from describing the coupling relation between the interior enclosure and the adjacent space. The total electric field can be derived from the relation between voltage response and field distribution inside the enclosure. This method proves that the BLT equation can handle complex enclosures by modifying the electromagnetic topology relationship. Several monitor points are presented to demonstrate the validity and accuracy of this method. The results indicate that the proposed method has a good agreement with numerical methods over a wide frequency range while it can dramatically improve the calculation speed. The proposed algorithm can be used to perform fast calculations on the effect of enclosure dimensions on shielding effectiveness. We investigated the effect of dimensional parameters on the shielding effectiveness of the enclosure. We found that due to the electric field direction, the variation of enclosure height can hardly affects the shielding effectiveness.

REFERENCES

[1] J. Bridges, "Proposed recommended practices for the measurement of shielding effectiveness of high-performance shielding enclosures," *IEEE Trans. Electromagn. Compat*, vol. EMC-10, no. 1, pp. 82-94, 1968.

[2] S. Georgakopoulos, C. Birtcher, and C. Balanis, "HIRF penetration through apertures: FDTD versus measurements," *IEEE Trans. Electromagn. Compat*, vol. 43, no. 3, pp. 282-294, 2001.

[3] R. Araneo and G. Lovat, "Fast MoM analysis of the shielding effectiveness of rectangular enclosures with apertures, metal plates, and conducting objects," *IEEE Trans. Electromagn. Compat*, vol. 51, no. 2, pp. 274-283, 2009.

[4] B. Audone and M. Balma, "Shielding effectiveness of apertures in rectangular cavities," *IEEE Trans. Electromagn. Compat*, vol. 31, no. 1, pp. 102-106, 1989.

[5] B.-L. Nie, P.-A. Du, Y.-T. Yu, and Z. Shi, "Study of the shielding properties of enclosures with apertures at higher frequencies using the transmission-line modeling method," *IEEE Trans. Electromagn. Compat*, vol. 53, no. 1, pp. 73-81, 2011.

[6] Z. Kubík and J. Skála, "Shielding effectiveness simulation of small perforated shielding enclosures using FEM," *Energies*, vol. 9, no. 3, p. 129, 2016.

[7] M. P. Robinson, T. M. Benson, C. Christopoulos, J. F. Dawson, M. D. Ganley, A. C. Marvin, S. J. Porter, and D. W. P. Thomas, "Analytical formulation for the shielding effectiveness of enclosures with apertures," *IEEE Trans. Electromagn. Compat*, vol. 40, no. 3, p. 9, 1998.

[8] M. P. Robinson, J. D. Turner, D. W. P. Thomas, J. F. Dawson, M. D. Ganley, A. C. Marvin, S. J. Porter, T. M. Benson, and C. Christopoulos, "Shielding effectiveness of a rectangular enclosure with a rectangular aperture," *Electronics Letters*, vol. 32, no. 17, pp. 1559-1560, 1996.

[9] F. Tesche, "Topological concepts for internal EMP interaction," *IEEE Trans. Antennas. Propagat*, vol. 26, no. 1, pp. 60-64, 1978.

[10] F. M. Tesche, J. M. Keen, and C. M. Butler, "Example of the use of the BLT equation for EM field propagation and coupling calculations," *URSI Radio Science Bulletin*, vol. 2005, no. 312, pp. 32-47, 2005.

[11] F. M. Tesche, "On the analysis of a transmission line with nonlinear trerminations using the time-dependent BLT equation," *IEEE Trans. Electromagn. Compat*, vol. 49, no. 2, pp. 427-433, 2007.

[12] B.-L. Nie and P.-A. Du, "An efficient and reliable circuit model for the shielding effectiveness prediction of an enclosure with an aperture," *IEEE Trans. Electromagn. Compat*, vol. 57, no. 3, pp. 357-364, 2015.

[13] M.-C. Yin and P.-A. Du, "An improved circuit model for the prediction of the shielding effectiveness and resonances of an enclosure with apertures," *IEEE Trans. Electromagn. Compat*, vol. 58, no. 2, pp. 448-456, 2016.

[14] P. Dehkhoda, A. Tavakoli, and R. Moini, "An efficient and reliable shielding effectiveness evaluation of a rectangular enclosure with numerous apertures," *IEEE Trans. Electromagn. Compat*, vol. 50, no. 1, pp. 208-212, 2008.

[15] Y. Gong and B. Wang, "An efficient method for predicting the shielding effectiveness of an enclosure with multiple apertures," *J. Electromagn. Waves Appl*, vol. 34, no. 8, pp. 1057-1072, 2020.

[16] J. Sun, Y. Gong, and L. Jiang, "An improved model for the analysis of the shielding performance of an apertured enclosure based on EMT theory and BLT equation," *J. Electromagn. Waves Appl*, vol. 36, no. 2, pp. 246-260, 2022.

[17] Y. Kan, L.-P. Yan, X. Zhao, H.-J. Zhou, Q. Liu, and K.-M. Huang, "Electromagnetic topology based fast algorithm for shielding effectiveness estimation of multiple enclosures with apertures," *Acta Phys Sin*, vol. 65, no. 3, p. 030702, 2016.

[18] K. Gupta, R. Garg, I. Bahl, and P. Bhartia, *Coplanar Lines: Coplanar Waveguide and Coplanar Strips*, vol. 2, Artech House, 1996.

[19] N. Marcuvitz, *Waveguide Handbook*, Institution of Electrical Engineers, 1986.

Jin-Cheng Zhou was born in Jiangsu, China, in 1990. He received a B.A. degree in Xi'an Technological University, China in 2008. He is currently working on his Ph.D. at the School of Information and Electronics of Beijing Institute of Technology. His research interests include radio propagation, EMC, and EM protection.

Xue-Tian Wang was born in Jiangsu, China, in 1961. He received a Ph.D. from the Department of Electronic Engineering of Beijing Institute of Technology in 2002. He has been working at Beijing Institute of Technology as a researcher since August 2001, and he has been a professor since 2003. His research interests include EMC, EM protection, and electromagnetic radiation characteristics.

Localization of Breast Tumor Using Four Elements UWB Wearable Antenna

Mazhar B. Tayel[1], Tamer G. Abouelnaga[2], and Nehad M. Badran[3]

[1]Department of Electrical Engineering
Faculty of Engineering Alexandria, University-Alexandria, Egypt
profbasyouni@gmail.com

[2]Microstrip Circuits Department
Electronics Research Institute ERI, Cairo, Egypt
tamer@eri.sci.eg

[3]Department of Electrical and Computer Engineering
Higher Institute of Engineering and Technology-Kafr Elsheikh, Egypt
nehadbadran1990@gmail.com

***Abstract* –** In this paper, four wearable UWB antennas are designed to detect and locate tumor cells placed within a heterogeneous phantom at different positions. The proposed antenna is operated within the 4.90 GHz to 15.97 GHz bandwidth range. It is fabricated, measured, and nearly matched between measured and simulated results. A cavity is formulated to back each antenna within the proposed detection system for increasing penetration and gain of propagated electromagnetic waves of the antenna design. The S-parameter of the proposed system was used to detect and locate a small tumor. The SAR results show that the absorbed power by the breast phantom tissues satisfies the IEEE standards which confirms the appropriateness of the proposed antennas for breast cancer early detection and localization system.

***Index Terms* –** cavity, heterogeneous phantom, specific absorption rate (SAR), wearable UWB antenna.

I. INTRODUCTION

In December 2020, the International Agency for Research on Cancer (IARC) announced that breast cancer has overtaken the most diagnosed type of cancer in the world. In 2021, the World Health Organization (WHO) declared breast cancer to be the most common type of cancer globally, accounting for 12% of all new cases of cancer [1]. Breast cancer arises in the glandular tissue of the breast in ducts (85%) and lobules of (15%) and is called at this stage “in situ”. This stage (stage 0) has a low chance of spreading and converting to metastasis. After a while, this stage may progress and strike surrounding tissues and then spread to nearby lymph nodes and become a regional metastasis or to other organs in the human body and become distant metastasis [2]. Tumor size is a strong predictor of long-term mortality [3]. It is recommended to detect breast cancer at or less than 2 cm [4].

Breast microwave imaging (MI) in literature is split into microwave breast imaging several techniques and image reconstruction algorithms [5]. Different methods for several techniques in breast MWI (breast cancer early detections) were used. Table 1 shows many early breast cancer UWB antennas and compares them. The first method of breast MWI relied on an antenna array. There are various compositions from antenna arrays are proposed in literature papers, and ranked as hemispherical, enclosed, and planer arrays [5]. In [6], constructed a compact, single polarization, flexible UWB antenna array, in a configuration identical to that of a bra for breast cancer detection. In [7], established a compact, single and dual polarization, flexible UWB antenna array, in a structure related to that of a bra for breast cancer detection and significantly better penetration for propagated electromagnetic waves by utilizing a reflector with the arrays. In [8], formulated clinical model as a wearable interface for a case consisting of multi-static time-domain pulsed radar and flexible antenna array inundated in bra. The clinical model is highly cost-effective and related to the normal table model. The regular difference for the data of the reflection coefficient for flexible microstrip antenna array at 1.5 GHz was used to locate and detect the tumor at thirteen numerous places in the human breast [9]. The second method of MWI of the breast depended on a single antenna element. These antennas include Vivaldi antennas, monopole antennas, and bowtie antennas, in addition to fractal and horn antennas [5]. In [10], a wearable microstrip patch UWB antenna as a new design had demonstrated to detect early tumors with enlarged bandwidth from 1.6 GHz to 11.2 GHz. In [11], a compact flexible single-element UWB antenna

Submitted On: July 27, 2022
Accepted On: December 5, 2022
https://doi.org/10.13052/2022.ACES.J.371002

Table 1: Comparison among early breast cancer detection antennas

Reference	Single element size (mm^2)	No. of elements	ε_r	Substrate thickness (mm)	Length of single element/λ (mm)	BW (GHz)	$\Delta f/f_0$
[6]	18 × 18	16	3.5	0.1	0.250	2 – 5	0.86
[7]	20 × 20	16	3.5	0.1	0.280	2 – 4	0.67
[8]	20 × 20	16	3.5	0.1	0.280	2 – 4	0.67
[9]	58.43 × 26.45	4	2.64	2.2	0.470	1.45 – 1.54	0.06
[10]	70 × 60	2	1.6	1.6	0.740	1.6 – 11.2	1.5
[11]	22 × 20	1	3.5	0.05	0.410	2 – 4	0.67
[12]	25 × 36	1	3.4	0.16	0.730	2 – 4	0.67
In this paper	28 × 20	4	2.9	0.1016	0.830	4.90 – 15.97	1.06

with an inhomogeneous breast phantom was presented for MWI and tumor early detection. It was operated in the range of 2 to 4 GHz while having a size of 20 × 22 mm^2. Kapton substrate with a relative permittivity of 3.5 has been used as a substrate. In [12], a compact flexible monopole single-element UWB antenna with an inhomogeneous breast phantom for breast cancer detection Kapton polyimide using a CST simulator and MEMS technology with biological breast tissues. It was operated in the range of S-Band (2-4 GHz) while having a size of 25 × 36 mm^2. All the mentioned researches suffer from small (single element length/λ) and low fractional bandwidth value of single element antenna.

In this paper, Four UWB wearable antennas and four cavities are suggested for the breast phantom examination to detect and locate tumor tissues inside the human breast. Firstly, the evolution of a single UWB wearable antenna is accomplished in four steps and verified. Secondly, the cavity is utilized around each wearable antenna for significantly nicer penetration for radiated electromagnetic waves. Finally, the proposed phantom with and without tumor tissues is simulated with the proposed detection system which is consisted of four UWB wearable antennas and a cavity around each antenna. S-parameters from the single-element antenna are reported by using CST Microwave Studio 2020 and are compared with the measured results for the fabricated proposed antenna by using Vector Network Analyzer (VNA). S_{11} from the single-element antenna can detect and diagnose the presence of malignant cells. The tumor position is identified by other reflection coefficients of all antennas. SAR estimation is also investigated for the proposed phantom. The proposed detection system indicates that the two processes of early detection and localization for tumors 3 mm in size inside a human breast are possible.

II. The PROPOSED ANTENNA DESIGN

A. Antenna element

The antenna design is an important part of the overall performance of microwave imaging systems. Breast microwave imaging systems need to antenna element which radiates pulses over a wide range of frequencies and operates in the Ultra-Wideband (UWB) that the Federal Communication Commission (FCC) assigned a bandwidth of (3.1 to 10.6 GHz) for measurements, communications, and radar [13].

The growth of the proposed antenna configuration is accomplished in the four stages as illustrated in Fig. 1. The structure of the octagon antenna element with a partial ground plane is altered for the desired operating bandwidth. The structure of the octagon's antenna element is modified from stage 1 to stage 2. The conclusions of the return loss of the development process are demonstrated in Fig. 2. The return loss of the designed octagon antenna element with the partial ground plane in stage 1 is ≤ -10 dB for the frequency range of 8.7897 GHz to 17.11 GHz. In stage 2, the number of partial octagons is increased in radiating patch to enhance the return loss. Subsequently, the return loss is accomplished for the frequency range of 8.6159 GHz to 16.599 GHz. In stage 3, a rectangular shape structure is added to the ground plane. The resonating behavior of the antenna is altered by this addition. The result of this improvement is visualized in the return loss graph in Fig. 2. In this stage the lower frequency range of the return loss has improved. Then the modified antenna covered the Ultra-wideband region from 5.1315 GHz to 16.272 GHz. The rectangular-shaped structure is replaced with a radial stub in stage 4. The shape modification considers the like self-similarity and slots which played an important role to widen the bandwidth. Now, this replacement shifted the bandwidth from 5.1315 GHz to 4.9007 GHz at the lower frequency and from 16.272 GHz to 15.968 GHz at the higher frequency. The optimized size of the proposed antenna is 28 mm × 20 mm. The radiating patch and ground plane are printed on the substrate. The Ultra-Lam 3850 dielectric constant of 2.9 and thickness of 0.1016 mm is used as an antenna flexible substrate. The proposed antenna structure is shown in Figs. 3 (a) and (b). The fabricated antenna is tested with Vector Network Analyzer (VNA) for validation purposes in Fig. 3 (c). Table 2 shows the optimized dimensions of the proposed antenna. Figure 4

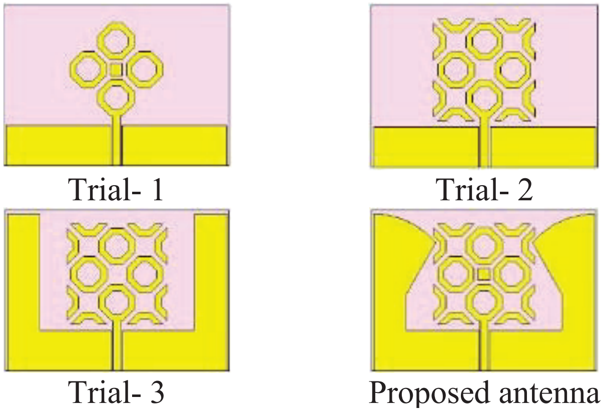

Fig. 1. Evolution stages for designing the proposed antenna.

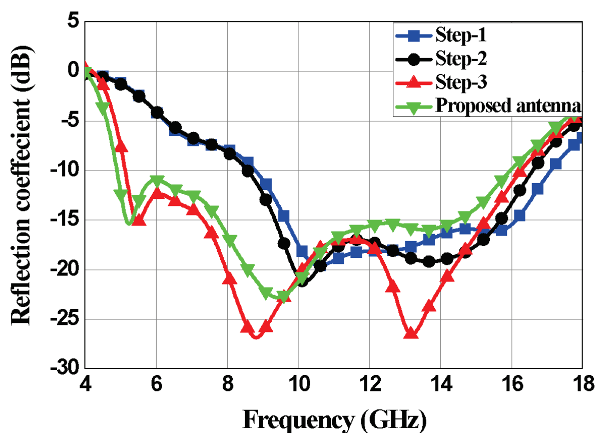

Fig. 2. The return loss results of the evolution process of the proposed antenna.

shows the fabricated antenna top and bottom views. The return loss of the fabricated antenna and its simulated counterpart is shown in Fig. 5. These results are closely matched. Variation in the simulation and measurement results between 8-11 GHz shown below might be due to fabrication errors and accuracy parameters or to the soldering used in linking the SMA connector to the feedline of the antenna and the SMA connector effect. Figure 6 shows the 3D radiation pattern of the antenna; the antenna has an omnidirectional radiation pattern. Also, the beam width (angular width) is 58.8%. Figure 9 shows the radiation pattern in the x-z plane. Table 3 shows the comparison among the evolution stages of the proposed UWB wearable antenna.

B. Effect of antenna bending

The wearable antennas are required to be bent as human breast shape. To investigate the bending effect on the proposed wearable UWB antenna, the antenna is bent around foam cylinders with different radii at 30, 60, 90,

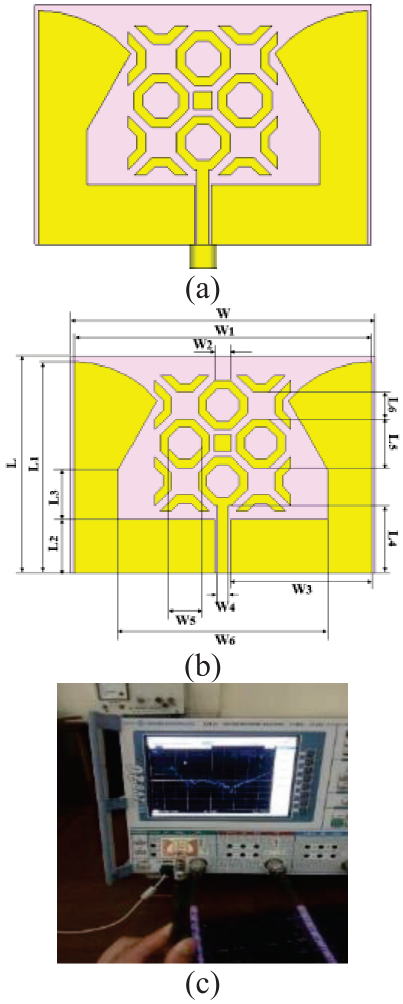

Fig. 3. (a) The proposed antenna structure. (b) The proposed antenna dimension. (c) The measurement setup.

120, and 180 mm [14, 15]. The 2D antenna representation as flat and with regards to the bending angles are depicted in Fig. 8. The return loss results of the different radii of bending are shown in Fig. 9.

C. Cavity-backed UWB wearable bent antenna

The concept of cavity-backed antenna is creating reflectors on all sides of the antenna except the front side of

Table 2: The proposed antenna dimensions

Par.	**W**	**W_1**	**W_2**	**W_3**	**W_4**
Dim. ([0-9] mm)	28	27.4	1.5	13	1
Par.	**W_5**	**W_6**	**L**	**L_1**	**L_2**
Dim. (mm)	3	19.4	20	19.5	5
Par.	**L_3**	**L_4**	**L_5**	**L_6**	**θ**
Dim. (mm)	4.5	6.5	4.5	2.5	50

Table 3: The proposed antenna parameters

		Stage 1	Stage 2	Stage 3	Proposed antenna
Antenna Shape		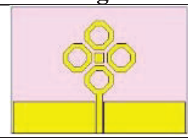	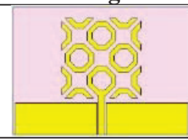	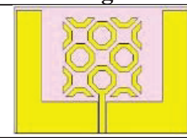	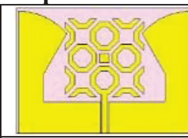
Bandwidth (GHz)		8.79 – 17.11	8.5871 – 16.61	5.131 – 16.275	4.9 – 15.97
Gain (dBi)		3.69	3.81	5.63	5.81
Directivity (dBi)		3.72	3.86	5.66	5.85
3dB BW (degree)		60.6	59.6 °	59.2	58.8
Radiation Efficiency (%)		99.21	98.88	99.27	98.93
Total Efficiency (%)		94.46	96.00	98.88	98.42
Radiation Pattern	E - Plane	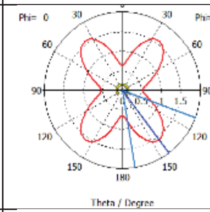	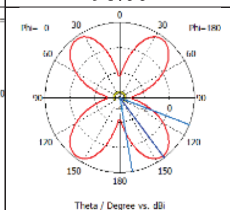	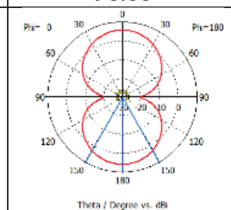	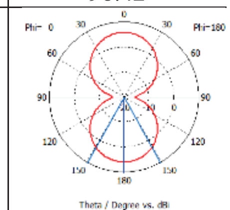
	H - Plane	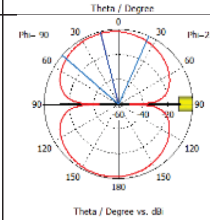	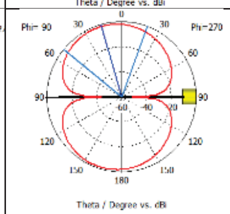	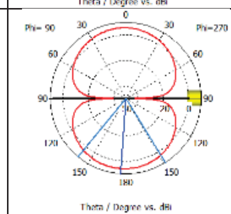	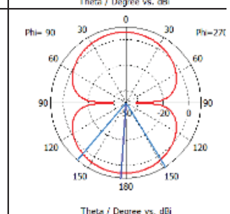
	3D	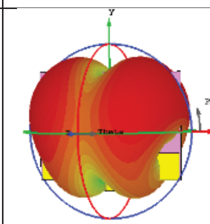	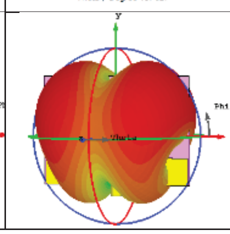	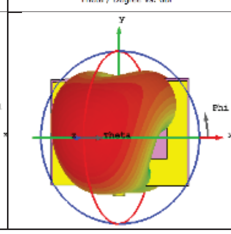	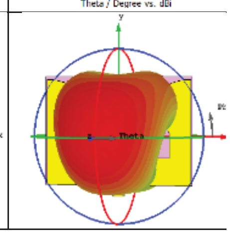

it [16] and increasing the gain of the antenna. The dimension of the proposed cavity structure is 40 mm x 36 mm x 13.1618194 mm. The front side of the cavity structure is shown in Fig. 10 (a). The top side of the cavity structure is shown in Fig. 10 (b). Figure 11 shows the return loss

(a) (b)

Fig. 4. The fabricated antenna (a) top view and (b) back view.

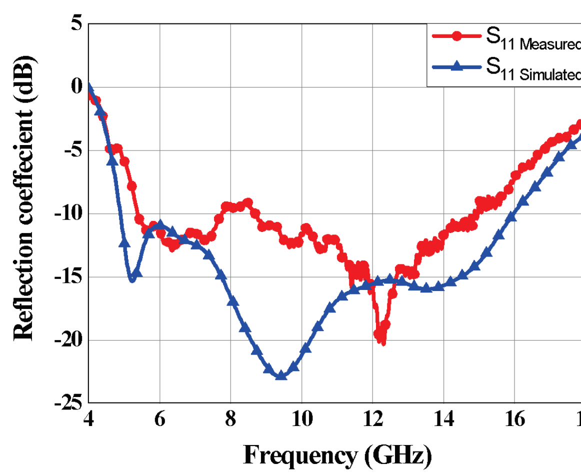

Fig. 5. The return loss of the fabricated antenna and simulated antenna.

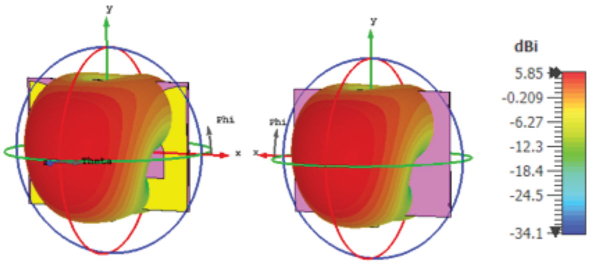

Fig. 6. The radiation pattern of the proposed antenna with metamaterial from the front side and backside.

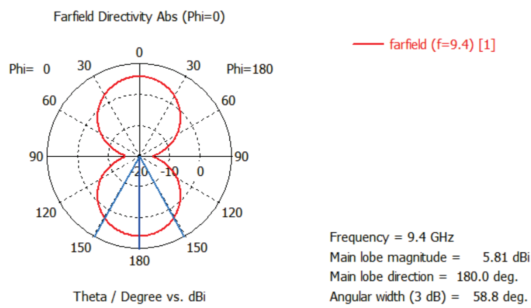

Fig. 7. The XZ plane of the radiation pattern.

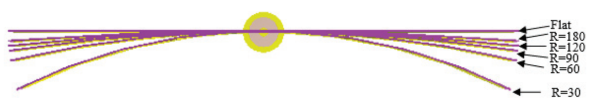

Fig. 8. The 2D flat antenna and bending around a radius at 30, 60, 90, 120, and 180 mm.

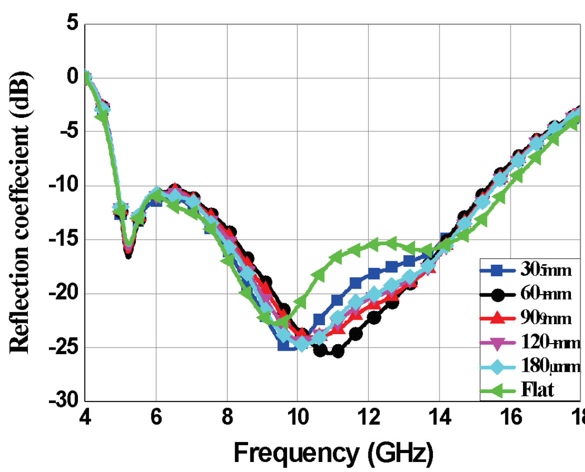

Fig. 9. The return loss results at different bending radii.

results of bending the antenna with a radius of 90 mm without a cavity and cavity-backed antenna. Figure 12 shows the 3D radiation pattern of the cavity-backed an-

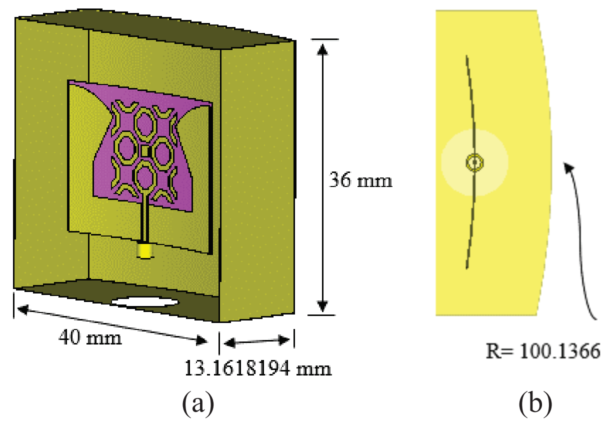

Fig. 10. (a) The front side of the cavity structure. (b) The top side of the cavity structure.

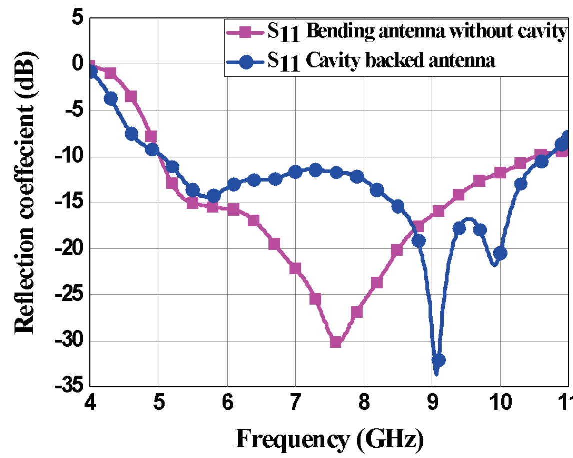

Fig. 11. The return loss of bending antenna without cavity and cavity-backed antenna.

tenna, one noticed that the cavity increases the directivity of the wearable antenna from 5.852 dBi to 10.65 dBi and the beam width (angular width) changes from 58.8% to 50.3% at the same frequency 9.4 GHz. The gain changes from 5.805 dBi to 10.6 dBi. Figure 13 shows the radiation pattern in the x-z plane.

III. THE PROPOSED DETECTION SYSTEM

A. Breast phantom

A heterogeneous phantom is used. It is structured in a 3-D hemisphere shape. It consists of various layers of breast tissues (skin, fat, glandular tissues, and tumors). Figure 14 shows the different layers of the proposed heterogeneous phantom. Tables 4 and 5 show the dimensions of the different layers of the breast and the electromagnetic parameters (Thickness T, outer radius $R_{out\ (mm)}$, inner radius $R_{in\ (mm)}$, Relative permittivity (ε),

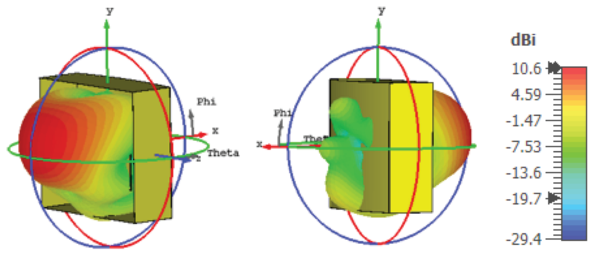

Fig. 12. The radiation pattern of the proposed antenna with cavity from the front side and backside.

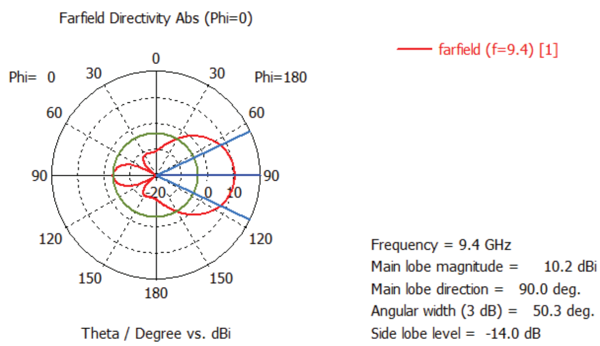

Fig. 13. The XZ plane of the radiation pattern.

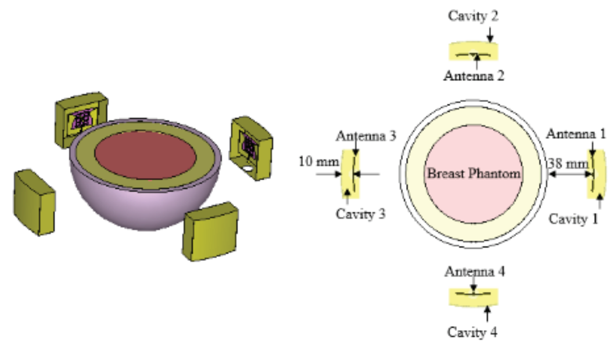

(a) (b)

Fig. 15. (a) The front side of the detection system, (b) The top side of the detection system.

Table 4: Breast different layers of breast dimensions

Tissues	$T_{(mm)}$	$R_{out\ (mm)}$	$R_{in\ (mm)}$
Skin	5	60	55
Fat	15	55	40
Glandular	40	40	0

conductivity (σ), Density(ρ), Specific heat capacity (cp), and Thermal conductivity (k)) respectively [17, 18].

B. Antennas setup

Four antennas are bent around the human breast. Antenna 1 and antenna 3 are opposite to each other, antenna 2 and antenna 4 are opposite to each other, each antenna far distance from the breast skin by 38 mm, and the radius of the bending of the antenna is equal to 90 mm. The distance between the cavity and the antenna is 10 mm. The radius of the bent cavity is 100 mm. Figure 15 shows the front and top sides positions of the proposed cavities backed by bent antennas and the breast phantom.

IV. RESULTS AND DISCUSSION

A. Tumor detection

Breast cancer originates in the glandular tissue of the breast, so we always try to detect and locate the tumor early within this glandular tissue (stage I), where it is less likely to spread. Firstly, the proposed system is operated in the case of healthy breast tissues free of any tumors and then reports the coupling coefficients of the four proposed antennas for comparison with the coupling coefficients in the situation of unhealthy tissue containing tumors. Next, we split the glandular layer within the proposed breast into four quadrants: I, II, III, and IV. We hypothesized a tumor in the first quadrant, simulated the proposed system, and recorded the results again. Afterward, the tumor was eliminated from the first quadrant and immersed in another quadrant, and the system was simulated and the results were recorded again. The simulations were performed 4 times for each position of 4 tumor locations: P1 in quarter I, P2 in quarter II, P3 in quarter III, and P4 in quarter IV. The phantom quadrants and the positions of tumors are shown in Fig. 16.

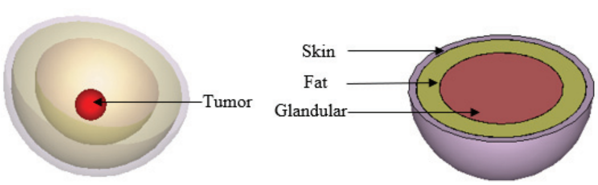

Fig. 14. Different layers of the proposed heterogeneous phantom.

The reflection coefficients S_{11}, S_{22}, S_{33}, and S_{44} for five cases, healthy breast tissue cases, and the four positions of the tumor in the unhealthy tissue at 9.34 GHz are presented in Table 6 and Fig. 17–20, respectively. Figure 21 shows the coupling between the four adjacent antennas, where a very low coupling, very good isolation, and good spatial diversity are achieved, where the coupling coefficients S_{12} is -47.57 dB at 9.47 GHz, S_{13} is -48 dB at 8.35 GHz and S_{14} is -47.32 dB at 9.47 GHz.

In the absence of a tumor case, the coupling coefficient S_{11} is equal to S_{44} and S_{22} is equal to the coupling coefficient S_{33}. In the case of a tumor in the first quadrant (P1), the values of S_{22} and S_{44} remain equal to the same values as it was in the absence of a tumor but the values

Table 5: The electromagnetic parameters of the proposed phantom

Tissues	Dielectric properties		ρ (Kg/m^3)	cp (J/K/Kg)	k (W/K/m)
	ε (F/m)	σ (S/m)			
Skin	36	4	1085	3765	0.4
Fat	9	0.4	1069	2279	0.3
Glandular	11−15	0.4−0.5	1050	3600	0.5
Tumor	50	4	1050	3600	0.5

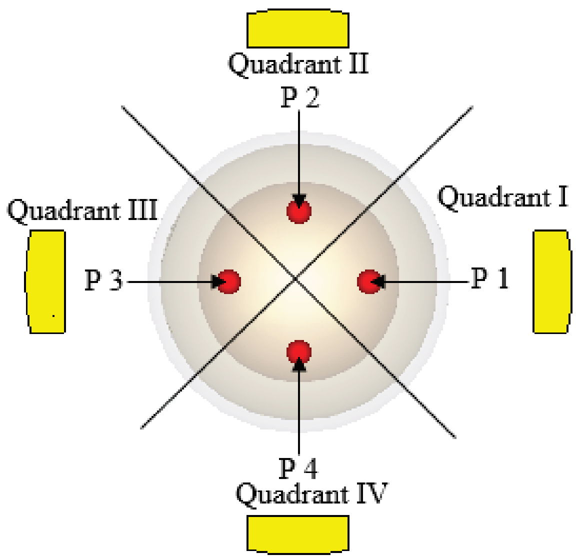

Fig. 16. The phantom splitting and the positions of tumors.

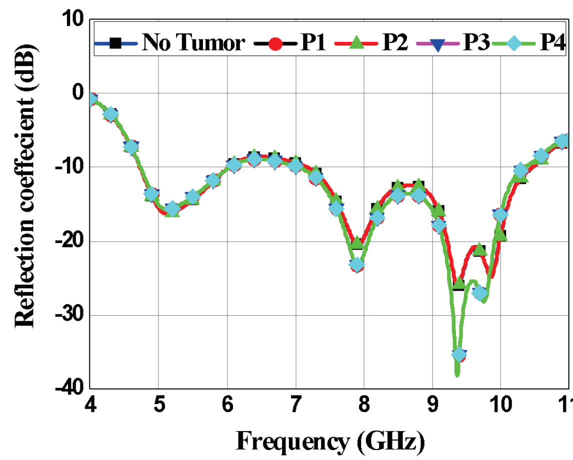

Fig. 17. The reflection coefficients S_{11} for all cases.

Table 6: The reflection loss of the five cases

	Tumor positions				
	No tumor	P1	P2	P3	P4
S_{11} (dB)	25.5	34.5	25.4	34.7	25.4
S_{22} (dB)	28.3	28.1	66.4	28.1	61.9
S_{33} (dB)	28.3	63.6	28	68.5	28
S_{44} (dB)	25.5	25.4	34.5	25.4	34.3

of S_{11} and S_{33} change so that the value of S_{33} is greater than the value of S_{11} and less than 65 dB. In the case of a tumor in the second quadrant (P2), the values of S_{11} and S_{33} remain equal to the same values as it was in the absence of a tumor but the values of S_{22} and S_{44} change so that the value of S_{22} is greater than the value of S_{44} and greater than 65 dB. In the case of a tumor in the third quadrant (P3), the values of S_{22} and S_{44} remain equal to the same values as it was in the absence of a tumor but the values of S_{11} and S_{33} change so that the value of S_{33} is greater than the value of S_{11} and greater than 65 dB. In the case of a tumor in the fourth quadrant (P4), the values of S_{11} and S_{33} remain equal to the same values as it was in the absence of a tumor but the values of S_{22} and S_{44} change so that the value of S_{22} is greater than the value of S_{44} and less than 65 dB.

The simulations were done at different distances between the antenna and the cavity at 5, 10, and 15 mm but the best results were at 10 mm. Many parameters affect that distance as antenna resonance frequency and the tumor positions.

B. Specific Absorption Rate (SAR) analysis

Faraday's law states that the magnetic field of the coil transmits radio frequency energy and generates an electric field within the tissues of the human body and the absorbed radio frequency energy is recycled into heat [19]. Therefore, tissue heating has health effects on patients as a result of their exposure to radio frequency, and these effects can be measured and controlled by the so-called Specific Absorption Rate (SAR) [20]. The Specific Absorption Rate (SAR) is a measure of the absorption rate of Radio Frequency (RF) power by biological tissue while it is exposed to Radio Frequency (RF) energy. For calculating the SAR value, we need a volume, its mass has 1 gram or 10 grams and this volume must be

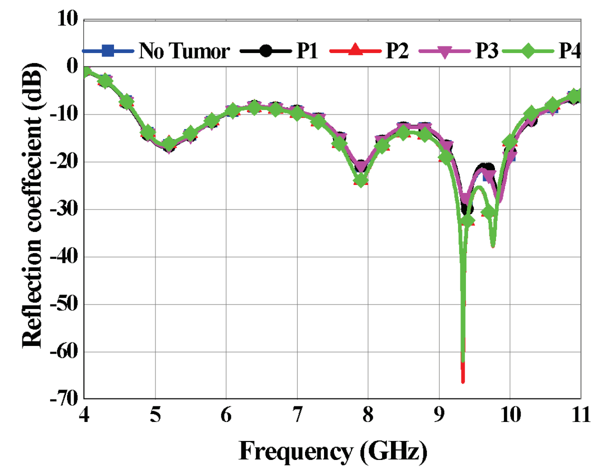

Fig. 18. The reflection coefficients S_{22} for all cases.

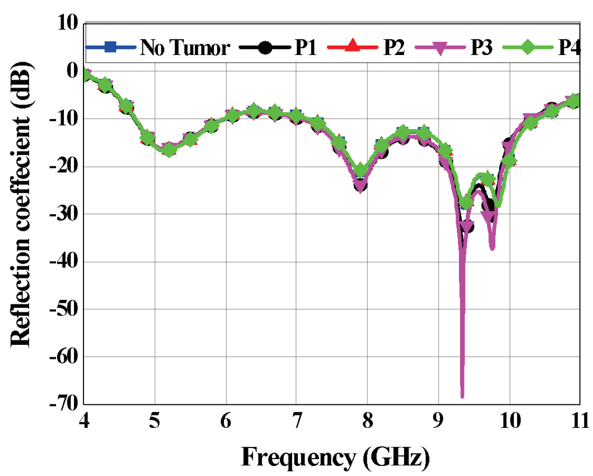

Fig. 19. The reflection coefficients S_{33} for all cases.

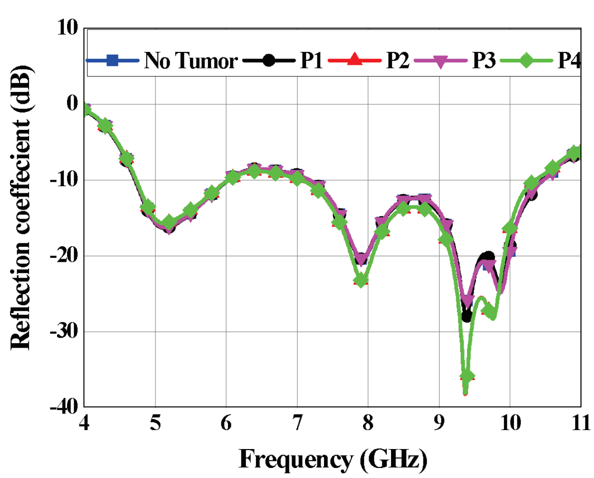

Fig. 20. The reflection coefficients S_{44} for all cases.

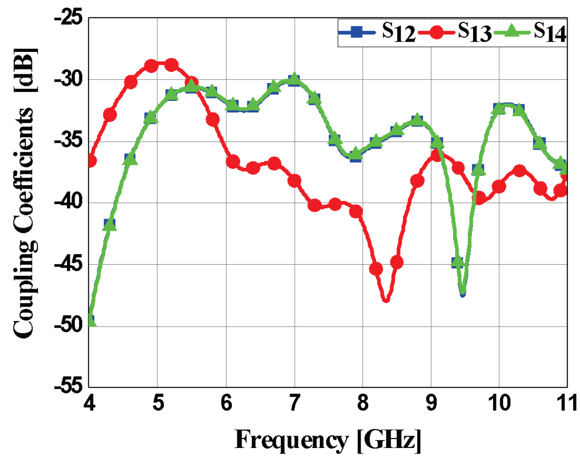

Fig. 21. The coupling coefficients S_{12}, S_{13}, and S_{14} for the proposed detection system.

a cubic shape and contains the peak electric field by the condition of the IEEE Standard 1528 [21].

The local SAR is the value of SAR at each point inside the phantom tissues $[W/Kg]$ and it is defined by Eq.1 [20]:

$$SAR_{local}\ (r,\omega) = \frac{\sigma(r,\omega)\,|E(r,\omega)|^2}{2\rho(r)}\,. \tag{1}$$

The average SAR is the integral of the local SAR at each point on the cube and then divided by the mass of the cube and it is defined by Eq.2:

$$SAR_{average}\ (r,\omega) = \frac{1}{v}\int \frac{\sigma(r,\omega)\,|E(r,\omega)|^2}{2\rho(r)}dr, \tag{2}$$

where $\sigma(r,\omega)$ is the conductivity of the material of the phantom $[S/m]$, $\rho(r)$ is the mass density of the tissue $[Kg/m^3]$, $E(r,\omega)$ is the electric field $[V/m]$,(r) is the position vector, and ω is the frequency.

The SAR analysis of the heterogeneous phantom using the proposed bending antenna system is carried out

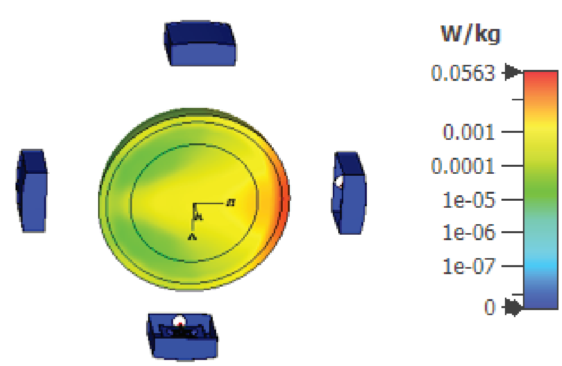

Fig. 22. The maximum spatial average SAR value using 1g.

by the Biomedical environment of the CST. The spatial average of SAR values of 1 g and 10 g volumetric samples for heterogeneous phantoms are analyzed at 9.34 GHz frequency. These results (Fig. 22) show that the maximum spatial average SAR value using 1g and 10g samples are 0.0563 $[W/Kg]$ and $5.2 \times 10{-}4$ $[W/Kg]$] respectively at 0.5 W at the phantom. These values are significantly below the maximum limit assigned by Federal Communications Commission (FCC) in the United States, which is 1.6$[W/Kg]$ averaged over 1 g volume, and the standard in Europe, is 2 $[W/Kg]$ averaged over 10 g volume.

V. CONCLUSION

A configuration and implementation of a UWB wearable antenna were introduced to detect the malignant tissues inside the human breast. The UWB wearable antenna bandwidth extends from 4.90 GHz to 16 GHz. Good agreement was achieved between measured and simulated results. The proposed cavity-backed antenna achieved high directivity, high gain, and reasonable beamwidth. A heterogeneous breast phantom with a 3mm tumor radius was tested at 9.34 GHz for tumor detection and localization processes. SAR results were investigated using 1g and 10g standards and had shown the appropriateness of the proposed antennas for breast cancer early detection and localization system.

REFERENCES

[1] WHO | World Health Organization.

[2] U.S. Breast Cancer Statistics.

[3] S. A. Narod, “Tumour size predicts long-term survival among women with lymph node-positive breast cancer,” vol. 19, pp. 249-253, 2012.

[4] A. B. Miller, C. Wall, C. J. Baines, P. Sun, T. To, and S. A. Narod, “Twenty-five-year follow-up for breast cancer incidence and mortality of the Canadian National Breast Screening Study: randomized screening trial,” Obstetrical & Gynecological Survey, vol. 69, pp. 329-330, 2014.

[5] H. M. El Misilmani, T. Naous, S. K. Al-Khatib, K. Y. Kabalan, “A survey on antenna designs for breast cancer detection using microwave imaging,” *IEEE Access*, vol. 8, pp. 102570-102594, 2020.

[6] H. Bahrami, E. Porter, A. Santorelli, B. Gosselin, M Popovic, and L. A. Rusch, “Flexible sixteen monopole antenna array for microwave breast cancer detection,” *36th Annual International Conference of the IEEE Engineering in Medicine and Biology Society*, Chicago, IL, pp. 3775-3778, Aug. 2014.

[7] H. Bahrami, E. Porter, A. Santorelli, B. Gosselin, M. Popovic, and L. A. Rusch, “Flexible 16 antenna array for microwave breast cancer detection,” *IEEE Transactions on Biomedical Engineering*, vol. 62, no. 10, pp. 2516-2525, Oct. 2015.

[8] E. Porter, H. Bahrami, A. Santorelli, B. Gosselin, L. A. Rusch, and M. Popović, “A wearable microwave antenna array for time-domain breast tumor screening,” *IEEE Transactions on Medical Imaging*, vol. 35, no. 6, pp. 1501-1509, Jun. 2016.

[9] M. Mamun U. Rashid, A. Rahman, L. C. Paul, J. Rafa, B. Podder, and A. K. Sarkar, “Breast cancer detection & tumor localization using four flexible microstrip patch antennas,” *International Conference on Computer, Communication, Chemical, Materials, and Electronic Engineering (IC4ME2)*, Rajshahi, Bangladesh, Jul. 2019.

[10] F. Alsharif and C. Kurnaz, “Wearable microstrip patch ultra-wide band antenna for breast cancer detection,” *41st International Conference on Telecommunications and Signal Processing (TSP)*, Athens, Greece, Jul. 2018.

[11] A. Afyf, L. Bellarbi, A. Achour, N. Yaakoubi, A. Errachid, and M. A. Sennouni, “UWB thin film flexible antenna for microwave thermography for breast cancer,” *International Conference on Electrical and Information Technologies (ICEIT)*, Tangiers, Morocco, May 2016.

[12] A. Afyf, A. Elouerghi, M. Afyf, M. A. Sennouni, and L. Bellarbi, “Flexible wearable antenna for body centric wireless communication in S-band,” *International Conference on Electrical and Information Technologies (ICEIT)*, Rabat, Morocco, Mar. 2020.

[13] T. Abouelnaga and E. A. Abdallah, “Ultra-compact UWB power divider for 5G Sub-6 GHz wireless communication system,” *International Journal on Communications Antenna and Propagation (IRECAP),* vol. 12, no. 2, pp. 90-97, 2022.

[14] S. J. Chen, B. Chivers, R. Shepherd, and C. Fumeaux, “Bending impact on a flexible ultrawideband conductive polymer antenna,” *International Conference on Electromagnetics in Advanced Applications (ICEAA)*, Turin, Italy, Sep. 2015.

[15] A. I. Hammoodi, H. Al-Rizzo, A. A. Isaac, A. S. Kashkool, K. Gamer, and H. Khaleel, “Studying the effect of bending on the performance of flexible dual-band microstrip monopole antenna,” *IEEE Conference on Antenna Measurements & Applications (CAMA)*, Syracuse, NY, Oct. 2016.

[16] D. Awan, S. Bashir, and W. Whittow, “High gain cavity backed UWB antenna with and without band notch feature,” *Loughborough Antennas & Propagation Conference (LAPC)*, Loughborough, UK, Nov. 2013.

[17] M. Abdel-Haleem, T. Abouelnaga, M. Abo-Zahhad, and S. Ahmed, "Enhancing microwave breast cancer hyperthermia therapy efficiency utilizing fat grafting with horn antenna," *International Journal of RF and Microwave Computer-Aided Engineering*, vol. 31, no. 6, pp. 1-13, 2021.

[18] P. T. Nguyen, A. M. Abbosh, and S. Crozier, "Thermo-dielectric breast phantom for experimental studies of microwave hyperthermia," *IEEE Antennas and Wireless Propagation Letters*, vol. 15, pp. 476-479, 2015.

[19] T. M. Fiedler, M. E. Ladd, and A. K. Bitz, *SAR Simulations & Safety, NeuroImage*, vol. 168, pp. 33-58, 2018.

[20] V. Sathiaseelan, "Application of numerical modeling techniques in electromagnetic hyperthermia," *Applied Computational Electromagnetics Society (ACES) Journal*, vol. 7, no. 2, pp. 61-71, 2022.

[21] T. Abouelnaga, I. Zewail, and M. Shokair, "Design of 10 $\times$10 massive MIMO array in sub-6 GHz smart phone for 5G applications," *Progress in Electromagnetics Research B*, vol. 91, pp. 97-114, 2021.

Mazhar Basyouni Tayel was born in Alexandria, Egypt on Nov. 20th, 1939. He graduated from Alexandria University Faculty of Engineering Electrical and Electronics department in 1963. He has published many papers and books in electronics, biomedical, and measurements. Mazhar Basyouni Tayel received a B.Sc. with an honor degree in 1963, and then his Ph.D. in Electro-physics in 1970. He had this Prof. Degree of the elect. And communication and Biomedical Engineering and systems in 1980. Now he is Emeritus Professor since 1999. From 1987 to 1991 he worked as the chairman of the communication engineering section of EED BAU-Lebanon, and from 1991 to 1995 he worked as Chairman of the Communication Engineering Section, of EED Alexandria University, Alexandria, Egypt. Also from 1995 to 1996, he worked as a chairman of the EED Faculty of Engineering, BAU-Lebanon. Additionally, from 1996 to 1997, he worked as the Dean of the Faculty of Engineering, BAU - Lebanon. From 1999 to 2009, he worked as a senior professor in the Faculty of Engineering, Alexandria University, Alexandria, Egypt. He has been an Emeritus Professor at the Faculty of Engineering, Alexandria University, Alexandria, Egypt since 2009. He has also worked as a general consultant in many companies and factories and is a member of the supreme consul of Egypt.

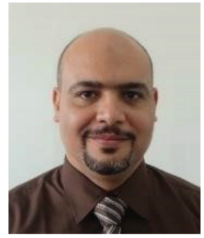

Tamer Gaber Abouelnaga was born in November 1976. He received his B.Sc. degree (1994–1999, honors degree) in Electronics Engineering from Menofiya University, Egypt, an M.Sc. degree (2002–2007), and a Ph.D. degree (2007–2012) in Electronics and Communications from Ain Shams University. He works as a Researcher (2012–2017) and an Associate Professor (2018-current) in Microstrip Circuits Department at the Electronics Research Institute in Egypt. He works as Students Affairs Vice Dean (2018–2019) and Community Service, Environmental Development Vice Dean (2019-2022) at the Higher Institute of Engineering and Technology in Kafr Elsheikh, and Students Affairs Vice Dean (2022-2023) at the College of Industry and Energy Technology, New Cairo Technological University (NCTU), Egypt. He has published 42 papers, 29 papers in peer-refereed journals and 13. papers in international conferences regarding antennas, couplers, filters, and dividers for different microwave applications.

Nehad Mohamed Badran is a Master's Student at the Faculty of Engineering at Alexandria University, Egypt. She was born in El-Beheira, Egypt in December 1990. She received a B.Sc. degree in Electronics and Communication Engineering from HIET, Kafr El-Shiekh, Egypt in May 2012. She has been a demonstrator at the Higher Institute of Engineering and Technology (HIET) in Kafr El-Shiekh, Egypt since 2013. Her current research focus is Biomedical Engineering, especially microwave breast cancer detection and treatment.

Dual-band Bandpass Plasmonic Filter Based on Effective Localized Surface Plasmon Resonators

Zixiang Zhou[1], Liangliang Liu[1,2], Xinhua Li[1], Jinrui Shen[1], Guodong Han[3], and Zhuo Li[1]

[1]Key Laboratory of Radar Imaging and Microwave Photonics
Ministry of Education, College of Electronic and Information Engineering,
Nanjing University of Aeronautics and Astronautics, Nanjing 211106, China.

[2]State Key Laboratory of Millimeter Waves,
Southeast University, Nanjing, 210096, China.

[3]The 54th Research Institute of CETC, Shijiazhuang, 050081, China.
Corresponding authors: llliu@nuaa.edu.cn; lizhuo@nuaa.edu.cn

***Abstract* –** A dual-band bandpass plasmonic filter based on quarter-wavelength effective localized surface plasmon resonators (ELSPRs) is proposed in this work. Compared with conventional microstrip resonators, ELSPRs have a larger unloaded quality factor and compact size, which can be flexibly designed. Since the harmonics of quarter-wavelength ELSPRs are located only at odd times of their dominant mode frequency, we can not only miniaturize the filter but achieve excellent out-of-band rejection performance. For demonstration, we design and fabricate a dual-band bandpass plasmonic filter, whose size is only 0.0396 λ_0^2 , the center frequency is 3.1 GHz and 3.6 GHz, and the relative bandwidth is 10.7% and 7.7% respectively. Measurement results show excellent agreement with the simulations. Our results provide a route for realizing ultra-compact and high-performance functional devices for the fifth generation (5G) applications.

***Index Terms* –** dual-band bandpass filter, effective localized surface plasmons, harmonic suppression.

I. INTRODUCTION

In recent years, dual-band and multi-band bandpass filters are in high demand for module miniaturization in modern mobile communication systems. Various dual-band bandpass filter (DBPF) structures have been proposed and implemented. For instance, a substrate-integrated waveguide DBPF [1] with low insertion loss and flattening features was proposed. However, its size is still relatively large, and the return loss is not more than 15 dB. A differential dielectric strip resonator (DSR) filter with a dual-band bandpass was realized by loading a pair of ground bars underneath the traditional half-wavelength DSR with high permittivity [2]. Although the unloaded quality factor (Q_u) of this structure reaches 695, it is not flat and compact enough. Although stepped-impedance resonators (SIRs) are commonly used in the DBPF design [3, 4], their application is limited since the resonance frequencies of different SIRs modes are interrelated. Although great effort has been made for multimode resonators [5-11] in the DBPFs design, improvement in balancing various indicators such as Q_u, insertion loss (IL), and size is still limited.

Recently, a novel effective localized surface plasmon resonator (ELSPR) has been proposed in [12–16]. A simplified half-wavelength ($\frac{\lambda_g}{2}$, λ_g denotes the guide wavelength of the resonator at the center frequency) planar ELSPR was put forward and used as a building block in bandpass filter design. The ELSPR is much smaller compared with the conventional microstrip resonator thanks to the high dielectric constant ceramic used. Additionally, the ELSPR has a much higher quality factor than the conventional microstrip resonator. For conventional BPFs based on parallelly-placed microstrip resonators, most energy is transmitted through the lossy substrate between two adjacent microstrip resonators which would lead to large IL. However, for the ELSPR-based BPF design, the medium between two adjacent ELSPRs is the air, which can greatly decrease the insertion loss. So, in this work, we go one step further and use the quarter-wavelength ELSPRs in the BPF design to further decrease the filter size and suppress even harmonics.

In this paper, based on our recent work on single-bandpass filter design using $\frac{\lambda_g}{2}$ ELSPRs, we propose a DBPF based on quarter-wavelength ($\frac{\lambda_g}{4}$) ELSPRs, which is of compact size, high return loss (RL), low IL, and large Q_u.

II. QUARTER-WAVELENGTH ELSPR

As the number of metal wires decreases from 6 to 2 in Figs. 1 (a)-(c), we can observe that hexapolar

Submitted On: July 1, 2022
Accepted On: November 29, 2022
https://doi.org/10.13052/2022.ACES.J.371003

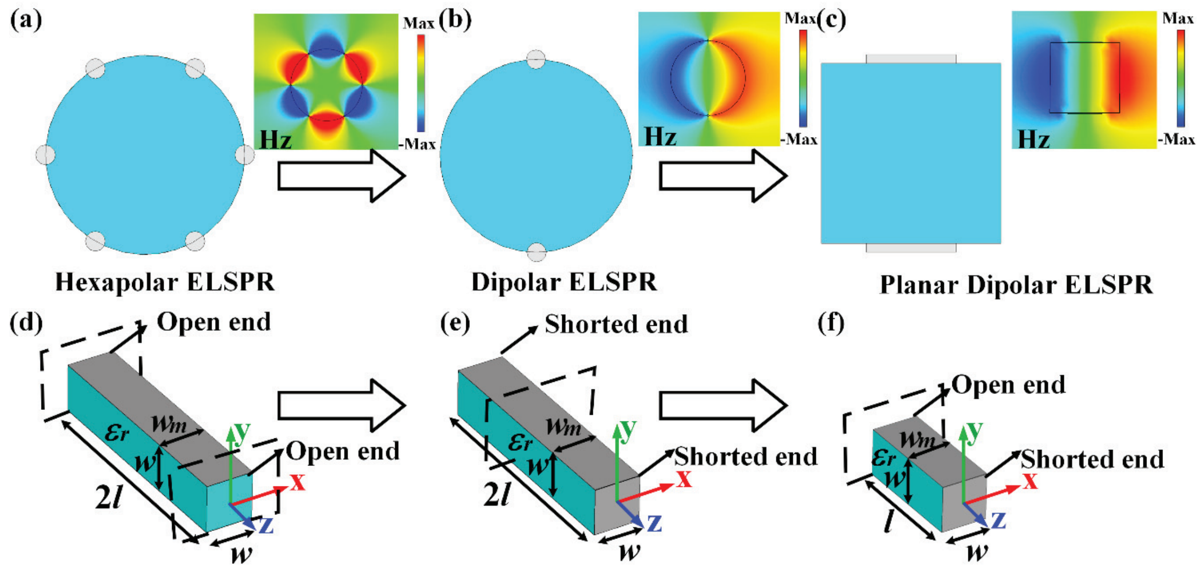

Fig. 1. (a-c) Cross-sectional view and magnetic field distribution of the hexapolar ELSPR, dipolar ELSPR, and planar dipolar ELSPR respectively. (d) A simplified ELSPR with open circuits at both ends. (e) A simplified ELSPR with short circuits at both ends. (f) A $\frac{\lambda_g}{4}$ planar ELSPR with a short circuit at one end and an open circuit at the other end. The 'blue' region denotes the dielectric substrate and the 'grey' part denotes the metal patch.

resonance could not be supported and only dipolar resonance survives. Also, the ELSPR with a rectangular cross-section can be readily fabricated and integrated with planar circuits. Two $\frac{\lambda_g}{2}$ ELSPRs with the same length $2l$ and cross-section dimension are shown in Figs. 1 (d) and (e). The only difference is that the $\frac{\lambda_g}{2}$ ELSPR in Fig. 1 (d) has two open ends and that in Fig. 1 (e) has two shorted ends. However, they have nearly the same resonance frequencies. For further miniaturization, we proposed an $\frac{\lambda_g}{4}$ ELSPR in Fig. 1 (f), which is open at one end and short at the other end. Based on image theory, this $\frac{\lambda_g}{4}$ ELSPR is equivalent to a $\frac{\lambda_g}{2}$ ELSPR in terms of its fundamental mode frequency. According to [15], the fundamental mode frequency of the proposed $\frac{\lambda_g}{4}$ ELSPR can be calculated as:

$$f_a = \frac{c\sqrt{\frac{2}{Re(\varepsilon_r+1)}}}{4l}, \tag{1}$$

where, c is the speed of light in a vacuum, ε_r is the relative permittivity of the medium, and l is the physical length of the $\frac{\lambda_g}{4}$ planar resonator.

Figures 2 (a) and (b) show the electric field lines of the $\frac{\lambda_g}{4}$ ELSPR at the open and shorted ends, and it can be seen that the ELSPR mode is only located at the open end. For comparison between the $\frac{\lambda_g}{2}$ and $\frac{\lambda_g}{4}$ ELSPRs, we consider in Fig. 2 the evolution of the dipolar mode's resonance frequency and quality factor with the variations of the resonator's dimensions. In Fig. 2 (c), we observe that the resonance frequencies of both $\frac{\lambda_g}{2}$ and $\frac{\lambda_g}{4}$ ELSPRs decrease with increasing length l when the metal width $w_m = 0.5mm$ is kept constant and is insensitive to the variations of the side length w. In Fig. 2 (d), for both ELSPRs, the Q_u increases with the increase of w_m when w is fixed and the length $l = 10mm$ is kept constant. We also observe in Fig. 2 (e) that the Q_u of both the two resonators decreases with the increase of the length l while the side length $w = 2mm$ and metal width $w_m = 2mm$ are kept constant. In contrast, the $\frac{\lambda_g}{4}$ ELSPR has a lower Q_u than the $\frac{\lambda_g}{2}$ one due to the increasing metallic loss at the shorted end. In Fig. 2 (f), we also compare the mode frequency distributions for both $\frac{\lambda_g}{2}$ and $\frac{\lambda_g}{4}$ ELSPRs with the same fundamental mode frequency at 3.3GHz. It is obvious that the $\frac{\lambda_g}{4}$ ELSPR has resonances located only at odd times of its fundamental mode frequency. For clearance, the resonance frequencies and Q_u of the first five modes for the $\frac{\lambda_g}{2}$ ELSPR and the first three modes of the $\frac{\lambda_g}{4}$ ELSPR are calculated and listed in Table 1. In the next section, the $\frac{\lambda_g}{4}$ ELSPR is used as a basic unit in the DBPF design.

III. DUAL-BAND BANDPASS FILTER BASED ON PLANAR $\frac{\lambda_g}{4}$ ELSPR

A. Design of single-band $\frac{\lambda_g}{4}$ bandpass filter

In general, to implement a DBPF, one should first design two third-order single bandpass filters separately and then combine them by using T-junctions. For the

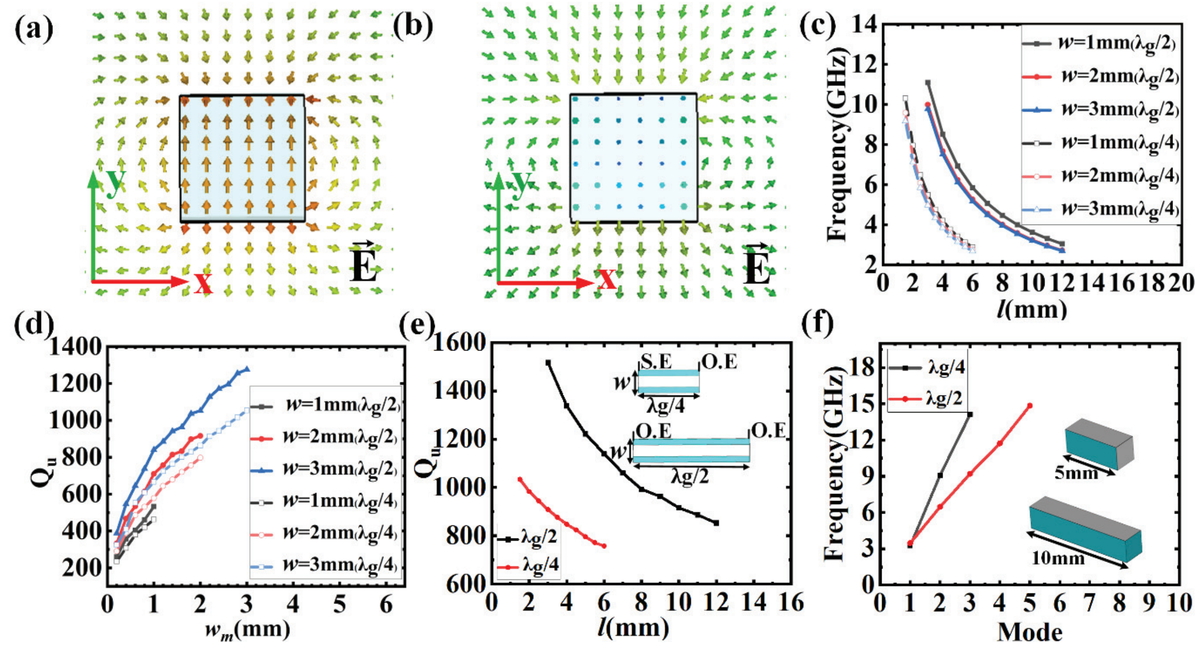

Fig. 2. (a) and (b) Electric field line distributions at the open and shorted end respectively. (c) Evolution of the resonance frequencies of ELSPRs with different l and w. (d) Evolution of Q_u with the variation w_m. (e) Evolution of Q_u with the variation l. (f) Evolution of the resonance frequencies of the $\frac{\lambda_g}{4}$ and $\frac{\lambda_g}{2}$ planar ELSPRs with mode number.

Table 1: Comparison of the resonance modes and the corresponding Q_u of the $\frac{\lambda_g}{2}$ and $\frac{\lambda_g}{4}$ planar ELSPRs

	Mode 1		Mode 2		Mode 3		Mode 4		Mode 5	
	f_0	Q_u	f_0	Q_u	f_0	Q_u	f_0	Q_u	f_0	Q_u
$\frac{\lambda_g}{2}$	3.46	809	6.47	1152	9.20	1418	11.73	1650	14.85	1222
$\frac{\lambda_g}{4}$	3.26	797	9.09	1353	14.12	1771	/	/	/	/

low 5G band or sub-6GHz (450MHz-6GHz) application, two representative center frequencies of 3.1GHz and 3.6 GHz are employed respectively for the design of the proposed ELSPRs. For each ELSPRs-based bandpass filter, the same design framework is shown in Fig. 3 (a), in which three $\frac{\lambda_g}{4}$ ELSPRs are parallelly placed to realize the band-pass filtering function through their mutual coupling. Hereinafter, to better understand the overall design process of the ELSPRs-based filter, we take the central operating frequency of 3.6 GHz as an example and list the design steps of the single bandpass plasmonic filter as follows (we remark that the design in our work can cope with various design requirements, and the operating frequencies can be flexibly tuned by changing the ELSPRs' geometry):

Step 1: Given design specifications as:

1. Center frequency: $f_0 = 3.6$ GHz ;
2. Relative bandwidth: FBW=7.7% ;
3. RL > 20 dB ;
4. IL < 1 dB.

Step 2: Select a three-pole Chebyshev low-pass filter prototype with a bandpass ripple of 0.1 dB. With the normalized low-pass cutoff frequency $\Omega_c = 1$, the low-pass prototype parameters are $g0 = 1$, $g_1 = 1.0316$, $g_2 = 1.1474$, $g_3 = 1.0316$, and $g_4 = 1$, respectively. Thus, we can determine the coupling coefficients and external quality factor (Q_e) as [17]:

$$M_{12} = M_{23} = \frac{FBW}{\sqrt{g_2 g_3}} = 0.071, \quad (2)$$

$$Q_e = \frac{g_0 g_1}{FBW} = 13.4. \quad (3)$$

Step 3: A Ceramic material with a relative permittivity of 12.3 and loss tangent of 2.36×10^{-4} is selected as the material of the resonator. Silver is deposited on the top and bottom of the dielectric as well as on the short end. The substrate is made of Rogers RT5880 with a thickness of 0.508 mm. Thus, the ELSPR's length is 9.5 mm according to Eq. (1).

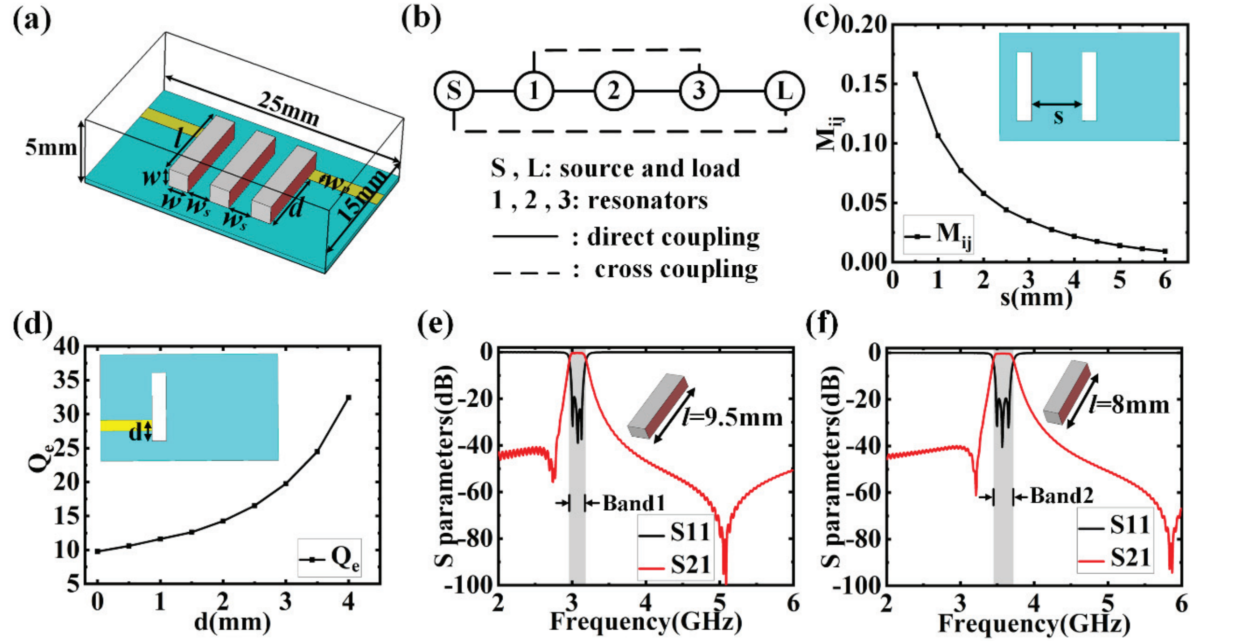

Fig. 3. A Single BPF based on $\frac{\lambda_g}{4}$ planar ELSPR. (a) Schematic diagram of the BPF. (b) Coupling routes. (c) Coupling coefficient between two adjacent ELSPRs. (d) The calculated Q_e of the BPF. (e) and (f) S-parameters of filter I and II with passband Band 1 and Band 2 respectively.

Table 2: Design parameters of single BPF based on $\frac{\lambda_g}{4}$ planar ELSPR

f_0	l	w	w_s	d	w_p
3.1	9.5mm	2mm	2.2mm	7.9mm	1.54mm
3.6	8mm	2mm	2.1mm	7.3mm	1.54mm

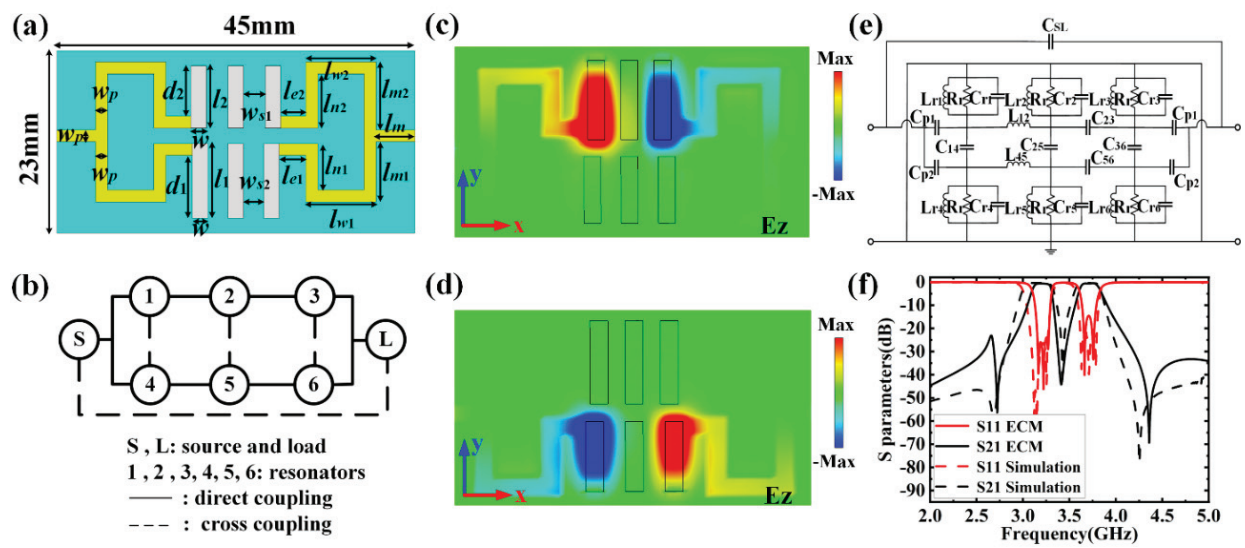

Fig. 4. (a) Layout of the proposed DBPF based on $\frac{\lambda_g}{4}$ ELSPR. (b) Coupling routes. (c) and (d) Distributions of the electric field z-component at the center frequency of 3.1GHz and 3.6GHz respectively. (e) ECM of the proposed DBPF. (f) S-parameters comparison between the ECM simulation in Advanced Design System and CST simulations.

Table 3: Design parameters DBPF based on $\frac{\lambda_g}{4}$ planar ELSPRs

l_1	l_2	w	w_{s1}	w_{s2}	d_1	d_2	w_p	lm
9.5mm	8.0mm	2.0mm	2.1mm	1.8mm	8.0mm	6.5mm	1.54mm	5.0mm
l_{m1}	l_{m2}	l_{w1}	l_{w2}	l_{n1}	l_{n2}	l_{e1}	l_{e2}	
8.3mm	8.5mm	9.1mm	9.1mm	6.0mm	7.0mm	3.5mm	4.7mm	

Table 4: ECM elements for the miniaturized DBPF

L_{r1}	L_{r2}	L_{r3}	L_{r4}	L_{r5}	L_{r6}	L_{12}	L_{45}
0.204nH	0.174 nH	0.313 nH	0.215 nH	0.198 nH	0.217 nH	2.6 nH	3.443 nH
C_{r1}	C_{r2}	C_{r3}	C_{r4}	C_{r5}	C_{r6}	C_{23}	C_{56}
9.05pF	9.981 pF	6.8pF	11.71 pF	9.46 pF	8.031 pF	2.119 pF	1.138 pF
R_r	C_{14}	C_{25}	C_{36}	C_{SL}	C_{p1}	C_{p2}	
0.01Ω	0.385 pF	1.495 pF	1.69 pF	0.025 pF	5.544 pF	11.6 pF	

Step 4: Find the evolution curve in Fig. 3 (c) of the coupling coefficient M_{ij} between Resonators i and j $(i,\ j = 1,\ 2,\ 3;\ 4,\ 5,\ 6)$ with the variation of coupling distance s by using the eigenmode solver in CST, in which M_{ij} can be extracted from the following relationship [18]:

$$M_{ij} = \frac{f_{p2}^2 - f_{p1}^2}{f_{p2}^2 + f_{p1}^2}, \tag{4}$$

where f_{p1} and f_{p2} indicates the two split resonance frequencies of the two parallelly-coupled ELSPRs. Find the evolution curve in Fig. 3 (d) of the Q_e with the variation of feeding position d by using the eigenmode solver in CST, in which Q_e can be extracted by [19]:

$$Q_e = \frac{\omega_0}{\Delta\omega \pm 90^\circ}, \tag{5}$$

where ω_0 is the resonance angular frequency and $\Delta\omega\ \pm\ 90^\circ$ is determined by the absolute bandwidth corresponding to the actual phase variation of 90° at ω_0.

Determine the initial value of $s = 1.7mm$ by fitting the value from Eq. (2) in Fig. 3 (c) and the initial value of $d = 1.7mm$ by fitting the value from Eq. (3) in Fig. 3 (d).

Step 5: Optimize the S-parameters of the filter by fine-tuning s and d. Finally, the expected design specifications are achieved and shown in Fig. 3 (e), in which the center frequency is 3.1GHz, the relative bandwidth is 10.7%, and the RL is greater than 23dB. Figure 3 (f) shows the S-parameter of the other single pass-band filter with the center frequency at 3.6 GHz and relative bandwidth of 7.7%. The corresponding optimized structural parameters are listed in Table 2.

B. Design of DBPF based on $\frac{\lambda_g}{4}$ ELSPR

We then designed a DBPF by introducing two T-junctions at the input and output ports and combining the above two third-order single-band bandpass filters. The electrical length of the two microstrip lines connecting the T-junction and the side resonator in one bandpass filter is about $\frac{\lambda_g}{4}$ corresponding to the passband central frequency of the other one. Thus, the coupling between these two filters can be minimized. Figures 4 (a) and (b) show the layout of our proposed ELSPRs-based DBPF and its corresponding coupling route, respectively. Figures 4 (c) and (d) show the distributions of the z-component of the electric fields at the two passband center frequencies of 3.1 GHz and 3.6 GHz respectively. It is seen that the two passbands have very high isolations. After optimizations in CST, the final structural dimensions in Fig. 4 (a) can be obtained and listed in Table 3.

C. Equivalent circuit model

To facilitate the understanding of the mechanism of the ELSPs-based DBPF, we give the corresponding model of the equivalent circuit model (ECM) in Fig. 4 (e). A parallel RLC circuit consisting of equivalent inductance L_{ri}, capacitance C_{ri}, and resistance R_r can be used to represent the ELSPR. L_{ij} and C_{ij} represent the electrical coupling between two adjacent resonators. C_p indicates port coupling. C_{SL} indicates the electrical cross-coupling between the load and source. The ECM elements in Fig. 4 (e) are listed in Table 4 in Fig. 4 (f), the corresponding S-parameters derived from the ECM in Advanced Design System and the simulations in CST are compared. Good consistency between these two curves indicates that ECM can be reasonable to describe the DBPF.

D. Fabrication and measurement

Figure 5 (a) shows a picture of the fabricated DBPF, in which the circuit is encapsulated in a height of 5mm aluminum shielding box. Two SMA coaxial connectors are used for the signal input and output. The S-parameters are measured by using the Agilent N5230C vector network analyzer. Figure 5 (b) shows excellent agreement between the simulated and measured S-parameters. The two passbands center at 3.1 GHz and 3.6 GHz and the relative bandwidths are about 10.7% and 7.7%. The insertion losses are less than 0.8 dB

Table 5: Performance comparison between the proposed ELSPR-based DBPF and other DBPFs in previous works

Reference	f_0 (GHz)	IL(dB)	RL(dB)	FBW	Filter Size
[1]	3.5/5.24	1.52/1.65	15/15	2.86%/3.81%	$1.5129\lambda_0{}^2$
[3]	2.45/5.8	1.8/3.0	10/10	12%/7%	$0.0452\lambda_0{}^2$
[8]	2.4/5.2	0.6/1.4	12/12	13.7%/6.3%	$0.1932\lambda_0{}^2$
[20]	2.4/5.2	3.6/3.1	15/23	5.8%/6.4%	$0.0240\lambda_0{}^2$
[21]	4.32/5.52	2.79/2.92	27.8/25.6	5.76%/4.98%	$0.0635\lambda_0{}^2$
This work	**3.1/3.6**	**0.53/0.75**	**20/20**	**10.7%/7.7%**	$\mathbf{0.0396\lambda_0{}^2}$

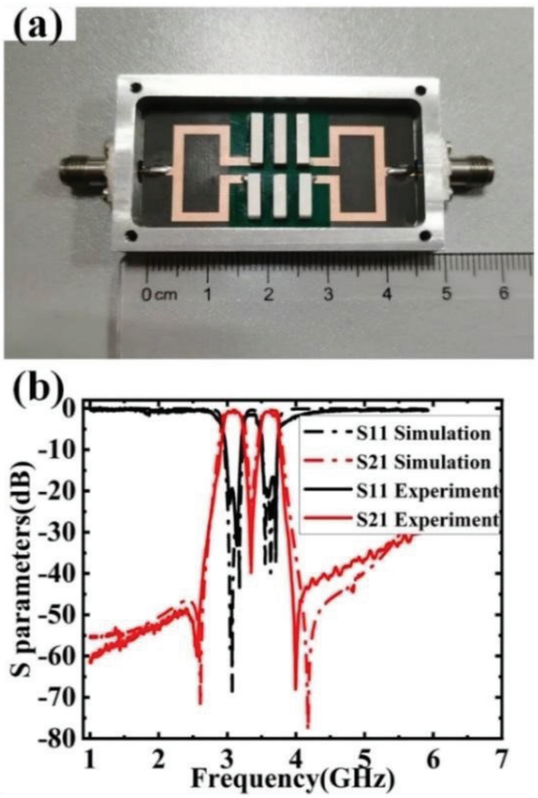

Fig. 5. (a) The fabricated DBPF. (b) Simulated and measured S-parameters.

and the return losses are higher than 20 dB in both pass bands. The upper stopband rejection is greater than 20 dB over a wide frequency range from 4 to 6 GHz. The electrical size of the DBPF is approximately 0.0396 $\lambda_0{}^2$. Compared with published DBPFs in [1, 3, 8, 20, 21] in Table 5 (λ_0 denotes the free-space wavelength at the center frequency). It is seen that the proposed ELSPRs-based DBPF features an excellent balance among various indices including IL, RL, size, and bandwidth.

IV. CONCLUSION

In this work, we explore the characteristics of $\frac{\lambda_g}{4}$ ELSPR and design a compact DBPF by using $\frac{\lambda_g}{4}$ planar ELSPR to suppress even-order harmonics. Simulation and measurement results show that the DBPF can achieve an ultra-compact size, easy integration, low insertion loss, high selectivity, and wide out-of-band rejections. Our design provides a new route to design compact DBPFs and has potential applications in 5G communication systems.

ACKNOWLEDGMENT

This work was supported in part by the National Natural Science Foundation of China (No. 61871215, 61771238, 61701246), State Key Laboratory of Millimeter Waves (No. K202209), and Six talent peaks project in Jiangsu Province (No.2018-GDZB-009).

REFERENCES

[1] P. Li, H. Chu, D. Zhao, and R. S. Chen, "Compact dual-band balanced SIW bandpass filter with improved common-mode suppression," *IEEE Microwave and Wireless Components Letters*, vol. 27, no. 4, pp. 347-349, 2017.

[2] Z. Tan, Q.-Y. Lu, and J.-X. Chen, "Differential dual-band filter using ground bar-loaded dielectric strip resonators," *IEEE Microwave and Wireless Components Letters*, vol. 30, no. 2, pp. 148-151, 2020.

[3] J.-T. Kuo, T.-H. Yeh, and C.-C. Yeh, "Design of microstrip bandpass filters with a dual-passband response," *IEEE Trans. Microwave Theory Techniques*, vol. 53, no. 4, pp. 1331–1337, Apr. 2005.

[4] B. Wu, C.-H. Liang, Q. Li, and P.-Y. Qin, "Novel dual-band filter incorporating defected SIR and microstrip SIR," *IEEE Microwave and Wireless Components Letters*, vol. 18, no. 6, pp. 392–394, Jun. 2008.

[5] J. Xu, W. Wu, and C. Miao, "Compact and sharp skirts microstrip dual-mode dual-band bandpass filter using a single quadruple-mode resonator (QMR)," *IEEE Trans. Microwave Theory and Techniques*, vol. 61, no. 3, pp. 1104-1113, 2013.

[6] S. Sun, "A dual-band bandpass filter using a single dual-mode ring resonator," *IEEE Microwave and Wireless Components Letters*, vol. 21, no. 6, pp. 298-300, 2011.

[7] S. Fu, B. Wu, J. Chen, S.-J. Sun, and C.-H. Liang, "Novel second-order dual-mode dual-band filters using capacitance loaded square loop resonator," *IEEE Trans. Microwave Theory and Techniques*, vol. 60, no. 3, pp. 477-483, 2012.

[8] Y. C. Li, H. Wong, and Q. Xue, "Dual-mode dual-band bandpass filter based on a stub-loaded patch resonator," *IEEE Microwave and Wireless Components Letters*, vol. 21, no. 10, pp. 525-527, 2011.

[9] L. Gao, X. Y. Zhang, and Q. Xue, "Compact tri-band bandpass filter using novel eight-mode resonator for 5G WiFi application," *IEEE Microwave Wireless Components Letters*., vol. 25, no. 10, pp. 660–662, Oct. 2015.

[10] Z. Liu, G. Xiao, and L. Zhu, "Triple-mode bandpass filters on CSRR-loaded substrate integrated waveguide cavities," *IEEE Trans. Components, Packaging and Manufacturing Technology*, vol., 6, no. 7, pp. 1099–1105, Jul. 2016.

[11] S.-W. Wong, S.-F. Feng, L. Zhu, and Q.-X. Chu, "Triple-and quadruple mode wideband bandpass filter using simple perturbation in single metal cavity," *IEEE Trans. Microwave Theory and Techniques*, vol. 63, no. 10, pp. 3416–3424, Oct. 2015.

[12] C. Della Giovampaola and N. Engheta, "Plasmonics without negative dielectrics," *Physical Review. B, Condensed Matter and Materials Physics*, vol. 93, no. 19, May 2016, Art. no. 195152.

[13] Z. Li, L. L. Liu, H. Y. Sun, Y. H. Sun, C. Q. Gu, X. L. Chen, Y. Liu, and Y. L, "Effective surface plasmon polaritons induced by modal dispersion in a waveguide," *Physical Review Applied*, vol. 7, no. 4, pp. 044028, Apr. 2017.

[14] Z. Li, L. L. Liu, A. I. Fernandez-Dominguez, J. F. Shi, C. Q. Gu, F. J. Garcia-Vidal, and Y. Luo, "Mimicking localized surface plasmons with structural dispersion," *Advanced Optical Materials*, vol. 7, no. 10, 2019.

[15] Q. Jiang, Y. Yu, Y. Zhao, Y. Zhang, L. Liu, and Z. Li, "Ultra-compact effective localized surface plasmonic sensor for permittivity measurement of aqueous ethanol solution with high sensitivity," *IEEE Trans. Instrumentation and Measurement*, vol. 70, pp. 1-9, 2021.

[16] Y. Yu, L. Liu , Q. Jiang, Y. Zhao, Y. Zhang, Y. Luo, C. Gu, and Z. Li, "Ultracompact effective localized surface plasmonic bandpass filter for 5G applications," *IEEE Trans. Microwave Theory and Techniques*, vol. 69, no. 4, pp. 2220-2228, 2021.

[17] J.-S. Hong and M. J. Lancaster, "Cross-coupled microstrip hairpin-resonator filters" *IEEE Trans. Microwave Theory and Techniques*, vol. 46, no. 1, pp. 118-122, 1998.

[18] J.-S. Hong and M. J. Lancaster, "Couplings of microstrip square open-loop resonators for cross-coupling planar microwave filters" *IEEE Transactions on Microwave Theory and Techniques*, vol. 44, no. 12, pp. 2099-2108, 1996.

[19] J.-S. Hong and M. J. Lancaster, *Microstrip Filters for RF/Microwave Applications*. Wiley, New York, NY, USA, 2011.

[20] S. Xu, K. Ma, F. Meng, and K. S. Yeo, "Novel defected ground structure and two-side loading scheme for miniaturized dual-band SIW bandpass filter designs," *IEEE Microwave and Wireless Components Letters*, vol. 25, no. 4, pp. 217-219, 2015.

[21] H.-Y. Gao, Z.-X. Tang, X. Cao, Y.-Q. Wu, and B. Zhang, "Compact dual-band SIW filter with CSRRS and complementary spiral resonators," *Microwave and Optical Technology Letters*, vol. 58, no. 1, pp. 1-4, 2016.

Zixiang Zhou was born in Benxi, Liaoning, China, in 1998. She received her B.S. degree in Electronic Information Science and Technology from Nanjing University of Aeronautics and Astronautics (NUAA) in 2020. She is currently pursuing an M.E. degree at NUAA. Her current research interests include effective localized surface plasmons and filters.

Liangliang Liu (M'17) received a B.S. degree in information engineering, an M.E. degree in Electromagnetic Field and Microwave Technology, and Ph.D. degree in Communication and Information System from Nanjing University of Aeronautics and Astronautics (NUAA), China, in 2010, 2013, and 2017, respectively. From Mar. 2017 to Nov. 2020, he joined Nanjing University of Information Science and Technology as an associate professor. From Nov. 2017 to Oct. 2019, he worked at Nanyang Technological University, Singapore, as a Research Fellow. He is currently an associate professor with the College of Electronic and Information Engineering at NUAA. He has published over 60 papers in international refereed journals and conference proceedings. His current research interests include microwave and millimeter-wave devices and antennas, spoof surface plasmons, effective surface plasmons, and coding metasurface.

Xinhua Li was born in Chifeng, Inner Mongolia, China, in 1997. She received her B.S. degree in Information Engineering from Nanjing University of Aeronautics and Astronautics (NUAA) in 2019. She is currently pursuing an M.S. degree at NUAA. Her current research interests include spoof localized surface plasmonic skyrmions and sensors.

Jinrui Shen was born in Pingliang, Gansu, China in 1998. She received her B.S. degree in Electronic Information Science and Technology from Nanjing University of Aeronautics and Astronautics (NUAA) in 2020. She is currently pursuing an M.E. degree at NUAA. Her current research interests include spoof magnetic localized surface plasmons.

Guodong Han was born in Shandong Province, China, in 1980. He received a B.S. degree in Electronic Engineering from the Nanjing University of Aeronautics and Astronautics, Jiangsu, China, in 2003, and M.S. and Ph.D degrees in Electromagnetic and Microwave Technology from the Nanjing University of Aeronautics and Astronautics, Jiangsu, China, in 2005 and 2008, respectively.

From 2008 to 2011, he has been worked at Nanjing Research Institute of Electric Institute (NRIET), Jiangsu, China, as a primary engineer. His work is focused on the active phased array antenna systems in radar. From 2011 to 2013, he completed his postdoctoral work studying the active phased array in the satellite communication field at the 54th Research Institute of China Electronics Technology Group Corporation. Since 2013, he has been involved in the development ofactive/passive antenna system for satellite communication. His research interests include active phased array antenna systems and active components in the RF and microwave frequencies. He has published more than 30 contributory papers in referred journals and international conference proceedings. His team has developed S-band, Ku-band, and Ka-band phased array antennas for satellite communications, which have been applied to mobile platforms such as airborne, vehicular and shipborne. His team has also developed phased array antennas for spaceborne platforms.

Zhuo Li was born in Wuhan, China, in 1979. He received a B.S. degree in Electronic Engineering and an M.E. degree in Electromagnetic Fields and Microwave Techniques from Nanjing University of Aeronautics and Astronautics (NUAA), Nanjing, China, in 2001 and 2004, respectively, and a Ph. D. degree in Radio Engineering from the State Key Laboratory of Millimeter Waves, Southeast University, Nanjing, in 2009. From 2015 to 2016, he was a Visiting Scholar with the Department of Physics at Arizona State University, Tempe, AZ, USA. He is currently a Full Professor at the College of Electronic and Information Engineering at NUAA. He has authored or co-authored over 120 papers in refereed journals and conference proceedings, including Advanced Science, Advanced Optical Materials, Nano Letters, Physical Review Applied, IEEE Transactions on Microwave Theory and Techniques, IEEE Transactions on Antennas and Propagation, and IEEE Transactions on Electromagnetic Compatibility. His current research interests include plasmonic metamaterials, computational electromagnetics, electromagnetic compatibility in avionics and auto-electrical systems.

Prof. Li is an IEEE member, a Senior Member of the Chinese Institute of Electronics and a Committee Member of the Antenna Branch of the Chinese Institute of Electronics.

Analysis of Super-Solar Integrated Patch Antenna for Sub-6 GHz and Beyond 6 GHz Millimeter Wave 5G Applications

Suresh Babu T. Naganathan[1], Sivakumar Dhandapani[2], and Thirumaraiselvan Packirisamy[3]

[1]Department of Electronics and Communication Engineering
Adhiparasakthi Engineering College, Melmaruvathur, Tamilnadu-603 319, India
sureshbabutns@gmail.com

[2]Department of Computer Science and Engineering
AMET University, Kanathur-603 112, Tamilnadu, India
dgsivakumar@gmail.com

[3]Department of Electronics and Communication Engineering
Adhiparasakthi Engineering College, Melmaruvathur, Tamilnadu-603 319, India
thirumarai@hotmail.com

Abstract **–** This article describes a new compact parasitic patch-loaded transparent patch antenna with a copper ground plane for wireless-fidelity (Wi-Fi) and 5^{th} generation (5G) millimeter-wave (mm-wave) applications. The proposed antenna uses two rectangular parasitic patches with a rectangular main radiation patch. The L-shaped strips are also added to the main radiation patch and one of the rectangular parasitic patches to cover both the sub-6 GHz and beyond 6 GHz mm-wave 5G frequency spectrums. The same transparent patch antenna with a solar ground plane is built, and its effect is parametrically studied alongside the integration of a polycrystalline silicon solar cell. The proposed antennas with a dimension of $42\times30\times2$ mm^3 are fabricated and experimentally validated for impedance and radiation characteristics. In terms of impedance bandwidth, the proposed copper ground plane antenna offers 36.89% (5.04-7.32 GHz), 5.15% (14.35-15.11 GHz), 6.23% (27.08-28.79 GHz), and 21.34% (31.64-39.81 GHz). The solar cell serves as both a photovoltaic generator and the ground plane of the transparent antenna. The same radiating patch with a solar ground plane offers impedance bandwidth of 36.03% (4.47-6.56 GHz), 14.4% (9.6-11.12 GHz), 2.55% (22.14-22.71 GHz), and 27.9% (28.79-39.05 GHz) for 5G applications.

Index Terms **–** 5G applications, integrated antennas, mm–wave, patch antennas, solar cells.

I. INTRODUCTION

The intensive research into 5G technology is a strong sign of the technological transformation required to address the growing demand and needs for high-speed connectivity and Internet of Things (IoT)-based applications. Researchers can refine their study objectives and contribute to progress, thanks to the timely improvement in 5G technology. Not only smartphones, but also various IoT devices will use 5G technologies to provide various services such as smart buildings, smart cities, and more, which will necessitate a 5G antenna with low latency, low path loss, and a steady radiation pattern [1]. With all these services and features, the demand for a high data rate will rise in the future.

To meet the demands of sufficient bandwidth and higher data rates for next-generation wireless communications, mm-wave frequency bands are emerging to overcome over-utilized spectra below 6 GHz and become a good choice for next-generation wireless communications. As of now, 4G long-term evolution (LTE) technology has integrated a number of commercial services that have high data rates, high-speed connectivity, and high throughput into a single network. Nonetheless, this large update poses certain bandwidth limitation difficulties, which limit the demand for an advanced wireless network. Therefore, mm-wave 5G technology is one of the best ways to get faster data speeds because it uses more carrier frequencies. In terms of wireless communication, microstrip antennas are one of the best options for mm-wave applications because they have a small footprint and are cheap to make and use.

Several articles on the co-design of 4G and 5G have been published [2–7]. Due to the limited space in smartphones, combining 4G LTE and 5G mm-wave antennas is difficult. Several feeding strategies based on slotted

Submitted On: August 15, 2022
Accepted On: November 7, 2022
https://doi.org/10.13052/2022.ACES.J.371004

arrays [8] and proximity-coupled feeding [9] have been reported to improve the radiation characteristics of 5G antennas. Antenna-in-Package (AiP) is a packaging technology that incorporates active chipsets and mm-wave antennas into ordinary surface-mount devices to achieve high integration [10, 11]. MIMO systems [12, 13] require special consideration due to their simultaneous radiating capabilities, which result in increased channel capacity. The antenna array in a mobile device should produce two orthogonal polarizations to avoid multipath fading and allow MIMO to work at higher data rates [14, 15].

Numerous ways have been proposed by researchers to improve the operational bandwidth, radiation gain, and η (efficiency) of mm-wave patch antennas. Defected ground structure (DGS) with different shapes and sizes is one of the most extensively used approaches in antennas [16, 17] for reducing component size, increasing operational bandwidth and gain, and suppressing higher-order harmonics and undesirable cross-polarization. Metamaterials are a potential technology for improving mm-wave antenna performance, miniaturization, and ease of manufacture [18, 19]. Vertically connected split ring metaplates [20] and double-layer concentric ring metaplates [21] are used to improve the gain performance of a patch antenna that can be used in mm-wave (5G).

It has been proposed to widen bandwidth by loading stacked or coplanar parasitic patches around a microstrip patch. Proposals include stacking parasitic patches on top of an inset-fed patch [22], a radiation element composed of a slim rectangular patch with a surrounding U-shaped parasitic patch [23], by incorporating two semicircular-shaped parasitic patches [24], and a microstrip patch fed by a coaxial probe is loaded with coplanar parasitic patch arrays [25]. To suit cost-effective needs, an FR4 printed circuit board has recently been used as the substrate. Many low-cost mm-wave antennas [26–32] have been reported, including planar inverted-F antennas (PIFA) [28], U-shaped slot patch antennas [29], ball grid array (BGA) packaged ring slot antennas [30], BGA surface-mount bowtie antenna [31], and double-curved metal in multilayer printed circuit boards [32].

Advanced feeding design, elaborate parasitic structures, and improved beam scanning capability for 5G mobile terminals support the dual-polarized feature with multiband coverage [33, 34]. Many circularly polarized mm-wave antennas have been reported, including a slotted SIW cavity antenna [35] and a special-shaped ring-slot structure on the ground layer with an Archimedean spiral radiator [36]. For high-speed point-to-point mm-wave data transfer, researchers have come up with a dual-array antenna system with a compact feeding network [37], a reflectarray resonant element based on a dielectric resonator antenna (DRA) [38], and a dual-band array antenna design with a beam-steerable property [39].

The growth of low-power embedded devices in consumer and commercial applications has encouraged alternative energy research. It includes wireless networks, power transfer, the IoT, and electric cars. IoT proliferation requires more scalable and robust communication networks that can supply greater data rates while using less energy per device. Many independent devices use solar energy to power equipment due to the rapid growth of solar cell technology and the necessity to work on green connectivity with Earth- and space-based communications systems. Solar cell manufacturing surfaces are limited and must be shared with other components and communication systems. One of the best ways to share exposed surface area, lower device costs, and make sure everything works together is to combine antennas and solar cells. The integration of antennas with solar cells is thus attractive, with many designs reported in the literature [40–63]. The current state of the art in integration strategies can be divided into two categories: sub-solar integrated type and super-solar integrated type. The antennas of the sub-solar integrated type are placed beneath the solar cells, while the antennas of the super-solar integrated type are placed above the solar cells.

Sub-solar integrated type antennas [40] have been created for 2.225 GHz micro and large spin satellites, with solar cells positioned on or around the antenna. The stepped slot sub-solar antenna [41], which covers 5.12-5.36 GHz and 7.32-8.02 GHz where the solar cell works as an RF ground plane, is proposed for Wi-Max and future mobile communications. Sub-solar techniques [42–48] for autonomous communication systems use slot antennas positioned beneath the solar panel so that the emitting surface is not shaded. The antenna element should be small and placed between the solar cells. As a result, the super solar approach is gaining popularity.

Transparent meshed patch antennas for the super-solar approach have properties similar to normal microstrip patch antennas while using less metal and being optically transparent for cube-sat and other small satellites around 2.4 GHz applications [49–53], self-powered UWB applications [54], and Ku-band ground-to-space satellite communications [55]. A transparent conformal slot antenna [56] has been reported for X-band cube-sat applications. Transparent conductive oxide (TCO) patch antennas have been described for terrestrial applications [57], UWB wireless communications and RF energy harvesting [58], and X-band applications [59]. For X-band and cube-sat applications, an optically transparent reflectarray antenna on solar cells [60, 61] is described. The super-solar opaque antenna [62] for remote sensing systems consists of a small slot antenna that shadows the solar cells and patch antennas that are placed between the solar cells. To date, there has been no in-depth discussion of the mm-wave patch antenna in combination with a solar cell.

A tetra-band suspended parasitic patch loaded transparent patch antenna with ground planes of both copper and the solar cell is provided in this study, and it serves as a 5G for sub-6 GHz and beyond 6 GHz mm-wave applications. Simulations of the design using Computer Simulation Technology's (CST) Microwave Studio (MWS) Software yield encouraging results.

II. ANTENNA DESIGN AND ANALYSIS

The proposed compact transparent antenna geometry and its dimensions are illustrated in Fig. 1. The antenna is made up of two rectangular parasitic patches connected by the primary radiation patch. Furthermore, two L-shaped strips are inserted on the primary radiation patch and the right side of the rectangular parasitic patch. The main rectangular patch, parasitic patches, L-shaped strips, and infinite ground plane are all built from 0.025 mm thick copper foil.

The transparency of the antenna is achieved by using a transparent substrate having dimensions of $42\times30\times2$ mm^3 in the form of Plexiglass, having a loss tangent of 0.00037 and a dielectric constant of 3.4, which is calculated using the cavity perturbation method [64, 65].

The resonance frequency of the cavity is described as follows:

$$f_{mnp} = \frac{\upsilon}{2\sqrt{\mu_r\varepsilon_r}}\sqrt{\left(\frac{m}{a}\right)^2+\left(\frac{n}{b}\right)^2+\left(\frac{p}{d}\right)^2}\ Hz, \quad (1)$$

where f_{mnp} is the resonant frequency, with mode numbers m, n, and p and corresponding dimensions a, b, and

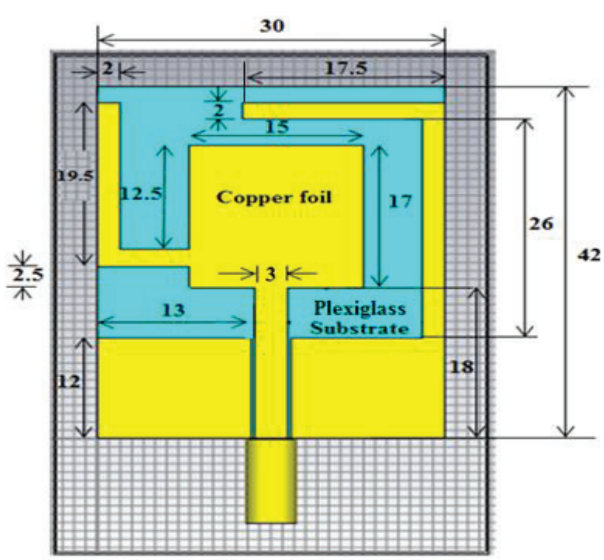

Fig. 1. Geometry and dimensions of the proposed antenna.

d; μ_r and ε_r are the relative permeability and permittivity of the cavity filling; and υ is the speed of light in vacuum, respectively. In this case, by using microwave cavity perturbation theory, the dielectric properties of the sample are determined by means of the differential measurement between the empty and a sample-filled cavity resonator. The permittivity ε of the substrate sample is described as follows:

$$\varepsilon = \left(\frac{V_c}{V_s}\right)\left(\frac{f_c-f_s}{2f_s}\right), \quad (2)$$

where V_c and V_s are the volumes of the empty cavity and the sample inserted, f_c and f_s are the resonant frequencies of the empty cavity and the sample inserted, respectively. The conductive patch and ground are glued to the plexiglass using adhesive so as to overcome the air gap while sticking the copper foil. Furthermore, the same transparent patch antenna is integrated with a poly-silicon solar cell ground plane with a thickness of 0.2 mm and the same dimensions as the antenna substrate. Figure 2 shows the fabricated prototype of the antennas.

CST-MWS numerical simulation software based on the Finite-Difference Time-Domain (FDTD) approach is used to carry out and optimize the proposed antenna designs and simulations. In addition, the feed point is carefully selected and optimized for impedance matching. Figure 3 depicts the evolution of the proposed 5G mm-wave radiator. Figure 4 depicts the S_{11} properties during the evolution steps. The antenna design starts with a simple rectangular microstrip patch radiator, whose length and width are determined by the basic rectangular antenna equations [66].

The width W, the effective dielectric constant ε_{eff}, effective length L_{eff}, length extension ΔL, and the actual length L of the patch can be computed as follows:

$$W = \frac{c}{2f_r}\sqrt{\frac{2}{\varepsilon_r+1}}, \quad (3)$$

$$\varepsilon_{eff} = \frac{\varepsilon_r+1}{2}+\frac{\varepsilon_r-1}{2}\frac{1}{\sqrt{1+12\frac{h}{W}}}, \quad (4)$$

$$L_{eff} = \frac{c}{2f_r\sqrt{\varepsilon_{eff}}}, \quad (5)$$

$$\Delta L = 0.412h\frac{\left(\varepsilon_{eff}+0.3\right)\left(\frac{W}{h}+0.264\right)}{\left(\varepsilon_{eff}-0.258\right)\left(\frac{W}{h}+0.8\right)}, \quad (6)$$

and

$$L = L_{eff}-2\Delta L, \quad (7)$$

where f_r is the resonance frequency, c is the speed of light in free space, h is the substrate thickness, and ε_r is the relative permittivity of the dielectric substrate, respectively.

Figure 3 (a) shows a rectangular microstrip patch with a coaxial-fed that can resonate at frequencies ranging from 4.66 GHz to 5.42 GHz. Furthermore, as shown

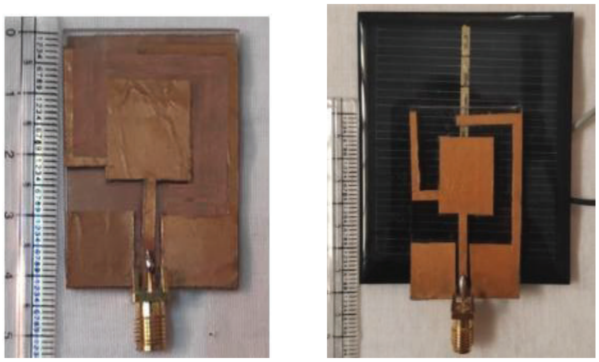

(a) (b)

Fig. 2. Photograph of the fabricated antenna: (a) Copper ground plane; (b) Solar cell ground plane.

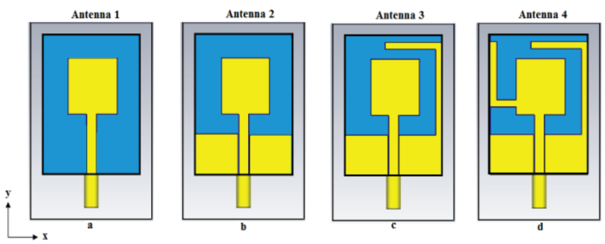

Fig. 3. Evolution of the proposed patch antenna: (a) Primary rectangular patch radiator. (b) Two rectangular parasitic patches incorporated in antenna 1. (c) First L-shaped strip incorporated in antenna 2 on the right side of the rectangular parasitic patch. (d) Second L-shaped strip incorporated additionally in antenna 3 on the primary rectangular patch radiator.

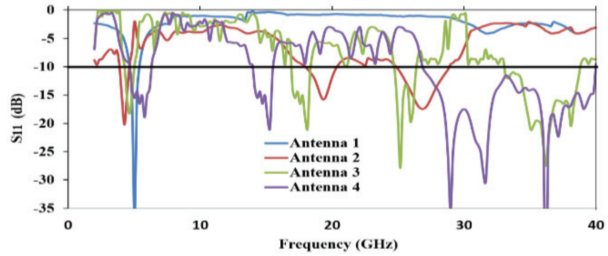

Fig. 4. S_{11} characteristics during the evolution steps.

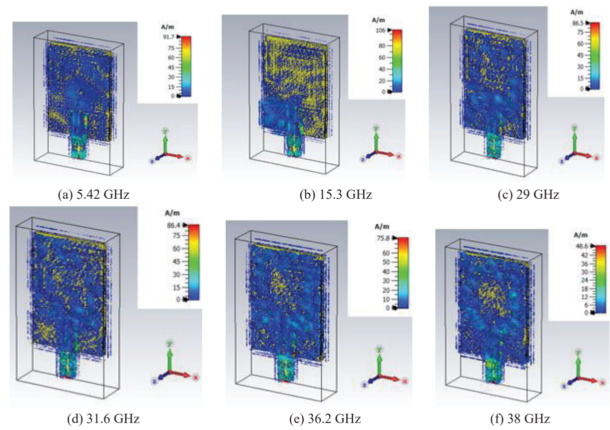

Fig. 5. Snapshots of the simulated current distributions of the proposed antenna at different frequencies.

in Fig. 3 (b), two rectangular parasitic patches are integrated adjacent to the bottom of the microstrip line to cover the 3.9-4.66 GHz, 18-20.2 GHz, and 25-28.8 GHz frequency spectrums with an $|S_{11}| \leq -10$ dB. Furthermore, by attaching the first L-shaped strip to the right side of the rectangular parasitic patch (see Fig. 3 (c)), we obtain resonant modes with frequencies ranging from 4.28-5.04 GHz to 17-18.3 GHz, 24.8-26.3 GHz, and 33.2-38.7 GHz, respectively. Furthermore, by including the second L-shaped strip on the main radiation patch (see Fig. 3 (d)), three resonant modes covering the 4.85-6.18 GHz Wi-Fi sub-6 GHz band, 14.16-15.49 GHz, and 29.89-39.81 GHz 5G mm-wave were excited. Due to its super wide bandwidth, the simulation results show that Antenna 4 (see Fig. 3 (d)) is more suitable for use in future 5G mm-wave communications, and it is also simple in design with ease of manufacture.

The surface current distribution of the antenna can be used to study the resonant properties of the proposed plexiglass-based transparent patch antenna with a copper ground plane. Figure 5 depicts the proposed antenna's simulated surface current distribution at frequencies of 5.42, 15.3, 29, 31.6, 36.2, and 38 GHz, with the high-pitched color representing the strongest surface current distribution area. According to this, at 5.12 GHz, the majority of the power is radiated across the surface of the antenna's rectangular parasitic patches and L-shaped strips, whereas at 15.3 GHz, the primary radiator, two L-shaped strips, and the right-side rectangle parasitic patch have the most power. The results demonstrate that the two L-shaped strips have the greatest influence on the formation of resonance modes in the lower and upper bands, respectively. Similarly, at 29, 31.6, 36.2, and 38 GHz, the most power is emitted on the surface of the primary radiator and rectangular parasitic patches placed near the microstrip feed, resulting in super wideband performance.

III. MEASUREMENTS AND RESULTS

The fabricated prototype, displayed in the inset of Fig. 6, was characterized in the frequency range of 1-44 GHz using a microwave vector network analyzer (serial number: KEYSIGHT N9951A). In Fig. 7, the simulated and measured $|S_{11}|$ and VSWR responses of two cases of the proposed transparent patch antenna with the copper ground and solar cell ground are compared.

Table 1 shows the measured results of the proposed antennas at the desired operating band of frequencies,

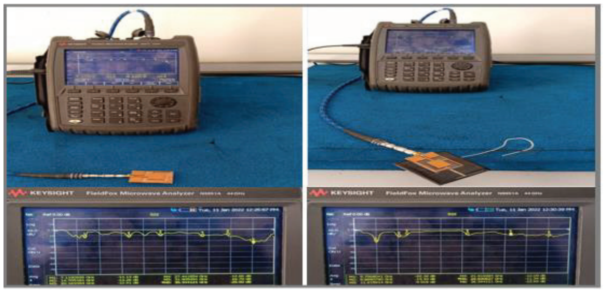

Fig. 6. Snapshots of the KEYSIGHT N9951A Network Analyzer for measuring S-parameters.

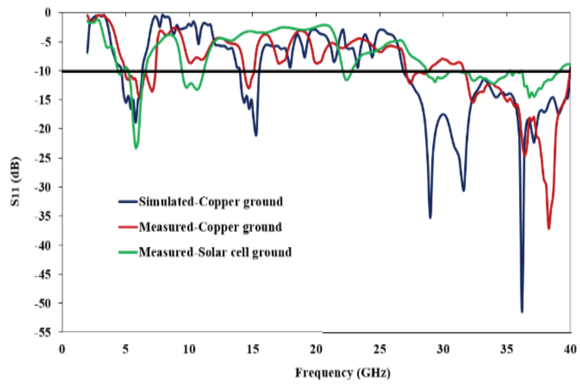

(a)

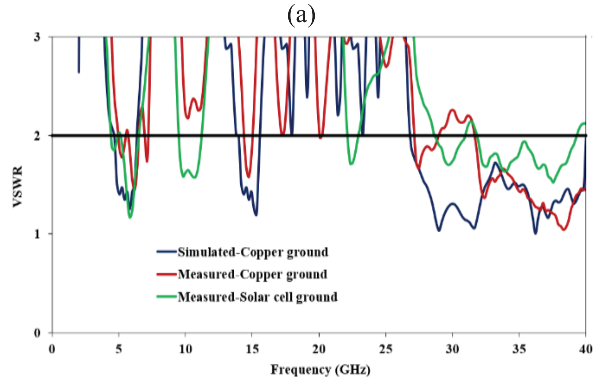

(b)

Fig. 7. (a) Measured and simulated return loss $|S_{11}|$ of the proposed antenna. (b) Measured and simulated VSWR of the proposed antenna.

allowing them to operate in the Wi-Fi and 5G operational bands. There is a reasonable accord between the experimental results and the simulated results for the proposed transparent antenna. However, some minor deviations are observed due to losses (transmitting antenna, connector, and cable loss) in the measurement setup, fabrication tolerances, and the resulting imperfections in the resulting dimensions.

The far-field radiation patterns are measured in an anechoic room with a standard horn antenna. Figure 8 shows the antenna under test (AUT) in the anechoic chamber. For pattern characteristics measurement, the transmitting horn antenna and test antenna (TA) were separated by a distance of 4 m. Now, the E-plane radiation patterns of the proposed transparent antenna were estimated by both simulation and experiment. They were then plotted in Figs. 9 (a)-(d) for frequencies of 5.5, 28.79, 36.7, and 38.1 GHz, respectively. A good correlation is achieved between simulated and measured omnidirectional radiation patterns. Table 2 shows the simulated and measured peak gains of proposed antennas at the desired operating band of frequencies.

A dedicated set of measurements to evaluate the effects of the proposed patch integrated into the photovoltaic generation of solar cells is also described. The open-circuit voltage (V_{OC}) and short-circuit current (I_{SC}) of solar cells are measured under the midday sun to assess the shading effect on solar photovoltaic output, as illustrated in Fig. 10.

From the measurement, the solar cell carries the current I_{SC} = 97.4 mA with the voltage V_{OC} = 4.35 V when there is no integrated antenna with the solar cell. Nevertheless, the identical solar cell is integrated with an antenna; the measured I_{SC} current and V_{OC} voltage are 61.4 mA and 3.88 V, respectively. The open-circuit voltage has a small difference, as expected because a relatively stable open-circuit voltage is a feature of solar cells in partially shaded scenarios. The small decrease in short-circuit current mismatches the theoretical transparency, which may be caused by non-strict conditions of measurement. The voltage-current (VI) characteristic of

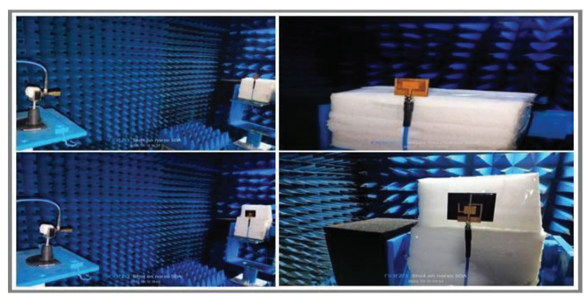

Fig. 8. Photograph of the measurement environment, which includes the anechoic chamber, the standard horn antenna, and the proposed antennas.

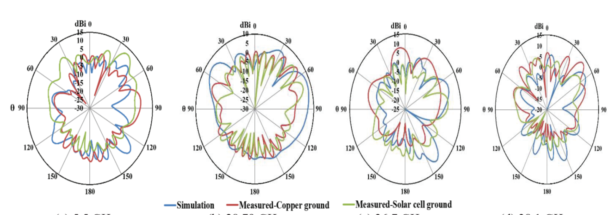

Fig. 9. Gain radiation pattern of the proposed antenna for (a) 5.5 GHz, (b) 28.79 GHz, (c) 36.7 GHz, (d) 38.1 GHz.

Table 1: Measured results of the proposed antennas

Antenna Type	Operating band of frequencies (GHz)	Impedance bandwidth (%)	S_{11} (dB)	VSWR
Transparent antenna with a copper ground plane	5.04–7.32	36.89	−14.67	1.44
	14.35–15.11	5.15	−13.04	1.57
	27.08–28.79	6.23	−12.25	1.66
	31.64–39.81	21.34	−37.09	1.04
Transparent antenna with a solar cell ground plane	4.47–6.56	36.03	−23.29	1.171
	9.6–11.12	14.4	−13.20	1.58
	22.14–22.71	2.55	−11.57	1.71
	28.79–39.05	27.9	−14.60	1.57

Table 2: Simulated and measured peak gain of proposed antennas

Frequency (GHz)	Simulated Gain (dBi)	Measured Gain (dBi)	Measured Gain (dBi)	Percentage error between simulated and measured results	
	Copper ground	Copper ground	Solar cell ground	Copper ground	Solar cell ground
5.5	8.58	6.74	11.6	21.44%	35.2%
28.79	8.14	5.93	4.94	27.15%	39.3%
36.7	10.3	8.09	5.67	21.45%	44.95%
38.1	9.99	12.5	6.38	25.13%	36.14%

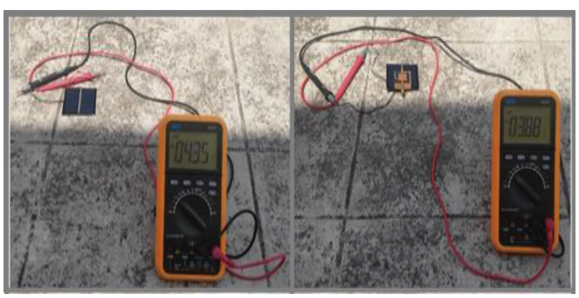

Fig. 10. Measurement of V_{OC} and I_{SC} of the solar cell with and without antenna integration.

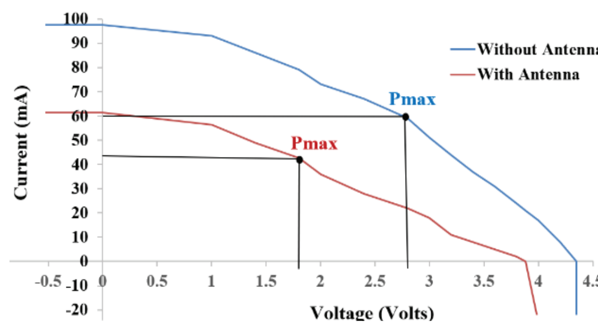

Fig. 11. The V-I characteristics of a solar cell with and without an antenna.

solar cells integrated with and without antennas is shown in Fig. 11. When sunlight strikes a solar cell, it emits photons, which are tiny bundles of energy whose energy is higher than the energy gap and which provide electrons and holes in the depletion area with energy. They function as a battery while the electrons are directed towards the N-type and the holes towards the P-type. This flow of electrons and holes creates a negative current in a short circuit. The same maximum current and voltage may be maintained beyond the short-circuit current and open-circuit voltage by attaching an external battery in reverse bias and forward bias circumstances, respectively.

The maximum useful power is the area of the largest rectangle that can be formed under the V-I curve. If V_m and I_m are the values of voltage and current under this condition, then the maximum power (P_{max}) can be computed as follows:

$$P_{max} = V_{max} \times I_{max}\ mW. \tag{8}$$

The observed maximum power (P_{max}) of the solar cell without and with the antenna is 423.69 mW and 238.24 mW, which is a slight decrease in maximum output DC power of 185.456 mW and also commonly acceptable.

A comparison of a list of reviewed 5G antennas and solar-integrated antenna designs may be found in Table 3 and Table 4. A comparison of solar-integrated antennas with and without a built-in solar panel is shown in Table 5 below.

Table 3: Comparison table for 5G antennas

Ref. No.	**Antenna type**	**Frequency of Operation (GHz)**	**Antenna size (mm)**	**Substrate**	**Impedance bandwidth %**	**Realized Gain (dBi)**
[2]	Handset	25-30	23 X 7 X 4	RO4350B	NR	7
[3]	MIMO	25-38	17.5 X 14 X 0.254	Rogers 5870	41	10.5
[4]	MIMO	23–39	6 X 8 X 0.508	Polycarbonate	51.6	7.2 dB
[6]	Slot array	23-29	35 X 2.5 X 0.381	Rogers 5880	23.07	12.5
[7]	MIMO	3.5*, 4.3*& 24-38	14 X 10 PIFA	FR4	11.4, 9.3 & 50.9	NR
[8]	SIW slot	28.6*	35.72 X 12 X 2.16	Rogers 5880	5.6	7.27
[9]	Proximity-coupled	26.04-28.78	42.5 X 36.4 X 7.2	Taconic TLY-5	9.8	21
[10]	AiP phased	30.4*	6 X 6	Organic	2.6	4
[11]	AiP phased	28.27-28.97	3 X 3.5 X 0.55	Stainless steel	2.4	14.09
[12]	MIMO	24.25-27.5	31.2 X 31.2 X 1.57	Rogers 5880	15.6	8.732
[13]	MIMO	25-30	18 X 12 X 0.2	Neltec NY9220	18	11.3
[14]	End-fire	28*	20 X 20 X 20	Nelco NY9220	9	8-10
[15]	End fire	28-33	20 X 3.5 X 0.254	Rogers 4350B	NR	6
[16]	MIMO-DGS	25.1-37.5	12 X 12 X 0.8	Rogers 5880	34.44	10.6
[17]	Patch-DGS	28-38	50 X 50 X 0.508	Rogers 5880	32	18.65
[18]	Metasurface	23.7-29.2 36.7-41.1	6.9 X 6.9 X 1.5	Rogers 5880	20.7 11.3	7.2 10.9
[19]	Metasurface	23.9-31.4	12.84 X 12.84 X 0.46	RO4350B	27.1	13.6
[20]	Metamaterial	26.58-29.31	18 X 22 X 0.81	RO4003C	9.77	11.94
[21]	Metamaterial	27.1-29.56	18 X 22 X 0.81	RO4003	8.68	11.59
[22]	Patch array	24.35-31.13	7 X 6.2 X 0.508	Rogers 5880	24.4	19.88
[23]	Patch array	25.3-30.2	3.5 X 3 X 0.935	Taconic TLY-5	17.7	16.4
[24]	Patch	24-40	12 X 4.6 X 0.8	Rogers 5880	68.06	19
[25]	Patch array	27-31.35	11 X 11 X 0.257	HL972LF(LD)	15	9.26
[26]	Patch array	25.8-29.8	2 X 2.2 X 1.3	RO4003C	14.28	5.5
[27]	SIW Array	24.25-29.5	5.3 X 5.3 X 0.254	RO4350B, FR4	26.8	7.4±0.6
[28]	PIFA	24.7-29.6	4.5 X 4.5 X 1.3	FR4	15.3	5.85
[29]	Patch-BGA	30.8-35.7	5 X 5 X 1.3	FR4	15.21	3.2-4.2
[30]	bowtie-BGA	29.75*	6 X 6 X 1.6	FR4, RO4350B	37.3	7.59
[31]	BGA	26.6-35.7	5 X 5 X 1.3	FR4	29.2	5.2
[32]	Aperture-coupled	27-30 27.4-34.2	15 X 15 X 0.67	ITEQ IT-88GMW	10.52 22.1	7.8 8
[33]	Patch array	24.25-28.35 37-43.5	18.2 X 4.1 X 1.07	RO4350B RO4450F	15.58 17.1	5.8 6.2
[35]	SIW cavity	28*	20.9 X 20.9 X 0.508	Rogers 5880	4.6	16
[36]	Archimedean spiral patch	21.1-34.1	30 X 15 X 0.254	Rogers 5880	46.4	6.49
[37]	Dual-Array	31.30-39	2.34 X 3.12 X 0.5	Rogers 5880	20.26	16.4
[38]	DRA	24-28	8 X 2.4 X 2.2	DR	15.38	NR
[39]	Phased Array	17.7-19.3 27.3-29.1	55 X 110 X 0.787	N9000 PTFE	8.89 6.42	13.5 15.5
Proposed antenna	Patch	5.04-7.32 5G14.35-15.11 27.08-28.79 31.64-39.81	42 X 30 X 2	Plexiglass	36.89 5.15 6.23 21.34	6.74 5.93 8.09 12.5

*Resonant frequency NR-Not Reported SIW- Substrate-integrated waveguide

Table 4: Comparison table for super-solar integrated antennas

Ref. No.	Frequency of Operation (GHz)	Antenna Patch size (mm)	Substrate	Impedance bandwidth %	Realized Gain (dBi)
[49]	2.61*	35.0 X 40.8	Cover glass	NR	8.4
[50]	2.461-2.476	30.5 X 30.5	Cover glass	2	5.15
[51]	2.43*	25.15 X 25.15	Borosilicate glass	7.25	4.4
[52]	2.45*	26.8 X 24.1	Borosilicate glass	NR	5
[54]	2.33-10.8	45 X 31	Acrylic	NR	4.1
[55]	11.7 - 12.22 14.0 - 14.5	18 X 15	Plexiglas	NR	6.05 7.61
[56]	10*	97 X 75	AF32 glass	NR	4.1
[57]	3.4–3.8	85 X 55	Perspex & Glass	4.3	3.96
[58]	2.2 - 12.1	44.6 X 25.5	Glass	NR	3 - 5
[59]	8.51 - 9.10	157 X 157	Glass	> 35	20.14
[61]	25*	110 X 80	Soda lime glass	NR	41.3
[62]	0.4435–0.455	80 X 40	Rogers Duroid 5880	2.55	2.5
Proposed antenna with solar cell	4.47-6.56 9.6-11.12 22.14-22.71 28.79-39.05	42 X 30	Plexiglass	36.03% 14.4% 2.55% 27.9%	11.6 4.94 5.67 6.38

NR-Not Reported *Resonant frequency

Table 5: Performance of the proposed antennas with and without integration

Ref. No.	Antenna parameter	Antenna with solar cells	Antenna without solar cells	Solar cell parameter	Solar cell with antenna	Solar cell without antenna
[51]	Gain	4.4 dBi	4.9 dBi	P_{max}	NR	NR
[52]	NR	NR	NR	η	$\sim$76 %	$\sim$78 %
[54]	NR	NR	NR	P_{max} η	65.5 mW 13.1 %	NR
[55]	Gain	6.79 dBi	8.05 dBi	P_{max}	10.23 μW	12.42 μW
[56]	Gain	4.1 dB	6.4 dB	η	17.4 %	18 %
[57]	Gain	3.96 dBi	NR	P_{max}	NR	345.6 mW
[58]	Return loss	-29 dB	-33 dB	V_O	74.4 mV	76.1 mV
[59]	Efficiency	38.8 %	NR	V_{OC} I_{SC}	0.571 V 1.80 A	0.576 V 1.84 A
[61]	Efficiency	80%	NR	P_{max}	1020 mW	NR
Proposed antenna with solar cell	Gain	11.6 dBi (4.47-6.56 GHz)	6.74 dBi (5.04-7.32 GHz)	P_{max}	238.24 mW	423.69 mW
		4.94 dBi (9.6-11.12 GHz)	5.93 dBi (14.35-15.11 GHz)			
		5.67 dBi (22.14-22.71 GHz)	8.09 dBi (27.08-28.79 GHz)			
		6.38 dBi (28.79-39.05 GHz)	12.5 dBi (31.64-39.81 GHz)			

NR-Not Reported V_O- Output voltage

IV. CONCLUSION

A compact parasitic patch loaded transparent patch antenna with the ground plane of both copper conductor and the solar cell was fabricated and tested, presenting a commendable agreement between simulation and measurement for 5G mm-wave applications. The proposed super solar patch antenna operates at the measured frequency bands of 4.47-6.56 GHz, 9.6-11.12 GHz, 22.14-22.71 GHz, and 28.79-39.05 GHz, covering the required sub-6 GHz and beyond 6 GHz mm-wave 5G frequency bands. When the proposed antenna is compared to other published results in the literature, the proposed antenna provides remarkable enhancements in terms of gain, bandwidth, and size reduction. Additionally, the performance of the proposed antenna is assessed with the embedding of a solar cell as a ground. It is found that the antenna performance in terms of S_{11} and VSWR has not been affected. The performance of the used solar cell is measured in terms of V-I characteristics to show no major effects on solar energy harvesting. The proposed solar integrated antenna will aid in the future engineering evolution of the low-profile microstrip patch antenna to satisfy the demands of mm-wave green wireless applications.

ACKNOWLEDGMENT

The authors would like to thank Tamil Nadu State Council for Science and Technology (http://www.tanscst.nic.in/) for sponsoring this work (EEE-1326) under short-term Grants SPS 2021-2022.

REFERENCES

[1] R. Dangi, P. Lalwani, G. Choudhary, I. You, and G. Pau, "Study and investigation on 5G technology: A systematic review," *Sensors*, vol. 22, no. 1, pp. 1-32, 2021.

[2] J. Kurvinen, H. Kähkönen, A. Lehtovuori, J. Ala-Laurinaho, and V. Viikari, "Co-designed mm-wave and LTE handset antennas," *IEEE Trans. Antennas Propag.*, vol. 67, no. 3, pp. 1545-1553, 2019.

[3] M. I. Magray, G. S. Karthikeya, K. Muzaffar, and S. K. Koul, "Corner bent integrated design of 4G LTE and mm-wave 5G antennas for mobile terminals," *Prog. Electromagn. Res. M*, vol. 84, pp. 167-175, 2019.

[4] I. S. Masoodi, I. Ishteyaq, K. Muzaffar, and M, I. Magray, "Low-cost substrate based compact antennas for 4G/5G side-edge panel smartphone applications," *Prog. Electromagn. Res. Lett.*, vol. 91, pp. 145-152, 2020.

[5] J. Khan, D. A. Sehrai, and S. Ahmad, "Design and performance comparison of metamaterial-based antenna for 4G/5G mobile devices," *Int. J. Electron. Commun. Eng.*, vol. 12, no. 6, pp. 382-387, 2018.

[6] M. Ikram, E. A. Abbas, N. Nguyen-Trong, K. H. Sayidmarie, and A. Abbosh, "Integrated frequency-reconfigurable slot antenna and connected slot antenna array for 4G and 5G Mobile handsets," *IEEE Trans. Antennas Propag.*, vol. 67, no. 12, pp. 7225-7233, 2019.

[7] N. Kumar and R. Khanna, "A two element MIMO antenna for sub-6 GHz and mm-Wave 5G systems using characteristics mode analysis," *Microw. Opt. Technol. Lett.*, pp. 1-9, Sep. 2020.

[8] R. B. Di Renna, V. P. R. M. Souza, T. N. Ferreira, L. J. Matos, J. A. M. Souza, and G. L. Siqueira, "A new double-sided substrate-integrated waveguide slot array antenna for 5G applications," *Microw. Opt. Technol. Lett.*, vol. 61, no. 3, pp. 1-6, 2018.

[9] H. A. Diawuo and Y.-B. Jung, "Broadband proximity-coupled microstrip planar antenna array for 5G cellular applications," *IEEE Antennas Wirel. Propag. Lett.*, vol. 17, no. 7, pp. 1286-1290, 2018.

[10] D. Liu, X. Gu, C. W. Baks, and A. Valdes-Garcia, "Antenna-in-package design considerations for Ka-band 5G communication applications," *IEEE Trans. Antennas Propag.*, vol. 65, no. 12, pp. 6372-6379, 2017.

[11] J. Park, D. Choi, and W. Hong, "Millimeter-wave phased-array antenna-in-package (AiP) using stamped metal process for enhanced heat dissipation," *IEEE Antennas Wirel. Propag. Lett.*, vol. 18, no. 11, pp. 2355-2359, 2019.

[12] N. Shoaib, S. Shoaib, R. Y. Khattak, I. Shoaib, X. Chen and A. Perwaiz, "MIMO antennas for smart 5G devices," *IEEE Access*, vol. 6, pp. 77014-77021, 2018.

[13] Z. Wani, M. P. Abegaonkar, and S. K. Koul, "Millimeter-wave antenna with wide-scan angle radiation characteristics for MIMO applications," *Int. J. RF Microw. Comput. Aided Eng.*, vol. 29, no.5, pp. 1-9, 2019.

[14] G. S. Karthikeya, S. K. Koul, Ajay K. Poddar, and U. Rohde, "Ultra-compact orthogonal pattern diversity antenna module for 5G smartphones," *Microw. Opt. Technol. Lett.*, pp. 1-10, Mar. 2020.

[15] R. M. Moreno, J. Ala-Laurinaho, A. Khripkov, J. Ilvonen, and V. Viikari, "Dual-polarized mm-wave end-fire antenna for mobile devices," *IEEE Trans. Antennas Propag.*, vol. 68, no. 8, pp. 5924-5934, 2020.

[16] S. F. Jilani, and A. Alomainy, "Millimetre-wave T-shaped MIMO antenna with defected ground structures for 5G cellular networks," *IET Microw. Antennas Propag.*, vol. 12, no. 5, pp. 672-677, 2018.

[17] K. R. Mahmoud and A. M. Montaser, "Optimised 4 × 4 millimetre-wave antenna array with DGS using hybrid ECFO-NM algorithm for 5G mobile

networks," *IET Microw. Antennas Propag.*, vol. 11, no. 11, pp. 1516-1523, 2017.

[18] T. Li and Z. N. Chen, "A dual-band metasurface antenna using characteristic mode analysis," *IEEE Trans. Antennas Propag.*, vol. 66, no. 10, pp. 5620-5624, 2018.

[19] W. Wan, M. Xue, L. Cao, T. Ye, and Q. Wang, "Low-profile broadband patch-driven metasurface antenna," *IEEE Antennas Wirel. Propag. Lett.*, vol. 19, no. 7, pp. 1251-1255, 2020.

[20] M. J. Jeong, N. Hussain, J. W. Park, S. G. Park, S. Y. Rhee, and N. Kim, "Millimeter-wave microstrip patch antenna using vertically coupled split ring metaplate for gain enhancement," *Microw. Opt. Technol. Lett.*, pp. 1-6, 2019.

[21] M. Jeong, N. Hussain, A. Abbas, S. Y. Rhee, S. M. Lee, S.-K. Gil and N. Kim, "Performance improvement of microstrip patch antenna using a novel double-layer concentric rings metaplate for 5G millimeter wave applications," *Int. J. RF Microw. Comput. Aided Eng.*, vol. 31, no. 2, pp. 1-10, 2020.

[22] M. Khalily, R. Tafazolli, P. Xiao, and A. A. Kishk, "Broadband mm-wave microstrip patch array antenna with improved radiation characteristics for different 5G applications," *IEEE Trans. Antennas Propag.*, vol. 66, no. 9, pp. 4641-4647, 2018.

[23] J. Xu, W. Hong, Z. H. Jiang, and H. Zhang, "Wideband, low-profile patch array antenna with corporate stacked microstrip and substrate integrated waveguide feeding structure," *IEEE Trans. Antennas Propag.*, vol. 67, no. 2, pp. 1368-1373, 2019.

[24] P. Ramanujam, C. Arumugam, R. Venkatesan, and M. Ponnusamy, "Design of compact patch antenna with enhanced gain and bandwidth for 5G mm-wave applications," *IET Microw. Antennas Propag.*, vol. 14, no. 12, pp. 1455-1461, 2020.

[25] M. Xue, W. Wan, Q. Wang, and L. Cao, "Low-profile millimetre-wave wideband microstrip antenna with parasitic patch arrays," *IET Microw. Antennas Propag.*, vol. 15, pp. 364-370, 2021.

[26] M. S. Rahimi, E. V. Pinto dos Anjos, P. Taghikhani, and V. Volski, "A cost-efficient 28 GHz integrated antenna array with full impedance matrix characterization for 5G NR," *IEEE Antennas Wirel. Propag. Lett.*, vol. 19, no. 4, pp. 666-670, 2020.

[27] I. L. de Paula, S. Lemey, D. Bosman, Q. Van den Brande, O. Caytan, J. Lambrecht, M. Cauwe, G. Torfs, and H. Rogier, "Cost-effective high-performance air- filled SIW antenna array for the global 5G 26 GHz and 28 GHz bands," *IEEE Antennas Wirel. Propag. Lett.*, vol. 20, no. 2, pp. 194-198, 2021.

[28] X. Wang, X. Liu, W. Zhang, D. Hao, and Y. Liu, "Surface-mount PIFA using ball grid array packaging for 5G mm-Wave," *Prog. Electromagn. Res. Lett.*, vol. 98, pp. 55-60, 2021.

[29] X. Wang, X. Liu, W. Zhang, D. Hao, and Y. Liu, "Surface mounted microstrip antenna using ball grid array packaging for mm-Wave systems integration," *Prog. Electromagn. Res. Lett.*, vol. 98, pp. 105-111, 2021.

[30] X. Liu, W. Zhang, D. Hao, and Y. Liu, "Surface-mount bowtie antenna element for millimeter-wave applications," *Microw. Opt. Technol. Lett.*, pp. 1-7, 2020.

[31] X. Liu, W. Zhang, D. Hao, and Y. Liu, "Cost-effective surface-mounted patch antenna with ring slot using ball grid array packaging for 5G millimeter-wave applications," *Prog. Electromagn. Res. Lett.*, vol. 99, pp. 127-133, 2021.

[32] N. -C. Liu and J. -H. Tarng, "Double-curved metal in multilayer printed circuit boards for bandwidth enhancement of millimeter-wave patch antennas," *IEEE Trans. Compon. Packag. Manuf. Technol.,* vol. 11, no. 7, pp. 1088-1096, 2021.

[33] Y. He, S. Lv, L. Zhao, G. -L. Huang, X. Chen, and W. Lin, "A Compact dual-band and dual-polarized millimeter-wave beam scanning antenna array for 5G mobile terminals," *IEEE Access*, vol. 9, pp. 109042-109052, 2021.

[34] R. Mittra, A. Nasri, and R. Kumar Arya, "Wide-Angle Scanning Antennas for Millimeter-Wave 5G Applications," *Engineering*, vol. 11, pp. 60-71, 2022.

[35] M. Asaadi and A. Sebak, "High-gain low-profile circularly polarized slotted SIW cavity antenna for MMW applications," *IEEE Antennas Wirel. Propag. Lett.*, vol. 16, pp. 752-755, 2017.

[36] H. Chen, Y. Shao, Y. Zhang, C. Zhang, and Z. Zhang, "A low-profile broadband circularly polarized mm-wave antenna with special-shaped ring slot," *IEEE Antennas Wirel. Propag. Lett.*, vol. 18, no. 7, pp. 1492-1496, 2019.

[37] H. U. Tahseen, L. Yang, and W. Hongjin, "A dual-array antenna system for 5G millimeter-wave applications," *Applied Computational Electromagnetics Society (ACES) Journal*, vol. 36, no. 10, pp. 1319-1324, 2021.

[38] N. F. Sallehuddin, M. H. Jamaluddin, M. R. Kamarudin, and M. H. Dahri, "Reflectarray resonant element based on a dielectric resonator antenna for 5G applications," *Applied Computational Electromagnetics Society (ACES) Journal*, vol. 36, no. 7, pp. 844-851, 2021.

[39] N. O. Parchin, O. M. Dardeer, A. S.I. Amar, C. H. See, and R. Abd-Alhameed, "Dual-band phased array 5G mobile-phone antenna with switchable and hemispherical beam pattern coverage for MIMO-diversity communications," *Applied Computational Electromagnetics Society (ACES) Journal*, vol. 36, no. 12, pp. 1602-1609, 2021.

[40] M. Tanaka, Y. Suzuki, K. Araki, and R. Suzuki, "Microstrip antenna with solar cells for microsatellites," *Electronics Letters*, vol. 31, no. 1, pp. 5-6, 1995.

[41] T. N. Suresh babu and D. Sivakumar, "Stepped slot patch antenna with copper ground plane and solar cell ground plane for future mobile communications," *Prog. Electromagn. Res. C*, vol. 98, pp. 187-198, 2020.

[42] S. Vaccaro, C. Pereira, J. R. Mosig, and P. de Maagt, "In-flight experiment for combined planar antennas and solar cells (SOLANT)," *IET Microw. Antennas Propag*., vol. 3, no. 8, pp. 1279-1287, 2009.

[43] S. V. Shynu, J. Roo Ons Maria, J. Ammann Max, and B. Norton, "Dual band a-Si:H solar-slot antenna for 2.4/5.2 GHz WLAN applications," *Radioengineering*, vol. 18, no. 4, pp. 354-358, 2009.

[44] O. Yurduseven and D. Smith, "A solar cell stacked multi-slot quad-band PIFA for GSM, WLAN and WiMAX networks," *IEEE Microw.Wireless Compon.Lett.*, vol. 23, no. 6, pp. 285-287, 2013.

[45] O. Yurduseven and D. Smith, "Solar cell stacked dual-polarized patch antenna for 5.8 GHz band WiMAX network," *Electronics Letters*, vol. 49, no. 24, pp. 1514-1515, 2013.

[46] R. Caso, A. D'Alessandro, A. Michel, and P. Nepa, "Integration of slot antennas in commercial photovoltaic panels for stand-alone communication systems," *IEEE Trans. Antennas Propag.*, vol. 61, no. 1, pp. 62-69, 2013.

[47] M. Elsdon, O. Yurduseven, and X. Dai, "Wideband metamaterial solar cell antenna for 5 GHz Wi-Fi communication," *Prog. Electromagn. Res. C*, vol. 71, pp. 123-131, 2017.

[48] B. Bai, Z. Zhang, X. Li, C. Sun, and Y. Liu, "Integration of microstrip slot array antenna with dye-sensitized solar cells," *Sensors*, vol. 20, no. 6257, pp. 1-13, 2020.

[49] T. W. Turpin and R. Baktur, "Meshed patch antennas integrated on solar cells," *IEEE Antennas Wirel. Propag. Lett.*, vol. 8, pp. 693-696, 2009.

[50] T. Yasin and R. Baktur, "Circularly polarized meshed patch antenna for small satellite application," *IEEE Antennas Wirel. Propag. Lett.*, vol. 12, pp. 1057-1060, 2013.

[51] S. Sheikh, "Circularly polarized meshed patch antenna," *IEEE Antennas Wirel. Propag. Lett.*, vol. 15, pp. 352-355, 2016.

[52] KS. K. Podilchak, D. Comite, B. K. Montgomery Brendan, Y. Li, V. Gómez-Guillamón Buendía, and Y. M. M. Antar, "Solar-panel integrated circularly polarized meshed patch for cubesats and other small satellites," *IEEE Access*, vol. 7, no. 96560-96566, 2019.

[53] T. Yasin, R. Baktur, T. Turpin, and J. Arellano, "Analysis and design of highly transparent meshed patch antenna backed by a solid ground plane," *Prog. Electromagn. Res. M*, vol. 56, pp. 133-144, 2017.

[54] O. Yurduseven, D. Smith, and M. Elsdon, "UWB meshed solar monopole antenna," *Electronics Letters*, vol. 49, no. 9, 2013.

[55] F. Nashad, S. Foti, D. Smith, M. Elsdon, and O. Yurduseven, "Ku-band suspended meshed patch antenna integrated with solar cells for remote area applications," *Prog. Electromagn. Res. C*, vol. 83, pp. 245-254, 2018.

[56] T. Yekan and R. Baktur, "An X band patch antenna integrated with commercial triple-junction space solar cells," *Microw. Opt. Technol. Lett.*, vol. 59, no. 2, Dec. 2017.

[57] M. J. Roo-Ons, S. V. Shynu, M. J. Ammann, S. J. McCormack, and B. Norton, "Transparent patch antenna on a-Si thin-film glass solar module," *Electronics Letters*, vol. 47, no. 2, pp. 85-86, 2011.

[58] T. Peter, T. A. Rahman, S. W. Cheung, R. Nilavalan, H. F. Abutarboush, and A. Vilches, "A novel transparent UWB antenna for photovoltaic solar panel integration and RF energy harvesting," *IEEE Trans. Antennas Propag.*, vol. 62, no. 4, pp. 1844-1853, 2014.

[59] B. Xi, X. Liang, Q. Chen, K. Wang, J. Geng, and R. Jin, "Optical transparent antenna array integrated with solar cell," *IEEE Antennas Wirel. Propag. Lett.*, vol. 19, no. 3, pp. 457-461, 2020.

[60] P. Dreyer, M. Morales-Masis, S. Nicolay, C. Ballif, and J. Perruisseau-Carrier, "Copper and transparent-conductor reflectarray elements on thin-film solar cell panels," *IEEE Trans. Antennas Propag.*, vol. 62, no. 7, pp. 3813-3818, 2014.

[61] Y.n-S. Chen, Y.-H. Wu, and C.-C. Chung, "Solar-powered active integrated antennas backed by a transparent reflectarray for cubesat applications," *IEEE Access*, vol. 8, no. 137934-137946, 2020.

[62] T. Alam, A. F. Almutairi, M. Samsuzzaman, M. Cho, and M. T. Islam, "Metamaterial array-based

meander line planar antenna for cube satellite communication," *Scientific Reports*, vol. 11, no. 14087, pp. 1-12, 2021.

[63] S. B. T. Naganathan and S. Dhandapani, "Patch antenna integrated on solar cells for green wireless communication: A feature oriented survey and design issues," *Int. J. RF Microw. Comput. Aided Eng.*, vol. 32, no. 1, pp. 1-29, 2021.

[64] A. Kumar and S. Sharma, "Measurement of dielectric constant and loss factor of the dielectric material at microwave frequencies," *Prog. Electromagn. Res.*, vol. 69, pp. 47-54, 2007.

[65] C. Steiner, S. Walter, V. Malashchuk, G. Hagen, I. Kogut, H. Fritze, and R. Moos, "Determination of the dielectric properties of storage materials for exhaust gas aftertreatment using the microwave cavity perturbation method," *Sensors*, vol. 20, pp. 1-18, 2020.

[66] R. Garg, P. Bhartia, I. Bahl, and A. Ittipiboon, *Microstrip Antenna Design Handbook*, Artech House inc., Norwood, January 2001.

Suresh Babu T. Naganathan received a B.E. degree in Electronics and Communication Engineering from Madurai Kamaraj University, India, in 1997 and an M.E. degree in Power Electronics and Drives from Anna University, India, in 2009, respectively. He is currently working as an Assistant Professor in the Department of Electronics and Communication Engineering at Adhiparasakthi Engineering College, Tamilnadu, India. His research interests include those in the areas of electromagnetics, antenna design, and wave propagation.

Sivakumar Dhandapani received a B.E. degree in Electronics and Communication Engineering from the University of Madras, India, in 1995, an M.E. degree in Process Control and Instrumentation from Annamalai University, India, in 2002, and the Ph.D. degree in Faculty of Information and Communication from Anna University, India, in 2010, respectively. He is now a Professor at AMET University, Tamil Nadu, India.

Thirumaraiselvan Packirisamy received B.E. degree in Electronics and Communication Engineering from Allagappa Chettiar College of Engineering and Technology, Karaikudi in 1992 and M.E. degree in Telecommunication Engineering from Multimedia University, Malaysia in 2006. He completed Ph.D. in Information and Communication Engineering at Anna University, Chennai in 2018. He has more than 30 years of experience in teaching and research and currently working as Professor in Adhiparasakthi Engineering College, Melmaruvathur. His research interests include Wireless Communication, Body Area Networks, Electromagnetic Wave Propagation and Biomedical Engineering. He has published several research papers in reputed journals and international conferences.

Determination of the Physical Integrity of Ethernet Cables by Obtaining their Transmission Line Parameters from Measured Impedance Profiles

Olusegun Ogundapo[1] and Alistair P. Duffy[2]

[1]School of Engineering
American University of Nigeria, PMB 2250, Yola-Nigeria
olusegun.ogundapo@aun.edu.ng, segundapo@gmail.com

[2]School of Engineering and Sustainable Development
De Montfort University, LE1 9BH, United Kingdom
apd@dmu.ac.uk

***Abstract* –** A method of determining the physical integrity of Ethernet cables by obtaining their transmission line parameters (resistance, inductance, capacitance, and conductance) from their measured impedance profiles are presented. The transmission line parameters were extracted across the cable lengths rather than frequencies used in most research. The method can be used to examine the physical integrity of Ethernet cables before their deployment. The study of the physical integrity of Ethernet cables is very important because, in typical installations, cables can be manipulated in the form of repeated coiling and uncoiling. The installation handling stress can adversely affect the signal integrity especially if they are substandard Ethernet cables. In this paper, four Ethernet cables were subjected to three coiling and uncoiling tests to represent installation handling stress. The impedance profiles of the four cables across their lengths were measured for the three handling stress test conducted. The computation of the transmission line parameters of the Ethernet cables using measured impedance profiles was implemented with the aid of Matrix Laboratory (MATLAB). The outcome of the research showed that the method presented will be very useful to cable installers and contractors in making objective decisions in the choice of cables for deployment.

***Index Terms* –** Ethernet cables, impedance profile, physical integrity, transmission line parameters.

I. INTRODUCTION

Ethernet over twisted pair cables has over the years provided a cost-effective solution for network connectivity as it offers low cost, ease of use, and scalability [1–3]. The use of Ethernet over twisted pair cables can now be found in Internet of things (IoT), industrial and automotive applications [4, 5]. The trend for future Ethernet over twisted pair cables is now towards higher bandwidths on shorter cable lengths [6, 7].

It has been observed that the way twisted pair cables are packaged and handled during installation could undermine their physical structure especially if they are non-standard compliant and counterfeit [8, 9]. There are also the problems of non-compliant cables due to poor quality control [10]. The availability of copper-clad aluminum cables (CCA) in the market that have been termed unfit for use as communication cables is another problem of great concern to cable engineers and installers [11, 12].

There is, therefore, the need for cable engineers to examine the physical integrity of selected cables in the market before their deployment to ensure that signal degradation will be minimized after installation. Most of the research in the literature is focused on computing the transmission line parameters across their frequencies [13–15]. This paper provides a method of examining the physical integrity of the Ethernet cables by obtaining the resistance, inductance, capacitance, and conductance (RLCG) across their lengths from measured impedance profiles using MATLAB. The method presented also enables cable engineers to have a view of where the length of the cable is adversely affected. Four twisted pair cables including a CCA cable were subjected to three times-coiling and stretching tests to study their physical integrity.

II. MATERIALS AND METHODS

A. Cable materials

The cable materials used for the computation of RLCG parameters from the measured impedance profiles are:

- Cable 1: insulating material is polyethylene, conductor material is copper, the diameter of the conductors is 0.57 mm, and the distance between the centers of the conductors is 0.99 mm.
- CCA cable 2: insulating material is polyethylene,

Submitted On: May 23, 2022
Accepted On: November 7, 2022

https://doi.org/10.13052/2022.ACES.J.371005

conductor material is copper, cladding material is copper, diameter of the conductors is 0.57 mm, and the distance between the centers of the conductors is 1.03 mm.

- Cable 3: insulating material is polyethylene, conductor material is copper, diameter of the conductors is 0.54 mm, and the distance between the centers of the conductors is 0.96 mm.
- Cable 4: insulating material is polyethylene, conductor material is copper, diameter of the conductors is 0.57 mm, and the distance between the centers of the conductors is 1.01 mm.

B. Methodology

The RLCG parameters per unit-length for a single pair of cables will be computed from their measured impedance by using the mathematical expression for the transmission line parameters.

The R, L, G, and C can be calculated as expressed in [16] as follows:

The resistance (R) per meter is:

$$R = \frac{2R_s}{\pi d}.(\Omega/\mathrm{m}), \tag{1}$$

where the surface resistivity R_s is:

$$R_s = \sqrt{\frac{\pi f \mu_c}{\sigma_c}}. \tag{2}$$

The inductance per meter is:

$$L = \frac{\mu}{\pi} In \left[\left(\frac{D}{d} \right) + \sqrt{\left(\frac{D}{d} \right)^2 - 1} \right] (\mathrm{H/m}). \tag{3}$$

The conductance per meter is:

$$G = \frac{\pi \sigma}{In \left[\left(\frac{D}{d} \right) + \sqrt{\left(\frac{D}{d} \right)^2 - 1} \right]} (\mathrm{S/m}). \tag{4}$$

The capacitance per meter is:

$$C = \frac{\pi \varepsilon}{In \left[\left(\frac{D}{d} \right) + \sqrt{\left(\frac{D}{d} \right)^2 - 1} \right]} (\mathrm{F/m}), \tag{5}$$

where D is the distance between the centers of the conductors, d is the diameter of the conductor, μ_c is the permeability of the conductor, σ_c is the conductivity of the conductor, σ is the conductivity of the insulating material, ε is the effective permittivity of the insulating material, μ is the permeability of the insulating material and f is the frequency in Hz.

The attenuation constant (α), which is the real part of the propagation constant (γ), is expressed in [17] as:

$$\alpha = \frac{1}{2} \left(R\sqrt{\frac{C}{L}} + G\sqrt{\frac{L}{C}} \right), \tag{6}$$

Similarly, the phase constant (β), which is the imaginary part of the propagation constant (γ), is given in [17] as:

$$\beta = \omega \sqrt{LC}. \tag{7}$$

Therefore, the propagation constant (γ) from equations (6) and (7) is:

$$\gamma = \frac{1}{2} \left(R\sqrt{\frac{C}{L}} + G\sqrt{\frac{L}{C}} \right) + j\omega\sqrt{LC}, \tag{8}$$

The RLCG parameters for a single pair of the cable can now be computed from the cable impedance given in [15, 18] as:

$$R = Re\,(\gamma Z_o)\,(\Omega/\mathrm{m}), \tag{9}$$

$$L = Im \frac{(\gamma Z_o)}{\omega} (\mathrm{H/m}), \tag{10}$$

$$C = Im \frac{\left(\frac{\gamma}{Z_o} \right)}{\omega} (\mathrm{F/m}), \tag{11}$$

$$G = Re \left(\frac{\gamma}{Z_o} \right) (\mathrm{S/m}), \tag{12}$$

where Z_o is the twisted pair cable impedance measurements in ohms due to handling stress test.

C. Measurement procedure

Four category 6 unshielded twisted pair (UTP) cables were selected for the impedance profile measurements. The cables selected are tagged Cable 1, Cable 2 (CCA), Cable 3, and Cable 4. The DSX-5000 cable analyzer that can handle testing and certification of category 6 cables was used for the impedance measurement [19, 20]. The UTP cables were tested in accordance with the International Standard ISO/IEC 11801 Class E, which can measure up to 250 MHz. The cable analyzer contains two main modes: "main" and the "remote", which have openings to connect them to standard link adapters [20]. These main and remote modes are connected through patch cord plugs to the cable under examination [20]. The DSX-5000 analyzer has a High-Definition Time Domain Reflectometry (HDTDR) embedded in it to measure the impedance profiles across the length of the cables. The schematic diagram of the cable analyzer set up for measurement is shown in Fig. 1.

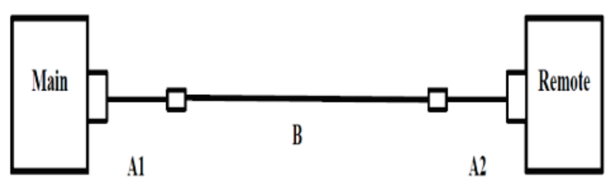

Fig. 1. The schematic diagram of the cable analyzer measurement setup. Note: A1 is the main mode link interface adapter with the patch cord plug, A2 is the remote link interface adapter with the patch cord plug, andB is the UTP cable under test.

Our research used the standard T568 pin connection with the registered (RJ45) connector for the four pairs of each cable to be measured. The four cables under the impedance profiles test consist of four twisted pairs each of which was labeled as orange, blue, green, and brown.

The coiling of the cables had a diameter of 30 cm so as to exceed the maximum bending allowed. The three test measurements taken are as follows:

- Measurement 1: cable used to form coils and stretched before test
- Measurement 2: cable in measurement 1 used to form coils and stretched before test
- Measurement 3: cable in measurement 2 used to form coils and stretched before test

III. MEASURED IMPEDANCE PROFILES

The measured impedance profiles across the lengths of the four cables at 250 MHz using the third coiling and uncoiling test results is shown in Figs. 2–4 for the orange, green and blue pairs. A view of Figs. 2–4 show that the CCA cable 2 is the most affected by the installation handling test as it gave a distinct variation in impedance profiles for all pairs.

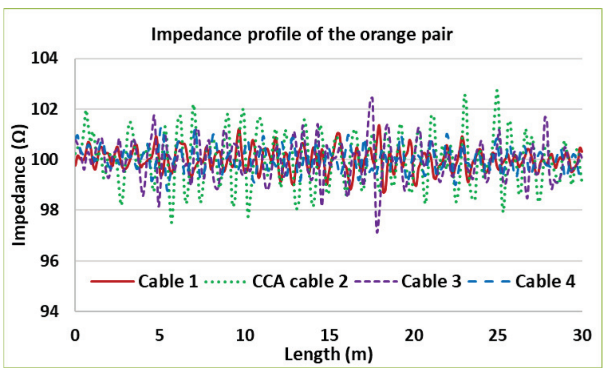

Fig. 2. Impedance profile of the orange pair.

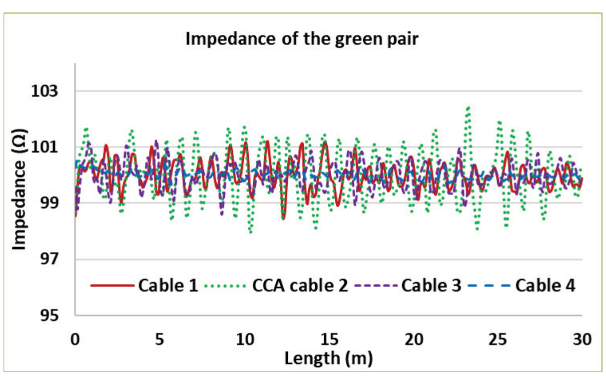

Fig. 3. Impedance profile of the green pair.

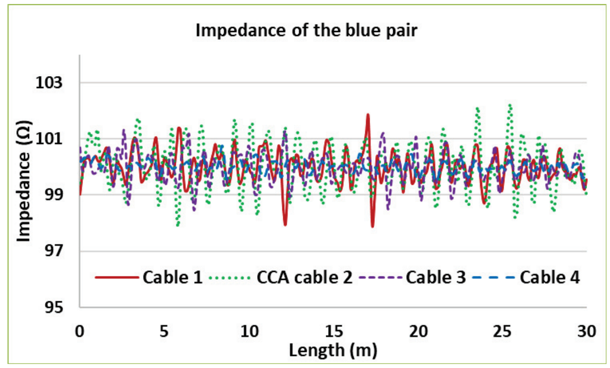

Fig. 4. Impedance profile of the blue pair.

IV. RESULT OF THE RLCG PARAMETERS EXTRACTED FROM MEASUREMENT

The results of the RLCG parameters across the lengths of the four cables at 250 MHz using the third coiling and uncoiling measured impedance results are shown from Figs. 5–16 for the orange, green, and blue

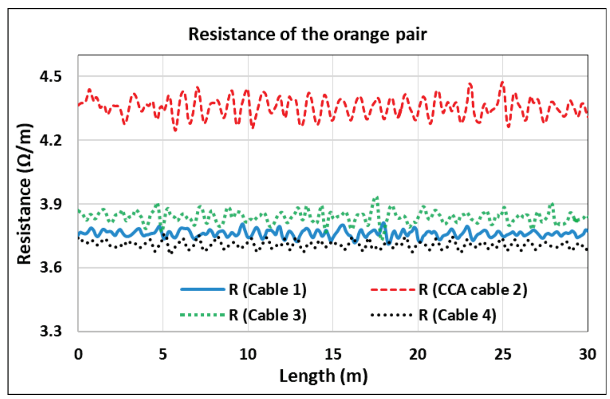

Fig. 5. Resistance comparison of the four cables using the orange pair.

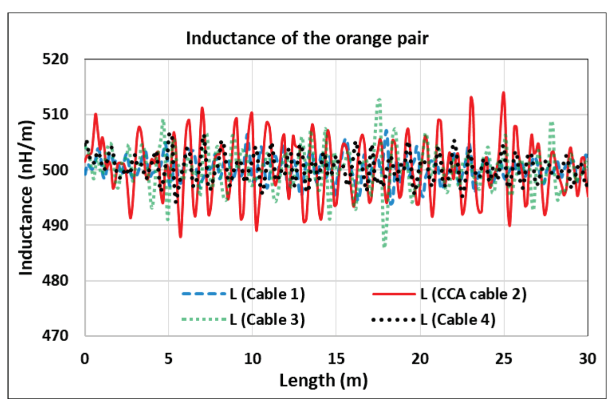

Fig. 6. Inductance comparison of the four cables using the orange pair.

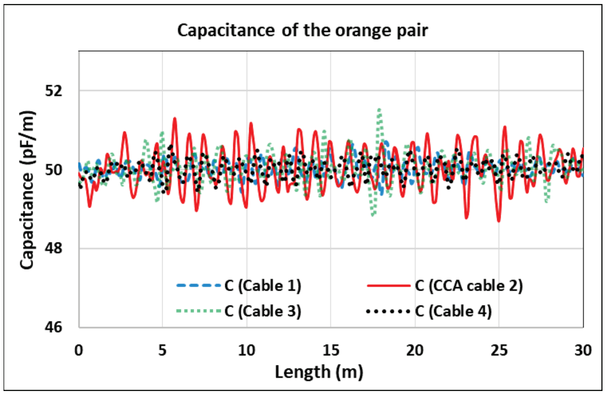

Fig. 7. Capacitance comparison of the four cables using the orange pair.

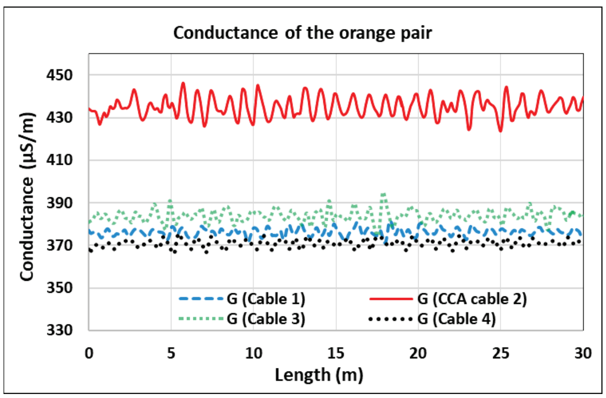

Fig. 8. Conductance comparison of the four cables using the orange pair.

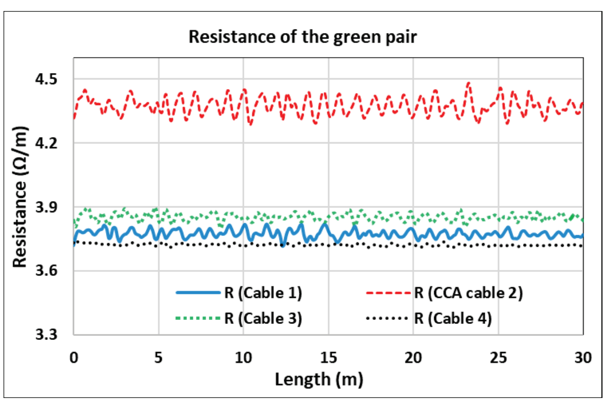

Fig. 9. Resistance comparison of the four cables using the green pair.

pairs. Figures 5–16 show that CCA Cable 2 had a wide margin for resistance and conductance in comparison to the other three cables, indicating that it is the most affected by the installation handling test.

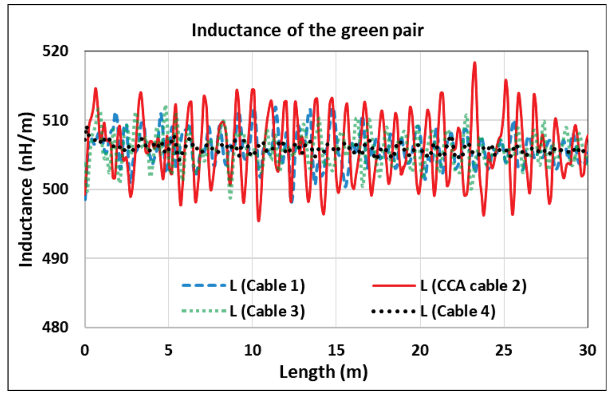

Fig. 10. Inductance comparison of the four cables using the green pair.

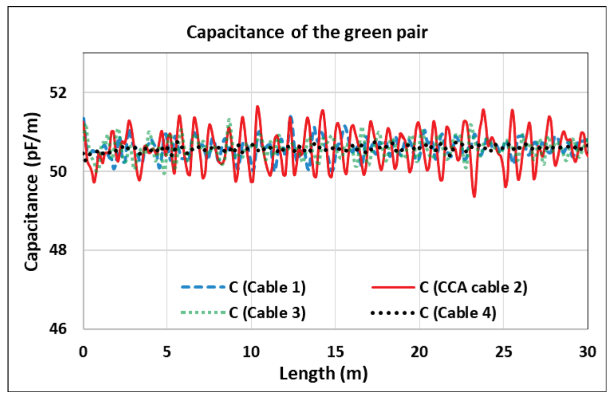

Fig. 11. Capacitance comparison of the four cables using the green pair.

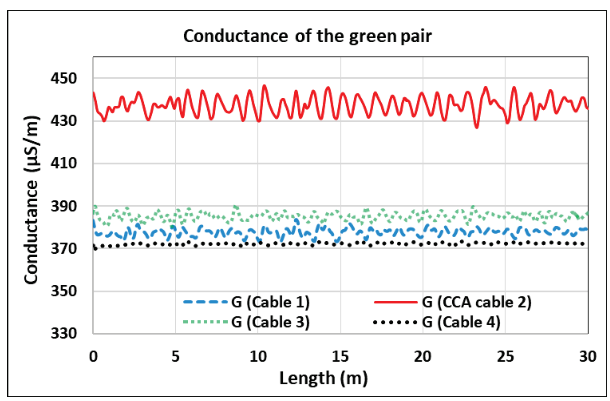

Fig. 12. Conductance comparison of the four cables using the green pair.

V. DISCUSSION OF THE RESILIENCE OF THE CABLES

The graphical results in Figs. 5–16 show that the CCA cable 2 gave a distinct wide margin in the resistance and conductance across the length than the three

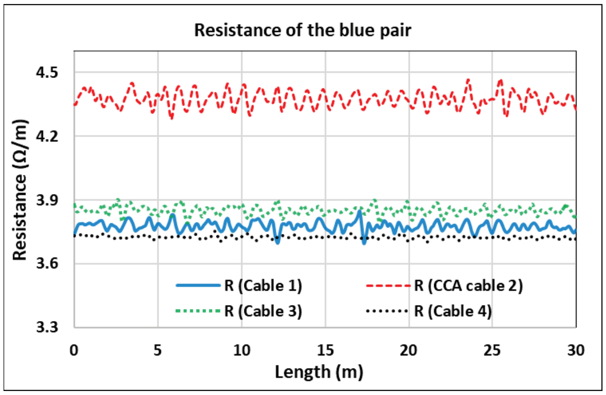

Fig. 13. Resistance comparison of the four cables using the blue pair.

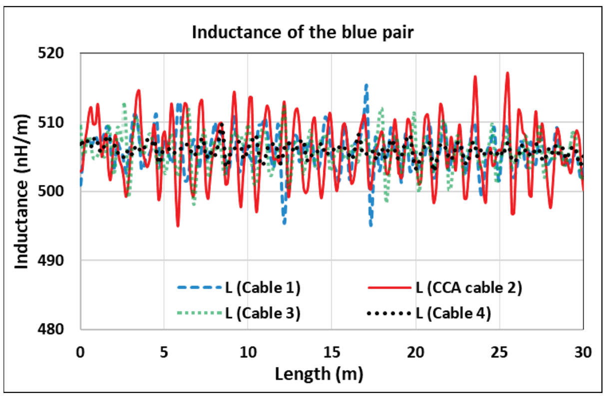

Fig. 14. Inductance comparison of the four cables using the blue pair.

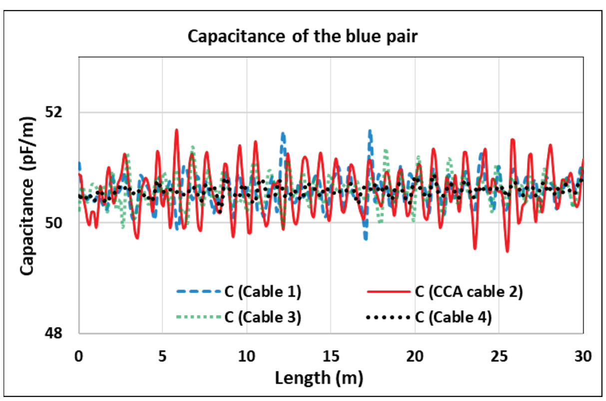

Fig. 15. Capacitance comparison of the four cables using the blue pair.

other cables for all pairs. This indicates that the CCA cable 2 gave the worst resilience after the third handling stress test than the three other cables. This confirms what is stated in literature that it is a bad communication cable. On the other hand, a view of the plots in Figs. 5–16 show that cable 4 gave the least changes in the RLCG

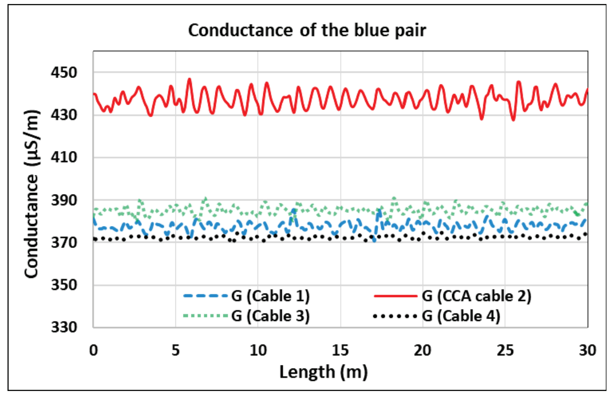

Fig. 16. Conductance comparison of the four cables using the blue pair.

parameters in comparison to the other three cables. This indicates that cable 4 gave the best resilience after the third test. The results of the test show that cable 4 has the best physical integrity as it is the least affected by the coiling and uncoiling tests.

VI. CONCLUSIONS

This paper has provided a method that can be used to determine the physical integrity of Ethernet cables by obtaining the RLCG parameters from their measured impedance profiles using MATLAB. The research was the determination of the transmission line parameters across their lengths to have a better view of the cable behavior. Four Ethernet cables were examined including a CCA cable termed unfit for use as a communication cable. The results of the study indicate that the CCA cable provided the worst resilience to the handling stress tests as it showed the highest changes in the RLCG parameters across the length. Cable 4 on the other hand, gave the best resilience to the handling stress tests as it showed the least changes in the RLGC parameters across the length. The method provided will be of help to cable engineers, installers, and contractors when selecting cables for deployment to minimize problems that may arise after installation.

REFERENCES

[1] A. Oliviero, *Cabling Part 1: LAN/Data Center Networks and Cabling Systems*, *5th Edition.* John Wiley and Sons Inc., 2014.

[2] A. Semenov, "Design requirements to tel- telecommunications long ethernet twisted pair cable," *XIV International Scientific-Technical Conference on Actual Problems of Electronics Instrument Engineering (APEIE)*, Khartoum, pp. 27-31, Oct. 2018.

[3] C. Spurgeon and J. Zimmerman, *Ethernet: The Definitive Guide, Second Edition*, O'Reilly Media, Inc, 2014.

[4] R. Elton, E. Hamood, A. Mohammed, and A. Osman, "Early warning firefighting system using the internet of things," *International Conference on Computer, Control, Electrical and Electronic Engineering (ICCCEEE)*, Khartoum, pp. 111-118, Aug. 2018.

[5] A. Gercikow, S. Schaffenroth, H. Schmidt, and A. Kolpin, "Measurement platform for physical-layer analysis of industrial and automotive ethernet," *IEEE Sensors Applications Symposium (SAS)*, Kuala Lumpur, pp. 122-128, Mar. 2020.

[6] P. McLaughlin, "The past, present and future of cabling technologies, products and standards," *Cabling Installation and Maintenance Magazine*, vol. 24, no. 12, pp. 27-29, Dec. 2018.

[7] O. Ogundapo, C. Nche, "Modeling the insertion loss of structured ethernet cabling standard using the scattering parameters," *Applied Computational Electromagnetics Society (ACES) Journal*, vol. 37, no. 4, pp. 435-440, Apr. 2022.

[8] B. Shuman, "Is your Ethernet cable tough enough," *Cabling Installation and Maintenance Magazine*, vol. 13, no. 9, pp. 25-27, Sep. 2003.

[9] P. McLaughlin, "Counterfeit cable is getting ugly," *Cabling Installation and Maintenance Magazine*, vol. 19, no. 8, pp. 31-32, Aug. 2011.

[10] Beyondtech, "The three major counterfeit communications cabling scams," *Cabling Installation and Maintenance Magazine*, vol. 21, no. 5, pp. 28-30, May 2017.

[11] P. McLaughlin, "Copper clad aluminum conductors, the latest counterfeiting ploy," *Cabling Installation and Maintenance Magazine*, vol. 19, no. 4, pp. 24-26, Apr. 2011.

[12] FLUKE Networks, Copper Clad Aluminum Cables (CCA). 2019. Available online: https://www.flukenetworks.com/content/application-note-copper-clad-aluminum-cables accessed on Apr. 16, 2022.

[13] M. Yamamura, Y. Kami, K. Murano, and F. Xiao, "Analysis of transmission line characteristics for twisted pair cables using the RLGC parameters of the cable," *Asia-Pacific Symposium on Electromagnetic Compatibility (APEMC)*, Taiwan, pp. 720-723, May 2015.

[14] C. Afifah, C. Alam, F. Seman, A. Asrokin, and N. Nohan, "Impact of cable bleeding into RLGC of twisted pair copper cable and achievable rate," *7th International Conference on Computer and Communication Engineering (ICCCE)*, Malaysia, pp. 321-326, Sep. 2018.

[15] M. Degerstrom, B. Gilbert, and E. Daniel, "Accurate resistance, inductance, capacitance and capacitance (RLCG) from uniform transmission line measurements," *IEEE-EPEP Electrical Performance of Electronic Packaging Conference*, San Jose, pp. 77-80, Oct. 2008.

[16] F. Ulaby, E. Michielssen, and U. Ravaioli, *Fundamentals of Applied Electromagnetics, 6th Edition,* Prentice Hall, 2010.

[17] D. Pozar, *Microwave Engineering, Fourth Edition*, John Wiley and Sons Inc., 2012.

[18] M. Sampath, "On Addressing the practical issues in the extraction of RLGC parameters for lossy multiconductor transmission lines using S-parameters models," *IEEE-EPEP Electrical Package*, San Jose, pp. 259-262, Oct. 2008.

[19] FLUKE Networks, "Datasheet: DSX-5000 cable analyzer." 2019. Available online: https://www.flukenetworks.com/content/datasheet-dsx-5000-cableanalyzer accessed on April 15, 2022.

[20] FLUKE Networks, "Versiv Cabling Certification Product Family User's Manual, Versiv Software Version 4.8." 2016. Available online: https://www.testequipmentdepot.com/fluke-networks/pdf/versiv_manual.pdf accessed on April 15, 2022.

Olusegun E. Ogundapo received a Ph.D. degree in Electronic Engineering from De Montfort University, United Kingdom. He also has an M.Sc. degree in Electrical Engineering from Ahmadu Bello University, Zaria, and a B.Eng. in Electrical and Electronic Engineering from the Federal University of Technology, Yola (now Modibbo Adama University), Yola-Nigeria. He is now an Assistant Professor at the School of Engineering, American University of Nigeria, Yola-Nigeria. His research interests are in computational electromagnetics, validation, data analysis, signal integrity, wireless/wired communication media analysis, and modeling.

Alistair P. Duffy received the B.Eng. (Hons.) degree in Electrical and Electronic Engineering and the M.Eng. degree from the University College, Cardiff, U.K., in 1988 and 1989, respectively. He received his Ph.D. degree from Nottingham University, Nottingham, U.K., in 1993 for his work on experimental validation of numerical modeling. He was awarded a D.Sc. in 2019 from Cardiff University for his work on the validation of computational electromagnetics. He is currently Director of the Institute of Engineering Sciences and Professor of Electromagnetics at De Montfort University, Leicester, U.K. He is also a Guest Professor at Harbin Institute of Technology, Harbin, China, a visiting professor at

Xi'an Jiaotong University, China, and a 2022 Visiting professor at EPFL, Switzerland. He is the author of approximately 300 articles published in journals and presented at international symposia. His research interests include CEM validation, communications cabling, and technology management.

Dr. Duffy is a Fellow of the IEEE, the Institution of Engineering and Technology (IET), and the Royal Society for the Encouragement of Arts, Manufactures and Commerce (RSA). He is the Immediate Past President of the IEEE EMC Society and Director-Elect of the IEEE. He is an Associate Editor of the IEEE Transactions on EMC and of the IEEE Letters on EMC Practice and Application. He was the General Chair of the IEEE Symposium on EMC + SIPI in 2020 and the joint symposium with EMC Europe in 2021.

Estimation of Soil Electric Properties and Water Content Through PolSAR Target Decomposition

Mai Z. Ibrahim[1], Ahmed I. Bahnacy[2], Khalid F. A. Hussein[3], and Asmaa E. Farahat[3]

[1]High Institute of Electronic Engineering (HIEE)
High Institute of Electronic Engineering, Belbeis, Egypt
eng.mai695@gmail.com

[2]Department of Electronics and Communication Engineering
Faculty of Electronic Engineering, Menouf, 32952, Egypt
bahnacy@hotmail.com

[3]Microwave Engineering Department
Electronics Research Institute, Cairo, 11843, Egypt
fkhalid@eri.sci.eg, asmaa@eri.sci.eg

***Abstract* –** A new method is proposed to recover the electric properties and water content of ground soil by applying the Target Decomposition (TD) theory for Polarimetric Synthetic Aperture Radar (PolSAR) images. The proposed method depends on the ε-σ characteristic curves of the soil which are unique for each soil type at a specific frequency. This method is examined for the clayey type soil which is found in most naturally vegetated land areas. Also, a novel method is developed for the realistic simulation of PolSAR images of natural lands, including forest regions, grasslands, and bare lands being prepared for gardens or crop cultivation. This method is based on the reverse of the PolSAR TD theory. The numerical results presented in this paper are concerned with the characterization of the most common type of clayey soil. Also, some of the numerical results presented in the present paper aim to achieve realistic PolSAR datasets using the inverse TD theory. Finally, some numerical results are presented for quantitative assessment of the method proposed to recover the properties and water content of the clayey soil using the datasets which are obtained through realistic simulations of forested areas, gardens, grasslands, and bare lands being prepared for cultivated plants. It is found, through the numerical investigations and quantitative assessment, that the dielectric constant, electric conductivity and water content of the investigated clayey types of soil are accurately estimated.

***Index Terms* –** PolSAR, soil properties, target decomposition.

I. INTRODUCTION

The electric properties of the soil are of great importance in production agriculture. The dielectric constant and soil electric conductivity are measures of the amount of water content and salts in the soil. The soil's electric properties are important indicators of soil fertility and soil health. It affects crop yields, crop suitability, plant nutrient availability, and the activity of soil microorganisms, which influence key soil processes including the emission of greenhouse gases such as nitrogen oxides, methane, and carbon dioxide. For certain non-saline soils, determining the electric conductivity can be a convenient and economical way to estimate the amount of nitrogen available for plant growth [1].

In another field, many of the methods applied for the detection of buried landmines and unexploded ordinance make use of electromagnetic signals penetrating the land soil. The Ground-Penetrating Radar (GPR) is considered the most promising technology for this purpose because of its ability to detect both metallic and non-metallic anti-personnel landmines by non-invasive subsurface sensing. However, the electric properties of the soil medium are critical parameters for buried object detection using the GPR because they control the contrast between the buried object and the soil in which it is buried. Additionally the electric properties of the soil control propagation, attenuation, and reflection of electromagnetic waves. Under some soil conditions, the landmine signature is of high quality while under others no signature can be detected at all [2].

Soil moisture is the quantity of water contained in soil on a volumetric or gravimetric basis [3, 4].

Submitted On: April 25, 2022
Accepted On: October 12, 2022
https://doi.org/10.13052/2022.ACES.J.371006

Soil moisture influences meteorological and climatic processes, although surface soil moisture only constitutes 0.0012% of all water available on the earth [5]. Soil moisture is important in modeling the ecosystem dynamics and the biogeochemical cycles but it has not had widespread application in modeling these processes because it is a variable that is very difficult to measure a spatially comprehensive basis [6]. The soil moisture gives also important information for agriculture irrigation. An accurate estimate of the spatiotemporal variations of soil moisture is critical for numerous large-scale environmental studies [7]. The large spatial and temporal variability that soil water content exhibit in the natural environment is the characteristic that makes it difficult to measure and use in earth science applications.

The use of radar data to retrieve soil moisture is of considerable importance in many domains, including agriculture, hydrology, and meteorology [6]. Despite many advantages that can be derived from the knowledge of soil moisture distribution, the measurement of soil moisture has a few limitations. However, the measurement of soil moisture not only depends on target characteristics such as surface roughness, vegetation cover, dielectric constant, and topography but also depends on various combinations of the radar sensor parameters including frequency, polarization, and angle of incidence (θ) with respect to nadir [9]. The measurements depend on the separation of the effects of water content and other factors such as surface roughness or soil texture which affect the backscattered signal. Unfortunately, most of the studies deal with the relationships obtained between the backscattering coefficient and soil moisture for a given set of radar configuration parameters. In [9], the soil moisture is estimated approximately from the microwave backscattering coefficients for the case of bare soil. In [10], soil surface parameters are retrieved from fully polarimetric SAR data.

Polarimetric Target Decomposition (TD) enables the physical interpretation of synthetic aperture radar (SAR) images more easily by fitting physical models of electromagnetic scattering to the PolSAR observations [11].

The theory of TD formulates the total scattering from a ground target as the sum of elementary scattering mechanisms to interpret the scattering from a land target as the weighted contributions of multiple physical mechanisms. This facilitates the identification, recognition, and classification of possible land targets with distinguishing polarization features.

In this paper, a novel method is applied to estimate the electric properties and the water content of ground soil using the TD theorem and the ε-σ characteristic curves of the soil which are unique for each soil type at a specific frequency. The proposed method is examined for clayey soil found in most naturally vegetated land areas. Also, a novel method is developed in the present paper for realistic simulation of PolSAR images for natural lands including forest regions, grasslands, and bare lands being prepared for gardens or crop cultivation. This method is based on the reverse of the PolSAR TD theory. The numerical results presented in this paper are concerned with the characterization of the clayey soil found in most of the natural lands, especially the vegetal regions. Also, some numerical results are presented to get datasets for a novel technique that is proposed for the realistic simulation of PolSAR images. Finally, some numerical results are presented for quantitative assessment of the method proposed for the estimation of the electric properties and water content of the clayey soil found in the forested areas, gardens, grasslands, and bare lands being prepared for cultivated plants.

II. ELECTRIC PROPERTIES OF THE GROUND SOIL OF CLAYEY TYPE

Clayey soil is the most common type of ground soils found in vegetal natural lands such as the natural grasslands, forest regions, and the soils prepared for cultivated crops. Clay is a type of fine-grained natural soil material that contains hydrous aluminum phyllosilicates (clay minerals) that develops plasticity when wet. Geologic clay deposits are mostly composed of phyllosilicate minerals containing variable amounts of water trapped in the mineral structure. Clays are plastic due to particle size and geometry as well as water content and become hard, brittle, and non–plastic upon drying or firing. Water does not percolate quickly enough through clayey soil. The water needs a relatively long time to soak into the earth. If the clayey soil is watered too much all at once, water just runs off and is wasted. Moreover, the clayey soil types retain water well and, hence, should be watered less frequently. The excess water should be gotten away otherwise the plants' roots are drowned.

The dielectric constant of the ground soil (ε_g) is complex and can be given as follows:

$$\varepsilon_g = \varepsilon_{rg} - j\varepsilon_{ig}. \tag{1-a}$$

The imaginary part of the relative permittivity is expressed in terms of the soil conductivity, σ_g, as follows:

$$\varepsilon_{ig} = \frac{\sigma_g}{2\pi f \varepsilon_0}. \tag{1-b}$$

The electric properties of the most common types of ground soils are dispersive with the frequency. It has its complex dielectric constant varying with the frequency. The electric properties of the soil are, also, strongly dependent on its volumetric water content and the continuous change of the soil water content leads to simultaneous continuous and monotonic variations of real dielectric constant, ε_{rg}, and conductivity, σ_g [12]. At any microwave frequency, the two electric properties ε_{rg} and σ_g are strongly correlated, which allows a mathematical relation between them to be calculated. This enables the expression of σ_g as a single-valued function of ε_{rg} as follows:

$$\sigma_g = F(\varepsilon_{rg}). \quad (2)$$

Given a microwave frequency, the ε-σ characteristic curve expressed in (2) is unique for each type of soil and provides important information that describes the relationship between the real dielectric constant, ε_{rg}, and the electric conductivity, σ_g, at the frequency of operation. These characteristic curves have great importance for the recovery of the electric properties and water content of the soil using the technique introduced in this work.

III. POLSAR TARGET DECOMPOSITION FOR ESTIMATION OF SOIL PROPERTIES AND WATER CONTENT

The covariance matrix of the PolSAR data is given by (A.1) of the Appendix. This covariance matrix is normalized, as given in (A.7) of the Appendix, and it has a unity ratio of the backscattered power, i.e. the summation of its main diagonal elements is equal to 1; hence:

$$\widehat{\sigma}_P^2 = \widehat{\sigma}_{hh}^2 + 2\widehat{\sigma}_{hv}^2 + \widehat{\sigma}_{vv}^2 = 1. \quad (3)$$

The PolSAR target decomposition theory with five-component scattering model [13] can be applied to get the following expansion of $\widehat{\Sigma}$:

$$\widehat{\Sigma} = a_s\hat{C}_s + a_d\hat{C}_d + a_v\hat{C}_v + a_w\hat{C}_w + a_h\hat{C}_h, \quad (4)$$

where $\hat{C}_s$, $\hat{C}_d$, $\hat{C}_v$, $\hat{C}_w$, and $\hat{C}_h$ are the normalized basis covariance matrices used to decompose $\widehat{\Sigma}$ and represent the basic scattering mechanisms due to single bounce of the incident wave on the rough soil surface, double-bounce on right-angle corners, volume scattering, wire (edge) scattering, and helix scattering. The expressions of these matrices are supplied in the appendix.

In the present analysis, due to the use of normalized covariance matrices on both sides of (4), the power balance implies that the coefficients a_s, a_d, a_v, a_w, and a_h are real unknown coefficients and, also, requires:

$$a_s + a_d + a_v + a_w + a_h = 1. \quad (5)$$

The contributions of wire and helix scattering mechanisms to the PolSAR data result from the human made structures which are usually found in urban areas. Such constituents are not found in natural lands such as forested regions grasslands, bare (unplanted) soil areas, deserts, sea surfaces, etc. Under this consideration, one can set $a_h = a_e = 0$ in (5). Thus, the decomposition of the normalized covariance matrix of the PolSAR data collected for the ground regions with natural land covers can be achieved using the following scattering model that is based on the three natural scattering components:

$$\widehat{\Sigma} = a_s\hat{C}_s + a_d\hat{C}_d + a_v\hat{C}_v, \quad (6\text{-a})$$

with the following condition which is necessary for power balance:

$$a_s + a_d + a_v = 1. \quad (6\text{-b})$$

Using the expressions of the normalized basis covariance matrices $\hat{C}_s$, $\hat{C}_d$, and $\hat{C}_v$, supplied in the appendix, the application of (6) results in the following system of equations:

$$\widehat{\sigma}_{hh}^2 = \frac{|\beta|^2}{1+|\beta|^2}\, a_s + \frac{|\alpha|^2}{1+|\alpha|^2}\, a_d + \frac{3}{8}\, a_v, \quad (7\text{-a})$$

$$2\widehat{\sigma}_{hv}^2 = \frac{1}{4}\, a_v, \quad (7\text{-b})$$

$$\widehat{\sigma}_{vv}^2 = \frac{1}{1+|\beta|^2}\, a_s + \frac{1}{1+|\alpha|^2}\, a_d + \frac{3}{8}\, a_v, \quad (7\text{-c})$$

$$\widehat{\sigma}_{hh,vv}^2 = \frac{\beta}{1+|\beta|^2}\, a_s + \frac{\alpha}{1+|\alpha|^2}\, a_d + \frac{1}{8}\, a_v, \quad (7\text{-d})$$

where the expression for α and β supplied in the appendix.Considering that $\alpha = \alpha_r + j\alpha_i$ and $\beta = \beta_r + j\beta_i$, the nonlinear system of equations (7) can, generally, be seen as composed of five real equations in seven real unknowns (a_s, a_d, a_v, α_r, α_i, β_r, and β_i). Thus, the solution of such a system may result in an infinite number of possible and acceptable solutions unless other constraints related to the ground soil properties are imposed to get the correct solution for the seven unknowns.

IV. THE PROPOSED METHOD FOR ESTIMATION OF SOIL PROPERTIES AND WATER CONTENT

The most common three types of natural lands (see Fig. 1) are investigated in the present work: the forest regions, grasslands, and bare soils. The forest regions need a three-component scattering model for the decomposition of the covariance matrix as the contribution of the single-bounce, double-bounce, and volume scattering should all be considered in the PolSAR data. The grasslands need a two-component scattering model due to the contributions of the single-bounce and volume scattering. The bare soils need a single-component scattering model as only the single bounce of the incident wave on the rough soil surface of the bare land constitutes the SAR data.

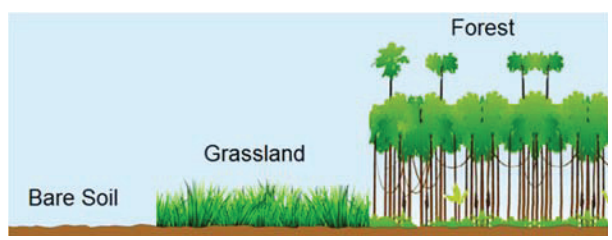

Fig. 1. The most common types of natural ground: Bare soils, grasslands, and forest regions.

Parameter β, appearing in (7), is related to the single bounce of the incident wave on the rough surface of the ground soil. As given in the appendix, for a given look angle (θ_i) of the SAR, this parameter is uniquely determined by the complex relative permittivity of the soil (ε_{rg}, σ_g). On the other hand, the parameter α, appearing in (7), is related to the double-bounce of the incident wave on the right-angle corners formed by the horizontal surface of the ground soil and the vertical surface of the tree trunks. As given in the appendix, for a given look angle (θ_i), this parameter depends on the complex relative permittivity of the soil and that of the tree trunks. The complex dielectric constant of a tree trunk measured at the trunk surface is usually constant for a specific frequency and is weakly dependent on the water content of the tree [14]. Thus, for a specific tree type, the parameter α is strongly dependent on the complex relative permittivity of the ground soil (ε_{rg}, σ_g). As the electric parameters (ε_{rg}, σ_g) of a ground soil of a specific type are determined by its water content, parameters α and β can be uniquely determined by the water content of the ground soil beneath the vegetation.

A. Estimation of electric properties and water content of the ground soil of forest regions

Regarding the decomposition of $\widehat{\Sigma}$ given by (6) for all types of natural land covers, it should be considered, for the forest regions, that $a_s \neq 0$ due to the significant contribution of the single bounce of the incident wave on the rough soil surface beneath the forest trees, $a_d \neq 0$ due to strong contribution of double-bounce on the right-angle corners formed by the horizontal ground surface and vertical tree trunks, and $a_v \neq 0$ due to the volume scattering from the huge tree canopy layer. Thus, the three components of backscattering are all present in the PolSAR data of the forest regions.

Considering $a_v = 8\,\widehat{\sigma}_{hv}^2$ as given by (7-b), the system of equations given by (7) can be reduced to take the following form:

$$a_s + a_d = 1 - 8\widehat{\sigma}_{hv}^2, \tag{8-a}$$

$$\frac{1-|\beta|^2}{1+|\beta|^2}\, a_s + \frac{1-|\alpha|^2}{1+|\alpha|^2}\, a_d = \widehat{\sigma}_{vv}^2 - \widehat{\sigma}_{hh}^2, \tag{8-b}$$

$$\frac{\beta}{1+|\beta|^2}\, a_s + \frac{\alpha}{1+|\alpha|^2}\, a_d = \widehat{\sigma}_{hh,vv}^2 - \widehat{\sigma}_{hv}^2. \tag{8-c}$$

In this case, the system (8) can be seen as composed of four real equations and six real unknowns (a_s, a_d, α_r, α_i, β_r, and β_i). It seems that, unless other constraints are imposed, the system given by (8) cannot have a unique solution. Using (8-a) and (8-b), the coefficients a_s and a_d can be obtained in terms of the other complex unknowns α and β as follows:

$$a_s = 1 - 8\widehat{\sigma}_{hv}^2 - \frac{\widehat{\sigma}_{vv}^2 - \widehat{\sigma}_{hh}^2 - \frac{1-|\beta|^2}{1+|\beta|^2}\left(1 - 8\widehat{\sigma}_{hv}^2\right)}{\frac{1-|\alpha|^2}{1+|\alpha|^2} - \frac{1-|\beta|^2}{1+|\beta|^2}}\ , \tag{9-a}$$

$$a_d = \frac{\widehat{\sigma}_{vv}^2 - \widehat{\sigma}_{hh}^2 - \frac{1-|\beta|^2}{1+|\beta|^2}\left(1 - 8\widehat{\sigma}_{hv}^2\right)}{\frac{1-|\alpha|^2}{1+|\alpha|^2} - \frac{1-|\beta|^2}{1+|\beta|^2}}. \tag{9-b}$$

A third complex equation can be formulated as a quantity δ_F being equal to the difference between the left-hand and right-hand sides of (8-c), where:

$$\delta_F = \frac{\beta}{1+|\beta|^2}\, a_s + \frac{\alpha}{1+|\alpha|^2}\, a_d - \left(\widehat{\sigma}_{hh,vv}^2 - \widehat{\sigma}_{hv}^2\right). \tag{10}$$

The coefficients a_s and a_d can be substituted from (9) into (10) to get δ_F completely expressed in terms of α and β which are uniquely determined by ε_{rg} and σ_g as given by (A.9) and (A.10), respectively. In this way, the problem is formulated as follows: Find the values of ε_{rg} and σ_g to get $\delta_F = 0$. Thus, a complex equation given by (1) in two real unknowns (ε_{rg} and σ_g) is formulated. A constraint on the relation between the two unknowns is given by the ε-σ characteristic curve, expressed in (2), that uniquely characterizes the soil beneath the vegetation. In this way, a unique solution for ε_{rg} and σ_g can be obtained by minimizing δ_F given by (10), and, then, the ε-σ characteristic curve can be used to uniquely determine the water content of the soil. Also, the parameters α and β can be calculated using (A.9) and (A.10), respectively, and substituted into (9) to get the unknown coefficients a_s and a_d. Thus, the contribution of each of the three scattering mechanisms is determined by the triplet (a_s, a_d, a_v) and, hence, the imaged land is classified.

B. Estimation of electric properties and water content of the ground soil of grasslands

Regarding the expansion of $\widehat{\Sigma}$ given by (6) for natural land covers, it should be considered, for the grasslands, that $a_s \neq 0$ due to the significant contribution of the single bounce of the incident wave on the rough soil surface beneath the grass leaves, $a_d = 0$ due to absence of double-bounce, and $a_v \neq 0$ due to the volume scattering from the dense leaves of the grass. Thus, for grasslands, the normalized covariance matrix $\widehat{\Sigma}$ has only two components of scattering and can be decomposed as follows:

$$\widehat{\Sigma} = a_s \hat{C}_s + a_v \hat{C}_v. \tag{11}$$

For grown grasslands, $a_s \neq 0$ and $a_v \neq 0$ and, hence, the application of (11) results in the following system of equations:

$$a_v = 8\widehat{\sigma}_{hv}^2, \tag{12-a}$$

$$a_s = 1 - 8\widehat{\sigma}_{hv}^2\ , \tag{12-b}$$

$$\frac{1-|\beta|^2}{1+|\beta|^2}\left(1 - 8\widehat{\sigma}_{hv}^2\right) = \widehat{\sigma}_{vv}^2 - \widehat{\sigma}_{hh}^2, \tag{12-c}$$

$$\frac{\beta}{1+|\beta|^2}\left(1 - 8\widehat{\sigma}_{hv}^2\right) = \widehat{\sigma}_{hh,vv}^2 - \widehat{\sigma}_{hv}^2. \tag{12-d}$$

Equation (12-c) can be rearranged and written in the following form:

$$1 + |\beta|^2 = \frac{2\left(1 - 8\widehat{\sigma}_{hv}^2\right)}{1 - 8\widehat{\sigma}_{hv}^2 + \widehat{\sigma}_{vv}^2 - \widehat{\sigma}_{hh}^2}. \tag{13}$$

The substitution from (13) into (12-d) gives the following solution for β:

$$\beta = \frac{2\left(\widehat{\sigma}^2_{hh,vv} - \widehat{\sigma}^2_{hv}\right)}{1 - 8\widehat{\sigma}^2_{hv} + \widehat{\sigma}^2_{vv} - \widehat{\sigma}^2_{hh}}. \quad (14)$$

A complex equation can be formulated as a quantity δ_G being equal to the difference between the left-hand and right-hand sides of (12-d), where,

$$\delta_G = \frac{\beta}{1+|\beta|^2}\ \left(1 - 8\widehat{\sigma}^2_{hv}\right) - (\widehat{\sigma}^2_{hh,vv} - \widehat{\sigma}^2_{hv}). \quad (15)$$

The equation $\delta_G = 0$ has a unique solution for ε_{rg} and σ_g and the corresponding water content can, then, be directly determined from the ε-σ characteristic curve of the specified type of the grassland soil. On the other hand, the contributions of the single-bounce and volume scattering mechanisms to $\widehat{\Sigma}$ is determined by the doublet (a_s, a_d) and, hence, the imaged land is classified.

C. Estimation of electric properties and water content of bare soil

Regarding the expansion of $\widehat{\Sigma}$ given by (6), it should be considered that, for the bare soil regions, only $a_s \neq 0$ due to the contribution of the single bounce of the incident wave on the rough soil surface. For the other two coefficients, one has $a_d = 0$ and $a_v = 0$ due to the absence of double-bounce and vegetation canopies, respectively. Thus, for bare soil areas, the normalized covariance matrix $\widehat{\Sigma}$ can be expressed as follows.

$$\widehat{\Sigma} = a_s \hat{C}_s. \quad (16)$$

As the covariance matrices on both sides of (16) are normalized, the following system of equations is obtained:

$$a_s = 1\ , \quad \text{(17-a)}$$

$$\frac{|\beta|^2}{1+|\beta|^2} = \widehat{\sigma}^2_{hh}, \quad \text{(17-b)}$$

$$\frac{\beta}{1+|\beta|^2}\ = \widehat{\sigma}^2_{hh,vv}. \quad \text{(17-c)}$$

Equation (17-b) can be rearranged and written in the following form:

$$1 + |\beta|^2 = \frac{1}{1 - \widehat{\sigma}^2_{hh}}. \quad (18)$$

By substitution from (18) into (17-c) gives the following solution for β:

$$\beta = \frac{\widehat{\sigma}^2_{hh,vv}}{1 - \widehat{\sigma}^2_{hh}}. \quad (19)$$

A complex equation can be formulated as a quantity δ_S being equal to the difference between the left-hand and right-hand sides of (17-c), where:

$$\delta_S = \frac{\beta}{1+|\beta|^2}\ - \widehat{\sigma}^2_{hh,vv}. \quad (20)$$

The equation $\delta_S = 0$ has a unique solution for ε_{rg} and σ_g; then the corresponding water content can directly be determined from the ε-σ characteristic curve of the specified type of the bare soil.

V. SIMULATION OF POLSAR IMAGES OF NATURAL LANDS

PolSAR datasets (test images) are required for testing the efficiency of the technique proposed in the present work for the classification of natural lands of clayey soil and estimation of water content. The natural lands investigated include forest regions, natural grasslands, and bare soils. Such datasets can be obtained by simulation. It is proposed to apply the target decomposition theory with the three-component scattering model as described in Section III to construct a covariance matrix that describes the statistical properties of the PolSAR data collected upon imaging the desired area of the natural land. The detailed procedure to generate a realistic PolSAR image can be described as follows.

- The texture (composition of ingredients) of the ground soil should be specified.
- The curves describing the relations between the electromagnetic properties of the ground soil type (with the texture specified in the previous step) and the water content should be known.
- The ε-σ characteristic curves of the soil at the PolSAR operating frequency should be known.
- The volumetric water content w_{ref} of the ground soil and the corresponding electric properties ε_{rg_ref} and σ_{g_ref} should be determined.
- The azimuth and range dimensions of the land area to be imaged (by simulation), L_A and L_R, should be given.
- The desired azimuth and range resolutions ρ_A and ρ_R, of the simulated PolSAR image should be given.
- Parameters α_{ref} and β_{ref} are evaluated by (A.9) and (A.10) as given in the appendix. For the forest regions, the electric properties of the tree trunks should be known (or assumed) to calculate α_{ref}.
- The normalized basis covariance matrices $\hat{C}_s$, $\hat{C}_d$, and $\hat{C}_v$ are evaluated using (A.8-a), (A.8-b), and (A.8-c) as given in the appendix.
- The desired contributions of the three scattering mechanisms a_{s_ref}, a_{d_ref}, and a_{v_ref} are determined according to actual constituents of the imaged land.
- A normalized covariance matrix, $\widehat{\Sigma}_{ref}$, is constructed by composition using the three-component scattering model given by (6) for the type of natural land.
- The desired level of the backscattered power to the power illuminating the SAR target (imaged land area), P_{ref}, should be determined.

- The covariance matrix is calculated, $\Sigma_{ref} = P_{ref}\widehat{\Sigma}_{ref}$.
- The dimensions (size) of the simulated PolSAR image in the azimuth and range directions are obtained as $M = L_A/\rho_A$ and $N = L_R/\rho_R$, respectively.
- Finally, the covariance matrix Σ_{ref} is used to generate a simulated three-channel image of $M \times N$ pixels defined by $S_{m,n} = \{S_{hh}, S_{hv}, S_{vv}\}_{m,n}$.

VI. RESULTS AND DISCUSSIONS

This section presents the numerical results concerned with, (i) Characterization of the clayey soil found in most of the natural lands, especially the vegetal regions. (ii) Application of the method proposed in Section V that uses the theory of SAR target decomposition for realistic simulation of PolSAR images. (iii) Application of the method proposed in Section IV for estimation of the electric properties and water content of the clayey soil found in the forested areas, gardens, grasslands, and bare lands being prepared to cultivate plants.

A. Texture of the clayey soil commonly found in natural lands

The clayey types of soil investigated in the present work are characterized in [12] through experimental measurements. The ingredients and volumetric density of this type of soil are listed in Table 1. This is the most common type of ground soil found in natural lands such as natural grasslands, forest regions, and the bare soils being prepared for cultivated crops.

Table 1: Composition of the clayey soil type used for testing the method introduced in the present work to estimate the soil properties [12]

Soil Type	Soil Composition (%)			Bulk Density (gm/cm^3)
	Sand	Slit	Clay	
Clayey	17.25	39.04	43.05	1.2

B. Dispersive electric properties and $\varepsilon - \sigma$ characteristic curves of the clayey soil

Clayey soil with the composite texture listed in Table 1 and 30% water content has its complex dielectric constant varying with the frequency as shown in Fig. 2 (a) [12]. The electric properties of this soil are also strongly dependent on its volumetric water content. The PolSAR systems used for vegetation monitoring usually operate at 1.27 GHz. For the clayey soil with the texture listed in Table 1, the curves describing the dependence of ε_{rg} and ε_{ig} on the volumetric water content at 1.27 GHz are deduced from those available in [12] at 900 MHz by the aid of the frequency dispersion curves presented in Fig. 2 (a). The curves describing the dependence of ε_{rg} and σ_g on the water content at 900 MHz and 1.27 GHz are presented in Fig. 2 (b). The continuous change of the soil water content leads to simultaneous continuous monotonic variations of its electric properties as shown in Fig. 2 (b). At any microwave frequency, the electric properties ε_{rg}, and σ_g are strongly correlated and, hence, a curve can be fitted between them as previously mentioned in Section II.

C. Realistic simulation of PolSAR datasets for natural lands

PolSAR datasets (test images) are required to test the methods introduced in the present work for the classification of natural lands of clayey soil and estimation of water content. The procedure described in Section V is applied to generate three datasets for the three types of natural lands investigated in this work.

For the simulated PolSAR images, it is considered that the working frequency is 1.27 GHz and the ground soil is clayey with the mixture of ingredients listed in Table 1. The ground soil has the ε-σ characteristic curves presented in Fig. 2 (c), the water content is 44% and the corresponding electric properties are $\varepsilon_{rg\_ref} = 25.16$ and $\sigma_{g\_ref} = 0.489\ S/m$. The electric properties of the tree trunks are $\varepsilon_{rw} = 4$, and $\sigma_w = 0.01\ S/m$. The corresponding values of α and β, given by (A.9) and (A.10), respectively, are $\alpha_{ref} = 4.7091 - j0.2981$, and $\beta_{ref} = 0.4073 + j0.0132$. Using these values, the normalized basis covariance matrices for the single-bounce, $\hat{C}_s$, double-bounce, $\hat{C}_d$, and volume scattering, $\hat{C}_v$, mechanisms can be calculated using (A.8-a), (A.8-b), and (A.8-c).

C.1. Covariance matrix for PolSAR images of forested areas

Consider a forested area with equal contributions of the three basic constituents (single-bounce, double-bounce, and volume scattering) to the backscatter data collected by a PolSAR system, i.e., $a_s = a_d = a_v = 1/3$. Considering that this forested area has a clayey soil of water content of 44%, the application of (6) with the obtained normalized covariance matrices, $\hat{C}_s$, $\hat{C}_d$, and $\hat{C}_v$, the normalized covariance matrix, $\widehat{\Sigma}_{F_{ref}}$, for the three-channel PolSAR image data of this forest region can be calculated.

C.2. Covariance matrix for PolSAR images of grasslands

Consider a grassland area for which the contribution of the double-bounce to the PolSAR data vanishes whereas the volume scattering caused by the grass leaves is twice that of the single-bounce scattering caused by the soil rough surface, i.e., $a_s = 1/3$, $a_d = 0$, and $a_v = 2/3$.

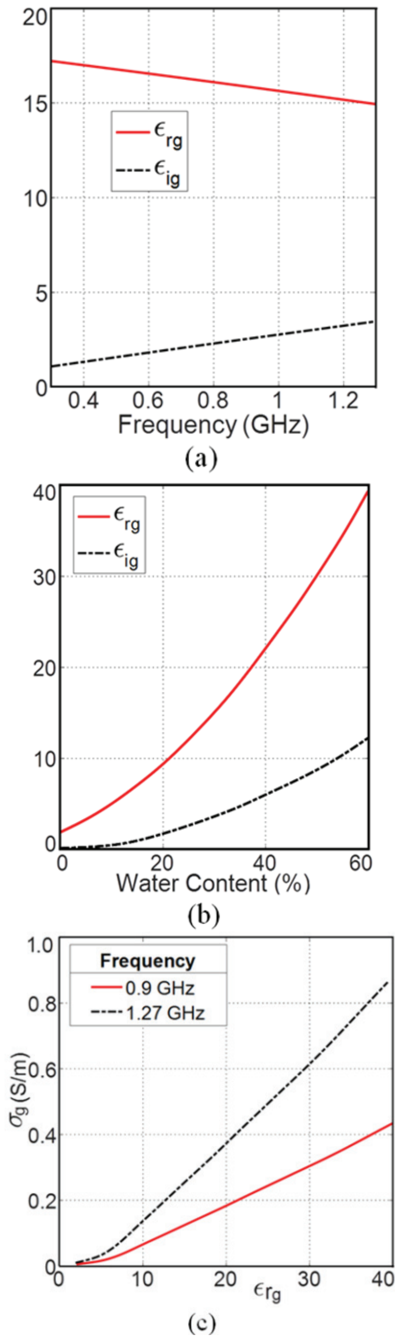

Fig. 2. Dependence of the complex relative permittivity of the clayey soil on the frequency and volumetric water content. (a) Dispersive properties at 30% water content, (b) Dependence of ε_{rg} and σ_g on the water content, (c) ε-σ characteristic curves.

Considering that this grassland area has a clayey soil of water content of 44%, the application of (6) with the obtained normalized covariance matrices $\hat{C}_s$, $\hat{C}_d$, and $\hat{C}_v$, the normalized covariance matrix, $\widehat{\Sigma}_{F_{ref}}$, for the three-channel PolSAR image data of this grassland.

C.3. Covariance matrix for PolSAR images of bare soil areas

An area of bare clayey soil with 44% water content has its backscattering attributed only to the single-bounce mechanism and, hence, the normalized covariance matrix for the three-channel PolSAR image data can be given directly as $\widehat{\Sigma}_{S_{ref}} = \hat{C}_s$.

C.4. Simulated PolSAR Images

C.4.1. Ground truth images of natural lands with clayey soil

To visualize the classified natural lands by monitoring the water content of the ground soil, a color map may be appropriate for this purpose. The RGB colors used for indicating the three basic scattering mechanisms in the natural land of the clayey soil described in Section VI-A, single-bounce, double-bounce, and volume scattering are, respectively, expressed as follows:

$$RGB_{SB} = (0.6,\ 0.6,\ 0.4\ ), \tag{21-a}$$

$$RGB_{DB} = (0.8,\ 0.2,\ 0.0\ ), \tag{21-b}$$

$$RGB_{VS} = (0.2,\ 0.6,\ 0.2\ ). \tag{21-c}$$

The RGB colors used to indicate the type of the natural land while monitoring the water content of the soil can generally be composed as follows:

$$RGB_{NaturalLand} = (a_s\ RGB_{SB} + a_d\ RGB_{DB} + a_v\ RGB_{VS})\ (1-w)^{0.7}, \tag{22}$$

where w is the volumetric water content.For example, the RGB color codes for the pure land types (forest, grasslands, and bare lands) of clayey soils are, respectively expressed as follows:

$$RGB_{Forset} = \left(\frac{1}{3}RGB_{SB} + \frac{1}{3}RGB_{DB} + \frac{1}{3}RGB_{VS}\right)(1-w)^{0.7}, \tag{23-a}$$

$$RGB_{GrassLand} = \left(\frac{1}{3}RGB_{SB} + \frac{2}{3}RGB_{VS}\right)(1-w)^{0.7}, \tag{23-b}$$

$$RGB_{BareLand} = RGB_{SB}(1-w)^{0.7}. \tag{23-c}$$

The color map shown in Fig. 3 is appropriate for simultaneous monitoring of the natural land type and the water content of the ground soil beneath the vegetation.

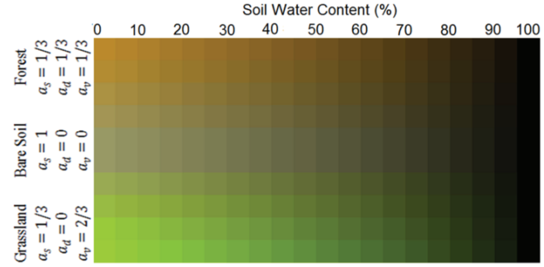

Fig. 3. Color map for classification of the natural lands with indication of the soil water content.

The RGB colors shown in this figure are generated using (23). For all the types of natural lands, the darkness of the corresponding color indicates the water content of the ground soil.

C.4.2. Simulated PolSAR Images for Natural Lands

An optical satellite image obtained from Google Maps for a region of cultivated land near Luxor Luxury Villa, in Luxor city, Egypt, is presented in Fig. 4 (a). A corresponding image is presented in Fig. 4 (b) to classify the different types of natural lands with the color code listed Table 2. The total dimensions of the land region to be imaged in the azimuth and range directions are $L_A = 365\ m$ and $L_R = 400\ m$, respectively.

The procedure described in Section V is applied to get the three-channel PolSAR images, where the corresponding resolutions are set as $\rho_A = 0.65\quad m$ and $\rho_R = 0.71\ m$, respectively. Thus, the size of the simulated PolSAR image is 560×565 pixels in the azimuth and range directions, respectively. A ground-truth image is presented in Fig. 5 (a) to indicate the land type by monitoring the soil water content according to the color map shown in Fig. 3. The generated three-channel PolSAR images are presented in Figs. 5 (b), (c), and (d). The image of the cross-polarization HV-channel, $|S_{hv}|$, Fig. 5 (c), shows a high level of the cross-polarized backscatter from the vegetal areas (forests and grasslands) whereas the water surface and bare lands have almost zero cross-polarization. Also, for the regions characterized by single-bounce scattering like water surface and bare land, the backscatter of the co-polarization VV-channel, $|S_{vv}|$, is significantly larger than $|S_{hh}|$, of the HH-channel.

Table 2: Color code for classification of natural land types included in the imaged region presented in Fig. 4

Color code	Type of natural land	Soil water content	Dielectric constant	Electric conductivity (S/m)
Forest 1	Forested area	19 %	8.907	0.1109
Forest 2	Forested area	29 %	14.45	0.2416
Forest 3	Forested area	44 %	25.16	0.4980
Forest 4	Forested area	54 %	33.56	0.7067
Grassland 1	Grassland	25 %	12.10	0.1860
Grassland 2	Grassland	39 %	21.33	0.4060
Grassland 3	Grassland	49 %	29.22	0.5958
Bare Land 1	Bare land	34 %	17.68	0.3172
Bare Land 2	Bare land	56 %	35.40	0.7567

D. Estimation of electric properties of clayey soil in natural lands

The proposed method is used to estimate the electric properties of different soil types.

(a)

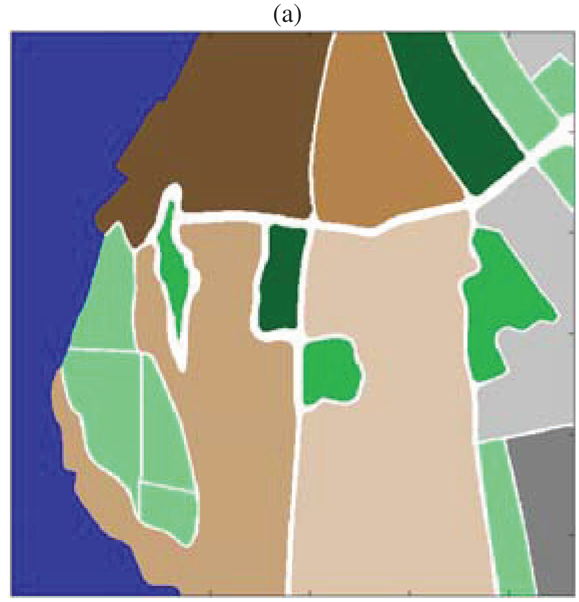

(b)

Fig. 4. Region of cultivated land near Luxor Luxury Villa, in Luxor city, Egypt, (a) satellite image obtained from Google Maps, (b) Color-coded classification image according to the type of land; Table 2 for legend.

D.1. Estimation of electric properties of clayey soil in forest regions

The method described in Section IV-A is used to estimate the properties of the ground soil of the forested area named "Forest 3", see Fig. 4, from the corresponding PolSAR data presented in Figs. 5 (b), (c), (d) with the ground truth shown in Fig. 5 (a).

The quantity δ_F, expressed in (10), is plotted as a function of ε_{rg} and σ_g in a three-dimensional plot as

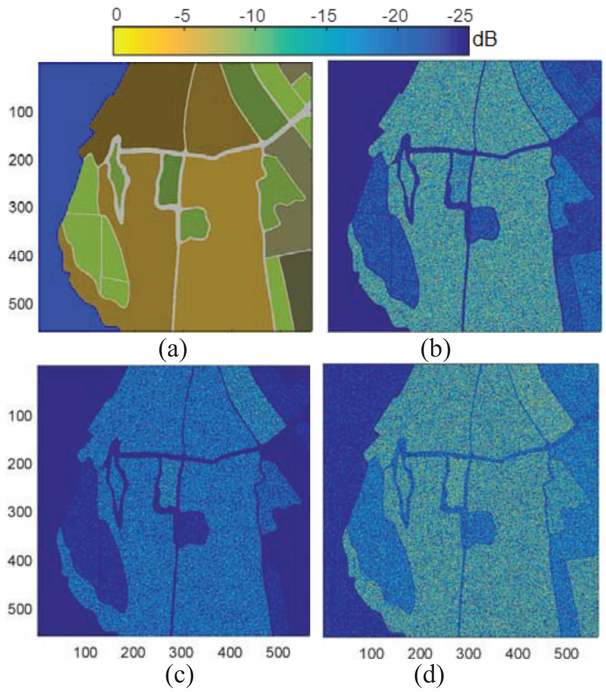

Fig. 5. Simulation of three-channel PolSAR image for the land region in Luxor city, (a) Ground-truth image showing the land type with indication of the soil water content, (b) $|S_{hh}|$, (c) $|S_{hv}|$, (d) $|S_{vv}|$, channels.

shown in Fig. 6. The ε-σ characteristic curve of the soil is also plotted in the (ε_{rg}-σ_g) plane of Fig. 6. It is shown that δ_F has a sharp minimum of 8×10^{-5} at the point $\varepsilon_{rg} = 25.2$ and $\sigma_g = 0.519\ S/m$, which almost lies on the ε-σ characteristic curve of the clayey soil as shown in Fig. 6, where the corresponding water content of the soil is 44.57%. The estimated values of the electric properties, ε_{rg} and σ_g, and the water content are listed in Table 3 with the resulting estimation errors. It is found that the percentage estimation errors are very small which reflects the efficiency of the proposed method to estimate the electric properties and water content of the soil using.

Table 3: The ground soil parameters used for generating the SAR data for the forested area named "Forest 3"; see Table 2. The estimated values of these parameters using the proposed method and the resulting estimation errors are listed in the last two rows of the table

Soil Parameter	Dielectric Constant ε_{rg}	Conductivity (S/m) σ_g	Water Content w
Ground Truth	25.16	0.498	44.00 %
Estimated	25.20	0.519	44.57 %
Percentage Error	0.16 %	4.1 %	1.3 %

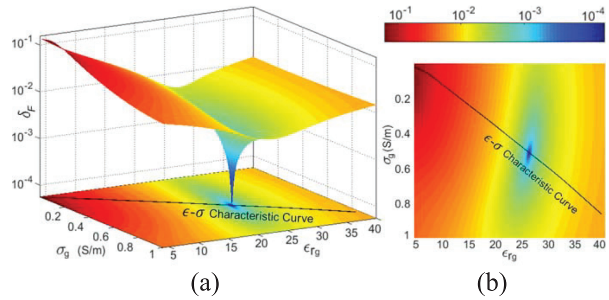

Fig. 6. Estimation of soil parameters for the forest region named "Forest 3". Plots of the quantity δ_F given by (10) versus the real dielectric constant ε_{rg} and conductivity σ_g of a clayeysoil; (a) 3D, (b) 2D, plot.

D.2. Estimation of electric properties of clayey soil in grasslands

The method described in Section IV-B is used to recover the electric properties of the ground soil of the grassland area named "Grass 1", see Fig. 4, from the corresponding PolSAR data presented in Figs. 5 (b), (c), (d) with the ground truth shown in Fig. 5 (a).

The quantity δ_G, expressed in (15), is plotted as a function of ε_{rg} and σ_g in a three-dimensional plot as shown in Fig. 7. The ε-σ characteristic curve of the soil is also plotted in the (ε_{rg}-σ_g) plane of Fig. 7. It is shown that δ_G has a sharp minimum of 9×10^{-4} at the point $\varepsilon_{rg} = 11.6$ and $\sigma_g = 0.181\ S/m$, which almost lies on the ε-σ characteristic curve of the clayey soil as shown in Fig. 7, where the corresponding water content of the soil is 24.1%. The recovered values of the electric properties, ε_{rg} and σ_g, and the water content are listed in Table 4 with the resulting estimation errors. It is found that these errors are very small, which reflects the efficiency of the proposed method to estimate the soil parameters.

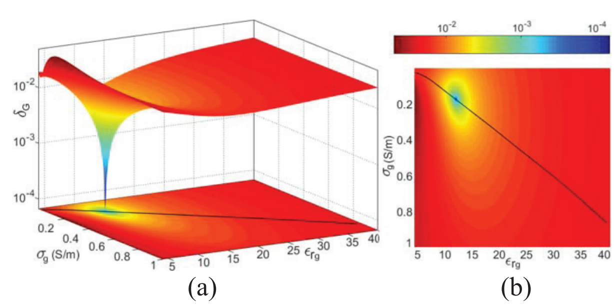

Fig. 7. Estimation of soil parameters for the grassland region named "Grass1". Plots of the function δ_G given by (15) versus the real dielectric constant ε_{rg} and conductivity σ_g of a clayey soil; (a) 3D, (b) 2D, plot.

Table 4: The ground soil parameters used for generating the SAR data for the forested area named "Grassland 1"; see Table 2. The recovered values of these parameters using the proposed method and the resulting percentage estimation errors are listed in the last two rows of the table

Soil Parameter	Dielectric Constant ε_{rg}	Conductivity (S/m) σ_g	Water Content w
Ground Truth	12.10	0.186	25.0 %
Estimated	11.60	0.181	24.1 %
Percentage Error	4.1 %	2.7 %	3.6 %

D.3. Estimation of electric properties of clayey bare soil

The method described in Section IV-C is used to recover the electric properties of the ground soil of the area named "Bare Land 2", see Fig. 4, from the corresponding PolSAR data presented in Figs. 5 (b), (c), (d) with the ground truth shown in Fig. 5 (a).

The quantity δ_S, expressed in (20), is plotted as a function of ε_{rg} and σ_g in a three-dimensional plot as shown in Fig. 8. The ε-σ characteristic curve of the soil is also plotted in the (ε_{rg}-σ_g) plane of Fig. 8. It is shown that δ_S has a sharp minimum of 9×10^{-4} at the point $\varepsilon_{rg} = 35.4$ and $\sigma_g = 0.757\ S/m$, which almost lies on the ε-σ characteristic curve of the clayey soil as shown in Fig. 8, where the corresponding water content of the soil is 56.0%. The recovered values of the electric properties, ε_{rg} and σ_g, and the water content are listed in Table 5 with the resulting estimation errors of the retrieved values. It is shown that the percentage errors are very small, which indicates the accuracy of the proposed method.

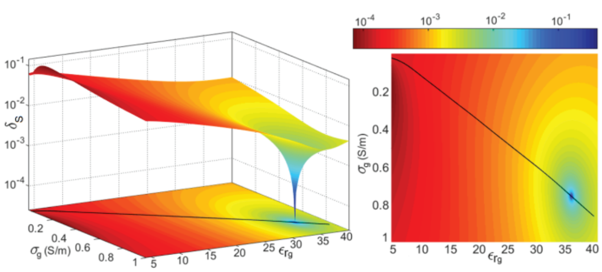

(a) (b)

Fig. 8. Estimation of soil parameters for the bare land region named "Bare Land 2". Plots of the function δ_S given by (20) versus the real dielectric constant ε_{rg} and conductivity σ_g of a clayey soil; (a) 3D, (b) 2D, plot.

Table 5: The ground soil parameters used for generating the SAR data for the forested area named "Bare Land 2"; see Table 2. The recovered values of these parameters using the proposed method and the resulting percentage error of the estimated values are listed in the last two rows of the table

Soil Parameter	Dielectric Constant ε_{rg}	Conductivity (S/m) σ_g	Water Content w
Ground Truth	35.40	0.759	56.0 %
Estimated	35.40	0.757	56.0 %
Percentage Error	0.0 %	0.26 %	0.0 %

VII. CONCLUSIONS

A new method is proposed to estimate the electric properties and water content of ground soil by applying the Target Decomposition (TD) theory for PolSAR images with the help of the ε-σ characteristic curves of the soil which are unique for each soil type at a specific frequency. This method is examined for the clayey type soil which is found in most naturally vegetated land areas. Also, a new method is developed based on the reverse of PolSAR TD theory, for realistic PolSAR images simulation of natural lands. Numerical results are presented for realistic PolSAR datasets using the proposed inverse TD theory method for Luxor city in Egypt. Also, numerical results are presented for quantitative assessment of the method proposed for the retrieval of the electric properties and water content of the clayey soil using the generated datasets. It is found, through the numerical investigations and quantitative assessment, that the dielectric constant, electric conductivity, and water content of the investigated clayey types of soil are accurately estimated.

APPENDIX

A.1. Covariance matrix for polarimetric SAR data

The reciprocity of backscattering of the radar pulse implies that $S_{hv} = S_{vh}$. Hence, the 3×3-element covariance matrix of the data collected by the four-channel PolSAR system can be expressed as three-channel data as follows.

$$\Sigma = [c_{11}\ c_{12}\ c_{13}\ c_{21}\ c_{22}\ c_{23}\ c_{31}\ c_{32}\ c_{33}]$$
$$= \left[\sigma_{hh}^2\ \sqrt{2}\sigma_{hh,hv}^2\ \sigma_{hh,vv}^2\ \sqrt{2}\sigma_{hv,hh}^2\ 2\sigma_{hv}^2\ \sqrt{2}\sigma_{hv,vv}^2\ \sigma_{vv,hh}^2\ \sqrt{2}\sigma_{vv,hv}^2\ \sigma_{vv}^2\right]. \quad \text{(A.1)}$$

The elements of the covariance matrix are the ensemble averages of the autocorrelation and cross-correlation of the scattering coefficients of the three channels [13]:

$$\Sigma = \left[\text{¡}|S_{hh}|^2\text{¿}\ \sqrt{2}\text{¡}S_{hh}S_{hv}^*\text{¿}\ \text{¡}S_{hh}S_{vv}^*\text{¿}\ \sqrt{2}\text{¡}S_{hv}S_{hh}^*\text{¿}\ 2\text{¡}|S_{hv}|^2\text{¿}\ \sqrt{2}\text{¡}S_{hv}S_{vv}^*\text{¿}\ \text{¡}S_{vv}S_{hh}^*\text{¿}\ \sqrt{2}\text{¡}S_{vv}S_{hv}^*\text{¿}\ \text{¡}|S_{vv}|^2\text{¿}\right]. \quad \text{(A.2)}$$

The backscattered power for each of the three channels (HH, HV, VV) is given by main diagonal elements c_{11}, c_{22}, and c_{33}:

$$c_{11} = \sigma_{hh}^2,\ \ c_{22} = 2\sigma_{hv}^2,\ \ c_{33} = \sigma_{vv}^2. \qquad (A.3)$$

The total ratio of the backscattered power to the power illuminating the SAR target can be formulated as the sum of the main diagonal elements of Σ:

$$\sigma_P^2 = c_{11} +\ c_{22} +\ c_{33} = \sigma_{hh}^2 + 2\sigma_{hv}^2 + \sigma_{vv}^2. \qquad (A.4)$$

The correlation between the co-polarized and cross-polarized channels (HH, HV) and (HV, VV) is described by the elements c_{23} and c_{32}:

$$c_{12} = c_{21}^* = \sqrt{2}\sigma_{hh,hv}^2,\ \ c_{23} = c_{32}^* = \sqrt{2}\sigma_{hv,vv}^2. \qquad (A.5)$$

The correlation between the co-polarized channels (HH, VV) is given by the elements c_{13} and c_{31}:

$$c_{13} = c_{31}^* = \sigma_{hh,vv}^2. \qquad (A.6)$$

A normalized covariance matrix $\widehat{\Sigma}$ of the PolSAR data have unity ratio of the backscattered power. It can be obtained by dividing the elements of Σ by σ_P^2 expressed in (A.4):

$$\widehat{\Sigma} = \frac{1}{\sigma_P^2}\,\Sigma$$
$$= \left[\widehat{\sigma}_{hh}^2\ \sqrt{2}\widehat{\sigma}_{hh,hv}^2\ \widehat{\sigma}_{hh,vv}^2\ \sqrt{2}\widehat{\sigma}_{hv,hh}^2\ 2\widehat{\sigma}_{hv}^2\ \sqrt{2}\widehat{\sigma}_{hv,vv}^2\ \widehat{\sigma}_{vv,hh}^2\right.$$
$$\left.\sqrt{2}\widehat{\sigma}_{vv,hv}^2\ \widehat{\sigma}_{vv}^2\ \right] \qquad (A.7)$$

A.2. Elementary covariance matrices

The theory of PolSAR target decomposition using the MCSM can be applied to expand the covariance matrix of the PolSAR data collected during microwave imaging of land covers involving both natural and man-made constituents [15–17].

A.2.1. Covariance matrices of the PolSAR backscatter data for elementary types of natural ground covers

The matrices $\hat{C}_s$, $\hat{C}_d$, and $\hat{C}_v$ are the normalized elementary covariance matrices characterizing the backscattering due to single bounce, double bounce, and volume (vegetation), respectively, which may constitute the natural ground covers and can be evaluated using the following approximate analytic expressions:

$$\hat{C}_s = \frac{1}{P_s}\left[\ |\beta|^2\ 0\ \beta\ \ \ 0\ 0\ 0\ \ \ \beta^*\ 0\ 1\ \right],\ \ P_s = 1 + |\beta|^2. \qquad (A.8\text{-a})$$

$$\hat{C}_d = \frac{1}{P_d}\left[\ |\alpha|^2\ 0\ \alpha\ \ \ 0\ 0\ 0\ \ \ \alpha^*\ 0\ 1\ \right],\ \ P_d = 1 + |\alpha|^2. \qquad (A.8\text{-b})$$

$$\hat{C}_v = \frac{1}{P_v}[1\ 0\ 1/3\ 0\ 2/3\ 0\ 1/3\ 0\ 1\,],\quad P_v = \frac{8}{3}, \qquad (A.8\text{-c})$$

where α and β are defined as follows [17]:

$$\alpha = e^{j2\ (\gamma_h - \gamma_v)}\ \frac{\Gamma_{gh}\,\Gamma_{gv}}{\Gamma_{wh}\,\Gamma_{wv}}, \qquad (A.9)$$

where Γ_{gh} and Γ_{gv} are the horizontal and vertical Fresnel reflection coefficients of the ground surface. Similarly, Γ_{wh} and Γ_{wv} are Fresnel reflection coefficients of the horizontal and vertical wall surface. The symbols γ_h and γ_v denote the phase attenuation of the horizontal and vertical electromagnetic waves, respectively.

β is the ratio of the HH backscatter to the VV backscatter of the single-bounce scattering model:

$$\beta = \frac{S_{hh}}{S_{vv}}. \qquad (A.10\text{-a})$$

In the first-order Bragg surface case β is defined as:

$$\beta = \frac{\Gamma_h}{\Gamma_v}, \qquad (A.10\text{-b})$$

where,

$$\Gamma_h = \frac{coscos\ \theta_i - \sqrt{\varepsilon_r - \theta_i}}{coscos\ \theta_i + \sqrt{\varepsilon_r - \theta_i}}, \qquad (A.11\text{-a})$$

$$\Gamma_v = \frac{(\varepsilon_r - 1)\,[\theta_i - \varepsilon_r\,(1 + \theta_i\ )\,]}{\left[\varepsilon_r coscos\ \theta_i + \sqrt{\varepsilon_r - \theta_i}\ \right]^2}, \qquad (A.11\text{-b})$$

where θ_i and ε_r are the incidence angle and the dielectric constant of the surface, respectively.

A.2.2. Covariance matrices of the backscatter from Man-made structures

The matrices $\hat{C}_h$ and $\hat{C}_w$ are the elementary covariance matrices characterizing the helix (rotating) scattering mechanism and wire (edge) scattering mechanism, respectively, which are found in the man-made structures and can be evaluated using the following approximate analytic expressions [17]:

$$\hat{C}_h = \frac{1}{4}\ \left[1\ j^u\sqrt{2}\ -1\ -j^u\sqrt{2}\ 2\ j^u\sqrt{2}\ -1\ ,-j^u\sqrt{2}\ 1\ \right],$$
$$u = \{1,\quad for\ right\ helix\ -1,\ for\ left\ helix\ . \qquad (A.12\text{-a})$$

$$\hat{C}_w = \frac{1}{1 + |\gamma|^2 + 2|\rho|^2}\left[|\gamma|^2\ \sqrt{2}\gamma\rho^*\ \gamma\ \sqrt{2}\gamma^*\rho\ 2|\rho|^2\right.$$
$$\left.\sqrt{2}\rho\ \gamma^*\ \sqrt{2}\rho^*\ 1\ \right], \gamma = \frac{S_{hh}}{S_{vv}},\ \ \rho = \frac{S_{hv}}{S_{vv}}. \qquad (A.12\text{-b})$$

REFERENCES

[1] F. Visconti and J. M. de Paz, “Electrical conductivity measurements in agriculture: the assessment of soil salinity,” Chapter 5, *New Trends and Developments in Metrology*, Intech Open, 2016.

[2] F. Lombardi, M. Lualdi, F. Picetti, P. Bestagini, G. Janszen, and L. A. D. Landro, “Ballistic ground penetrating radar equipment for blast-exposed security applications,” *MDPI Remote Sensing*, vol. 12, 2020.

[3] A. Al-Yaari, J. P. Wigneron, A. Ducharne, Y. H. Kerr, W. Wagner, G. D. Lannoy, R. Reichle, A. Al Bitar, W. Dorigo, P. Richaume, and A. Mialon, “Global-scale comparison of passive (SMOS)

and active (ASCAT) satellite based microwave soil moisture retrievals with soil moisture simulations (MERRA-Land)," *Remote Sensing of Environment,* pp. 614-626, 2014.

[4] W. Zhao and Z. L. Li, "Sensitivity study of soil moisture on the temporal evolution of surface temperature over bare surfaces," *International Journal of Remote Sensing,* vol. 34, pp. 3314-3331, 2013.

[5] K. Das and P. K. Paul, "Present status of soil moisture estimation by microwave remote sensing," *Journal of Cogent Geoscience,* vol. 1, 2015.

[6] R. T. Gharechelou, J. T. S. Sumantyo, and B. A. Johnson, "Soil moisture retrieval using polarimetric SAR data and experimental observations in an arid environment," *ISPRS International Journal of Geo-Information*, vol. 10, no. 10, pp. 711, 2021.

[7] J. Á. Mozos, J. Casalí, M. G. Audícana, and N. E. C. Verhoest, "Correlation between ground measured soil moisture and RADARSAT-1 derived nackscattering coefficient over an agricultural catchment of Navarre (north of Spain)," *Journal of Biosystems Engineering,* vol. 92, no. 1, pp. 119-133, Sep. 2005.

[8] G. Bertoldi, S. D. Chiesa, C. Notarnicola, L. Pasolli, G. Niedrist, and U. Tappeiner, "Estimation of soil moisture patterns in mountain grasslands by means of SAR RADARSAT2 images and hydrological modeling," *Journal of Hydrology*, vol. 516, pp. 245-257, 2014.

[9] S. A. M. Soliman, K. F. A. Hussein, and A. A. Ammar, "Electromagnetic simulation for estimation of forest vertical structure using PolSAR data," *Progress in Electromagnetics Research B (PIER B)*, vol. 90, pp. 129-150, 2021.

[10] D. Poreh, A. Iodice, A. Natale, and D. Riccio, "Software tool for soil surface parameters retrieval from fully polarimetric remotely sensed SAR data," *Sensors*, vol. 20, no. 18, pp. 1-20, 2020.

[11] V. Turkar and Y. S. Rao, "Effect of different target decomposition techniques on classification accuracy for polarimetric SAR data," *Technology Systems and Management Communications in Computer and Information Science*, vol. 145, pp. 138-145, 2011.

[12] M. Riahi and A. Tavangar, "Prognosis of the effects of soil characteristics on the performance of landmine detection in ground-penetrating radar system-a case study," *2nd International Conf. on Technical Inspection and NDT*, 2008.

[13] L. Zhang, B. Zou, H. Cai, and Y. Zhang, "Multiple-component scattering model for polarimetric SAR image decomposition," *IEEE Geoscience and Remote Sensing Letters*, vol. 5, no. 4, pp. 603-607, 2008.

[14] A. Mavrovic, A. Roy, A. Royer, B. Filali, F. Boone, C. Pappas, and O. Sonnentag, "Dielectric characterization of vegetation at L band using an open-ended coaxial probe," *Geosci. Instrum. Method. Data Syst.*, vol. 7, pp. 195-208, 2018.

[15] Y. Yamaguchi, A. Sato, W.-M. Boerner, R. Sato, and H. Yamada, "Four-component scattering power decomposition with rotation of coherency matrix," *IEEE Trans. Geosci. Remote Sens.*, vol. 49, no. 6, pp. 2251-2258, 2011.

[16] A. Freeman and S. L. Durden, "A three-component scattering model for polarimetric SAR data," *IEEE Trans. Geosci. Remote Sens.*, vol. 36, no. 3, pp. 693-973, May 1998.

[17] L. Zhang, B. Zou, H. Cai, and Y. Zhang, "Multiple-component scattering model for polarimetric SAR image decomposition," *IEEE Geoscience and Remote Sensing Letters*, vol. 5, no. 4, 2008.

Mai Z. Ibrahim was born in El-Sharqia, Egypt. She received her B.Sc. in Electronics and Electrical Communication Engineering from the Higher Institute of Engineering in Belbeis in May 2018. She is working currently toward an M.Sc in Synthetic Aperture Radar Image Processing for the Classification of Land Covers at the Faculty of Electronic Engineering, Menoufia University. Her area of research involves radar imagining techniques, remote sensing, and electromagnetic wave propagation.

Ahmed I. M. Bahnacy received his B.Sc. in Radio Communication Engineering, Faculty of Electronic Engineering, Menouf, Egypt, in May 1981. He received an M.Sc degree in Electrical Communications (Antennas), from the Faculty of Engineering, Cairo University, Cairo, Egypt, Nov. 1987. Ph.D. in Electrical Communications (Antennas), Faculty of Electronic Engineering, Menouf, Egypt, in 1993, in collaboration with Robert Gordon Institute of Technology (RGIT), Aberdeen, UK. Lecturer, Dept. of Electronics & Electrical Communications, Faculty of Electronic Engineering, Menouf, 32952, Egypt from 1993-2000. Assoc. Prof., Dept. of Electronics & Electrical Communications, Faculty of Electronic Engineering, Menouf 32952, Egypt since Dec. 2000. From 2001 to 2011, he was with the College of Technology in Tabouk, Saudi Arabia. He went back to his position in Egypt in 2011. In 2018 he became an Emeritus Professor in the same Department.

Khalid F. A. Hussein received his B.Sc., M.Sc., and Ph.D. degrees from the Department of Electronics and Electrical Communications, Faculty of Engineering, Cairo University, in 1990, 1995, and 2001, respectively. He is currently a professor at the Department of Microwave Engineering at the Electronics Research Institute. He has more than 29 years of research experience and more than 20 years of teaching experience in engineering colleges at various universities. He has supervised more than seventy doctoral and master theses. He has published more than 100 papers in international, regional, and local scientific journals and conferences. He has served as Head of the Microwave Engineering Department at the Electronics Research Institute for four years. He has been a member of the Egyptian Space Program (currently the Egyptian Space Agency) for more than eight years. He has worked as Principal Investigator for four research projects and Head of Research Group in four other research projects. He designed and implemented several satellite antennas from prototypes to finished products. He has provided scientific consultations and conducted field measurements related to the design and distribution of mobile communication base station antennas for good signal coverage on behalf of many Egyptian and international companies. His research interests include antennas, electromagnetic wave propagation, risk assessment of human exposure to microwave radiation, optical communications, photonics, quantum computing, radar systems, particularly ground penetrating radar (GPR), synthetic aperture radar (SAR), and remote sensing systems.

Asmaa E. Farahat received her B.Sc. and M.Sc. from the Department of Biomedical Engineering, Faculty of Engineering, Cairo University, in 2002 and 2006, respectively. She received her Ph.D. in 2012 from Ain Shams University. She is currently an Associate Professor at the Department of Microwave Engineering at the Electronics Research Institute. She has approximately 17 years of research experience. She has published more than 35 papers in international, regional, and local scientific journals and conferences. She has worked as a secondary investigator for three research projects. Her research interests include antennas, electromagnetic wave propagation, risk assessment of human exposure to microwave radiation, remote sensing systems, and radars.

A Topological Charge Continuously Tunable Orbital Angular Momentum (OAM) Electromagnetic Wave Generation Method Based on Fixed-length Delay Line Mixing Circuit

Yuliang Zhou[1], Xiaona Li[1], Kaiyuan Yao[1], Yong Mao Huang[2], and Haiyan Jin[1]

[1]School of Aeronautics and Astronautics
University of Electronic Science and Technology of China, Chengdu, China.
uestcjhy@uestc.edu.cn

[2]School of Electrical and Electronic Information
Xihua University, Chengdu, China

***Abstract* –** To overcome the drawback of complex structure and high cost attributed from the utilization of phase shifters to generate OAM in the conventional schemes, this paper proposes a new method for generating OAM based on a fixed delay line. By deriving the proposed system with fixed delay line theoretically, the relationship between the frequency of the input signal on the delay line and the topological charge of the OAM is obtained, and the topological charge of the generated OAM can be controlled by controlling the frequency. Furthermore, this paper proposes a vortex beam pointing control method based on phased array scanning, so as to realize the beam steering of OAM. It is then verified by using electromagnetic simulation, and the simulation results show that the proposed method is feasible. The proposed method not only has the advantages of simple structure and low cost, but also can generate OAM with continuously adjustable topological charge by controlling the frequency, which has the functions of topological charge reconstruction and dynamic adjustment.

***Index Terms* –** beam steering, continuous topological charge, delay line, vortex electromagnetic waves.

I. INTRODUCTION

In recent years, to increase the channel capacity and spectrum utilization, and to make the communication network more reliable and secure, the Orbital Angular Momentum technology [1, 2] has been introduced. The electromagnetic wave-carrying OAM is called vortex electromagnetic wave, and its wavefront phase is different from the plane structure of traditional plane wave due to carrying orbital angular momentum [3]. This feature provides a new direction for increasing information transmission capacity and improving spectral efficiency [4]. It is mentioned in [5] that vortex electromagnetic waves carry information about geometric shapes and material properties. Additionally, the orbital angular momentum multiplexing technology of vortex electromagnetic waves has extremely efficient frequency utilization and anti-interference ability [6], and has good application prospects. The research of vortex electromagnetic waves in optics has been relatively mature. Compared with the great role played by vortex electromagnetic waves in the field of optics, it cannot fully play the role of vortex electromagnetic waves in the field of wireless communication [7].

According to the existing literature, it can be determined that the main methods of generating orbital angular momentum are: helical reflector structure [8], transmission helical structure [9], transmission grating structure [10], and array antenna [11, 12]. At present, the method of using array antennas to excite vortex electromagnetic waves has been widely studied [13], but due to the high cost of phase-shifting devices in the array, it is not conducive to mass production and manufacturing. To reduce the cost of phased arrays that generate vortex electromagnetic waves, international researchers have adopted a variety of methods to reduce the cost of phased arrays, mainly in the following aspects: improving phase-shifting devices [14], reducing the cost of phase-shifters number [15], and make a reasonable array [16], so the related theory of vortex electromagnetic wave is still worthy of in-depth study.

II. GENERATION OF VORTEX ELECTROMAGNETIC WAVES BASED ON A FIXED DELAY LINE

The schematic diagram of the vortex electromagnetic wave generated by the uniform circular array is shown in Fig. 1 [17]. Based on the method of fixed delay line, the phase offset between each array element is controlled, so as to generate continuous topological charge OAM by changing the frequency. However, this

Submitted On: August 4, 2022
Accepted On: September 26, 2022

https://doi.org/10.13052/2022.ACES.J.371007

1054-4887 © ACES

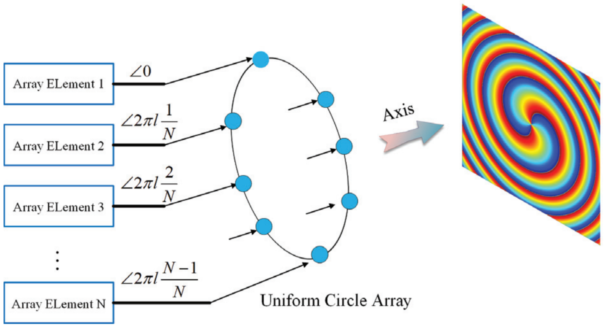

Fig. 1. Schematic diagram of vortex electromagnetic wave generated by uniform circular array.

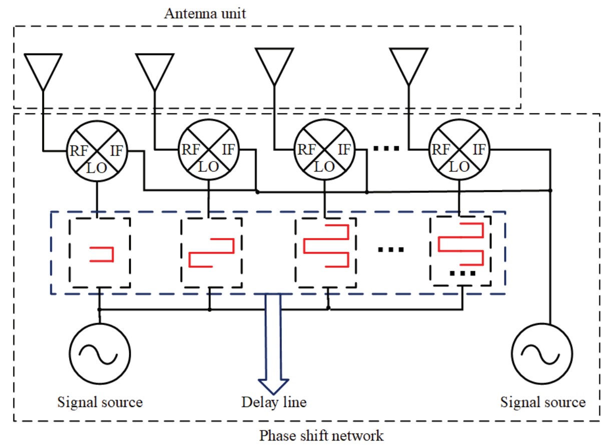

Fig. 2. Phase-shifting network structure based on delay line.

approach causes the beam's transmit frequency to vary with its topological charge. Since most communication systems require a constant transmit frequency, a heterodyne mixer can be added to each antenna element so that the radio frequency (RF) transmit signal appearing at each antenna element is the result of mixing an intermediate frequency (IF) signal and a local oscillator (LO) signal.

Based on the basic principle of the above-mentioned uniform circular array to excite vortex electromagnetic waves, this paper proposes a phase shifter-free vortex electromagnetic wave generation system, which includes a LO signal source and an IF signal source. The output end of the LO signal source is connected to the delay line, which is respectively connected to the input end of the heterodyne mixer. The other input terminal of each heterodyne mixer is connected to the IF signal source. The output terminals of each heterodyne mixer are connected to an one antenna unit and the antenna units are arranged in a circle at equal intervals. The specific schematic diagram is shown in Fig. 2. From Fig. 2, the specific method of exciting the vortex electromagnetic wave is based on the determined antenna element number and the initial vortex electromagnetic wave modulus. The phase shift of the LO signal entering each heterodyne mixer is determined, so as to obtain the length of each delay line. The heterodyne mixer is connected with the LO signal source through the delay line; the LO signal and the IF signal entering into it are mixed through the heterodyne mixer, then each mixed frequency signal is mixed through the antenna unit. The signal is transmitted to complete the generation of the vortex electromagnetic wave. Finally, the vortex electromagnetic wave with continuous topological charge can be obtained by changing the frequency of the LO signal. Accordingly, the relationship between the frequency of the LO signal and the topological charge of the generated vortex electromagnetic wave can be derived.

Set the IF signal and the LO signal:

$$S_{IF} = A\cos(\omega_1 + \psi_1), \tag{1}$$

$$S_{LO} = A\cos(\omega_2 + \psi_2), \tag{2}$$

It is known after mixing the two signals that if the frequency of the LO signal increases by $\delta\omega$, to ensure that the frequency of the output RF signal does not change after mixing, the frequency of the IF signal needs to be reduced by $\delta\omega$. Assuming the length of the delay line is l', according to the phase shift constant of the delay line, the phase shift $\delta\psi$ it can produce is:

$$\delta\psi = l'\omega\sqrt{\varepsilon\mu}, \tag{3}$$

It can be seen from Fig. 2 that if the delay line acts on the LO signal source, the LO will add a phase shift generated by the delay line and combined with Equation (3), namely:

$$S_{LO} = A\cos((\omega_2 + \delta\omega)t + \psi_2 + l'(\omega_2 + \delta\omega)\sqrt{\varepsilon\mu}), \tag{4}$$

The initial phase of the signal source ψ_1, ψ_2 can be set to 0. Assuming that the number of antenna elements is M, to obtain a vortex electromagnetic wave with a topological charge of l, the phase offset required by the mth antenna element $\delta\psi_m$ is:

$$\delta\psi_m = \frac{2lm\pi}{M}, \tag{5}$$

Then according to Equations (3) and (5), the length of the delay line corresponding to the mth antenna unit can be calculated as:

$$l'_m = \frac{2lm\pi}{M\omega_m\sqrt{\varepsilon_m\mu_m}}, \tag{6}$$

where ω_m is the angular frequency of the LO signal entering the m th delay line, ε_m is the dielectric constant of the m th delay line, and μ_m is the permeability of the m th delay line.

The above derivation process and conclusion are under the premise that the number of array elments of the antenna array is large enough, but the number of array elements of the antenna array is an important factor affecting the topological charge of the vortex electromagnetic wave. Although the topological charge number of vortex electromagnetic waves can take any integer value in theory, the maximum number of topological charges that can be generated is determined by the number of array elements of the antenna array that generates vortex electromagnetic waves compared with conventional arrays. The range of topological charges that can be generated by a circular phased array is:

$$-\frac{M}{2} < l < \frac{M}{2}, \tag{7}$$

where M represents the number of elements of the antenna array.When the topological charge l is greater than or equal to M, there will be no pure helical phase wavefront beam generation, which means that no perfect vortex electromagnetic wave can be obtained.

It can be seen from the above derivation that when the length of delay line is fixed, the number of OAM topological charge increases by 1 for every doubling of the signal frequency applied on the delay line. Within the range of OAM topological charges allowed by the number of array elements, the structure can produce OAM with tunable continuous topological charges only by adjusting the frequency.

Based on the uniform circular array with radius A, the number of array elements M is selected as 8, working frequencies of 10 GHz and 4 GHz were selected to conduct electromagnetic simulation. The simulation results are shown in Table 1.

It can be seen from Table 1 that the phase diagrams of electromagnetic waves generated by this method all present the shape of helical phase wavefront, which is a typical feature of vortex electromagnetic waves.The electromagnetic simulation results show that with the increase of the topological charge number, the generated side-lobe of the OAM pattern increases and the zero-depth region increases, indicating that the energy is gradually dispersed with the increase of the topological charge number. Additionally, according to the degree of color alternation, the phase change values of the vortex electromagnetic wave can be obtained respectively as $2\pi, 4\pi$, and 6π, corresponding to the topological charges of OAM being 1, 2 and 3. It further proves the feasibility of the OAM generation method without phase shifter proposed in this paper, and that the method is suitable for different working frequencies.

The above simulation results show that this method can generate relatively ideal vortex electromagnetic waves. Next, the topological charge of the generated vortex electromagnetic waves is fixed at 1, and the array radius and operating frequency parameters are modified. Phase diagrams of vortex electromagnetic waves corresponding to different operating frequencies. Table 2 shows the phase diagram results based on the 8-element uniform circular array. Where, λ_0 is the corresponding wavelength when the operating frequency is 10GHz. As can be seen from the table, the array radius and operating frequency will have a certain impact on the OAM. For a fixed frequency, as the array radius increases, the phase image of the OAM begins to appear phase aliasing; for a fixed radius, as the operating frequency increases, the phase image of the OAM begins to appear phase aliasing. This is because the side lobes of the radiation pattern of the uniform circular array increase, and the vortex electromagnetic wave radiation field is in the state

Table 1: At different frequencies, OAM with l being 1, 2, and 3 corresponds to 3-D Pattern, Amplitude, and Phase diagrams

\		3-D Pattern	Amplitude	Phase
10 GHz	$l=1$	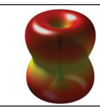	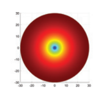	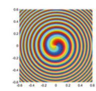
	$l=2$	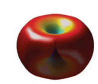	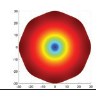	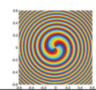
	$l=3$	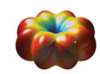	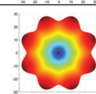	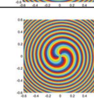
4 GHz	$l=1$	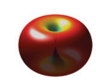	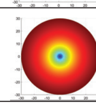	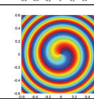
	$l=2$	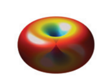	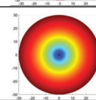	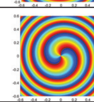
	$l=3$	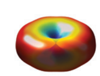	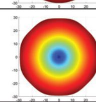	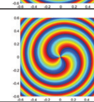

Table 2: Phase distribution of radiation field under different array radius and frequency when M is 8

Radius \ Frequency	$\lambda_0/4$	$2\lambda_0$	$3\lambda_0$
4 GHz	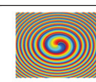	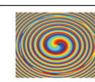	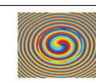
6 GHz	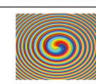	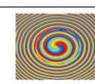	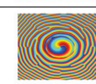
8 GHz	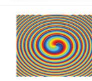	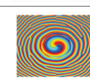	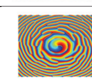
10 GHz	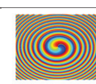	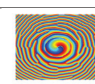	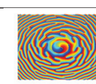

of superposition of the main lobe radiation and the side lobe radiation. When phase aliasing occurs, the vortex electromagnetic wave has not only one OAM mode, but also a superposition of different OAM modes in the main lobe and side lobes. [18] presents an algorithm for vortex beam optimization design that might be needed to optimize the sidelobe level of the vortex beam.

III. GENERATION OF VORTEX ELECTROMAGNETIC WAVES WITH ARBITRARY ORIENTATION BASED ON PHASED ARRAY

To generate a vortex electromagnetic wave with a topological charge number l , the excitation phase of the array element needs an additional phase β_n , which can be expressed as:

$$\beta_n = jl\psi, \tag{8}$$

Therefore, if we want to generate a vortex electromagnetic wave with a topological charge of l and a beam direction of (θ_0, ψ_0), the radiation function of the array is:

$$G(\theta,\psi) = \sum_{n=1}^{N} e^{il\psi_n} e^{jka(\sin\theta\cos(\psi-\psi_n)-\sin\theta_0\cos(\psi_0-\psi_n))}, \tag{9}$$

Setting $u = \sin\theta\cos\psi - \sin\theta_0\cos\psi_0, v = \sin\theta\sin\psi - \sin\theta_0\sin\psi_0 \rho = \sqrt{u^2+v^2}$, $\cos\xi = \frac{u}{\sqrt{u^2+v^2}}$, Equation (9) can be simplified as follows:

$$G(\theta,\psi) = \sum_{n=1}^{N} e^{il\psi_n} e^{jka\rho\cos(\xi-\psi_n)}, \tag{10}$$

Assuming N is infinite, Equation (9) can be rewritten for derivation, and then compared with the Bessel function of order l , the following formula can be obtained:

$$G(\theta,\psi) = Ne^{il\xi} e^{jl\frac{\pi}{2}} j^{ka\rho}, \tag{11}$$

According to Equation (11), OAM can still be generated by uniform circular array after phased control. Set simulation parameters for electromagnetic simulation verification. The uniform circular arrays with 8 elements are simulated respectively. The array radius is set to , and the transmit frequency is set to 10 GHz. The 8-element uniform circular array is simulated to analyze whether the vortex beam generated by the antenna array has a specific direction when the topological charge of the vortex electromagnetic wave is different.

The corresponding vortex electromagnetic wave amplitude and purity simulation diagrams are given in Fig. 3. It can be seen from Fig. 3 that for different pitch angles and different horizontal azimuth angles, the amplitude map can have a given orientation. Additionally, for a uniform circular array with an array element number of 8, when the topological charge of the vortex electromagnetic wave is 1, 2 and 3, the beams all have directions, so the beam direction of the vortex electromagnetic wave is not affected by the topological charge of the vortex electromagnetic wave. Therefore, the proposed method for designing vortex electromagnetic waves with arbitrary radiation patterns is feasible.

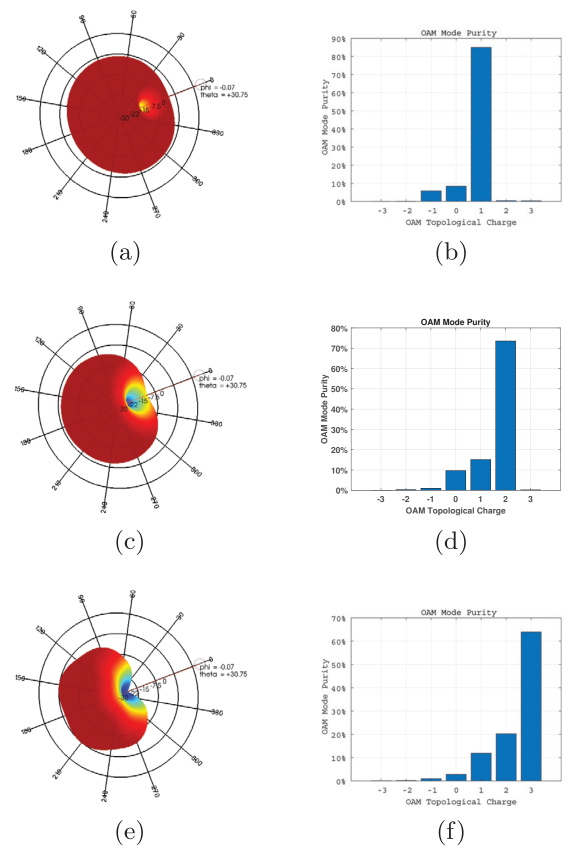

Fig. 3. M is 8, (a), (c), (e) is the amplitude map when L is 1, 2, and 3 respectively and (b), (d), (f) is the amplitude map when L is 1, 2, and 3 respectively.

It can be seen from the purity maps of different topological charge numbers represented by Figs. 3 (d), (e), and (f) that OAM waves with different topological charges still dominate after beam steering, but with the increase of topological charges, the dominant dominance gradually decreases. While the OAM purity decreases, it can be seen that the zero-depth region of the magnitude map relatively increases. This is because the phases of the phased array and the OAM are superimposed on the array antenna at the same time. Although the purity is not as good as before phase control, the main mode still dominates.

IV. CONCLUSION

Due to the high cost and single topological charge of using array antenna for exciting vortex electromagnetic waves, this work developed a novel method to generate vortex electromagnetic waves by using fixed delay line instead of phase shifters. Based on the fundamental theory analyses, it has been concluded that as when the length of the delay line is fixed, the frequency of the delay line is proportional to the topological charge of the vortex electromagnetic wave. Furthermore, the effects of different array radius and different radio frequency on the phase of vortex electromagnetic waves are discussed. For a fixed frequency, with the increase of the array radius, the phase image of OAM begins to appear phase aliasing; for a fixed radius, as the operating frequency increases, the phase image of OAM begins to appear phase aliasing. The propagation direction of the vortex electromagnetic wave generated by the proposed method is generally the axial direction of the vortex electromagnetic wave. However, to make the vortex electromagnetic wave have a specified beam direction, a vortex beam pointing control method based on phased array scanning is proposed. To make the vortex electromagnetic wave generated by the uniform circular array have a specified direction, it is necessary to add a phase varying on the basis of the phase originally required for exciting the vortex electromagnetic wave, so that the phase difference between the two adjacent array elements is related to the direction. Thereby the angles have a specific relationship so that the vortex beam is directed at a specified angle by adjusting the phase difference. Using the delay lines has greatly reduced the critical issue of high cost and complexity of the phase shifter when the vortex electromagnetic wave is generated by conventional uniform circular phased array. An OAM with continuous topological charge can be generated only by adjusting the frequency, which makes the potential application of vortex electromagnetic wave more practical and meaningful.

ACKNOWLEDGMENT

This research was supported by the Sichuan Province Science and Technology Support Program, (No.2022YFS0193) and Fundamental Research Funds for the Central Universities, (No.ZYGX2021YG LH025).

REFERENCES

[1] L. Allen, M. W. Beijersbergen, R. Spreeuw, and J. Woerdman, "Orbital angular momentum of light and the transformation of laguerre-gaussian laser modes," *Physical Review* A, vol. 45, no. 11, pp. 8185, 1992.

[2] L. Allen, M. Padgett, and M. Babiker, "IV the orbital angular momentum of light," *Progress in Optics*, vol. 39, Elsevier, pp. 291-372, 1999.

[3] A. M. Yao and M. J. Padgett, "Orbital angular momentum: origins, behavior and applications," *Advances in Optics and Photonics,* vol. 3, no. 2, pp. 161-204, 2011.

[4] B. Thidé, H. Then, J. Sjöholm, K. Palmer, J. Bergman, T. Carozzi, Y. N. Istomin, N. Ibragimov, and R. Khamitova, "Utilization of photon orbital angular momentum in the low-frequency radio domain," *Physical Review Letters*, vol. 99, no. 8, pp. 087701, 2007.

[5] H.-T. Chen, Z.-Q. Zhang, and J. Yu, "Near-field scattering of typical targets illuminated by vortex electromagnetic waves," *Applied Computational Electromagnetics Society (ACES) Journal,* pp. 129-134, 2020.

[6] A. E. Willner, H. Huang, Y. Yan, Y. Ren, N. Ahmed, G. Xie, C. Bao, L. Li, Y. Cao, Z. Zhao, J. Wang, M. P. J. Lavery, M. Tur, S. Ramachandran, A. F. Molisch, N. Ashrafi, and S. Ashrafi, "Optical communications using orbital angular momentum beams," *Advances in Optics and Photonics*, vol. 7, no. 1, pp. 66-106, 2015.

[7] O. Edfors and A. J. Johansson, "Is orbital angular momentum (oam) based radio communication an unexploited area?," *IEEE Transactions on Antennas and Propagation*, vol. 60, no. 2, pp. 1126-1131, 2011.

[8] Y. Liu, Y. Zheng, Q. Feng, and L. Li, "Orbital angular momentum mode spectrum analysis of multi-uca antenna for generating vortex electromagnetic wave," *International Conference on Microwave and Millimeter Wave Technology (ICMMT)*, IEEE, pp. 1-3, 2018.

[9] V. Vaishnavi, V. Priya, M. Kumar, S. Venkatesh, and S. G. A. Shanmugha, "Simulation of helical modulation in a focal plane array," in: *2014 International Conference on Communication and Signal Processing, IEEE*, pp. 1414-1418, 2014.

[10] F. E. Mahmouli and S. D. Walker, "4-gbps uncompressed video transmission over a 60-ghz orbital angular momentum wireless channel," *IEEE Wireless Communications Letters*, vol. 2, no. 2, pp. 223-226, 2013.

[11] M. Klemes, H. Boutayeb, and F. Hyjazie, "Orbital angular momentum (oam) modes for 2-d beam-steering of circular arrays," *IEEE Canadian Conference on Electrical and Computer Engineering (CCECE)*, IEEE, pp. 1-5, 2016.

[12] H.-T. Chen, R. Pan, W.-Z. Sun, and S.-Y. He, "Microstrip reflectarray for generation of electromagnetic waves with beam vorticity," *Applied Computational Electromagnetics Society (ACES) Journal*, vol. 33, no. 5, pp. 488-493, 2018.

[13] T. Yuan, Y. Cheng, H.-Q. Wang, and Y. Qin, "Generation of oam radio beams with modified uniform

circular array antenna," *Electronics Letters*, vol. 52, no. 11, pp. 896-898, 2016.

[14] J. Rao, G. Trunk, and D. Patel, "Two low-cost phased arrays," *IEEE Aerospace and Electronic Systems Magazine*, vol. 12, no. 6, pp. 39-44, 1997.

[15] B. Avser, J. Pierro, and G. M. Rebeiz, "Random feeding networks for reducing the number of phase shifters in limited-scan arrays," *IEEE Transactions on Antennas and Propagation*, vol. 64, no. 11, pp. 4648-4658, 2016.

[16] D. Ehyaie and A. Mortazawi, "A new approach to design low cost, low complexity phased arrays," *IEEE MTT-S International Microwave Symposium,* IEEE, pp. 1270-1273, 2010.

[17] T. Yuan, Y. Cheng, H. Wang, and Y. Qin, "Beam steering for electromagnetic vortex imaging using uniform circular arrays," *IEEE Antennas and Wireless Propagation Letters*, vol. 16, pp. 704-707, 2016.

[18] Q. Feng, Y. Lin, Y. Zheng, and L. Li, "Vortex beam optimization design of concentric uniform circular array antenna with improved array factor," *Applied Computational Electromagnetics Society (ACES) Journal*, vol. 36, no. 7, pp. 830-837, 2021.

Yuliang Zhou received a B.S. degree in Applied Physics and a Ph.D. degree in Communication and Information Systems from the University of Electronic Science and Technology of China, Chengdu, China, in 2012 and 2020, respectively. Now he is a Post-Doctoral Researcher with the School of Aeronautics and Astronautics, University of Electronic Science and Technology of China. From 2017 to 2018, he was with the Microwave Laboratory, University of Pavia, Pavia, Italy. His current research interests include substrate integrated circuits, leaky-wave antennas, and systems for wireless communication.

Xiaona Li was born in Xinzhou, Shanxi, China, in 1999. She is currently working toward a master's degree in Electronic Information from the University of Electronic Science and Technology of China, Chengdu, China. Her research interests include antennas, radio frequency circuits.

Kaiyuan Yao was born in Dengzhou, Henan, China in 2000 and obtained a degree certificate in Communication Engineering from Southwest Minzu University in 2021. He is currently working toward a master's degree in Traffic and Transportation from the University of Electronic Science and Technology of China, Chengdu, China. His research interests include antennas and radio frequency circuits.

Yong Mao Huang received a B.S. degree in Communication Engineering and a Ph.D. degree in Communication and Information Systems from the University of Electronic Science and Technology of China, Chengdu, China, in 2010 and 2017, respectively. From 2014 to 2015, he was with the Department of Electrical Engineering, University of South Carolina, Columbia, SC, USA. He is currently an Assistant Professor with the School of Electrical Engineering and Electronic Information, Xihua University, Chengdu. He has authored or coauthored over 40 peer-reviewed articles. His current research interests include RF/microwave/millimeter-wave circuits and systems for wireless communication, radar and sensing applications, substrate integrated circuits, and reconfigurable components.

Haiyan Jin received a B.S. degree in Electronic Information Technology and an M.S. and Ph.D. degrees in Electrical Engineering from the University of Electronic Science and Technology of China (UESTC), Chengdu, China, in 2001, 2006, and 2010, respectively. From 2013 to 2014, he was a Post-Doctoral Researcher with the Poly-Grames Research Center, École Polytechnique de Montreal, University of Montreal, Montreal, QC, Canada, where he focused on beam forming antennas. Since 2010, he has been with the School of Information and Communication Engineering, UESTC, where he is currently an Associate Professor. He has authored or coauthored over 50 publications in peer-reviewed journals and international conferences/symposia. His current research interests include the antenna array designs and substrate integrated techniques for microwave and millimeterwave communication systems.

Modeling the Performance Impact of Cubic Macro Cells Used in Additively Manufactured Luneburg Lenses

Brian F. LaRocca[1] and Mark S. Mirotznik[2]

[1]Department of the Army
Aberdeen Proving Ground, Aberdeen, MD 21005, USA
brian.f.larocca.civ@army.mil

[2]Electrical Engineering Department
University of Delaware, Newark, DE 19716, USA
mirotzni@udel.edu

Abstract **–** Finite Element Analysis (FEA) is used to determine the sensitivity of feed placement on a Luneburg lens (LL) having large scale cubic discretization of its permittivity distribution. This is of practical importance for lenses fabricated using additive manufacturing, allowing accurate prediction of performance, and potentially reducing overall print time. It is shown that the far-field relative side lobe level (RSLL) is most sensitive to this form of discretization, and the impact to multi-feed and single-feed applications is considered. It is shown that for single-feed applications, large cubic macro cells are beneficial and provide a RSLL above that achieved with the continuous and non-uniform shelled counterparts.

Index Terms **–** 3D printing, finite element analysis, Luneburg lens, unit cells.

I. INTRODUCTION

While spatially graded dielectrics, also known as graded-index (GRIN) structures, are popular devices in optics and photonics, they have historically been used less frequently at radio frequencies (RF). However, there has been a recent surge of interest in using RF GRIN antennas as low-cost alternatives to phased arrays. One of the most popular RF GRIN structures is the well-known LL [1-4]. The LL is a spherical device in which every point on the surface is the focal point of a plane wave incident from the opposing surface. This unique property is leveraged to realize passive beam steering antennas capable of directing a single or multiple beams over wide scan angles.

While the LL concept has been known for nearly 80 years [1], our ability to reliably manufacture them has been aided by recent advancements in additive manufacturing (AM) technologies and materials. Prior to AM, fabricating a structure with spatially graded dielectric properties was an expensive and challenging manufacturing problem.

Over the last eight years, a host of papers have been published on the use of AM to fabricate the LL and other GRIN devices [5-11]. While these previous studies have demonstrated AM's ability to fabricate functional RF GRIN lenses, what has not been well characterized is the impact of non-spherical discretization larger than a small fraction of a wavelength.

In this paper, a full wave computational study is presented that quantifies the effect of introducing a discretization beyond that of the unit cell scale, in other words, at the macro cell scale. As illustrated in Fig. 1, it considers a cubic macro cell that is comprised of an

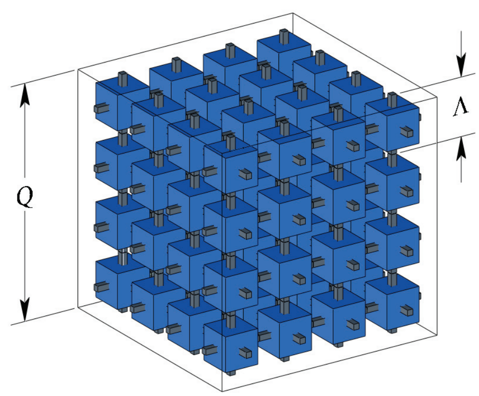

Fig. 1. A macro cell being composed of an integral number of identical unit cells such as depicted in Fig. 2.

integral number of identical unit cells such as that shown in Fig. 2. On the surface of the lens, the cells are allowed to conform to the spherical surface, but otherwise the lens is comprised of identically sized macro cells, each with a permittivity equal to that of the underlying unit

Submitted On: May 25, 2022
Accepted On: September 29, 2022
https://doi.org/10.13052/2022.ACES.J.371008

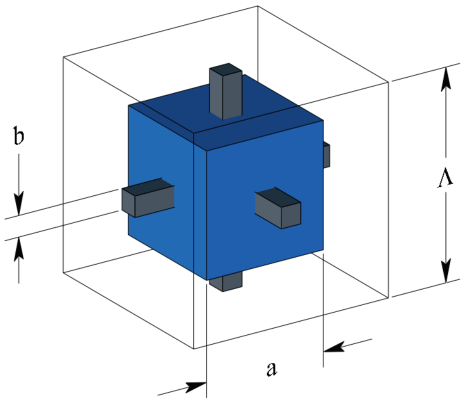

Fig. 2. A typical Unit cell. The effective permittivity of the cell is controlled by manipulating the volume of printed material $\approx a^3$, to the total volume of the cell Λ^3.

cells. Visualizations resulting from this discretization are shown in Fig. 3.

The ability to additively manufacture the sub-wavelength unit cell lattice depicted in Fig. 1 has been successfully demonstrated by the researchers in [7] using the polymer jetting approach. In that research, the authors designed and built a 60 mm radius LL for operation at 10 GHz.

The material used in [7] is a UV-curable acrylic polymer of $\varepsilon_r = 2.7$ with a loss tangent of 0.02. For any given polymer, the authors in [11] determine the maximum useful radius of an additively manufactured LL by applying the constraint that the main beam of the radiation pattern contain at least 50% of accepted power. According to their results, a LL constructed with the polymer used in [7] may only have a maximum useful radius of $\approx 2.5\lambda$. To take advantage of the RSLL improvement that the macro cell quantization affords as shown in Table 1, the AM technique known as Fused Deposition Modeling (FDM) is required, due to the much lower loss of engineering thermoplastics. According to [11], FDM using Polycarbonate can produce a LL with a maximum useful radius of 11λ. The structure in Fig. 1 does require a dual nozzle FDM printer to dispense a support thermoplastic along with the Polycarbonate. Once the heated thermoplastic cools and hardens, the support plastic is flushed from the structure with water.

II. MODELING AND ANALYSIS

A. Simulation and model parameters

The 3D FEA of this research is performed using the COMSOL Multiphysics software [17] equipped with the RF Module. A sketch identifying the components of the physical model, is provided in Fig. 4. Depending upon the stage of analysis, the lens may have a permittivity

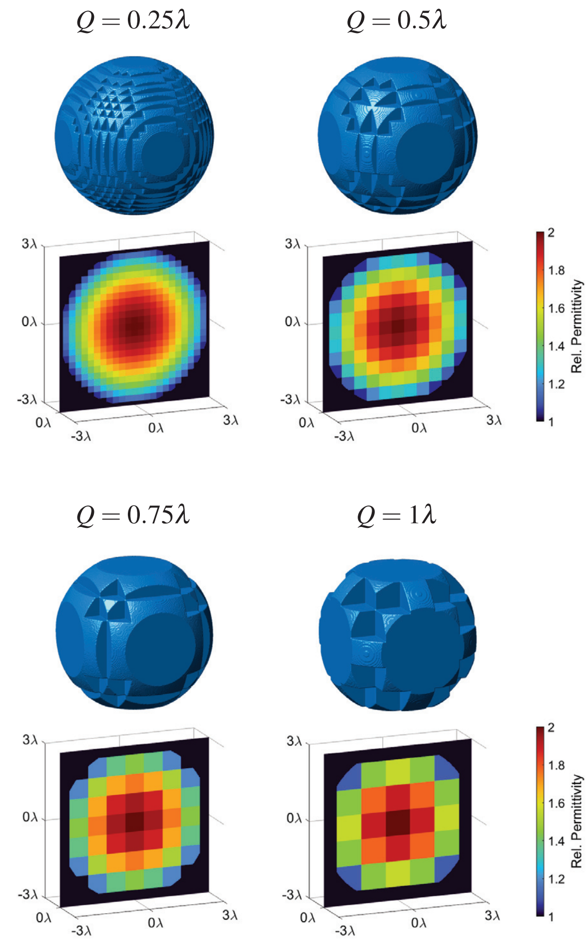

Fig. 3. Visualizations of macro cell LL as the cell edge length Q, is varied from 0.25λ to 1λ. Radius of lens is held constant at 3λ. Below each 3D model is a 2D slice through the center of the lens and colorized to reveal the relative permittivity distribution.

distribution that is either continuous or discretized into spherical layers or macro-cell cubes.

The waveguide feed is modeled as a circular port that matches the EIA WC59 designation with an internal diameter D_p of 0.594 inch. The port height H_p is fixed at 0.25 mm. The lowest order mode for a circular waveguide is TE_{11} followed by TM_{01} [18]. To ensure operation in the TE_{11} mode, the operating frequency f_o is set as follows:

$$f_0 = \sqrt{(f_c)_{11}^{TE} \cdot (f_c)_{01}^{TM}}, \tag{1}$$

where $(f_c)_{11}^{TE} \approx 11.6$ GHz and $(f_c)_{01}^{TM} \approx 15.2$ GHz. The simulation uses $f_0 = 13.3$ GHz yielding a free-space wavelength λ of ≈ 22.5 mm.

A behavioral model is used to implement Left Hand Circular (LHC) polarization for the waveguide feed. This is accomplished by defining two linearly polarized ports

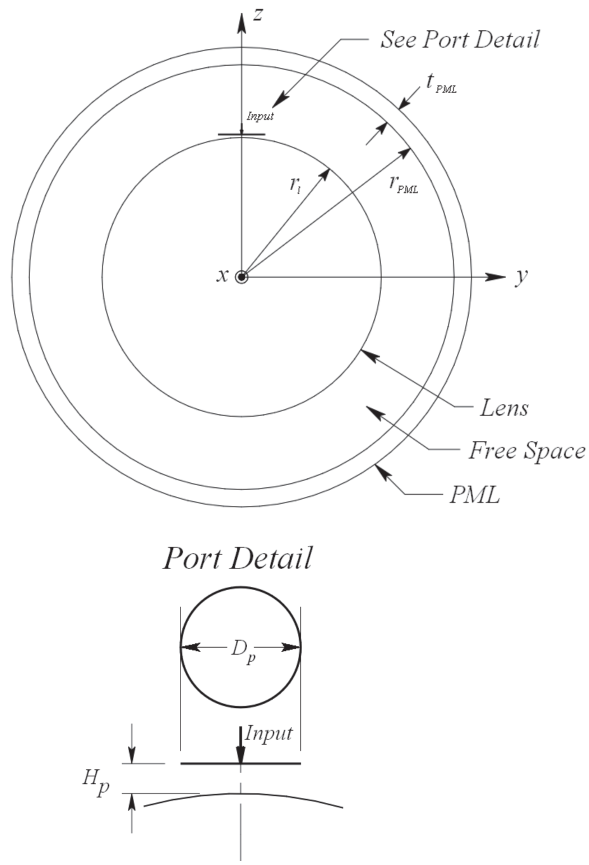

Fig. 4. Sketch of model used for this research consisting of a spherical LL, a circular waveguide feed, and a spherical Perfectly Matched Layer (PML).

on a single circular boundary, each with a polarization axis that is orthogonal to the other. An appropriate 90° phase difference is then applied to ensure counterclockwise field rotation when viewed along the direction of wave travel. The resulting polarization vector is written as:

$$\vec{E}_{LHC} = \frac{1}{E_m}\begin{bmatrix} E_\theta \\ E_\phi \end{bmatrix} = \frac{1}{\sqrt{2}}\begin{bmatrix} 1 \\ j \end{bmatrix}, \tag{2}$$

and $\hat{k} = \hat{\theta} \times \hat{\phi}$, where $\hat{k}$ is the unit propagation vector.

A spherical coordinate system as depicted in Fig. 5 is used throughout. Note that when describing far-field patterns, the radial distance r is irrelevant, and not provided.

B. Quantization of lens permittivity

The LL studied in this paper has a quantized permittivity distribution using what is referred to herein as macro cells. Other than conforming to the spherical lens surface, macro cells are modeled as equal sized dielectric cubes that are homogeneous, isotropic, and lossless. The permittivity throughout a given macro cell is, therefore,

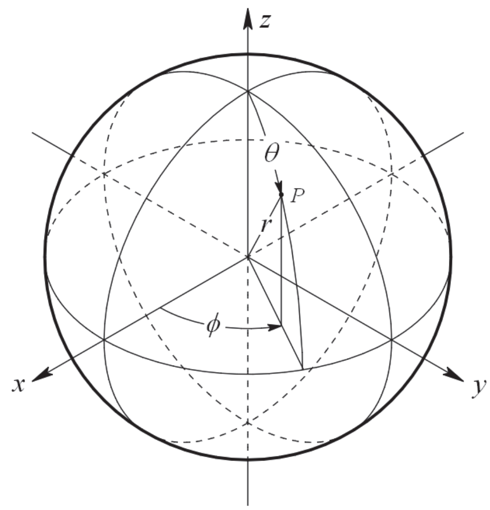

Fig. 5. Spherical coordinate system used throughout.

constant and is specified knowing the center point of the representative cube.

As a matter of convenience, the quantized permittivity distribution throughout the lens is generated indirectly by first mapping the set of Finite Element mesh vertices within the lens to the much smaller set of macro cell center points. Allowing u to represent the x, y, and z coordinates of a given mesh vertex, $\bar{u}$ to represent the corresponding coordinates associated with the center point of the enclosing macro cell, and Q to represent the macro cell edge length, then:

$$\bar{u} = Q \cdot \mathrm{round}\left(u/Q\right), \tag{3}$$

where $\mathrm{round}(\cdot)$ is to be understood as the standard "round to nearest integer" function. Once (3) is used to perform the mapping from mesh vertices to macro cell center points, i.e., $(x,y,z) \longmapsto (\bar{x},\bar{y},\bar{z})$, the relative permittivity is computed using the standard Luneburg equation. We first define the distance between the lens center to any macro cell center point as being $\bar{r} = \sqrt{\bar{x}^2+\bar{y}^2+\bar{z}^2}$. Then, for a lens of radius r_l that is centered at the origin of the mesh coordinate system:

$$\varepsilon_r = \begin{cases} 2-(\bar{r}/r_l)^2 & \text{if: } \bar{r} \leq r_l, \\ 1.0 & \text{otherwise.} \end{cases} \tag{4}$$

The sequential application of (3) then (4) achieve the desired mapping $(x,y,z) \longmapsto \varepsilon_r$. The *if* statement in (4) is necessary since there are always macro cells that protrude through the lens surface and have their center point outside of the lens surface. For these cases, the otherwise clause avoids inadvertently modeling an ε_r less than 1.0.

In Fig. 6, the relative permittivity distribution of a continuous LL is presented along with that of the discretized version. For the lens shown, $r_l = 3\lambda$ and $Q = 0.5\lambda$, where λ is a specified free space wavelength.

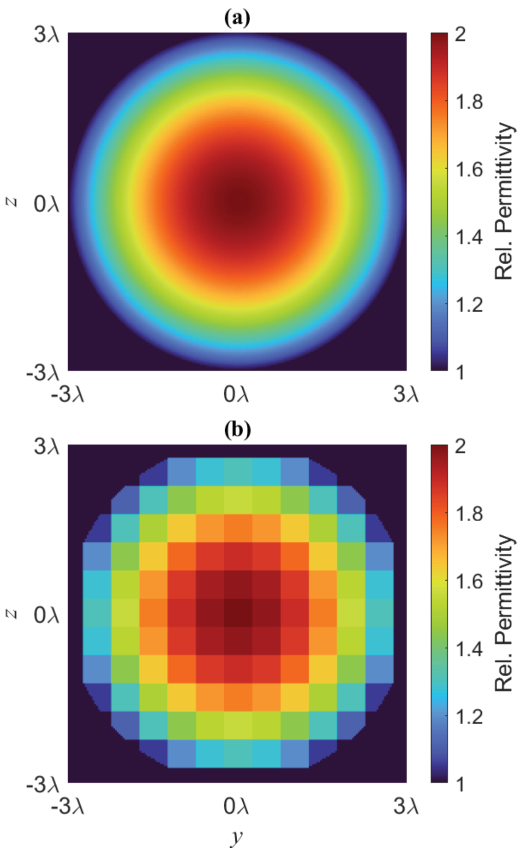

Fig. 6. LL relative permittivity distributions: (a) the continuous version, and in (b) the discrete counterpart.

The effective radius of discrete version along the coordinate axes is shorter than may be expected, and in fact, is equal to $r_l - Q/2$. This is a result of groupings of macro cells having an ε_r equal to that of free space. These can be thought of as virtual cells; thus, time nor material need be expended to produce them. For the lens shown, there are 30 out of 925 total cells that are virtual, i.e., have an $\varepsilon_r = 1$. With reference to the separation between the lens and the feed port in the detail of Fig. 4, H_p is always measured relative to the virtual surface of the LL residing at r_l.

To relate the concept of the macro cell to a fabricable device, we discussed the use of a much smaller subwavelength lattice structure as illustrated in Fig. 1 and Fig. 2. There the dimensions of the lattice are depicted by Λ, where Λ is much smaller than the wavelength, i.e., $\Lambda \ll \lambda$. A 3D array of these smaller structures represents a single macro cell (see Fig. 1) with an effective homogenous permittivity. This is a common approach when fabricating a LL using additive manufacturing methods.

The relationship between the effective permittivity ε_r of the macro cell and the smaller array of sub-wavelength geometries have been described in several of the references including [7] and are determined using effective media theory. Our full wave FEA model and analysis is at the macro cell scale. By doing so reduces the peak memory requirement by a factor of $\approx (\lambda/\Lambda)^3$ and enables meaningful 3D FEA on practical engineering workstations. In fact, the largest LL studied requires a peak memory requirement of $\approx$90 GB using the COMSOL RF module.

C. Far-field parameters

The ideal feed for a continuous LL is a point source placed on the surface of the lens. Furthermore, the radiation pattern of the point source is required to have a cosine shape with its peak oriented towards the center of the lens [16]. When this is the case, the system is said to have an aperture efficiency η_a equal to 1. In this context, η_a is interpreted as:

$$\eta_a = \frac{A_e}{A_l}, \tag{5}$$

where A_e represents the effective or achieved aperture, and A_l is the physical area of the lens aperture, being $\pi\, r_l^2$ [3]. In other words, for the ideal system:

$$A_e = A_l = \pi\, r_l^2. \tag{6}$$

The system gain g is defined as the ratio of A_e to the aperture of an isotropic reference A_{iso}, where:

$$A_{iso} = \frac{\lambda^2}{4\pi}. \tag{7}$$

Thus [3]:

$$g = \frac{A_e}{A_{iso}} = \frac{4\pi}{\lambda^2} A_e. \tag{8}$$

Combining (6) and (8), the boresight gain for a continuous LL with an ideal point source feed is therefore:

$$g = \frac{4\pi^2 r_l^2}{\lambda^2}. \tag{9}$$

In the analysis conducted herein, however, the lens feed is modeled as a circular waveguide. Under this feed condition, the aperture efficiency is less than unity and is dependent upon the effective aperture of the waveguide [16]. We therefore use (5) to write:

$$A_e = \eta_a A_l = \eta_a \pi\, r_l^2, \tag{10}$$

and upon combining (8) and (10), we have:

$$g = \eta_a \cdot \frac{4\pi^2 r_l^2}{\lambda^2}. \tag{11}$$

A range of spherical Luneburg lenses with a continuous permittivity distribution having radii from 1.5λ to 5λ in 0.5λ increments are evaluated. With each near-field solution, the COMSOL RF module generates the corresponding 3D far-field radiation pattern. Afterwards, the pattern is analyzed in MATLAB where gain is extracted, and the Relative Side Lobe Level (RSLL) and Half Power Beam Width (HPBW) are computed. In this research, the RSLL is taken as the difference in decibels between the gain of the main lobe and the highest side lobe [2].

The gain and aperture efficiency, η_a, are plotted versus lens radius in Fig. 7 (a), and the RSLL and HPBW are plotted in Fig. 7 (b). Additionally, the respective gain, RSLL, and HPBW for the ideal point source fed continuous lens is provided in each case. For this purpose, (12) provides the analytical expression of the far-field gain [16], and MATLAB post-processing computes the corresponding RSLL and HPBW. For these calculations, the lens radius is sampled every 0.01λ to ensure the resulting curves are smooth. Moreover, when compared to the ideal point source fed lens, the FEA results show lower gain, a slightly wider beam width and a better RSLL. Note that in (12), $J_1(\cdot)$ represents the Bessel function of the first kind of order one, and k is the free-space phase constant being equal to $2\pi/\lambda$. With the feed point source located at $\theta = 0^{\circ}$, the boresight gain evaluated with (12) is $g(180^{\circ},\phi) = 4\pi^2 r_l^2/\lambda^2$, and this value is identical to that provided earlier in (9).

$$g(\theta,\phi) = \frac{4\pi^2 r_l^2}{\lambda^2}\left[\frac{2\,J_1(kr_l sin(\theta))}{kr_l sin(\theta)}\right]^2. \qquad (12)$$

Examination of Fig. 7 (b) reveals that the RSLL derived from (12) appears to be constant and is therefore independent of the lens radius r_l. Although this result may not be deduced easily from (12), it is explicitly demonstrated for two values of r_l in Fig. 8. The ratio between the lens radius used in Fig. 8 (b) and Fig. 8 (a) is $10:1$. From (9), we therefore expect a 20 dB difference in boresight gains between the two, and this is indeed observed in Fig. 8. However, the RSLL is seen to remain constant at approximately 17.6 dB. Using inductive reasoning, we conclude that the RSLL of (12) is independent of r_l.

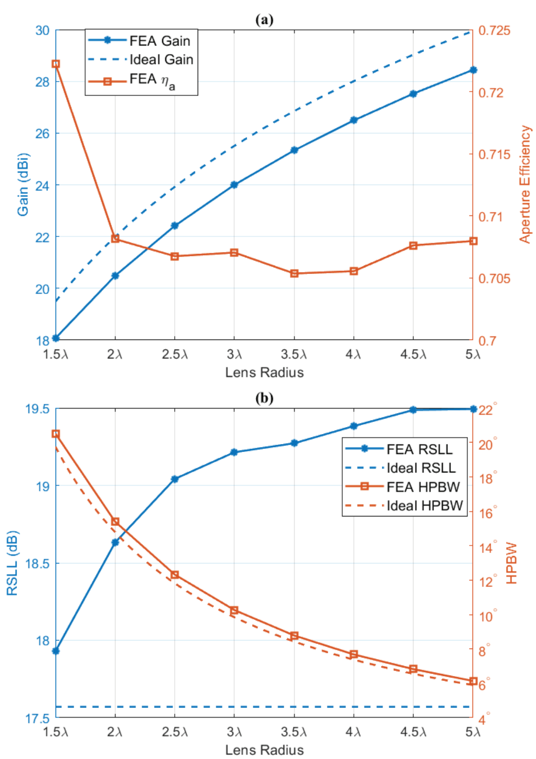

Fig. 7. Continuous LL performance vs lens radius. Solid traces are FEA results and dashed traces are derived from (12).

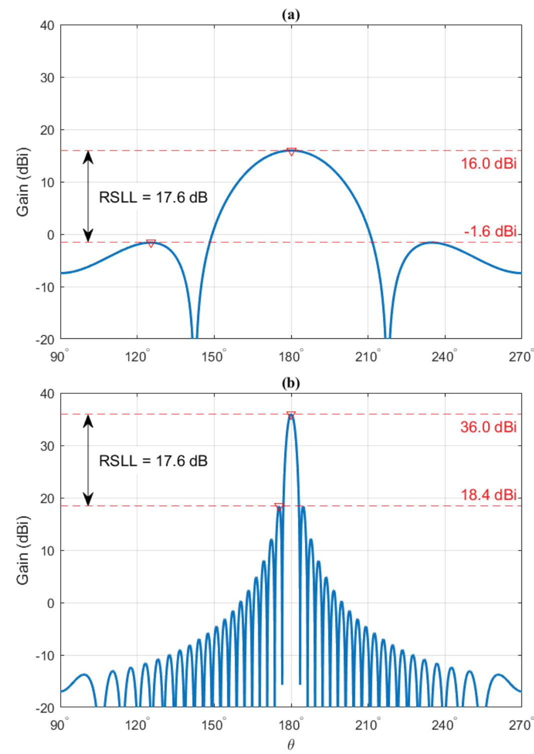

Fig. 8. RSLL measurement of radiation pattern specified by (12). In (a) $r_l = 1\lambda$ and in (b) $r_l = 10\lambda$.

D. Non-uniform shell

The prevalent method of fabricating the LL is to use a layered approach as depicted in Fig. 9. Using this construction method, a spherical dielectric core is surrounded by a series of spherical dielectric shells. The core and surrounding shells are homogeneous, with their respective permittivity and radius chosen to mimic a continuously graded LL. The optimum selection of these parameters proceeds once the number of layers is chosen and includes both closed form expressions [12] and iterative methods [13-15]. The equations of [12] are repeated here as a point of reference. They are simple and yet optimally approximate the continuous LL distribution for a given number of layers.

We begin with the continuous LL permittivity distribution. Using r to represent the radial distance from

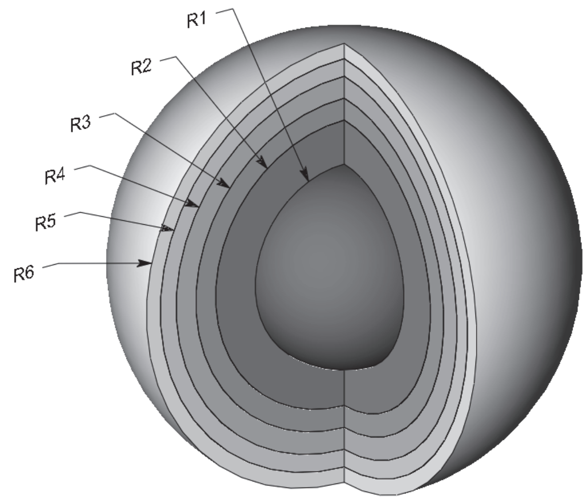

Fig. 9. Example of a multiple layer spherical LL with wedge cut out to expose interior construction. The central core has radius $R1$, and the five surrounding shells have outer radii of $R2$ through $R6$.

the lens center to any point within the lens, and r_l to represent the LL radius, the relative permittivity ε_{LL} at that point is given by:

$$\varepsilon_{LL} = 2 - \left(\frac{r}{r_l}\right)^2. \tag{13}$$

We now number the individual layers from 1 to N, where $n = 1$ corresponds to the core, and $n = N$ corresponds to the outer most layer. From [12], the relative permittivity ε_n of layer n is given by:

$$\varepsilon_n = 2^{(2N-2n+1)/(2N)}, \tag{14}$$

and the outer radius r_n of layer n is given by:

$$\begin{aligned} r_n &= r_l \cdot \sqrt{2 - \sqrt{\varepsilon_n \cdot \varepsilon_{n+1}}}, \\ &= r_l \cdot \sqrt{2 - 2^{(N-n)/N}}. \end{aligned} \tag{15}$$

The effectiveness of (14) and (15) in approximating (13) is demonstrated in Fig. 10 (a) for $N = 6$ and in Fig. 10 (b) for $N = 30$. From these two plots, it is observed that as the magnitude of slope of (13) increases, the layers become thinner and the permittivity contrast between layers decreases.

From Fig. 10, it is obvious that as the number of layers increases, the discrete permittivity profile becomes a better approximation to the continuous LL. However, large N is accompanied by stringent requirements in terms of precision for both layer permittivity ε_n and curvature. It is therefore necessary to select the minimum N at which design goals are still met. As demonstrated by the FEA results shown in Fig. 11, the radiation pattern of a lossless six-layer LL accurately approximates that of the continuous counterpart. In fact, the difference in

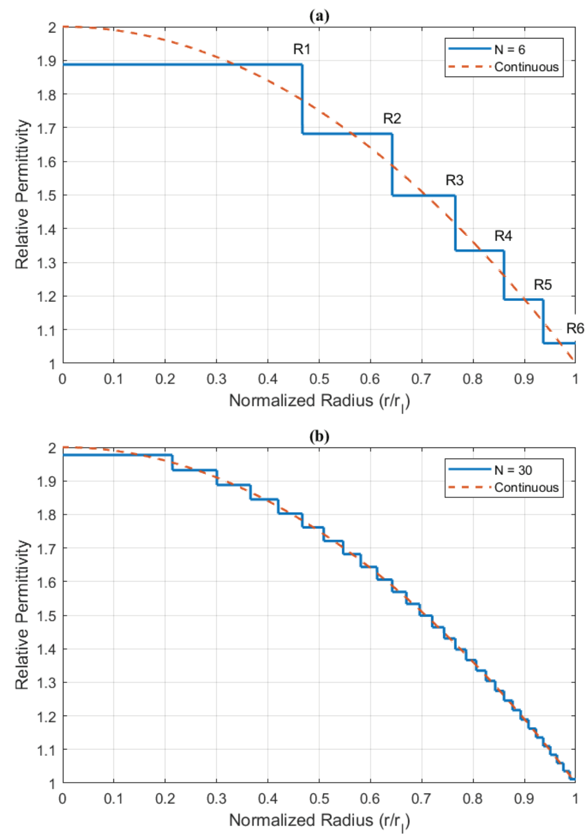

Fig. 10. Optimum layer relative permittivity ε_n versus normalized radius r/r_l for $N = 6$ in (a) and for $N = 30$ in (b). The layer radii $R1$ to $R6$ in (a) correspond to similarly marked layers in Fig. 9.

gain, RSLL, and HPBW between the two are:

$$\begin{aligned} G_6 - G_{LL} &= -0.13\ dB, \\ RSLL_6 - RSLL_{LL} &= -0.66\ dB, \\ HPBW_6 - HPBW_{LL} &= 0^\circ, \end{aligned} \tag{16}$$

where G_6, $RSLL_6$, and $HPBW_6$ refer to the metrics of the six-layer lens, and G_{LL}, $RSLL_{LL}$, and $HPBW_{LL}$ to that of the continuous version. It is not surprising that the performance of $N = 6$ lens is slightly less than the continuous prototype, and given reasonable manufacturing tolerances, increasing the layer count may not be beneficial. Fig. 12 provides insight into why $N = 6$ is a good choice for a layered LL that is designed using (14) and (15). By substituting x for r/r_l in (13) and integrating with respect to x, we derive the area under the continuous LL curve:

$$\begin{aligned} A_{LL} &= \int_0^1 \left(2 - x^2\right) \cdot dx, \\ &= 2 - 1/3, \\ &\approx 1.6667. \end{aligned} \tag{17}$$

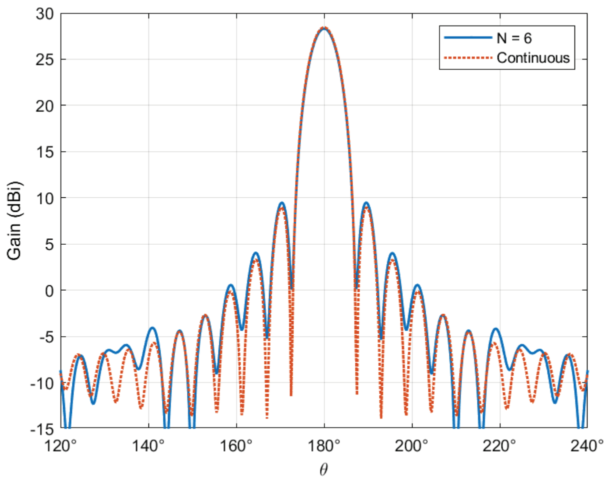

Fig. 11. FEA results providing gain comparison between a 6 layer LL and a continuous LL. Both lenses are modeled with lossless dielectrics and have a lens radius of $r_l = 5\lambda$.

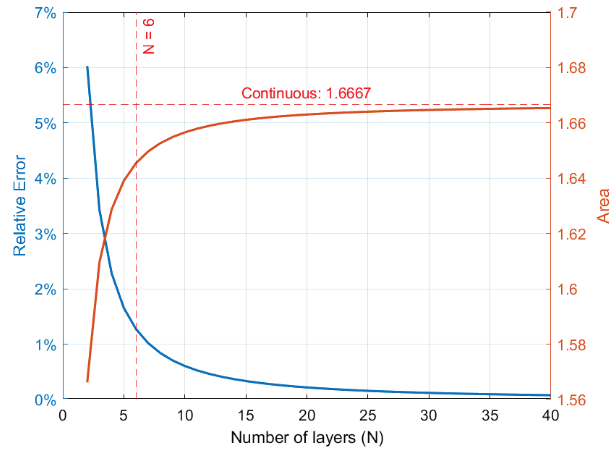

Fig. 12. Area under discrete LL permittivity distribution and the relative error versus the number of layers N.

Conversely, the area under the discrete approximation for a given number of layers N, is obtained using:

$$A_N = \frac{1}{r_l}\sum_{n=1}^{N} \varepsilon_n \cdot (r_n - r_{n-1}). \tag{18}$$

A useful relative error metric between the continuous version of (13) and the discrete N level approximation, can then be defined [12] as:

$$Error_N = 100\% \times \frac{(A_{LL} - A_N)}{A_{LL}}. \tag{19}$$

In Fig. 12, both A_N and $Error_N$ are plotted for $N = 2 \ldots 40$ layers. The constant A_{LL} is plotted as a dashed red horizontal asymptote, and A_N is a solid orange trace that approaches A_{LL} for large N. Referring to the vertical marker at $N = 6$ layers, it is seen that the error increases rapidly to the left and slowly to the right. Depending upon tooling capabilities and material availability, the engineer would probably select a design having $N = 6$ or 7 layers.

The results presented in Fig. 12 for discrete spherical shells agree with previously reported results given in [12-15]. This analysis provides a good baseline to compare results from the cubical macro-cell discretization described in the subsequent sections.

E. Port location sweep

In multibeam applications, antenna feeds are distributed across the lens surface, and it is therefore necessary to ascertain how feed location impacts the far-field radiation pattern. For the case of the spherical shell discretization, presented in the previous section, the radiation patterns are independent of feed location due to symmetry. However, this is not true for the case of the cubical macro-cells shown in Fig. 3.

Assuming feeds are facing the lens and radially directed, feed location is given by the spherical coordinate $(r_l + H_p, \theta_a, \phi_a)$, where the subscript a is used to avoid confusion with far-field coordinates. The port height H_p is fixed at 0.25 mm. The permittivity distribution of a LL with a non-zero macro cell edge length Q, does not contain a strict spherical symmetry. Thus, performance should be expected to depend upon θ_a and ϕ_a. To establish this dependence, FEA is performed on lenses over a range of Q and r_l, while the (θ_a, ϕ_a) of a single waveguide feed is swept. Given the symmetry of the lens, the sweep need only cover $0 \leq \theta_a \leq 90°$ and $0 \leq \phi_a \leq 45°$. An angular resolution of 11.25° is selected, and therefore $9 \times 5 = 45$ separate FEA runs are required to complete a single (Q, r_l) combination. With each run, far-field data is saved to a unique file. The files are post-processed in MATLAB, where boresight gain and Axial Ratio (AR) are extracted, and the RSLL, HPBW, and Polarization Loss Factor (PLF) are computed.

An example RSLL computation over a (θ_a, ϕ_a) sweep for the $(Q = 1\lambda, r_l = 5\lambda)$ lens is shown in Fig. 13. Because of the relatively large value of Q, there is an appreciable spread of values. It is also interesting to note that for $\theta_a = 0°$, $(\theta_a = 90°, \phi_a = 0°)$ and several other feed locations, the lens outperforms the continuous counterpart, i.e., the lens $(Q = 0, r_l = 5\lambda)$. Using the value read from the plot in Fig. 7 (b), this difference is as great as $20.30 - 19.49 = 0.81$ dB.

Lens radius r_l varies from 1.5λ to 5λ in 0.5λ steps, and cell size Q varies from 0.25λ to 1.0λ in 0.25λ steps. In Fig. 14, the lens $(Q = 1\lambda, r_l = 5\lambda)$ is shown along with an overlay of the port grid and the circular port boundary; both drawn to scale. The feed location in this example $(78.75°, 22.5°)$ yields the worst case RSLL for

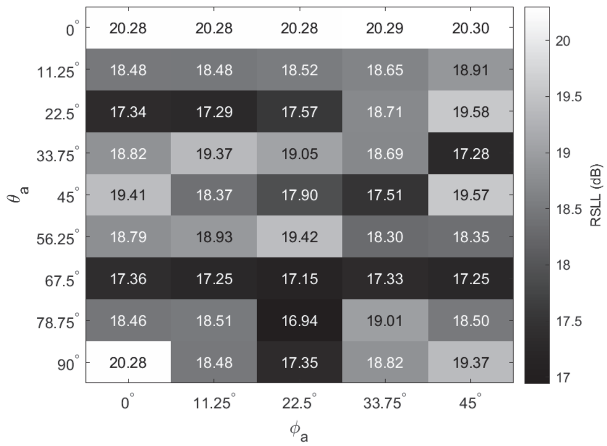

Fig. 13. RSLL matrix for the (θ_a, ϕ_a) sweep of lens $(Q = 1\lambda, r_l = 5\lambda)$. The spread in RSLL is 3.36 dB, however, there are multiple values that are better than that of the continuous reference.

this lens. The radiation pattern for the given port location is also shown.

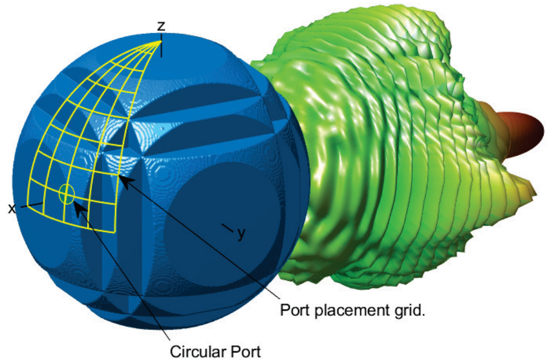

Fig. 14. Port placement is swept over a sector grid suspended above the lens surface.

Considerable axial asymmetry exists in the far-field radiation patterns for lenses with large Q. The RSLL calculation requires that the peak side lobe be identified, and the method employed slices the 3D pattern into a sequence of 2D cuts. In turn, each cut is analyzed in MATLAB using the standard findpeaks() function, with additional code to handle the circular nature of $g(\theta, \phi_{cut})$. The cut with the largest peak side lobe is recorded and used for determination of the RSLL of the pattern overall. A similar procedure is also used to determine the HPBW. An example pattern is shown in Fig. 15.

III. RESULTS

Results are presented as a series of contour plots that describe how the edge length Q of a macro cell impacts the far-field parameters, as the lens radius r_l is varied.

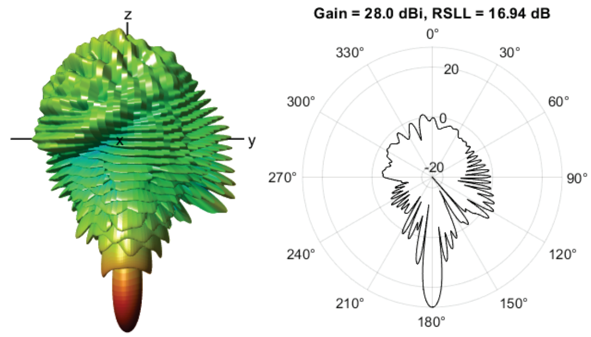

Fig. 15. The RSLL is determined by examining individual 2D cuts through the full 3D radiation pattern. Cuts are taken every 5° and are sampled with a θ resolution of 0.25°. This pattern is for the lens $(Q = 1\lambda, r_l = 5\lambda)$ with feed location of $(\theta_a = 78.75°, \phi = 22.5°)$.

Best- and worst-case results are provided, representing data taken only at the feed location (θ_a, ϕ_a) that produces the respective extremum. Results are shown for the far-field parameters of gain in Fig. 16, RSLL in Fig. 17, AR in Fig. 18, and HPBW in Fig. 19.

For gain and RSLL, the impact of $Q > 0$ is represented as a loss. The worst-case loss is equal to the

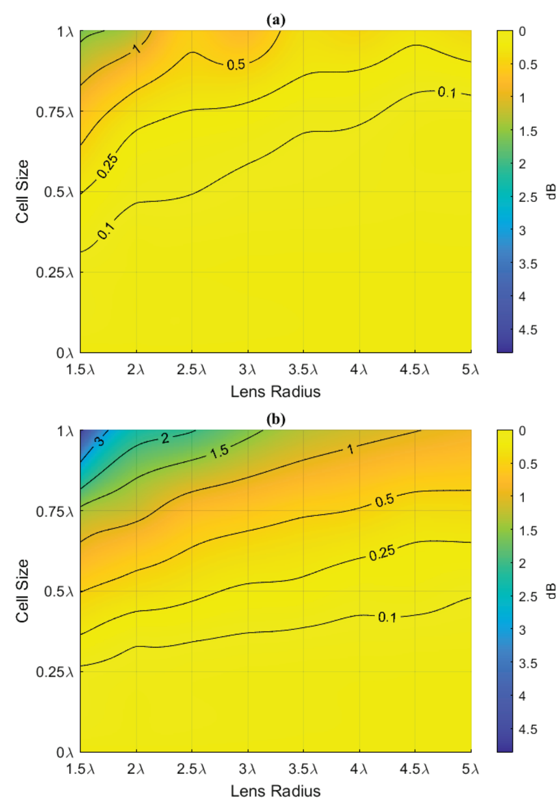

Fig. 16. Loss in gain due to quantization: (a) best case, and in (b) worst case.

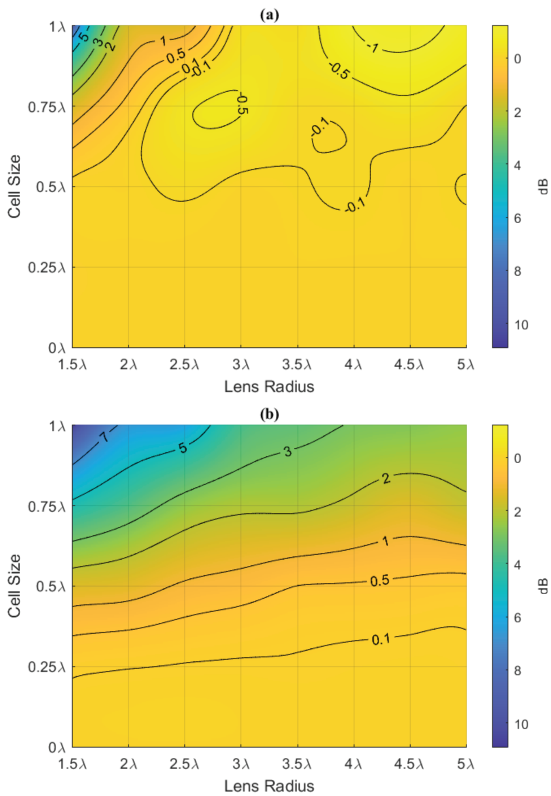

Fig. 17. Loss in RSLL due to quantization: (a) best case, and in (b) worst case. Best case includes areas where loss is negative. This means that the best case RSLL in these areas is better than the continuous counterpart lens.

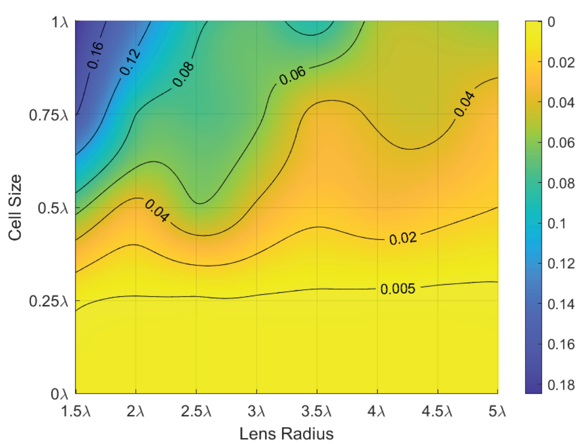

Fig. 18. Worst case increase in AR due to quantization. Best case increase in AR is ≈ 0 for all (Q, r_l) modeled and is not plotted.

gain or RSLL of the counterpart continuous lens, minus the minimum value of the respective (θ_a, ϕ_a) matrix for a given (Q, r_l). The best-case loss is equal to the gain or RSLL of the counterpart continuous lens, minus the maximum value of the respective (θ_a, ϕ_a) matrix for a given (Q, r_l). The gain vs. r_l for the continuous counterpart is shown in Fig. 7 (a) and it's RSLL in Fig. 7 (b).

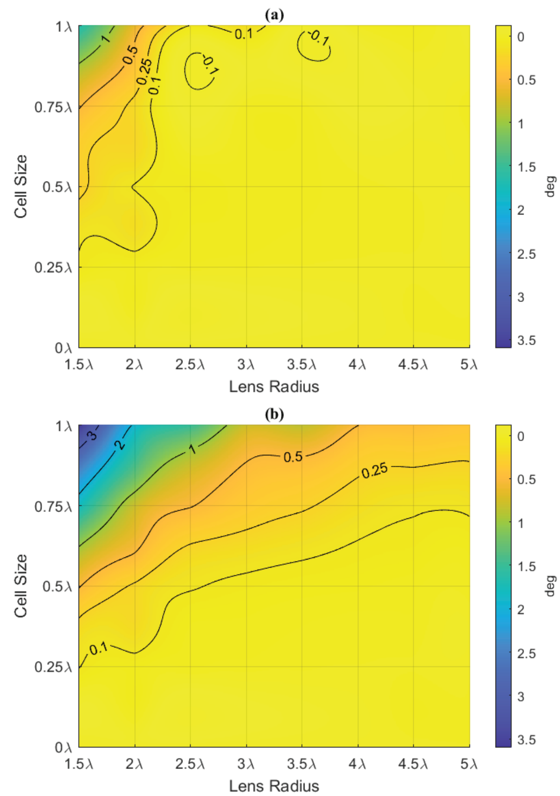

Fig. 19. Increase in HPBW due to quantization: (a) best case, and in (b) worst case. Best case includes an area where increase is slightly negative. This means that the best case HPBW in this area is narrower than the continuous counterpart lens.

For HPBW, the impact of $Q > 0$ is represented as an increase in beam width. The worst-case increase is equal to the maximum value of the HPBW (θ_a, ϕ_a) matrix for a given (Q, r_l), minus the HPBW of the counterpart continuous lens. The HPBW vs. r_l for the continuous counterpart is plotted in Fig. 7 (b). In the case if AR, the impact is just a larger value of AR. It is equal to the maximum value of the AR (θ_a, ϕ_a) matrix for a given (Q, r_l) less unity, since the AR of the continuous counterpart is exactly 1 for LHC polarization. The best-case increase in beam width is equal to the minimum value of the HPBW (θ_a, ϕ_a) matrix for a given (Q, r_l), minus the HPBW of the counterpart continuous lens. The best-case impact to AR is equal to the minimum value of the AR (θ_a, ϕ_a) matrix for a given (Q, r_l) less unity. However, for the range of Q and r_l modeled, the best-case impact to AR ≈ 0, and is therefore not plotted in Fig. 18.

The contour plots in Figs. 16–19 appear to represent the data as continuous values. However, the underlying

(Q, r_l) data is an $m \times n$ array, where m is the number of Q values that have been modeled, and n is the number of r_l values modeled. For the results presented here, $m = 5$ and $n = 8$. To produce the intervening data, the MATLAB curve fitting toolbox is used to smoothly fit a surface to the $m \times n$ available data points. Out of numerous possibilities, the thin-plate spline surface fitter is chosen for this purpose, since it produces a smooth surface and has favorable extrapolation properties [19]. The results shown here do not include extrapolated data.

Moreover, the contour plots are relative to the FEA results for a LL with $Q = 0$. Being relative to the continuous counterpart, these results directly show the impact due to quantization.

IV. DISCUSSION

The results presented in Section III are in terms of best- and worst-case impacts. Both cases are necessary, since the radiation pattern is dependent upon feed position for a LL with $Q > 0$. For multi-feed designs, the results provide the maximum spread in performance metrics over the set of feeds. If a feed pattern is sparse, it may be possible to optimize performance by avoiding certain feed locations. For single-feed designs, the worst-case impacts are ignored, and the feed should be located at an optimum position. In many instances, optimizing the dynamic range is paramount, which implies that the feed placement should optimize the RSLL. As you can see in Fig. 17 (a), this can result in a dynamic range improvement of over 1 dB for a 4.5λ radius lens with $Q = 1\lambda$, relative to the continuous LL.

The best-case feed position (θ_a, ϕ_a), varies with cell size Q and lens radius r_l. A histogram that simply counts the number of times a particular grid position (θ_a, ϕ_a) is the best location modeled is provided in Fig. 20. This histogram only considers the 32 lenses that have a non-zero cell size. Placement at $\theta_a = 0°$ includes 18 occurrences, and thus accounts for approximately 56% the lenses modeled.

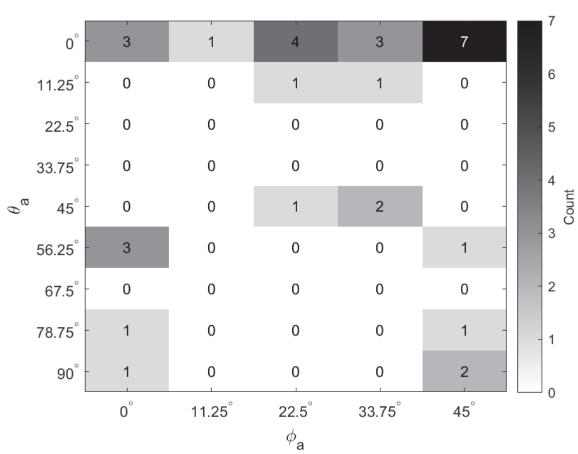

Fig. 20. Histogram of best feed placements.

Table 1 summarizes the quantization impact for a LL having a radius of 5λ. For further context, it includes the 6-layer optimal shell design of Section II.D. Also,

Table 1: Summary of discretization impact for a LL with a radius of 5λ. All values are relative to FEA results for a continuous LL. Negative loss or growth indicates that the impact is beneficial. For each edge length Q, the impacts are shown in two rows: top row is best case, bottom row is worst case

Lens	**Gain Loss (dB)**	**RSLL Loss (dB)**	**HPBW Growth**	**AR Growth**
6 Layer Shell	0.13	0.66	0.03°	0
$Q = 0.25\lambda$	0	0.01	0°	0
	0.01	0.05	0.01°	0
$Q = 0.5\lambda$	0.04	-0.12	0°	0
	0.11	0.34	0.02°	0.02
$Q = 0.75\lambda$	0.05	-0.10	0.02°	0
	0.38	1.83	0.13°	0.03
$Q = 1\lambda$	0.40	-0.81	−0.03°	0
	0.91	2.55	0.40°	0.06

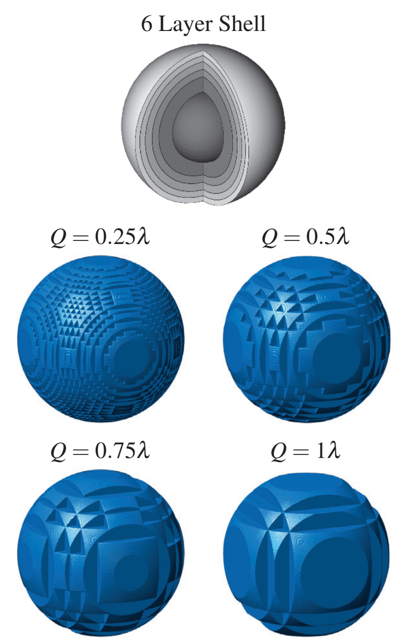

Fig. 21. Discrete versions of LL: non-uniform layered shell and cubic macro cell. Radius of lenses shown is 5λ. Performance of this set of five lenses is summarized in Table 1.

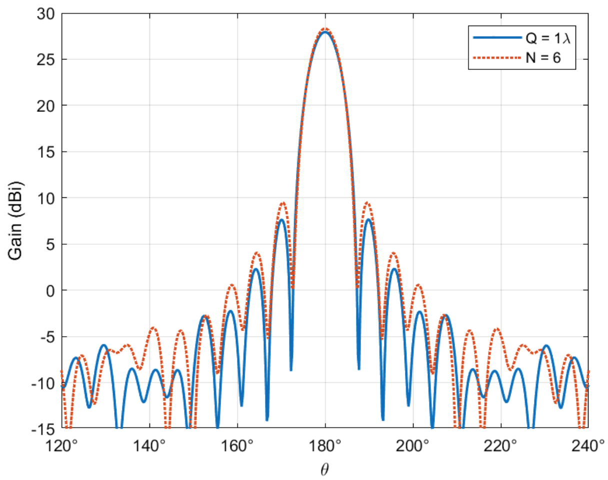

Fig. 22. Comparison of radiation patterns between best case $Q = 1\lambda$ and 6-layer shell LLs. Both lenses have a radius of 5λ. The difference in the RSLL between the two is 1.47 dB.

the five lenses included in this summary are shown in Fig. 21. From Table 1, it is seen that the shell design has similar performance to that of the worst-case $Q = 0.5\lambda$ lens. Thus, for multi-feed applications, the macro cell lens would at worse perform the same as the 6-layer design. For single feed applications, however, the $Q = 1\lambda$ lens provides 1.47 dB increased dynamic range over the 6-layer design. This is demonstrated in Fig. 22, where the radiation pattern of each is juxtaposed.

V. CONCLUSION

The far-field parameters of gain, RSLL, HPBW, and AR are not equally sensitive to the cubic macro cell quantization of the LL permittivity distribution. Observing the worst-case results in Figs. 16–19, a reasonable conclusion is that the ordering from least to greatest sensitivity is: AR, HPBW, gain, then RSLL.

RSLL sensitivity to feed location increases as the macro cell edge length Q is increased. Over the range of r_l investigated, this may limit $Q \leq 0.5\lambda$ for multi-feed applications. In this regard, it is shown that a lens with $r_l = 5\lambda$ and $Q = 0.5\lambda$ has a worst case RSLL that is 0.32 dB better than a similarly sized 6-layer non-uniform shell design. For single-feed use, and depending upon the lens radius, larger macro cells are beneficial and increase RSLL further. It is found that a lens with $r_l = 5\lambda$ and $Q = 1\lambda$ has an RSLL that is 0.81 dB better than a continuous LL and 1.47 dB better than the 6-layer non-uniform shell design.

Moreover, the results presented in Figs. 16–19 condense the effect of feed location on far-field parameter sensitivity into best- and worst-case contour plots. Over the range of Q and r_l investigated, the plots allow for determination as to the severity of performance impact and, therefore, inform decisions regarding the maximum macro cell size that can be tolerated for a given r_l.

REFERENCES

[1] R. K. Luneburg, *Mathematical Theory of Optics*, Brown University Press, Providence, 1944.

[2] B. Edde, *RADAR – Principles, Technology, Applications*, Prentice Hall PTR, New Jersey, 1993.

[3] R.C. Johnson, *Antenna Engineering Handbook*, McGraw-Hill, New York, 1993.

[4] Y. T. Lo and S. W. Lee, *Antenna Handbook - Vol. II Antenna Theory*, Van Nostrand Reinhold, New York, 1993.

[5] C. Babayigit, A. S. Evren, E. Bor, H. Kurt, and M. Turduev, “Analytical, numerical, and experimental investigation of a Luneburg lens system for directional cloaking,” *Phys. Rev.*, A 99, 043831, Apr. 2019.

[6] Z. Larimore, S. Jensen, A. Good, J. Suarez and M. S. Mirotznik, “Additive manufacturing of Luneburg lens antennas using space filling curves and fused filament fabrication,” *IEEE Transactions on Antennas and Propagation*, vol. 66, no. 6, pp. 2818-2827, Jun. 2018.

[7] M. Liang, W. R. Ng, K. Chang, K. Gbele, M. E. Gehm, and H. Xin, “A 3-D Luneburg lens antenna fabricated by polymer jetting rapid prototyping,” *IEEE Transactions on Antennas and Propagation*, vol. 62, no. 4, pp. 1799-1807, Apr. 2014.

[8] C. Wang, J. Wu, and Y. Guo, “A 3-D-printed wideband circularly polarized parallel-plate luneburg lens antenna,” *IEEE Transactions on Antennas and Propagation*, vol. 68, no. 6, Jun. 2020.

[9] S. Lei, K. Han, X. Li, and G. Wei, “A design of broadband 3-D-printed circularly polarized spherical Luneburg lens antenna for X-band,” *IEEE Antennas and Wireless Propagation Letters*, vol. 20, no. 4, Apr. 2021.

[10] B. LaRocca, M. S. Mirotznik, “Modeling the performance impact of anisotropic unit cells used in additively manufactured Luneburg lenses,” *Applied Computational Electromagnetics Society (ACES) Journal*, vol. 37, no. 1, pp. 50-57, 2022.

[11] B. LaRocca, M. S. Mirotznik, “An empirical loss model for an additively manufactured Luneburg lens antenna,” *Applied Computational Electromagnetics Society (ACES) Journal*, vol. 37, no. 5, pp. 554-567, 2022.

[12] C. S. Silitonga, Y. Sugano, H. Sakura, M. Ohki, and S. Kozaki, “Optimum variation of the Luneberg lens for electromagnetic scattering calculations,” *International Journal of Electronics*, vol. 84, no. 6, pp. 625-633, 1998.

[13] H. Mosallaei and Y. Rahmat-Samii, "Nonuniform Luneburg and two-shell lens antennas: Radiation characteristics and design optimization," *IEEE Transactions on Antennas and Propagation*, vol. 49, no. 1, pp. 60-69, Jan. 2001.

[14] B. Fuchs, L. Le Coq, O. Lafond, S. Rondineau, and M. Himdi, "Design optimization of multishell Luneburg lenses," *IEEE Transactions on Antennas and Propagation*, vol. 55, no. 2, pp. 283-289, Feb. 2007.

[15] H. Chou, Y. Chang, H. Huang, Z. Yan, T. Lertwiriyaprapa, and D. Torrungrueng "Optimization of three-dimensional multi-shell dielectric lens antennas to radiate multiple shaped beams for cellular radio coverage," *IEEE Access*, vol. 17, 2019.

[16] G. Guo, Y. Xia, C. Wang, M. Nasir, and Q. Zhu, "Optimal radiation pattern of feed of Luneburg lens for high-gain application," *IEEE Transactions on Antennas and Propagation*, vol. 68, no. 12, pp. 8139-8143, Dec. 2020.

[17] COMSOL Multiphysics® v. 5.6. www.comsol.com. COMSOL AB, Stockholm, Sweden.

[18] O. P. Gandhi, *Microwave Engineering and Applications*, Pergamon Press, New York, 1985.

[19] MATLAB, ver. 2021a, The Mathworks Inc., Natick, Massachusetts, 2021.

Brian F. LaRocca received B.S.E.E and M.S.E.E degrees from New Jersey Institute of Technology, Newark, NJ, USA in 1985 and 2000, respectively. From 1985 to 1996, he worked in industry, from 1996 to 2004 as a government contractor, and from 2004 to present as a civilian engineer with the Dept. of the Army at Ft. Monmouth, NJ, USA and Aberdeen Proving Ground, MD, USA. He received his Ph.D. degree in electrical engineering from the University of Delaware, Newark, DE, USA in the summer of 2022.

Mark S. Mirotznik (S'87–M'92–SM'11) received his B.S.E.E. degree from Bradley University, Peoria, IL, USA, in 1988, and his M.S.E.E. and Ph.D. degrees from the University of Pennsylvania, Philadelphia, PA, USA, in 1991 and 1992, respectively. From 1992 to 2009, he was a Faculty Member with the Department of Electrical Engineering, The Catholic University of America, Washington, DC, USA. Since 2009, he has been a Professor and an Associate Chair for Undergraduate Programs with the Department of Electrical and Computer Engineering, University of Delaware, Newark, DE, USA. He holds the position of Senior Research Engineer with the Naval Surface Warfare Center, Carderock Division. His current research interests include applied electromagnetics and photonics, computational electromagnetics, multifunctional engineered materials, and additive manufacturing.

A Highly Compact Sext-band Bandpass Filter with Simple Structure and Wide Bandwidth

Lei Bai, Yiqi Zhuang, and Zhibin Zeng

School of Microelectronics
Xidian University, Xi'an, 710071, China
bl-cherry@163.com, yqzhuang@xidian.edu.cn, zbzeng@163.com

***Abstract* –** A highly compact sext-band bandpass filter (BPF) is investigated in this paper, which adopts quad-section stepped impedance resonators (SIRs) along with a series of multiple open stubs. This quad-section SIRs are constructed by tri-section SIR loaded L-shaped resonator. To achieve compact size, the filter utilizes tri-section SIR and is embedded in the double L-shaped resonators. A series of multiple open stubs are introduced to improve fractional bandwidth and the return loss. A sext-band BPF centering at 1.12, 2.12, 2.78, 5.59, 6.59 and 8.97 GHz has been designed and fabricated. This highly compact sext-band with wide bandwidth and simple structure is constructed on Rogers 4350 with a dielectric constant of 3.66 and a height of 0.508 mm. The overall size of the fabricated filter is $0.15\lambda_g \times 0.16\lambda_g$. Good agreements are observed between the simulated and measured results.

***Index Terms* –** bandpass filter, open stubs, quad-section stepped impedance resonator(SIR), sext-band.

I. INTRODUCTION

Modern communication systems operate in multiple frequency bands to accommodate different applications, such as global positioning system (GPS), wireless local area network (WLAN), global system for mobile communication (GSM), long term evolution (LTE) channels, C-band satellite communication services (CSCS) and X-band satellite communication services (XSCS) [1]. Multiband bandpass filter (BPF), an indispensable component, is increasingly attracting the attention of design engineers and has been extensively studied in recent years. For designing multiband BPFs, multiple sets of resonators are employed [2, 3]. In [4], a multi-band BPF was designed, which combined a low-pass filter (LPF) with two open stub-loaded shorted stubs. Another tri-band BPF employed two pairs of the open-loop uniform impedance resonators (OLUIRs) with simple structure [5], the circuit size is $0.54\lambda_g \times 0.77\lambda_g$, it occupied a considerable large circuit size. Furthermore, more and more designers pay attention to designing multi-band BPF with more passbands. In [6], a high-selectivity quint-band BPF was constructed based on five tri-mode stub-load stepped-impedance resonators (SIR). Resonators of non-ideal sizes, numbering six or more, have been used for designing sext-band BPF [7] and a sept-band [8] BPFs. To reduce the number of resonators, multi-mode resonators (MMRs) [9]–[11] are frequently employed. The commonly used structures for multi-mode resonators are stub-loaded resonators [12, 13], stepped-impedance resonators [9, 12, 14] and ring resonator [15]. In [14], a quint-wideband BPF was presented, it adopted spiral and open-loop coupled structures with mixed electric and magnetic coupling (MEMC) to reduce design complexity, but the circuit size was relatively large. Sext-band BPFs utilizing cascading stages of SIRs and SIR-loaded tapered lines were reported in [16] and [17]. Although the number of resonators was reduced, the size was relatively large, and the return loss was poor. To realize multiple passbands, multiple modes and transmission zeros (TZs) are used. A single MMR with sept-band characteristics was presented in [18]. In [19], a wideband octa-band BPF was poposed, it utlilized a lowpass filter (LPF) loaded shotted stubs. However these sept-/octa-band BPF adopts one or more via holes. These above reported filters are either complex in structure (multiple via holes or multilayer), large in size or narrow in bandwidth. Therefore, the design of multi-band BPF with simple structure, compact size, and wide fractional bandwidth is a great challenge. In this paper, a highly compact sext-band BPF with compact size, wide bandwidth, and simple structure is presented. This filter adopts quad-section SIRs and multiple open stubs. Owing to the reduction of coupling section, a sext-band BPF design procedure is simple. The designed filter is analyzed by the full-wave electromagnetic (EM) simulation software HFSS. It is fabricated and measured using E5071C to verify the simulated results. The rest of this paper is organized as follow. In section II, the design of sext band filter is detailed and highlighted, which is composed three parts, including analysis of quad-section

Submitted On: December 22, 2021
Accepted On: October 17, 2022
https://doi.org/10.13052/2022.ACES.J.371009

SIRs, optimization of the quad-section SIRs and filter configuration. The simulated and measured results are prsented in section III The conclusion of this paper is drawn in section IV. The proposed filter has a simple structure, a miniature size and a wide bandwidth simultaneously. The passbands generated by the proposed BPF are suitable for GPS, WLAN, and XCSC communications and so on.

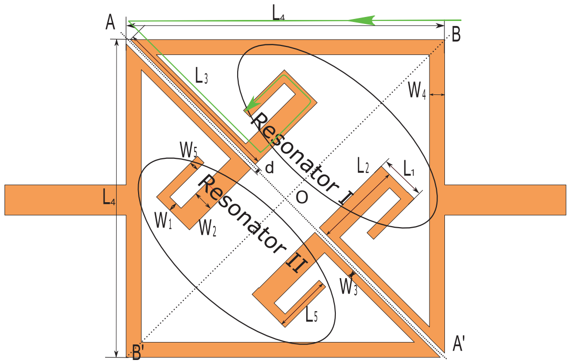

(a)

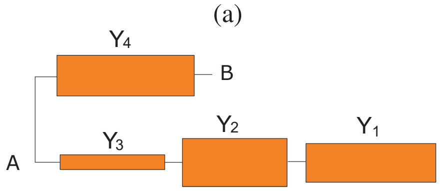

Equivalent transmission line model of quad-section SIR

(b)

Fig. 1. Schematic of quad-section SIRs and equivalent circuit of quad-section SIRs. (a) quad-section SIRs. (b) Equivalent transmission line model of quad-section SIRs.

II. DESIGN OF SEXT-BAND FILTER

A. Analysis of quad-section SIRs

Figure 1 (a) shows the geometry of the quad-section SIRs, which utilize two tri-section SIRs along with L-shaped resonator, so it is defined quad-section SIRs. Among which, resonator I and resonator II are coupled through the coupling gap. The width of the coupling gap is denoted by d. According to Fig. 1 (a), since the structure has a high degree of symmetry and can be seen as four identical parts, we only analyzed the transmission line model for one quarter of the structure (along the direction of the green arrow in Fig. 1 (a), i.e., the triangular AOB). The equivalent transmission line model is given in Fig. 1 (b). The characteristic admittances are Y_1, Y_2, Y_3, and Y_4, respectively, where Y_4 is the folded part consisting of (L_1, W_1) and (L_5, W_5). The corresponding electrical lengths are θ_1, θ_2, θ_3, and θ_4, respectively. The admittance ratios for the four different admittance

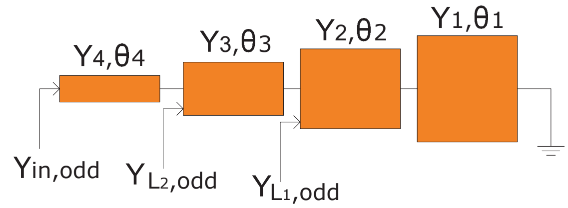

Odd-mode equivalent circuit

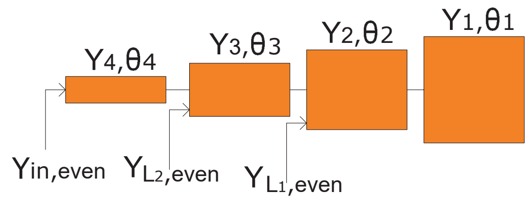

Even-mode equivalent circuit

Fig. 2. Basic odd- and even-mode equivalent circuit of quad-section SIRs.

are related through K_1, K_2 and K_3, where $K_1 = Y_1/Y_2$, $K_2 = Y_2/Y_3$, $K_3 = Y_3/Y_4$. Since the quad-section SIRs are symmetrical in structure, the odd- even-mode method is applied for its analysis and the relevant equivalent circuit is shown in Fig. 2 [20]. The input admittance of the odd-mode and even-mode excitation can be derived as follows.

Odd-mode:

$$Y_{in,odd} = jY_4 \frac{Y_{L_2,odd} + jY_4 tan\theta_4}{Y_3 + jY_{L_2,odd} tan\theta_4}, \tag{1}$$

where

$$Y_{L_2,odd} = jY_3 \frac{Y_{L_1,odd} + jY_3 tan\theta_3}{Y_3 + jY_{L_1,odd} tan\theta_3}, \tag{2}$$

$$Y_{L_1,odd} = jY_2 \frac{Y_2 tan\theta_2 tan\theta_1 - Y_1}{Y_2 tan\theta_1 + Y_1 tan\theta_2}, \tag{3}$$

Even-mode:

$$Y_{in,even} = jY_4 \frac{Y_{L_2,even} + jY_4 tan\theta_4}{Y_3 + jY_{L_2,even} tan\theta_4}, \tag{4}$$

where

$$Y_{L_{2,even}} = jY_3 \frac{Y_{L_1,even} + jY_3 tan\theta_3}{Y_3 + jY_{L_1,even} tan\theta_3}, \tag{5}$$

$$Y_{L_1,even} = -jY_2 \frac{Y_1 tan\theta_1 + Y_2 tan\theta_2}{Y_1 tan\theta_1 tan\theta_2 - Y_2}, \tag{6}$$

for simplicity, assuming $\theta = \theta_1 = \theta_2 = \theta_3 = \theta_4$. By imposing the resonance conditions, the resonance conditions $Y_{in,odd} = 0$ and $Y_{in,even} = 0$, the resonance frequencies of the odd-mode and the even-mode are determined by the respective equation:

$$\begin{aligned} K_2^2 tan^4\theta - (K_1K_2 + K_1^2K_2 + K_1K_2^2 + K_1K_3 \\ + K_1^2K_3 + K_2K_3) tan^2\theta + K_1K_2K_3 = 0, \end{aligned} \tag{7}$$

$$\begin{aligned} K_1K_2K_3 + K_1K_2 + K_1K_3 + K_2K_3 \\ -(K_1K_2^2 + K_2^2K_2 + K_1^2K_3 + K_2^2) tan^2\theta = 0, \end{aligned} \tag{8}$$

from Equation (7) and (8), the center frequency for each passband is simply chosen by adjusting the impedance ratio K_1, K_2, and K_3. The variation of the frequency ratios as a function of the admittance ratios K_1, K_2, and K_3 is shown in Fig. 3. It is pre-selected that the width of the line section (W_1) having the characteristic admittance Y_4 to be 1 mm (which corresponds to 52.3 Ω). In Fig. 3 (a), when K_2 and K_3 are fixed, f_1/f_6, f_2/f_6 and f_4/f_6 remain almost unchanged. The f_3/f_6 slightly reduces and f_5/f_6 greatly increases. When K_1 and K_3 have been fixed, f_1/f_6, f_2/f_6 are almost unchanged, the f_3/f_6 decreases, the f_4/f_6 and f_5/f_6 dramatically decreases (see Fig. 3 (b)). f_1/f_6, f_2/f_6 and f_3/f_6 are almost unchanged while f_4/f_6 and f_5/f_6 gradually increase in Fig. 3 (c). Therefore, by appropriately adjusting the quad-section SIRs, a basic multiple bands could be obtained at desired frequencies. Finally, the admittance ratios are calculated as K_1 = 1.4, K_2 = 0.7 and K_3= 1.2. Choosing characteristic impedance Z_1 = 63.7 Ω, Z_2 = 52.3 Ω, Z_3 = 75.0 Ω and Z_4 = 52.3 Ω.

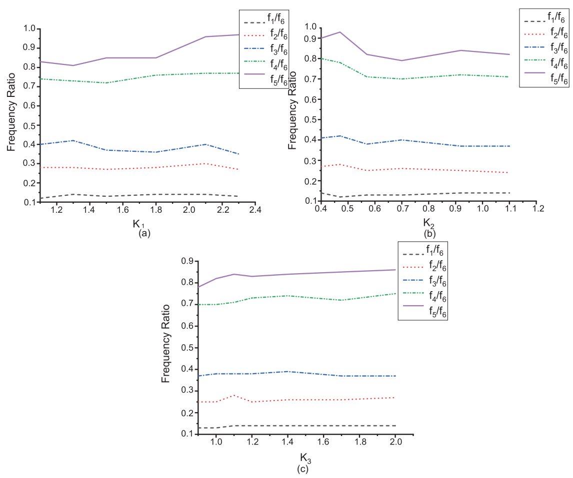

Fig. 3. Frequency characteristics of the proposed quad-section SIRs with varied admittance ratios.

B. Optimization of the quad-section SIRs

Based on the analysis above, the quad-section SIRs can generate the desired frequency bands. The dimensions of the quad-section SIRs (see Fig. 1 a)) are chosen as (all in mm): L_1 = 3.5, L_2 = 5.7, L_3 = 13.1, L_4 = 22, L_5 = 4.1, W_1 = 0.7, W_2 = 1, W_3 = 0.5, W_4 = 1, W_5 = 0.7. As shown in Fig. 4, when multiple open stubs are not loaded, the center frequencies of the quad-section SIRs are at 1.08, 2.12, 2.99, 3.87, 5.77, 6.53, and 7.9 GHz. It should be noted that the forth band is a false band with narrow bandwidth (see Fig. 4 black line). Since the length of the open stub can affect the resonant frequency, when the stub length is longer, the resonant frequency is lower [21]. To merge the false band with other frequency, multiple open stubs are introduced. A series of multiple open stubs are symmetrically loaded on L-shaped. From Fig. 4, with multiple open stubs, the center frequencies

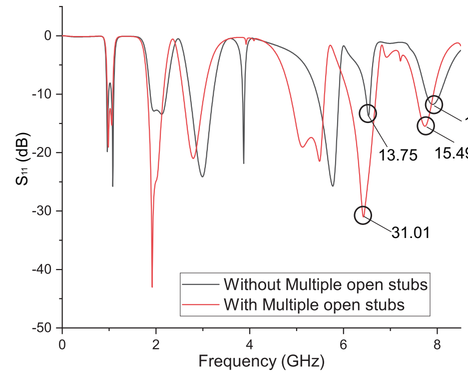

Fig. 4. The simulated S_{11} of the quad-section SIRs and loaded multiple stubs.

are at 0.98, 1.92, 2.79, 5.13, 6.42, and 7.74 GHz. Furthermore, loading open stubs can increase the bandwidth and improve the return loss. Their 3-dB fractional bandwidth are 19.4, 26.4, 26, 3.6, 18, 8.4, and 11.9% without open stubs, but the fractional bandwidth are 17.3, 27.1, 28.3, 21.6, 15.3, and 13% with open stubs, respectively. In addition, the first passband characteristic is better than the quad-section SIRs. The return loss of fifth and sixth bands are also clearly superior to the former.The return loss up to 31.01 dB after loading multiple open stubs in fifth passband compares to 13.75 dB before loading. The return loss in sixth passband are 15.49 dB and 11.76 dB, respectively.

Figure 5 shows the S-parameter varies from coupling gap. The first three center frequencies are constant, the sixth band slightly change and the forth and fifth bands obviously change. It can be obtained from Fig. 5 (a) that with the coupling gap from 0.075 to 0.125 mm, the forth and fifth bands from 5.03 to 5.49 GHz, from 6.08 to 6.4 GHz, respectively. When d from 0.075 to 0.125 mm, the return loss of the fifith passband can reach -30 dB. Furthermore, the minimal variation in insertion loss between fifth and sixth passband is shown in Fig. 5 (b). Finally, the proposed sext-band BPF is constructed by the quad-section SIRs and multiple open stubs, which is easy to build. Consequently, a sext-band with simple structure and wide fractional bandwidth is obtained. Additionally, the designed BPF has only two resonators and one coupling gap.

C. Filter Configuration

To verify the practicability of the proposed quad-section SIRs, a sext-band BPF, adopting quad-section SIRs along with a series of multiple open stubs is designed. The geometric configuration is shown in Fig. 6. In quad-section SIRs, double L-shaped resonators are symmetrically distributed on the outside and coupled into as quare structure, while the tri-section SIRs are embedded inside and loaded in the double L-shaped

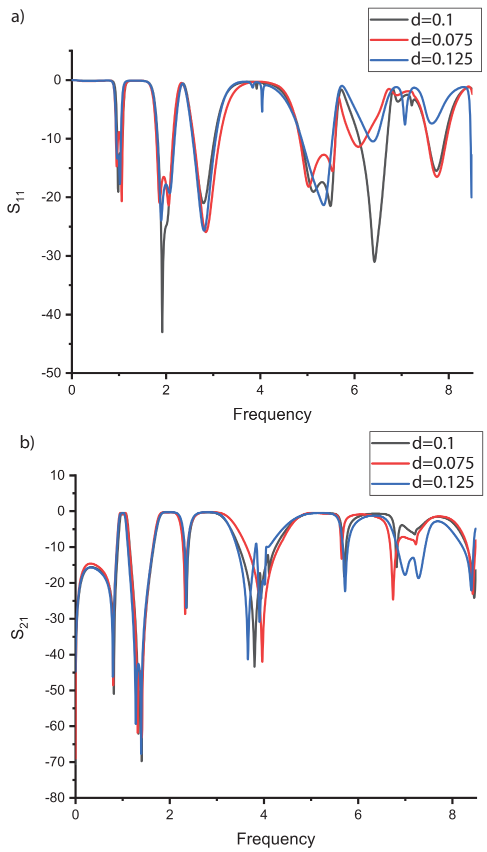

Fig. 5. The simulated S-parameters (S_{11} and S_{21}) of coupling gap.

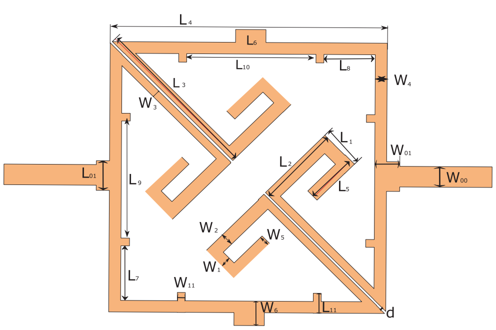

Fig. 6. Layout of designed sext-band BPF.

resonator. The quad-section SIRs can generate the desired passbands. In addition, a series of multiple open stubs are loaded on the L-shape resonators. These multiple open stubs are introduced to improve the bandwidth and return loss. In a multi-band BPF, the coupling is a significant factor that can increase the insertion loss and the return loss. Compared with other multi-band BPFs, the proposed BPF has only two resonators (Resnoator I and Resonator II) and no via hole that can greatly reduces its complexity and fabricated cost [14].

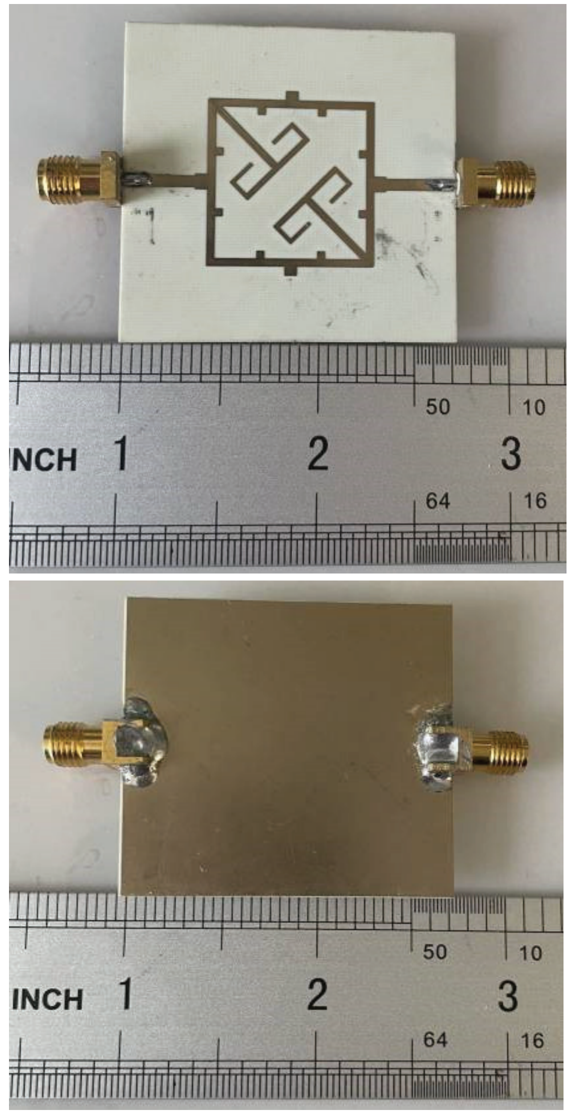

Fig. 7. Photograph of the proposed sext-band BPF.

III. SIMULATED AND MEASURED RESULTS

The proposed sext-band BPF is fabricated on a 0.508 mm thick Rogers RO4350 substrate with a dielectric constant of 3.66 and a loss tangent of 0.004. Figure 7 shows the photograph of fabricatred filter. The dimensions of the design optimized utilizing the Ansoft HFSS 15.0 are (millimeters): L_{01} = 2, L_1 = 3.5, L_2 = 5.7, L_3 = 13.1, L_4 = 22, L_5 = 4.1, L_6 = 1.6, L_7 = 6.5, L_8 = 6.5, L_9 = 7, L_{10} = 7, L_{11} = 2, W_{00} = 1.5, W_{01} = 2.6, W_1 = 0.7, W_2 = 1, W_3 = 0.5, W_4 = 1, W_5 = 0.7, W_6 = 2.2, W_{11} = 1, d = 0.1. Simulated and measured results of the designed filter are shown in Fig. 8. The measured centre frequencies are located at 1.12, 2.12, 2.78, 5.59, 6.59, and 7.97 GHz. Their 3-dB fractional bandwidths are 12.5, 26.4,

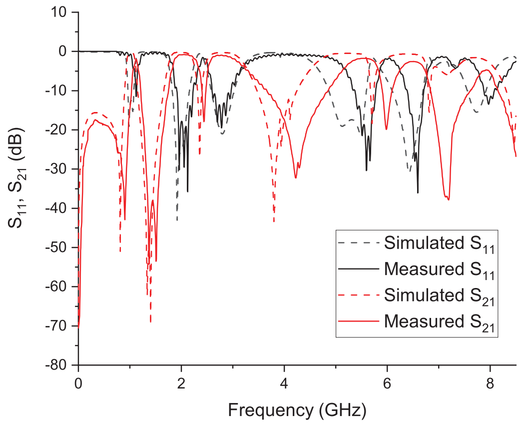

Fig. 8. Simulated and measured results.

27.0, 15.4, 10.5, and 9.8 %, respectively. The filter return losses are 11.5, 35.8, 19.5, 30.4, 36.1, and 13.5 dB. The filter size is 24.4 mm × 25.2 mm, which amounts to $0.15\lambda_g \times 0.16\lambda_g$, where λ_g is the guided wavelength on the substrate at the center of the first passband. The minor difference between the simulated and the measured results is due to production deficiency, connector losses and imperfection of the substrate.

The performance of the proposed sext-band is compared with other works, and a summary is given in Table 1. From Table 1, as in the literature [7, 16, 17], the filter proposed in this paper also generates 6 passbands, but has a wider fractional bandwidth. For example, all bandwidths in this paper are more than 10% higher than the corresponding bandwidths in the literature [7]. The fractional bandwidth also reaches 26.4%, which is much higher than the bandwidth of the second band in the other two literature. Moreover, the size of the proposed filters were reduced by 16.7% and 29.4%, respectively, compared to the literature [16, 17]. Compared to the literature [18], the presented work has a wider bandwidth even though their circuit sizes are approximately the same. Table 2 summarizes the comparison between the proposed filter and the recently proposed couterparts designed structure. The filter design proposed in this paper is simple, has low manufacturing cost, but is still able to produce more passbands while using fewer resonators and no via holes.

IV. CONCLUSION

This letter proposed a sext-band BPF aimed at large fractional bandwidth, highly compact size, and simple structure. The designed BPF adopts quad-section SIRs along with multiple open stubs, The quad-section SIRs utilize two tri-section stepped impedance resonators loaded double L-shaped resonators to achieve enough multi-band, and a series of multiple open stubs loaded double L-shaped resonators are added to improve the fractional bandwidth and return loss. The fabricated sext-band BPF's center frequencies are at 1.12, 2.12, 2.78, 5.59, 6.59, and 7.97 GHz. This makes it suitable for GPS, WLAN, CSCS and XSCS applications. Owing to these

Table 1: Comparisons with the other multi-band BPFs

Ref	ε_r	CFs(GHz)/ FBW(%)	Size ($\lambda_g \times \lambda_g$)
[7]	3.55	0.9/1.5 1.2/1.3 1.4/1.4 1.7/1.3 2/1.5 2.4/1.4	0.26 × 0.15
[16]	3.66	1.56/17.9 3.17/13.2 4.68/29 6.02/7.14 8.21/8.04 9.06/7.28	0.18 × 0.16
[17]	3.5	1.7/19.4 3.48/9.2 5.08/30 6.5/6.7 8.66/10.2 10.18/13	0.2 × 0.17
[18]	2.2	1/13 1.6/10.2 2.3/15.9 2.8/6.8 3.5/9.4 4.2/3 5/4.6	0.21 × 0.1
This work	3.66	1.12/12.5 2.12/26.4 2.78/27 5.59/15.4 6.59/10.5 7.97/9.8	0.15 × 0.16

Table 2: Comparisons with the other multi-band BPFs

Ref	NR	NB	Structure	Via Hole
[7]	6	6	SIRs	6 via hole
[8]	8	7	SL-SIR	4 via hole
[10]	2	5	MMR+open stubs	none
[18]	1	7	a single MMR	5 via hole
[19]	NA	8	short stubs+LPF	1 via hole
This work	2	6	quad-section SIRs+ open stubs	none

NA = not available; NR = number of resonators

NB = number of passbands

merits, it becomes a good choice for achieving sext-band bandpass characteristics.

ACKNOWLEDGMENTS

This work was supported in part by the National Natural Science Foundation of Shaanxi Province under Grant NO.2019KW-057 and 111 project.

REFERENCES

[1] Y. Zhang, L. Gao, and X. Y. Zhang, "Compact quad-band bandpass filter for DCS/WLAN/ WiMAX/5G Wi-Fi application," *IEEE Microwave Wireless Component Letter*, vol. 25, no. 10, pp. 645-647, Aug. 2015

[2] Y. Wu, L. Cui, Z. Zheng, W. Wang, and Y. Liu, "A simple planar dual-band bandpass filter with multiple transmission Poles and zeros," *Circuits and Systems II: Express Briefs*, vol. 65, no. 1, pp. 56-60, Jan. 2018.

[3] R. Gomez-Garcia, R. Loeches-Sanchez, D. Psychogiou, and D. Peroulis, "Multi-stub-loaded differential-mode planar multiband bandpass filters," *Circuits and Systems II: Express Briefs*, vol. 65, no. 3, pp. 271-275, Mar. 2018.

[4] Q. Yang, Y.-C. Jiao, and Z. Zhang, "Compact multiband bandpass filter using low-pass filter combined with open stub-loaded shorted stub," *IEEE Transactions on Microwave Theory and Techniques*, vol. 66, no. 4, pp. 1926-1938, Apr. 2018.

[5] M.-H. Weng, C.-W. Hsu, Y. Lin, C.-Y. Tsai, and R.-Y. Yang, "A simple method to design a tribandpass filter using open-loop uniform impedance resonators," *Journal of Electromagnetic Waves and Applications*, vol. 34, no. 1, pp. 103-115, Nov. 2019.

[6] C.-F. Chen, "Design of a compact microstrip quintband filter based on the tri-mode stub-loaded stepped-impedance resonators," *IEEE Microwave and Wireless Components Letters* , vol. 22, no. 7, pp. 357-359, Jul. 2012.

[7] K.-W. Hsu, J.-H. Lin, and W.-H. Tu, "Compact sext-band bandpass filter with sharp rejection response," *IEEE Microwave and Wireless Components Letters*, vol. 24, no. 9, pp. 593-595, Sep. 2014.

[8] C.-F. Chen, S.-F. Chang, and B.-H. Tseng, "Design of compact microstrip sept-band bandpass filter with flexible passband allocation," *IEEE Microwave and Wireless Components Letters*, vol. 24, no. 9, pp. 346-348, May 2016.

[9] D. Bukuru, K. Song, F. Zhang, Y. Zhu, and M. Fan, "Compact quad-band bandpass filter using quad-mode stepped impedance resonator and multiple coupling circuits," *IEEE Transactions on Microwave Theory and Techniques*, vol. 65, no. 3, pp. 783-791, Mar. 2017.

[10] X. Li, Y. Zhang, X. Zhang, L. Qu, and Y. Fan, "Compact quint-band Bandpass Filter design in a rigorous manner utilizing multimode stub-loaded taper," *Microwave and Optical Technology Letters*, vol. 60, no. 5, pp. 1230-1234, May 2018.

[11] B.-H. Zhu, Z. Wang, E. Kim, and N. Kim, "A quad-band bandpass filter using sept-mode double square-ring loaded resonator," *Microwave and Optical Technology Letters*, vol. 62, no. 5, pp. 1906-1913, May 2020.

[12] F. Wei, P.-Y. Qin, Y. Jay Guo, and X.-W. Shi, "Design of multi-band bandpass filters based on stub loaded stepped-impedance resonator with defected microstrip structure," *IET Microwaves, Antennas and Propagation*, vol. 10, no. 2, pp. 230-236, Jan. 2016.

[13] X. Kai-Da and Z. Fengyu, "High selectivity bandpass filter using three pairs of coupled lines loaded with shorted stubs," *Applied Computational Electromagnetics Society (ACES) Journal*, vol. 34, no. 10, pp.469-474, 2019.

[14] I. A. Yasir, Y. Tu, O.-P. Naser, I. T. E. Elfergani, A.-A. Raed, R. Jonathan, and J. M. Noras, "Mixed-coupling multi-function quint-wideband asymmetric stepped impedance resonator filter," *Microwave and Optical Technology Letters*, vol. 61, no. 5, pp. 1181-1184, May 2019.

[15] D. K. Choudhary and R. K. Chaudhary, "Miniaturized quad-band filter with improved selectivity using split ring resonators and metallic strips," *International Journal of RF and Microwave Computer-Aided Engineering*, vol. 31, no. 10, pp. 1-9, Oct. 2021.

[16] X. Li, Y. Zhang, Y. Tang, J. Xu, and Y. Fan, "Sext-band bandpass filter with compactness based on cascading stage of SIRs," *Microwave and Optical Technology Letters*, vol. 60, no. 2, pp. 306-310, Feb. 2018.

[17] X. Li, Y. Zhang, Y. Tian, Y. Yang, and Y. Fan, "Quad- and sext-band bandpass filter based on multimode resonator utilizing SIRs-loaded tapered-line," *Microwave and Optical Technology Letters*, vol. 60, no. 2, pp. 650-654, Feb. 2018.

[18] X. Bi, L. Wang, Q. Ma, B. Hu and Q. Xu, "A compact sept-band bandpass filter utilising a single multi-mode resonator" *IET Microwaves, Antennas and Propagation*, vol. 13, no. 12, pp. 2013-2019, 2019.

[19] Q. Yang, S. Liu, K.-D. Xu, and A. Zhang,"Compact octa-band bandpass filter based on controllable transmission zeros with wide upper stopband," *Applied Computational Electromagnetics Society*

(ACES) Journal, vol. 36, no. 9, pp. 1159-1163, Sep. 2021.

[20] J. Wang, S. He, F. You, W. Shi, J. Peng, and C. Li, “Codesign of high-efficiency power amplifier and ring-resonator filter based on a series of continuous modes and even–odd-mode analysis,” *IEEE Transactions on Microwave Theory and Techniques*, vol. 66, no. 6, pp.2867-1878, Jun. 2018.

[21] J. Chen, J.-Z. Chen, B. Wu, Y. L. Zhang, and C.-H. Liang, “Design of triple-band microstrip filter with transmission zeros using open stubs,” *Journal of Electromagnetic Waves and Applications*, vol. 26, no. 4, pp. 525-534, Apr. 2012.

Lei Bai received his Masters Degree in Signal and Information Processing from Xi’an University of Technology in 2012. He is currently a doctor at school of microelectronics, Xidian University, His research interests include passive filter design, high-speed integrated circuits, etc.

Yiqi Zhuang received the Ph.D. from Xidian University in 1995. He is the director of the National Integrated Circuit Talents Training Base, professor and doctoral supervisor. His current research interests include communication and power system integration, short-distance wireless communication, microelectronic device noise and reliability application technology, etc.

Zhibin Zeng received the Ph.D. from Xidian University. He has completed the design of wireless Bluetooth system, wireless WIFI system and analysis of signal integrity. He has published more than 10 articles on EI and SCI, and applied for more than 10 patents. His research interests include high-speed circuit design, embedded systems and analysis of signal integrity.

Dynamic Characteristics Analysis of Magnetic Levitation Rotor Considering Unbalanced Magnetic Pull

Shuyue Zhang[1], Zaibin Chen[1], Xiaolian Lv[1], Hongli Yan[1], Jihao Wu[2,3], and Yuanliang Zhou[1]

[1]School of Mechanical and Electrical Engineering
Chuzhou University, Chuzhou 239000, China
shuyue_zhang@126.com, zhouyl2014@mail.dlut.edu.cn

[2]State Key Laboratory of Technologies in Space Cryogenic Propellants
Technical Institute of Physics and Chemistry, Chinese Academy of Sciences, Beijing, 100190, China

[3]University of Chinese Academy of Sciences
Beijing, 100190, China

Abstract **–** The working principle of the motor can cause unbalanced magnetic pull (UMP) between stator and rotor unavoidably. Previous research about nonlinear vibration excited by UMP was focused on the rotor supported by traditional mechanical bearings or gas bearings. However, the magnetic levitation rotor is particular due to the low rigidity provided by the active magnetic bearing (AMB). UMP amplifies rotor vibration in the resonant zone and further excites the nonlinear electromagnetic force, thus producing different vibration phenomena. The paper calculates rotor orbit, spectra analysis, and time-history plot with numerical methods and studies the influence of the rotation speed, eccentricity, key control parameters, and UMP on rotor dynamics in detail. Results illustrate displacement response spectra of the magnetic levitation rotor are quite different from previous research results. The appearing frequency components are inducted by universal formulas in this paper. Furthermore, research shows a slight adjustment of the control parameters affect significantly harmonic components and vibration characteristics. The research results have practical reference significance for fault diagnosis, feature recognition, and controller optimization of the AMB-rotor system.

Index Terms **–** frequency response, magnetic levitation rotor, resonance, rotor orbit, unbalanced magnetic pull, vibration.

I. INTRODUCTION

Active magnetic bearings (AMBs) have the advantages of no wear, high rotation speed, and long life, and they can adjust rotor dynamics by active controlling [1]. Thus, AMBs show incredibly high usage potential in rotating machinery [2, 3]. However, AMBs have the supporting characteristics of ’negative stiffness’, and their electromagnetic forces are nonlinear. Stability and nonlinearity have been continuously researched hotpots.

Magnetic levitation rotating machinery is generally driven by a motor. The air gap between the motor’s stator and its rotor is unavoidably uniform and asymmetric, resulting in the unbalanced magnetic pull (UMP) [4]. UMP leads to unwanted vibrations, causes stability problems, and even produces rubbing between the rotor and the stator [5].

UMP has attracted widespread attention from researchers. Establishing the linear relationship between UMP and eccentricity is convenient for calculating rotor dynamics [6, 7], but the relationship is reliable only when the eccentricity is small enough. Belmans et al. proposed the air gap permeability method to calculate the magnetic flux density for UMP’s analytical formula [8]. Later on, many researchers applied Belmans’s results to determine the nonlinear UMP.

Guo Dan et al. [9] established the UMP’s analytical formula and summarized the vibration characteristics of the ordinary rotor considering UMP. Xu Xueping et al. investigated how the static eccentricity UMP and gravity affect the rotor’s vibration excited by only dynamic eccentricity UMP [10, 11]. Results concluded that the rotor system’s static load has the same influence on rotor dynamics as the static eccentric UMP. Xu also derived the UMP force of a tilting rotor and studied the rotor’s motion behavior in the case [12]. Hui Lui et al. [13] employed a multi-scale perturbation method to obtain the natural frequency and frequency response

Submitted On: October 18, 2021
Accepted On: October 12, 2022
https://doi.org/10.13052/2022.ACES.J.371010

characteristics of the rub-impact rotor-bearing system considering UMP. Li Hao et al. [14] analyzed the UMP's influence on the rotor system supported by gas bearings. In [15], the UMP's nonlinear effects on a colliding rotor for hydro-generator units were investigated by numeral calculations.

Rotor dynamics excited by UMP have been extensively investigated in the above literature, but most of them focus on traditional mechanical bearings or gas bearings. Relatively few studies pay attention to the coupling interaction between the AMB force and UMP. Du Tingshen et al. determined the UMP by the analytical method, and they applied numerical calculation software to verify [16]. Ji Li et al. studied the effects of various eccentricities and different loads on the UMP amplitude and phase [17]. Di Chong compared the UMPs with different eccentricities and proposed the structure optimization scheme of AMB to compensate for UMP [18]. The studies mentioned above did involve the UMP exerting on the magnetic levitation rotor; however, they didn't thoroughly discuss how UMP affects the dynamic characteristics, especially the motion behavior when the rotor is passing through critical speeds.

The stiffness of the AMB-rotor system is relatively small. The rotor generally needs to cross rigid body mode frequency before reaching the rated speed, which is different from the rotor system supported by mechanical bearings and gas bearings. The rotor vibrates intensely when near critical speeds. On this occasion, it tends to vibrate more wildly and more complicated if the UMP is increasing to a certain extent, inevitably causing the AMB to work in a nonlinear region. Additionally, unlike mechanical bearings and gas bearings, the supporting properties of the AMBs depend more on the control algorithms and control parameters rather than their physical structure [19]. Regardless offault detection, state maintenance, or AMB controller design, investigating the rotor's dynamic behavior under UMP is essential.

Therefore, this paper established the rotor system's motion differential equation incorporating nonlinear AMB force, nonlinear UMP, and unbalanced mass excitation force. The rotor system's dynamic behavior with different speeds, mass eccentricity, control parameters, and UMP are discussed in detail with numerical methods.

II. MODEL

A. Nonlinear AMB force

Figure 1 is the schematic diagram of the AMB-rotor system. The radial AMB has eight magnetic poles in all. The AMB force generated by the two pairs of magnets in one single degree of freedom (DOF) can be expressed as follows [1]:

$$f_a = \mu_0 N^2 A \cos\alpha \left[\frac{(i_0 + i(\mathrm{t}))^2}{(s_0 - s(t))^2} - \frac{(i_0 - i(\mathrm{t}))^2}{(s_0 + s(t))^2} \right], \quad (1)$$

where vacuum permeability μ_0 =4π∗10^{-7} N/A^2 denotes the number of coil turns, A denotes the area of magnetic poles, α denotes the angle between two adjacent magnetic poles, t denotes the time variable, s_0 denotes the static equilibrium position, s denotes the displacement of the offset equilibrium position, i_0 denotes the bias current, i denotes the control current controlling the rotor back to the equilibrium position (i_0 + i(t)), and (i_0 – i(t)) represent the total current of the two pairs of magnetic poles with the same DOF.

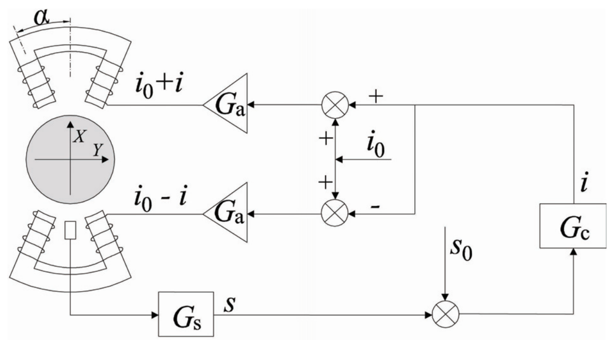

Fig. 1. Schematic diagram of AMB system.

Equation (1) is generally linearized to facilitate mathematical processing and controller design. However, this paper considers the nonlinear effects of AMB by computing the first three terms of the Taylor series. The AMB force expression in the x-direction could be obtained as follows:

$$F_{\mathrm{ax}} = \underbrace{\mu_0 N^2 A \cos\alpha \frac{4i_0}{2} i(t)}_{K_i} + \underbrace{\mu_0 N^2 A \cos\alpha \frac{4{i_0}^2}{{s_0}^3} x(t)}_{K_s} + \mu_0 N^2 A \cos\alpha \frac{8{i_0}^2}{{s_0}^5} x^3(t), \quad (2)$$

where k_i and k_s are the current stiffness and displacement stiffness of AMB. As shown in Fig. 1, in addition to the mechanical structure, the AMB system includes an electronic control system. The controller collects the rotor displacement signal from the displacement sensor and outputs the control current calculated by control algorithms. The control current is converted by the power amplifier to excite each stator winding, thereby generating the AMB attraction.

This research applies a general PID control algorithm. The sensor and power amplifier are modeled with gain G_s and G_a respectively. Thus, the mathematical model of the electronic control system can be expressed as follows:

$$G_c(s) = K_M\left\{G_s G_a\left(K_p + \frac{K_i}{T_i s+1} + \frac{K_d s}{T_d s+1}\right)\right\},$$

where s is the complex variable, K_p is the proportional coefficient, K_i is the integral coefficient, K_d is the differential coefficient, T_i is the integral time constant, and T_d is the differential time constant. To avoid saturation of the power amplifier, a dead zone is pre-set by assigning K_{M-} suitable parameters.

The most critical parameters of the PID controller are the proportional gain and differential gain, which determine the stable levitation and vibration attenuation capabilities. We can build a relationship between these two parameters and displacement stiffness and current stiffness [18]. Thus, the range of proportional gain and differential gain could be determined preliminarily by estimating the system's stiffness and damping. The assigned proportional gain and differential gain ensure that the system stiffness is equal to 2-3 times the 'nature stiffness', i.e., the absolute value of k_s. They also ensure the system damping ratio lies in the range of 20%-70%. In this way, the system can remain stable unless the power amplifier is saturated.

B. The nonlinear UMP

The sources of air gap eccentricity leading to UMP include dynamic eccentricity and static eccentricity. Dynamic eccentricity is caused by the rotor deviating from the equilibrium position during rotation. Incontrast, static eccentricity is caused by the not coinciding between the rotor's static equilibrium position and the motor stator's center. The mixed air gap eccentricity diagram is shown in Fig. 2. The outer circle is the motor stator's inner surface, with the center labeled C, while the internal circle is the outer of the motor rotor, the center marked O. O' is the transient position of the rotor. The offset r between O' and C can be written as:

$$r(t) = \overline{CO'} = \sqrt{(r_0\cos\gamma_0 + x)^2 + (r_0\sin\gamma_0 + y)^2}, \quad (3)$$

where r_0 is the initial eccentricity, and γ_0 is the initial phase angle.

The mixed eccentricity phase angle γ is expressed as follows:

$$\tan\gamma(t) = \frac{r_0\sin\gamma_0 + y}{r_0\cos\gamma_0 + x}. \quad (4)$$

When considering static and dynamic eccentricity simultaneously, the approximate expression of the air gap length at any spatial angle β is derived as follows [9]:

$$\delta(\beta,t) \approx \delta_0 - r(t)\cos[\beta - \gamma(t)], \quad (5)$$

where δ_0 is the average air gap length without the eccentricity. According to the principle of the motor [20], for the three-phase synchronous motor with only one pole pair, the MMF in the air gap is derived as follows:

$$F_p(\alpha,t) = F_j\cos(\Omega t - \beta), \quad (6)$$

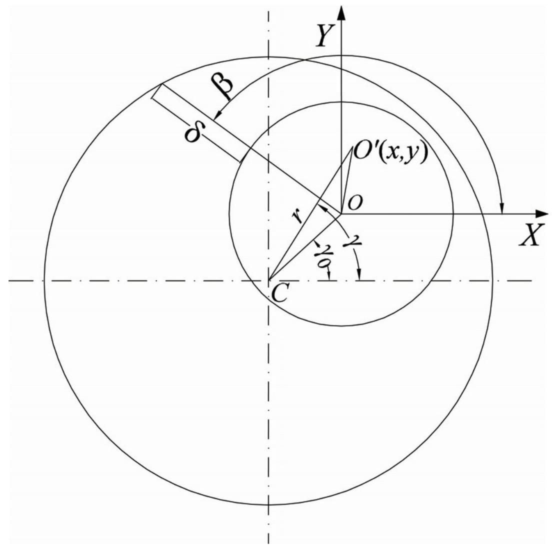

Fig. 2. Schematic diagram of motor's air gap with mixed eccentricity.

where F_j denotes the amplitude of MMF and Ω is the power supply frequency. Therefore, the flux density distribution in the air gap can be estimated as follows:

$$B(\alpha,t) = \frac{\mu_0 F_p(\beta,t)}{\delta(\beta,t)}. \quad (7)$$

According to [9], the above air gap permeability can be expanded using a Fourier series. Ignoring the tangential component of the magnetic density, assuming that the iron core permeability is infinite, and integrating Maxwell stress on the rotor surface, the UMP can be derived as follows:

$$\begin{cases} F_{px} = f_1\cos\gamma + f_2\cos(2\Omega t - \gamma) + f_3\cos(2\Omega t - 3\gamma) \\ F_{py} = f_1\sin\gamma + f_2\sin(2\Omega t - \gamma) - f_3\cos(2\Omega t - 3\gamma). \end{cases} \quad (8)$$

Among them,

$$f_1 = \frac{RL\pi}{4\mu_0}F_j^2\left(2\Lambda_0\Lambda_1 + \Lambda_1\Lambda_2 + \Lambda_2\Lambda_3\right),$$

$$f_2 = \frac{RL\pi}{4\mu_0}F_j^2\left(\Lambda_0\Lambda_1 + \frac{1}{2}\Lambda_1\Lambda_2 + \frac{1}{2}\Lambda_2\Lambda_3\right),$$

$$f_3 = \frac{RL\pi}{8\mu_0}F_j^2\left(\Lambda_0\Lambda_1 + \frac{1}{2}\Lambda_1\Lambda_2\right),$$

where R denotes the rotor radius, L denotes the air gap's axial length, and Λ_n denotes the air gap permeability:

$$\Lambda_n = \begin{cases} \frac{\mu_0}{\delta_0}\frac{1}{\sqrt{1-(r/\delta_0)^2}} & (n=0) \\ \frac{2\mu_0}{\delta_0}\frac{1}{\sqrt{1-(r/\delta_0)^2}}\left(\frac{1-\sqrt{1-(r/\delta_0)^2}}{r/\delta_0}\right)^n & (n>0). \end{cases}$$

Equation (8) shows that the UMP amplitude is mainly determined by the MMF and rotor's position for the structure-determined motor system.

C. The rotor model

The rotor adopts the Jeffcott model. The unbalanced mass force (UMF) can be expressed as follows:

$$\begin{cases} F_{\mathrm{ux}} = me\omega^2 \cos(2\pi\omega t + \varphi_0) \\ F_{\mathrm{uy}} = me\omega^2 \sin(2\pi\omega t + \varphi_0), \end{cases} \tag{9}$$

where m is the equivalent concentrated mass of the rotor at the disc, e is the mass eccentricity, and ω is the rotor's rotation frequency. φ_0 is the initial phase angle of unbalanced mass.

Combining Equations (2), (8), and (9), the differential equation for the lateral vibration can be obtained as follows:

$$\begin{cases} m\ddot{x} = F_{\mathrm{ax}} + F_{\mathrm{px}} + F_{\mathrm{ux}} \\ m\ddot{y} = F_{\mathrm{ay}} + F_{\mathrm{py}} + F_{\mathrm{uy}}. \end{cases} \tag{10}$$

Based on MATLAB/Simulink, we use the fourth-order Runge-Kutta method to calculate Equation (10). The parameters used in the simulation are listed in Table 1, related to AMB, and Table 2, related to UMP and UMF. The parameters used in this paper are consistent with the data in the two tables unless they are explicitly discussed.

D. Model verification

It can be seen from Equation (9) that the mass unbalance force of the rotor is small at low speed. Under the same UMP force, the smaller the mass unbalance force is, the smaller the distance r between the rotor center 'O' and the stator center 'C'. Additionally, according to the definition in Section 2.2, as the rotor approaches the stator center, the UMP force generated by the dynamic eccentricity gradually decreases. Therefore, the rotor is relatively less disturbed by the unbalanced mass force and UMP force at low speed, and thus the vibration displacement is small. This can also be confirmed by the subsequent simulation results.

Table 1: Parameters of the AMB System

Name	Value
Air gap of the AMB, s_0(m)	3.5e-4
Air gap of the auxiliary bearing, (m)	3e-4
Coil turns, N	94
Bias current, i_0(A)	1.5
Magnetic pole area, A(m^2)	2.21e-4
Current stiffness, k_i(N/A)	108
Displacement stiffness, k_s(N/m)	4.76e-5
Sensor gain, G_s(V/m)	20000
Power amplifier gain, G_A(A/V)	5
Saturation limit of amplifier, K$_M$(A)	(-1.5, 2.5)
Proportional gain, K_p	0.1
Integral gain, K_i	0.6
Differential gain, K_d	5.5e-5
Integration time constant, T_i	3/2π
Differential time constant, T_d	1/1600π

Table 2: Parameters of UMP and unbalance mass

Name	Value
Motor rotor radius, R(m)	60e-3
Motor stator length, L(m)	52e-3
Air gap, δ_0(m)	5e-3
Amplitude of the resultant MMF, F_j (A)	2000
Initial phase of motor eccentricity, γ (°)	225
Rotor equivalent concentrated mass, m(kg)	4.85
Mass eccentricity, e(m)	1e-10
Initial phase angle of mass eccentricity, φ_0 (°)	45

Thus, the relationship between the AMB's support force and rotor displacement is nearly linear, and the AMB can be regarded as a conventional bearing [21]. Hence, it is feasible to verify the accuracy of the model and calculation method proposed in this paper by comparing the rotor orbit at low speed with that in the commonly accepted literature [10, 12].

When the rotation frequency is 5, 10, 15, and 20 Hz, the rotor orbits are shown in Fig. 3. Their displacements lie in the range of 0.3 μm to 30 μm, not exceeding 2% of the AMB air gap. For the ordinary bearing rotor system considering UMP and UMF, the rotor orbits at the corresponding frequency are presented in [10] (Figs. 2 (a), (c), and (e)), as well as [12] (Fig. 6 (c)). These document results and our results are in good agreement. Thus the correctness of the program is verified.

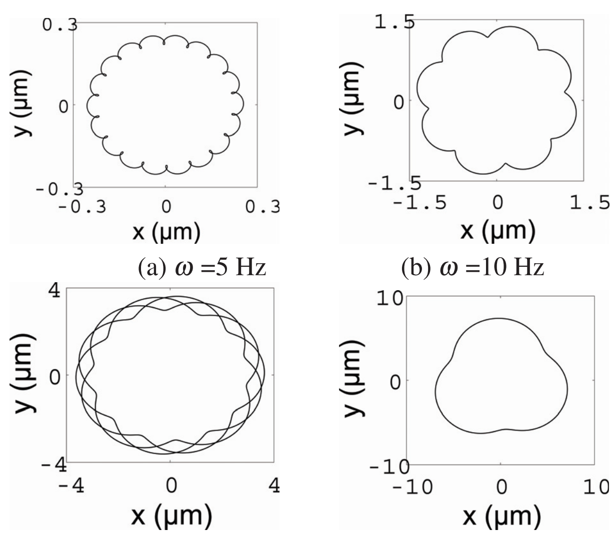

(a) ω =5 Hz (b) ω =10 Hz

(c) ω =15 Hz (d) ω =20 Hz

Fig. 3. Rotor orbit for different rotation speeds.

The following calculation includes two parts: (1) the time domain and frequency domain response characteristics with or without UMP are analyzed and compared, and (2) the effects of different factors on the vibration spectra, rotor orbits and control signals near the resonance zone are investigated.

It should be noted that since the initial phase angle of mass eccentricity and initial phase angle of motor eccentricity (see Table 2) are 45 and 225 degrees, respectively, the waveforms of the unbalanced force, the UMP force, and the current overtime in the x-direction and the y-direction are theoretically the same, with a fixed phase difference. Unless explicitly discussed, the unbalanced force, UMP force, and properties mentioned below refer to the x-direction.

III. DYNAMIC PROPERTIES WITH OR WITHOUT UMP

A. Time-domain properties during the run-up

While gradually increasing the rotation speed, we calculated the transient response of displacement and current every 0.5 Hz, and recorded the maximum and minimum values when in a stable state.

The displacement and total current response results from 0 to 100 Hz are shown in Fig. 4. The maximum and minimum envelopes of rotor displacement are symmetrical, so only the maximum is plotted in Fig. 4 (a) while Fig. 4 (b) presents not only the maximum value of the coil current but also the envelope of the minimum value. The envelope of the maximum value and the minimum value of the coil current is not symmetrical. This is because the minimum value of the coil current is theoretically negative when the vibration is severe, while in practice it appears to be zero due to saturation limitations. We use continuous and dashed lines to represent the cases with and without UMP, respectively. Furthermore, we also divided the run-up process into a low-speed zone, a resonance zone, and a high-speed zone to describe clearly. The figures indicate the vibration not only in the low-speed zone but also in the high-speed zone is relatively slight, and the required control signal is small whether the system is excited by UMP or not.

In contrast, UMP has a larger effect in the resonant zone. The figure presents that the system without UMP has only one resonant peak at 56 Hz. The vibration peak is about 104 μm. The total current fluctuates in the range of 0.44 A to 2.56 A. UMP's existence changes the vibration curve's shape and strengthens vibration intensity significantly in the resonance zone. UMP splits the resonant peak from one into two at 46 Hz and 54 Hz. These two peaks have symmetry about the power supply frequency of 50 Hz. The displacement in the resonant zone reaches 185 μm, exceeding half of the air gap. The current fluctuates from 0 to 3.28 A, coming to its lowest

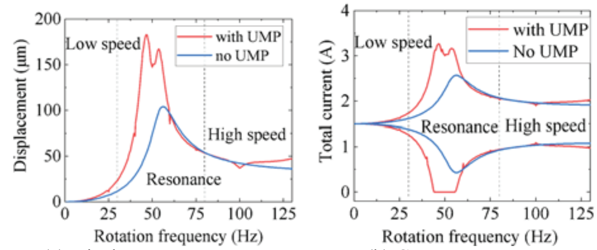

(a) Displacement response (b) Current response

Fig. 4. Amplitude response during run-up with or without UMP.

limit. It can be deduced that a little increment of disturbance may cause control failure and eventually produce a rub.

B. Rotor orbit and displacement spectra

The rotor orbit without considering the UMP at 56 Hz and its spectral analysis are shown in Figs. 5 (a) and (b). The orbit is a full circle, and its spectrum peaks appear at one, three, and five times the rotation speed. On this occasion, rotor motion behavior has no obvious nonlinear characteristics. It can be inferred that AMB mainly works in the linear range.

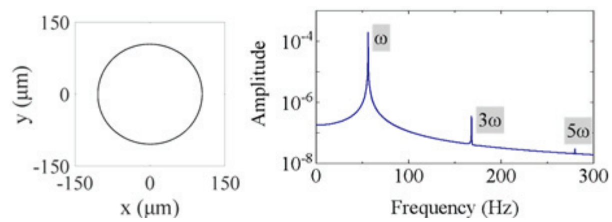

(a) (b)

Fig. 5. Rotor orbit and displacement spectrum at 56 Hz without UMP.

For the case with UMP, we calculate and display the rotor orbit and displacement response spectrum at the specific frequencies (35 Hz, 43 Hz, 49 Hz, 50 Hz, 55 Hz, 57 Hz, and 77 Hz) in the resonant zone and high-speed zone, as shown in Fig. 6.

The rotor's rotation motions and vibration characteristics are enriched by UMP, compared with Fig. 5. It shows that every displacement spectrum has two noticeable main harmonic components at ω_0 and ω_0 + 2(50-ω_0), consistent with the two main resonant frequencies in Fig. 4. Moreover, the peak at ω_0 is always more prominent than that at ω_0 + 2(50-ω_0). It can be attributed to the fact that UMP amplitude depends highly on the dynamic eccentricity caused by the UMF. When the rotation speed approaches the two main resonance speeds from the lower or higher speed, the harmonic amplitude at ω_0 + 2(50-ω_0) excited by UMP's introduction is gradually close to that at ω_0, which is reflected in the more

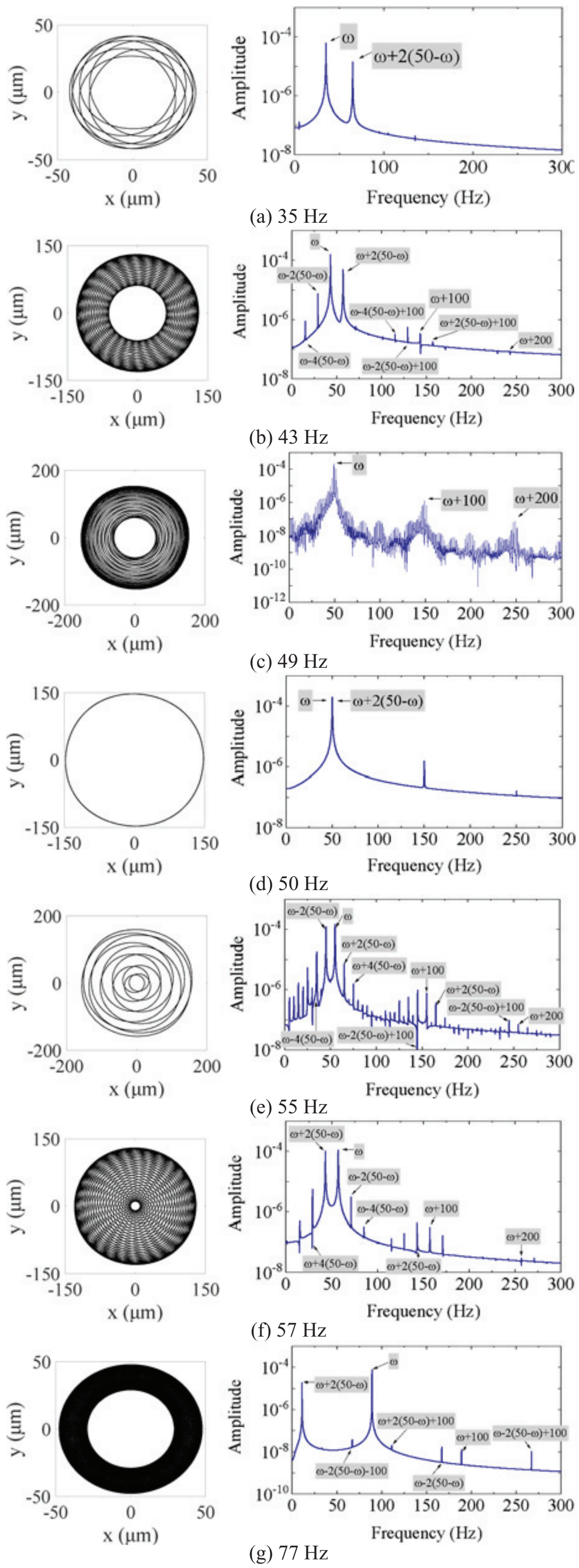

Fig. 6. Rotor orbit and displacement spectra with UMP for different rotation speeds.

significant fluctuation of rotor orbit ultimately. When the rotation speed is 50 Hz, UMP and UMF collectively focus on the same spectrum, and thus the rotor orbit is a circle.

The other sub-harmonics in Fig. 6 all occur at the frequency – the linear combination of rotation frequency and power supply frequency. Only Fig. 6 (c) is an exception, whose behavior is close to chaos due to excessive vibration. These sub-harmonic frequency components occupy an increasingly important position with the rotation speed close to two main resonant speeds, reflecting the nonlinearity in the resonant zone.

Furthermore, the frequency waterfall chart of dynamic response for different rotation speeds is displayed in Fig. 7.

Frequency components radiate to the outer periphery with 50 Hz, 150 Hz, and 250 Hz as the symmetric center point, on the whole. These frequencies can be uniformly described as $\omega_0 \pm 2n_1$ (50 - ω_0) + $2n_2 * 50$, (n_1 and n_2 are natural numbers), and their amplitudes gradually decrease as n_1 and n_2 increase.

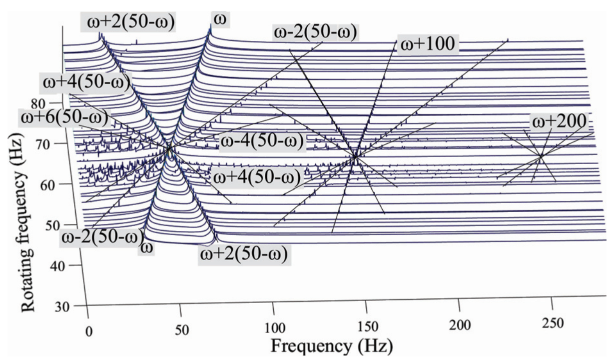

Fig. 7. Frequency waterfall chart of displacement response with the UMP.

The displacement spectra exhibit much difference from that in [9–12]. It can be concluded that their linear combinations between the rotation frequency and supply frequencies are different, i.e., there exist differences in the coupling effects of the magnetic field and the structure field between the AMB-rotor system and the ordinary bearing-rotor system. If the figure is investigated further, it is noticed that the upper half of the symmetry axis with a rotation frequency of 50 Hz in Fig. 7 is similar to that of the ordinary bearing-rotor system, although the direction where frequency components are enhanced is opposite.

IV. EFFECTS OF DIFFERENT FACTORS

A. Effects of mass eccentricity

The UMF is the fundamental reason that causes the rotating rotor to deviate from its static equilibrium position, resulting in the dynamic eccentric UMP. It is of great significance to investigate the vibration characteristics under different *e*. Figure 8 is the rotor's displacement response in the run-up process when *e* is 0.1e-4, 0.4e-4, 0.8e-4, and 1.2e-4.

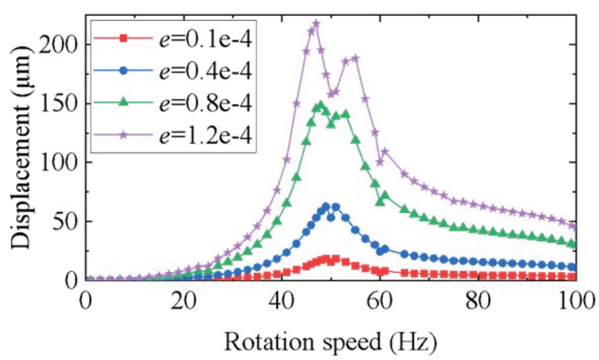

Fig. 8. Displacement response during the run-up for different *e*.

It can be seen that *e* amplifies displacement vibration of the whole run-up process and enlarges the effect of UMP as a result. The two resonant peaks split by UMP are away from each other, and the peaks become more and more outstanding with *e* increasing. Overall, the figure demonstrates that *e* plays a crucial role in the vibration behavior, which means with small UMF, the rotor can keep slight vibration even if UMP is quite large.

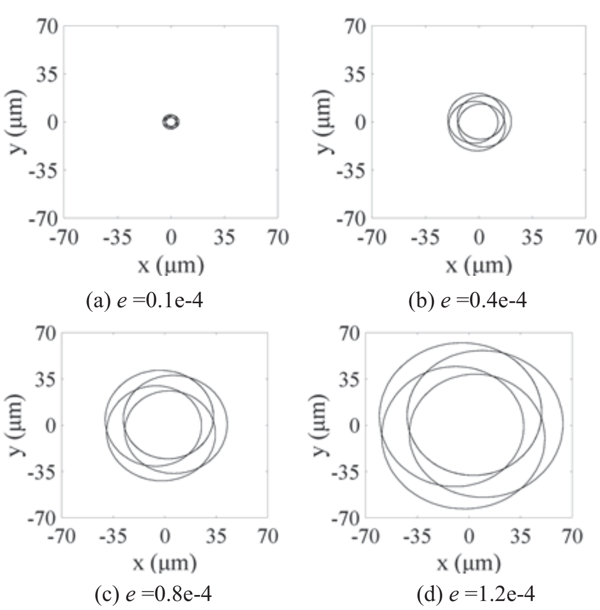

Fig. 9. Rotor orbit at 80 Hz for different *e*.

Specifically, an example of dynamic characteristics at a particular frequency for different *e* is described below. Figures 9-11 are the rotor orbit, displacement spectrum, and control current's time history at 80 Hz, respectively.

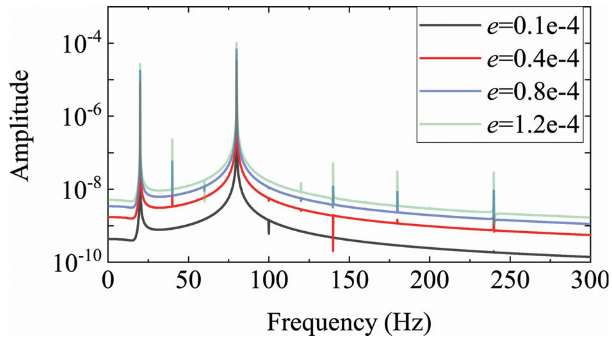

Fig. 10. Displacement response spectra at 80 Hz for different *e*.

Figure 9 show that increasing *e* has a negligible effect on the periodic numbers and the orbit shape, although it expands both the interior boundary and external boundary of rotor orbit. It is also can be observed that the frequency components of displacement response become more and more evident with *e* increasing as shown in Fig. 10.

Figure 11 depicts the fluctuation range of the control current being enlarged by *e*. As *e* increases, the control current waveform changed gradually from the single-period sine waveform similar to UMF to that with multiple periods, approaching the UMP. The reason for the phenomenon is that UMP increases rapidly with the displacement vibration increasing and progressively accounts for a higher proportion of the exciting force exerted on the rotor.

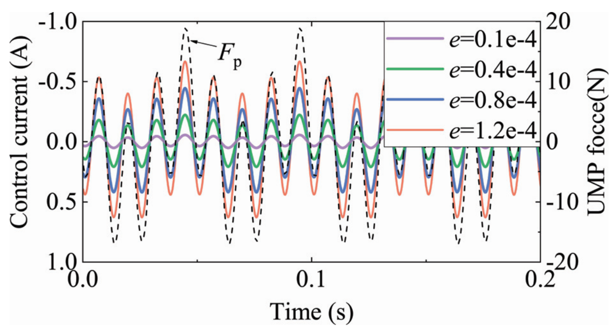

Fig. 11. Time history of the control current at 80 Hz for different *e*.

B. Effects of main control parameters

Unlike traditional mechanical bearings, the support characteristics of the AMBs are not fixed but are affected by the control parameters even when the mechanical structure and working conditions are determined. The influence of the main control parameters is investigated as follows.

(1) Proportional gain

Figure 12 is the displacement response in the run-up process when the proportional gain is at 0.08, 0.1, 0.12, and 0.14. It should be noted that to increase the applicable range of K_p, the mass eccentricity and the differential gain are reduced and increased to e = 0.8e-4 and K_d = 6, respectively. The other parameters remain the same as those in Tables 1 and 2.

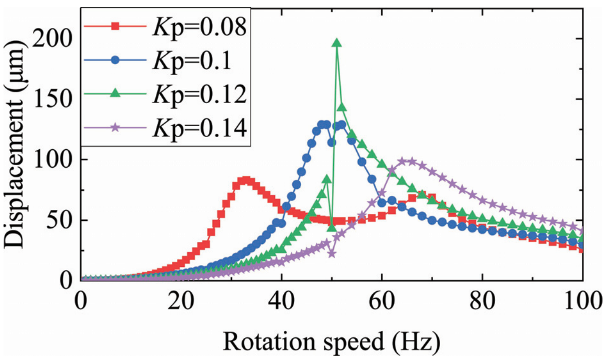

Fig. 12. Displacement response during the run-up for different K_p.

Results show that the increase of K_p moves progressively the entire resonance zone to the right in the coordinate system, which can be attributed to the fact that K_p has a positive correlation with the system stiffness. With a small K_p, two resonant peaks stand outstandingly on both sides of 50 Hz, far apart. In this case, the resonance zone has the characteristics of a wide span and low amplitude. When K_p is increasing, the two prominent resonant peaks are approaching each other, and the amplitude is gradually rising. Then, the two peaks merge into one, with the peak value dropping as K_p increases.

At 51 Hz, rotor orbit, displacement spectrum, and control current time history plot are analyzed in Figs. 13-15, respectively.

Figure 13 shows that as K_p varies, the circular orbit's inner boundary does not change as much as the external edge. It can also be concluded that the vibration at 51 Hz in the resonant zone shows a trend of first increasing and decreasing as K_p increases. The control current increases at the same pace as the displacement, as illustrated in Fig. 15. This is because the rise in K_p moves the left resonant peak in the coordinate system from the left of 51 Hz to the right side, which finally results in severe vibration at 51 Hz when K_p is assigned an intermediate value of 12000. Figures 13 (c) and 14 demonstrate that the motion state at K_p = 12000 is close to chaos. On this occasion, the control current has been saturated, as shown in Fig. 15.

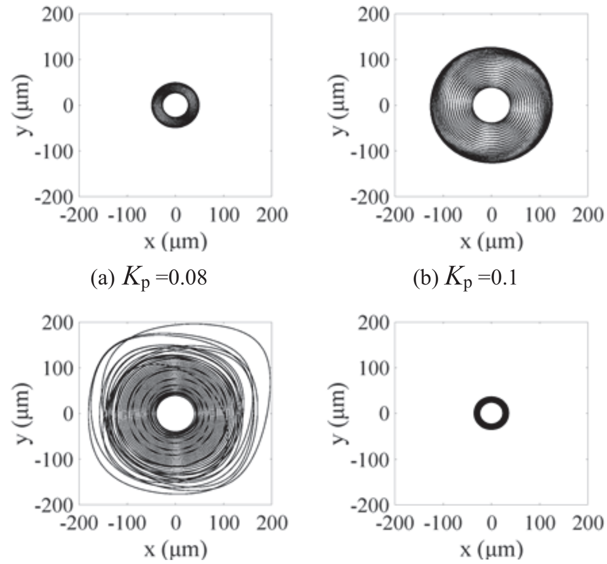

(a) K_p =0.08 (b) K_p =0.1

(c) K_p =0.12 (d) K_p =0.14

Fig. 13. Rotor orbit at 51 Hz for different K_p.

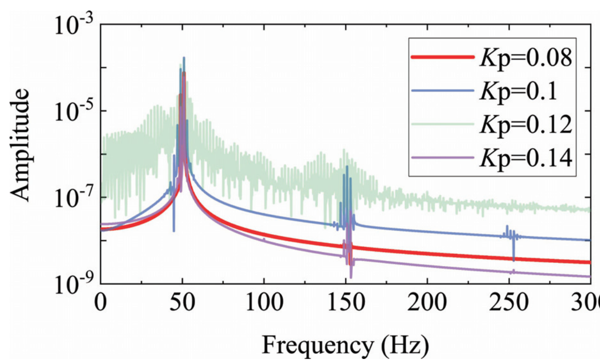

Fig. 14. Displacement response spectra at 51 Hz for different K_p.

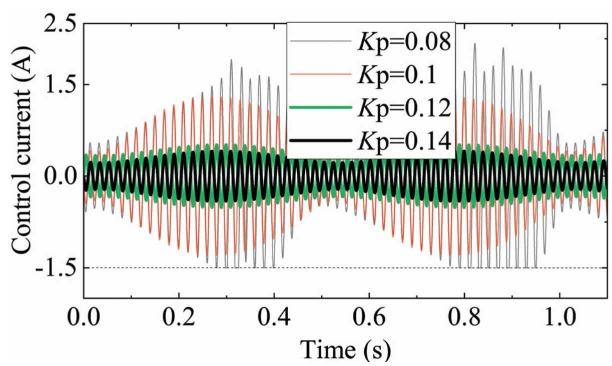

Fig. 15. Time history of the control current at 51 Hz for different K_p.

In summary, a critical conclusion we got is that a slightly larger K_p is more appropriate when controlling a rotor with a larger UMP. The rotor with a small K_p has a long span for the resonant zone. Simultaneously, the medium value of K_p concentrates the resonant peaks and enlarges the vibration, and too large K_p also has certain disadvantages, such as a smaller relative damping and larger control current.

(2) Differential gain

When the differential coefficient K_d is 5e-5, 6e-5, 9e-5, and 1.6e-4, while the other parameters are the same as those in Table 1 and Table 2, the displacement response during run-up is shown in Fig. 16. It can be found K_d has little effect on the resonance frequency but dramatically affects the resonance zone's amplitude, which is attributed to the fact that K_d mainly determines the system damping. Therefore, it is a very effective means to suppress the rotor vibration by improving the differential gain.

Figures 17 and 18 show the rotor orbit and displacement response spectra at 46 Hz for different K_d. When K_d is the smallest value of 5, continuous and abundant frequency components come into view in the displacement spectra of Fig. 18. From Fig. 17 (a), it also can be observed that the rotor is rotating irregularly, accompanied by large fluctuations. With the increase of K_d, the rotor orbit boundary's outer diameter is dropping much while the inner edges are reduced in a relatively gentle way. For further explanation in Fig. 18, the two prominent frequency components are reduced, and the others are suppressed and even eliminated. The time history of the control current in Fig. 19 shows that the current gradually changes from multi-period vibration to single-period vibration with differential gain increasing.

C. Effects of the UMP

The UMP exerted on the rotor in a static levitation state is called the static eccentricity UMP. The UMP

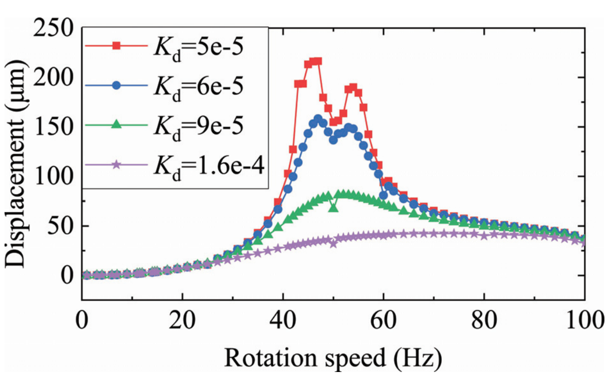

Fig. 16. Displacement response during the run-up for different K_d.

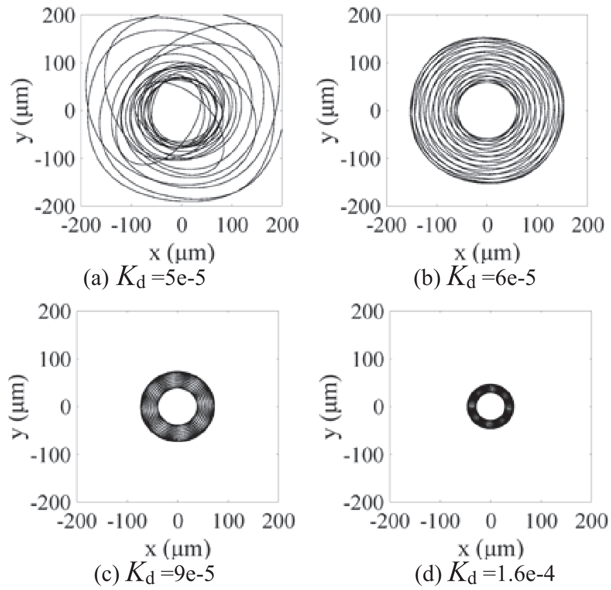

Fig. 17. Rotor orbit at 46 Hz for different K_d.

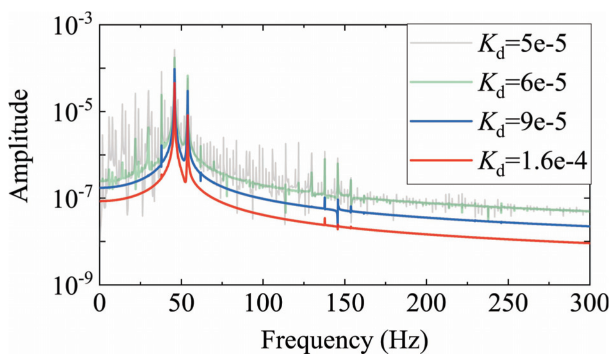

Fig. 18. Displacement response spectra at 46 Hz for different K_d.

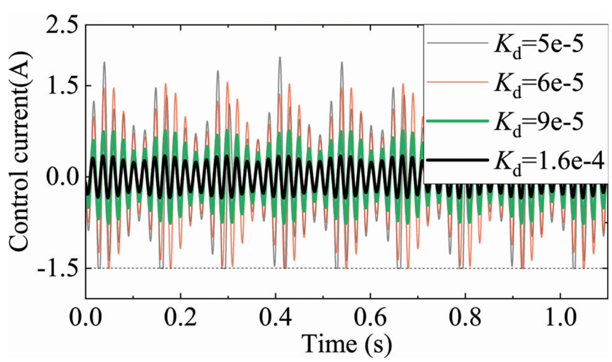

Fig. 19. Time history of the control current at 46 Hz for different K_d.

generated by leaving the stationary equilibrium position due to rotational movement is called the dynamic eccentricity UMP. We use the MMF F_j and the static eccentricity r_0 to measure the dynamic and static eccentric UMP, respectively.

(1) MMF

When F_j is smaller, though the vibration amplitude in Fig. 20 is more extensive, its vibration trend is similar to that without the UMP, as shown in Fig. 4. It is observed that the growth of UMP moves the resonance zone slightly to the left, expands its span, and increases the resonant peaks. Larger F_j splits the single resonant peak into two symmetrical peaks and drives the two away from each other. However, F_j plays a minor role in low-speed and high-speed regions.

Assigning F_j values of 500, 1100, 1700, and 2300, the rotor displacement response during the run-up is depicted in Fig. 20.

Figure 21 shows the rotor orbits with different F_j at 80 Hz of the high-speed range. It can be noticed that the interior boundary of the orbit zone gradually moves closer to the center as F_j increases, while the external edge seems like remaining constant. Consequently, F_j changes the orbit's shape by affecting the interior boundary's size instead of the number of periods.

The displacement response spectra are depicted in Fig. 22. It indicates that increasing F_j slightly attenuates the frequency components at rotation speed but strengthens and enriches the other spectra greatly. The time history of the control current is illustrated in Fig. 23. It reveals that the waveform of the control current changes from an apparent single-cycle motion to a multi-cycle motion composed of 80 Hz and 20 Hz. However, the current peak remains unchanged, about 0.5 A with F_j increasing.

(2) Static eccentricity

All of the above orbit plots are centrosymmetric, which is due to such a small value of the static eccentricity (r_0 =1e-10) adopted that it can be ignored. The aim is to remove the influence of r_0 and focus on the effects of other factors. However, r_0 is inevitable in reality and affects the rotor dynamic characteristics significantly.

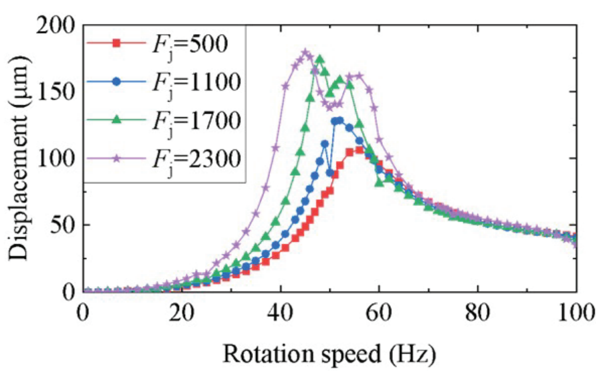

Fig. 20. Displacement response during the run-up for different F_j.

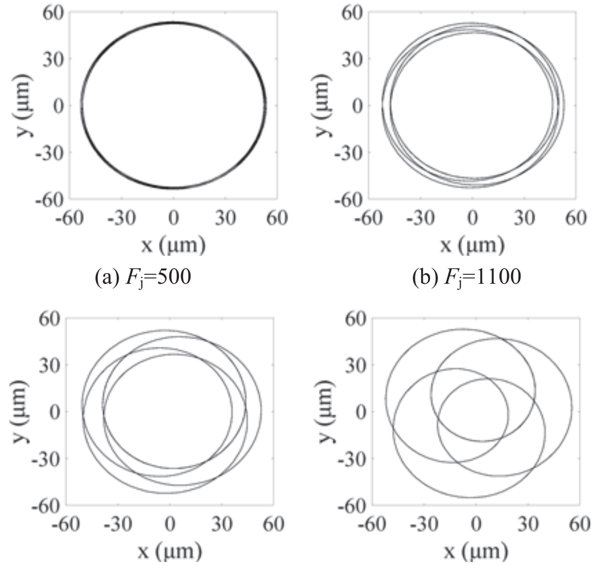

(a) F_j=500 (b) F_j=1100

(c) F_j=1700 (d) F_j=2300

Fig. 21. Rotor orbit at 80 Hz for different F_j.

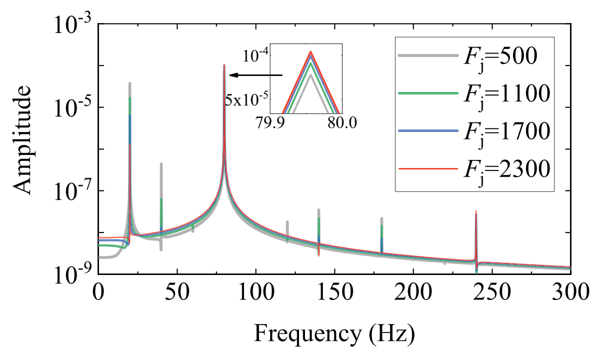

Fig. 22. Displacement response spectra for different F_j.

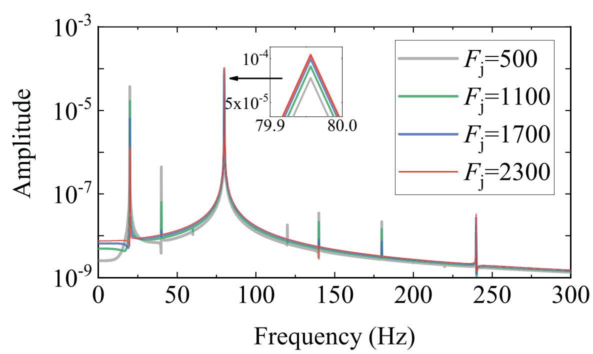

Fig. 23. Time history of the control current at 80 Hz for different F_j.

Figures 24 and 25 are the displacement response and the mixed eccentric phase angle γ (see Fig. 2) response with different r_0 during the run-up. Figure 24 shows that increasing r_0 narrows the resonance zone and moves it to the right in the coordinate's right. It also can be found that as r_0 reaches a certain threshold, the resonant peak decreases sharply. Similarly, according to Fig. 25, the rotor makes small rotations in the specific direction of the coordinate origin O (see Fig. 2) rather than making a revolution motion about O, as r_0 reaches the threshold. It is because in this case, the centrifugal effects generated by UMF are challenging to break free from the shackles of static eccentric UMP.

Figure 26 is the response of the maximum and minimum current during the run-up. It indicates that changing r_0 shifts the symmetry axis of the control current up and down. The control current's balanced position is upward with increasing according to the time history plot in Fig. 27.

Figure 28 shows the rotor orbit at 46 Hz. It demonstrates that the orbit shape affected by r_0 is axisymmetric rather than central symmetry. The displacement response

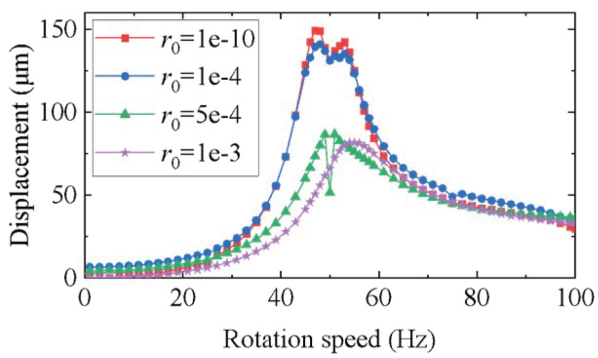

Fig. 24. Displacement response during run-up for different r_0.

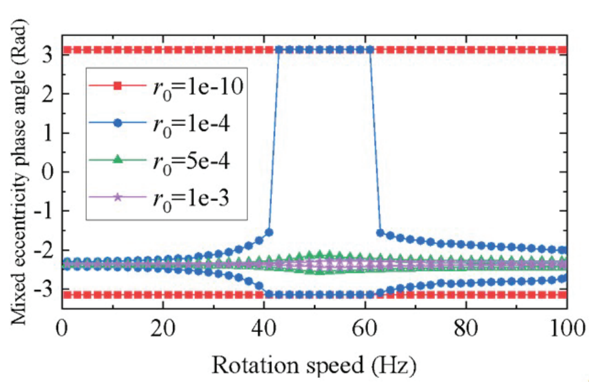

Fig. 25. Mixed eccentric phase angle response for different r_0.

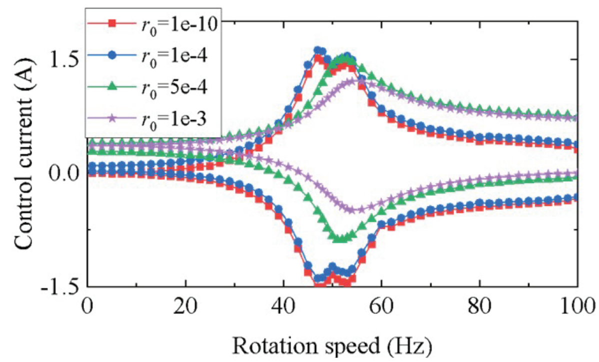

Fig. 26. Control current response for different r_0.

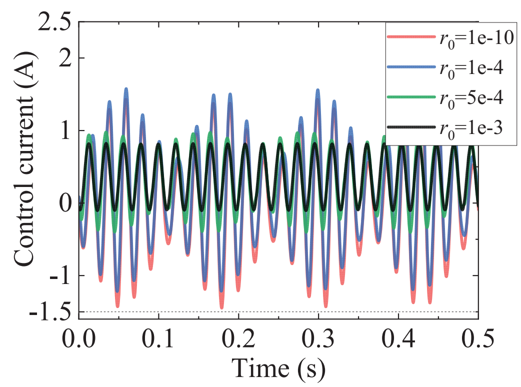

Fig. 27. Time history of the control current at 46 Hz for different r_0.

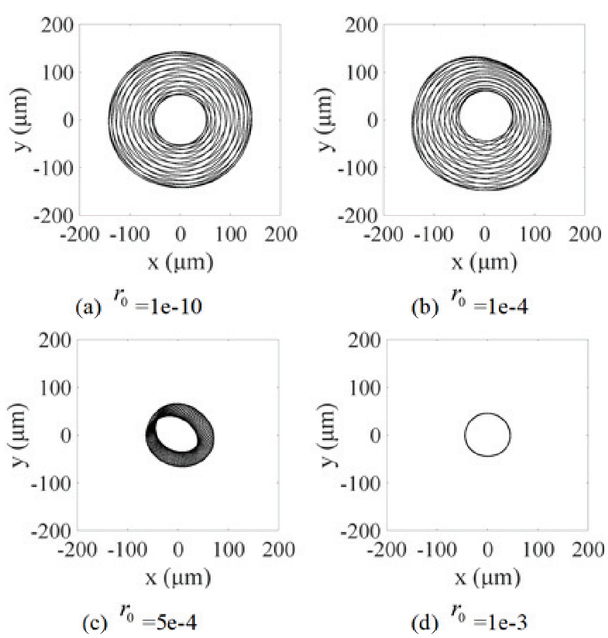

Fig. 28. Rotor orbit at 46 Hz for different r_0.

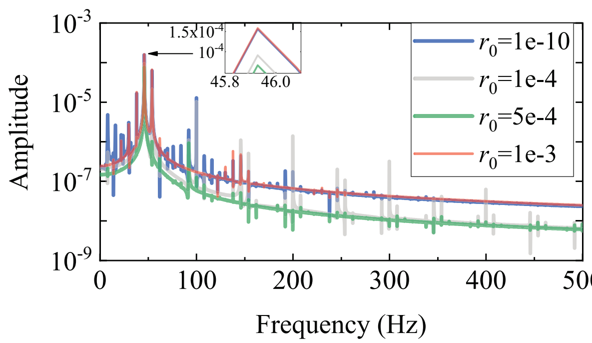

Fig. 29. Displacement response spectra at 46 Hz for different r_0.

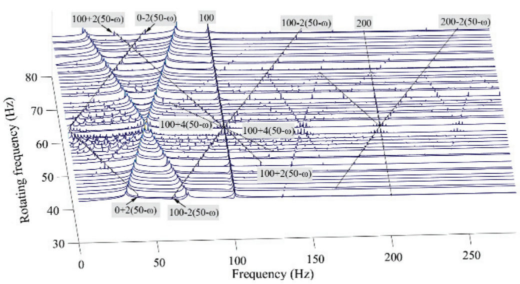

Fig. 30. Waterfall diagram of rotor displacement vibration with the static displacement r_0 =1e^{-4}.

spectra at 46 Hz in Fig. 29 shows that static eccentricity greatly enriches response frequencies compared with Fig. 7 at the same rotation frequency. It enhances the rotor nonlinear motion characteristics by causing new frequency components at 100 Hz and 200 Hz. These new spectra can be described with the uniform expression of $2k_1$ $*50 \pm 2k_2(50 - \omega_0)$ (k_1 and k_2 are natural numbers) and their amplitude has a negative relationship with k_1 and k_2, as shown in Fig. 30.

V. CONCLUSION

The rotor model suffering nonlinear UMP and nonlinear UMP AMB force is established. The effect of control parameters and UMP on the dynamic characteristics when the rotor crosses critical speeds is investigated in detail. The typical conclusions are summarized as follows:

(1) Displacement spectrum of the magnetic levitation rotor system with UMP is quite different from the previous research results with ordinary bearings. UMP splits the original single resonant peak into two symmetrical resonant peaks about the power supply frequency. UMP widens the frequency span of the resonant zone and amplifies the vibration during resonance. With the combined action of the UMP and AMB, the displacement spectrum appears abundant frequency components. Without considering the static eccentricity, these spectral frequencies can be described by $\omega_0 \pm 2n_1$ $(50 - \omega_0) + 2n_2{*}50$ (n_1 and n_2 are natural numbers).

(2) The effect of static eccentric UMP is similar to the force with constant direction and amplitude. To offset the static eccentric UMP, the controller actively generates the bias current as part of the control current. The static eccentric UMP excites the rotor's nonlinear dynamic characteristics, resulting in appearing new frequency components in the displacement response spectrum, coexisting with the previous frequency components. These new spectra can be summarized with the formula of $2k_1{*}50 \pm 2k_2(50 - \omega_0)$ (k_1 and k_2 are natural numbers).

(3) Though the AMB-rotor system without UMP works in a linear working state, UMP's existence may saturate the control current and thus strengthen the nonlinear characteristics of AMB force, which can easily produce control failure and rotor drop.

(4) A slight increment in control parameters causes a significant effect on the dynamic responses. In particular, K_p affects the amplitude and span of the resonance zone. K_d has an important impact on the vibration peak. Applying slightly larger K_p and K_d is recommended to narrow the resonance zone and suppress the resonant vibration of the AMB-rotor system with large UMP.

ACKNOWLEDGMENT

This work was supported by the fund of the State Key Laboratory of Technologies in Space Cryogenic Propellants, SKLTSCP202104.

REFERENCES

[1] G. Schweitzer, E. H. Maslen, H. Bleuler, M. Cole, and A. Traxler, *Magnetic Bearings Theory, Design, and Application to Rotating Machinery*, Springer-Verlag, Berlin, 2009.

[2] S. Y. Yoo, W. R. Lee, Y. C. Bae, and M. Noh, "Design of magnetically levitated rotors in a large flywheel energy storage system from a stability standpoint," *Journal of Mechanical Science and Technology*, vol. 24, no. 1, pp. 231-235, Jan. 2010.

[3] S. Y. Zhang, W. Pan, C. B. Wei, and J. H. Wu, "Structure design and simulation research of active magnetic bearing for helium centrifugal cold compressor," *Proc. of the Cryogenic Engineering Conference and International Cryogenic Materials Conference*, Madison WI, Jul. 2017.

[4] R. Belmans, W. Geysen, and H. Jordan, "Unbalanced magnetic pull and homopolar flux in three

phase induction motors with eccentric rotors," *International Conference on Electrical Machines*, vol. 3, pp. 916-921, 1982.
[5] R. K. Gustavsson and J. O. Aidanpaa, "The influence of nonlinear magnetic pull on hydropower generator rotors," *Journal of Sound and Vibration*, vol. 297, no. 3-5, pp. 551-562, 2006.
[6] U. Werner, "Rotordynamic model for electromagnetic excitation caused by an eccentric and angular rotor core in an induction motor," *Archive of Applied Mechanics*, vol. 8, no. 3, no. 8, pp. 1215-1238, 2013.
[7] H. Kim, J. Nerg, T. Choudhury, and J. Sopanen, "Rotordynamic Simulation Method of Induction Motors Including the Effects of Unbalanced Magnetic Pull," *IEEE Access*, no. 8, pp. 21631-21643, 2020.
[8] R. Belmans, A. Vandenput, and W. Geysen, "Calculation of the flux density and the unbalanced pull in two pole induction machines," *Archiv Für Elektrotechnik*, vol. 70, no. 3, pp. 151-161, 1987.
[9] D. Guo, F. Chu, and D. Chen, "The unbalanced magnetic pull and its effects on vibration in a three-phase generator with eccentric rotor," *Journal of Sound and Vibration*, vol. 254, no. 2, pp. 297-312, 2002.
[10] X. Xu, Q. Han, and F. Chu, "Electromagnetic vibration characteristics of an eccentric rotor with a static load," *Qinghua Daxue Xuebao/Journal of Tsinghua University*, vol. 56, no. 02, pp. 176-184, 2016.
[11] X. Xu, Q. Han, and F. Chu, "Nonlinear vibration of a generator rotor with unbalanced magnetic pull considering both dynamic and static eccentricities," *Archive of Applied Mechanics*, vol. 86, no. 8, pp. 1521-1536, 2016.
[12] X. Xu, Q. Han, and F. Chu, "A four degrees-of-freedom model for a misaligned electrical rotor," *Journal of Sound & Vibration*, no. 358. pp. 356-374, 2015.
[13] H. Liu, Y. Wu, and X. Wang, "Nonlinear normal modes and primary resonance for permanent magnet synchronous motors with a nonlinear restoring force and an unbalanced magnetic pull," *Nonlinear Dynamics*, vol. 97, no. 2, pp. 1197-1213, 2019.
[14] L. Zhang, Z. Ma, and B. Song, "Dynamic characteristics of a rub-impact rotor-bearing system for hydraulic generating set under unbalanced magnetic pull," *Archive of Applied Mechanics*, vol. 83, no. 6, pp. 817-830, 2013.
[15] H. Li, H. Geng, H. Lin, and S. Feng, "Analysis on dynamical properties of the foil bearing rotor system with the unbalanced magnetic pull," *International Journal of Applied Electromagnetics and Mechanics*, vol. 64, no. 1-4, pp. 181-189, 2020.
[16] T. Du, H. Geng, Y. Sun, H. Lin, Zhang Yanan, L. Yu, "Theoretical and experimental researches of active magnetic bearing systems for high-speed PM machines," *International Journal of Applied Electromagnetics and Mechanics*, vol. 59, no. 3, pp. 891-901, 2019.
[17] J. Li, J. Zhou, and H. Wu, "Vibration mechanism analysis of magnetic levitation rotor system for low temperature waste heat power generation," *Proc. of 16th International Symposium on Magnetic Bearings*, Beijing, China, no. 57, pp. 1-8, 2018.
[18] D. Chong, P. Ilya, J. Pyrhonen, X. Bao, "Unbalanced magnetic pull compensation with active magnetic bearings in a 2 MW high-speed induction machine by FEM," *IEEE Transactions on Magnetics*, vol. 54, no. 8, 2018.
[19] Z. Wang, C. Mao, and C. Zhu, "A design method of PID controller for active magnetic bearings-rigid rotor systems," *Process of the CSEE*, vol. 38, no. 20, pp. 6154-6163, 2018.
[20] B. Wu, W. Sun, Z. Li, and Z. Li, "Circular whirling and stability due to unbalanced magnetic pull and eccentric force," *Journal of Sound and Vibration*, vol. 330, no. 21, pp. 4949-4954, 2011.
[21] J. C. Ji, C. Hansen, and A. Zander, "Nonlinear dynamics of magnetic bearing systems," *Journal of Intelligent Material Systems & Structures*, vol. 19, no. 12, pp. 1471-1491, 2018.

Shuyue Zhang received a Ph.D. from the University of Chinese Academy of Sciences and a Bachelor's degree from Dalian University of Technology. Now she works at the School of Mechanical and Electrical Engineering, Chuzhou University. Her main research interests include rotor dynamic and active magnetic bearing control.

Zaibin Chen received his Ph.D. from University of Chinese Academy of Sciences and a bachelor degree from Sichuan University. Now he is an Assistant Professor in School of Mechanical and Electrical Engineering, Chuzhou University. His main research interests include servo motors and their control.

Xiaolian Lv received her Ph.D. from Shenyang Agricultural University. She is currently serving as a Professor in School of Mechanical and Electrical Engineering at Chuzhou University. Her research mainly concerns mechanical design theory and its application.

Hongli Yan now is an Associate Professor in School of Mechanical and Electrical Engineering, Chuzhou University. Her research interests mainly are communication system modeling and wireless communication.

Jihao Wu is currently a Professor and Ph.D. Supervisor of University of Chinese Academy of Sciences. His research interests are magnetic levitation rotating machinery, low temperature rotating machinery, and refrigeration machine.

Yuanliang Zhou received a Ph.D. from Dalian University of Technology. Now he is an Associate Professor of Mechanical and Electrical Engineering, at Chuzhou University. His research mainly concerns electromagnetic field simulation, electromagnetic materials, and their engineering application.